THE INTERACTIONS OF TWO DISEASE-LINKED MEMBRANE PROTEINS WITH THEIR BILAYER MILIEU

By

Kathleen Frances Mittendorf

Dissertation

Submitted to the Faculty of the

Graduate School of Vanderbilt University

in partial fulfillment of the requirements

for the degree of

DOCTOR OF PHILOSOPHY

in

Biochemistry

August, 2015

Nashville, Tennessee

Approved:

Charles R. Sanders, PhD

Melanie D. Ohi, PhD

Tina M. Iverson, PhD

Bruce D. Carter, PhD

Kevin L. Schey, PhD

To my loving parents,

Tom and Darla Mittendorf,

and to my brother and best friend, Isaac Mittendorf,

and my sister-in-law, Emma Mittendorf.

Thank you for always being there.

ACKNOWLEDGEMENTS

This work was made possible by NIH grants U54 GM94608, PO1 GM080512, RO1 NS0508815, RO1 DC007416, RO1 DK083187, R01 HL122010, and RO1 GM106672 (to Charles R. Sanders, PhD) and 1DP2OD004483 (to Melanie D. Ohi), as well as an NSF Graduate Research Fellowship Grant DGE0909667 (to the author). First and foremost, I would like to thank my mentor and Ph.D. advisor, Dr. Chuck Sanders.

Chuck has always done everything in his power to provide the resources necessary for my project, even when the NIH funding for this project stalled. He has also encouraged me to pursue my areas of interest in the project, even when those areas were outside the expertise of the Sanders lab. As a result, he has helped me foster a number of collaborations, which have been some of the greatest experiences of my graduate career. I know that the collaborative spirit of the Sanders lab will always stick with me. Chuck will always have my gratitude for pushing me to be the best scientist that I can be and for introducing me to a wonderful, collaborative scientific atmosphere. Thank you, Chuck, for the hours that you have spent with me, to ensure that I do the best work possible and become the best scientist I can be leaving the lab. I must also thank Chuck for your understanding of human situations that can interfere with scientific progress. Chuck makes the lab an incredibly supportive environment, and he is always very carefully considering “RCR” in more ways than one. His moral ethic is something I hope to carry with me as well. To him, I owe my future.

One of the collaborations Chuck encouraged me to develop was with the laboratory of Dr. Melanie D. Ohi. In Mel I have found a fantastic second mentor. Mel has encouraged me and pushed me when I have needed it. More than once she has convinced me to continue with my graduate studies, if only once she was aware of it. She also has encouraged me greatly to pursue becoming a principal investigator. She

has further been incredibly important in encouraging me to push through a number of personal challenges and in providing invaluable support during those times. Finally, Mel allowed me to share in the editing of a number of her R01 applications and in a number of papers in the lab. I have found these experiences to be an integral part of my training, and it has been incredibly important to me to be a part of them. It is safe to say that without Mel, I would not be the person or the scientist I am today.

I am also indebted to the NSF Graduate Research Program and the NIH via the Molecular Biophysics Training Program (MBTP) for providing funding for my research. These programs allowed me to have a number of experiences I would not otherwise have had. I must also thank Dr. Walter Chazin, who has served as a mentor to all of us on the training grant. Since I rotated in Walter's lab as a first year, I have found nothing but support from him. I am especially grateful for his teaching me as a singular student in the protein NMR class, his allowing me to TA the structural biology module, and his writing letters of reference during my postdoctoral search. I am incredibly grateful to call him another mentor and "honorary" committee member. I would also like to express my deepest gratitude to those graduate committee members whom I have not yet mentioned: Drs. Tina Iverson, Bruce Carter, and Kevin Schey. Their guidance, support, and encouragement have been invaluable. Additionally, they have gone above and beyond the duties of a committee member, attending almost every seminar I have given in graduate school—even those outside of their departments. I have found that I can bump into them on campus any given day and expect some new insight or encouragement for continued progress toward my degree. I am especially grateful to Tina, as she is the person who first piqued my interest in membrane protein research when I visited Vanderbilt on an interview weekend and has remained a wonderful faculty role model since the time of our first meeting. I am also grateful to Bruce and Kevin for

allowing me to conduct a number of preliminary experiments in their laboratories and for meeting with me countless times to discuss those experiments.

I must also thank a number of faculty members who have served as impromptu mentors and sources of support throughout my graduate career: Drs. Brandt Eichman, David Cortez, Scott Hiebert, Lauren Jackson, Ben Spiller, Borden Lacy, Puck Ohi, Tony Weil, Jen Gaddy, and Nick Reiter.

I extend my greatest appreciation to so many past and current Sanders and Ohi lab members. First, to those whose work directly contributed to the manuscripts that make up a bulk of this dissertation and who are or will be listed as coauthors on those publications: Drs. Yuanli Song, Zhenwei Lu, Brett Kronke, and Jonathan Schlebach, as well as Cheryl Law, Arina Hadziselimovic, and Mariena Silvestry. Specific thanks go as well to many lab members for their contributions to my training and for their friendship. To Dr. Wade Van Horn, a mentor and friend. I value his trust in me as an editor of grants and papers and his advice to me in times of personal and professional doubt. To Arina Hadziselimovic, for her molecular biology expertise, seamless lab managing skills, and a countless number of lunches at Panera and ice creams at Hot and Cold. To Dr. Yuanli Song, a valuable friend, mentor, and collaborator. To Dr. Jonathan Schlebach, for the “smoke breaks,” the intense scientific discussion, and the valuable friendship. To Dr. Zhenwei Lu, for experimental expertise in times of crisis and warm friendship. To Haley Harrington, the most efficient, effective, and dedicated undergraduate I will likely ever have the privilege to work with; Haley is more colleague than mentee. To Catherine Deatherage, for steadfast advice and troubleshooting expertise. To Cheryl Law, my office-mate and friend and provisioner of a valuable control. To Dr. Brett Kroncke, for his scripting knowledge, collaboration, and ever-questioning scientific approach. To Dr. Masayoshi Sakakura, my initial mentor in the lab. To Danielle Kelly for the assistance and training. To Dr. Paul Barrett, for his mentorship and assistance in a number of

professional milestones. To the newest Sanders lab postdocs, for mentorship, friendship, and good science: Hui Huang, Loren LaPointe, and Keenan Taylor. To Dr. Yoshimasa Takizawa and Melissa Chambers for friendship and training in electron microscopy. To Tasia Pyburn, Dr. Scott Collier, Dr. Elad Binshtein, and Nora Foegeding for collaborative spirit and assistance when I was lost in the Ohi lab. To Mariena Silvestry, for her continued instruction and cat-love.

My final thanks in the world of academia go out to friends and colleagues in other labs and departments who have offered kindness, scientific support and suggestions, baked goods and soups delivered at wee hours of the morning, and so much personal advice and support as we go through this journey of academia together. Most especially I must thank: Jessica Luzwick, Amanda Meyer Johnson, Dr. Tara Archuleta, Joe Alvin, , Dr. Natalie Shanks, Elaine Ritter, Michelle Stokes Krakowiak, Jamie Wenke, Marilyn Holt, Lisa Poole, Norie Sugitani, Dr. Bianca Sirbu, Dr. Amicia Elliot, Allyson (McLeod) Perry, Dr. Emma Sturgill, Dr. Stephanie Hirst DeLuca, Liz Ferrick, Kyle Becker, Amanda Taylor, Scott Kelly, Jake Hall, Justin Menestrina, Una Natterman, Kaleigh Bangor, Casey Brock, and, last, but far from least, Sonja Ostrow. I am especially grateful to those people who edited this thesis without obligation or reward: Lisa Poole and Loren LaPointe. Without the steadfast support of all these people—named and unnamed—and their midnight science discussions, Korean (or American) cooking, chocolate gifts, care, and love, I would not be the person or the scientist I am today. You are all my family.

Now I must thank those wonderful people who, despite not living in the world of academia, have nevertheless been incredibly patient and understanding supporters. Most especially, my first thanks must be extended to my family, without whom I would have never gotten through any stage of my education. Most especially I thank my mother, who inspired me to go into research. Her continued support, displays of strength and self-sacrifice, and her battle with a disease we don’t understand have been my

constant inspiration. All of my family have been so important: my father, who has been so supportive and has inspired me to be a better person; my little brother, my first and best friend, and his wife, Emma; my maternal grandparents, Grandpa and Grandma; my paternal grandparents, Granddad and Phis. Special thanks to the cousin who offers text support every day, Tracy, and a cousin who was there at a critical time, Dominique. Thanks extended also to Aunts Sarah, Debbie, Diana, and Madonna (not everyone was raised by a strong matriarchy), Uncles Mark and Larry, cousins Derek and Stephanie, Collin, Mandy, Jay, Jemal and Nikki, Cory, Stephen, Cassie, Levi, Julia, Heather and Alex, Josh and Amy, Jason, Gavin, Camryn. Also to my friends outside of science: Kortney Kennedy and Brooke Armstrong, who have been there always; Kip Denhartigh, my Nashville best bud and belay partner, who puts up with so much; Bryan Shelton, who has done so much for me; Dr. Angela Shields, Katelyn Carrick, Lindsay and Chris Seifert, who will always be part of me; to so many other climbers and friends; to Solomon Santistevan, for showing me what it means to care for someone; to Leigh Rast, a steady and important presence; to Kevin for his support early on; to Ace, to Natalie Burke, and to Natalie Paul, who were each, in their own ways, so very important. Finally, to the many amazing teachers I had throughout my life, inside and outside of the classroom: the teachers of Jefferson Elementary, Massac County High School, and the First United Methodist Church of Metropolis, and the extraordinary professors of DePauw University. I cannot name you all, but thanks especially are extended to these individuals: George Femmer, Ms. Rushing, Ms. Thomasson, Ms. McNichols, Ms. Hutcherson, Ms. Kindle, Ms. Murley, Ms. Gallip, Mr. Clark Speck, Ms. Rogers, Ms. Gill, Frau Pirtle, Mr. Rhodes, Ms. Bird, Ms. Bremer, Ms. Thompson, Mr. Pirtle, Dr. Gurnon, Dr. Crary, Dr. Schneider, Drs. Roberts, Dr. Hansen, Drs. Seaman, Dr. Vaglia, Dr. Dudle, Dr. Eppley, Dr. Hazel, Dr. Fornari, and Tavia Pigg. You will always be my teachers,

professors, mentors, and friends. One day, I hope you will call me colleague. Nothing would make me prouder.

TABLE OF CONTENTS

Page

LIST OF TABLES

LIST OF FIGURES

LIST OF ABBREVIATIONS

APP	Amyloid Precursor Protein
C99	99 residue C-terminal fragment of the amyloid precursor protein
PMP22	Peripheral Myelin Protein 22
CMTD	Charcot Marie Tooth Disease
MLA	Myelin-like Lipoprotein Assembly
NMR	Nuclear Magnetic Resonance
FMM	Fluid Mosaic Model
PS	Phosphatidylserine
PE	Phosphatidylethanolamine
ER	Endoplasmic Reticulum
GPI	Glycophosphatidylinositol
DRM	Detergent-Resistant Membranes
CMC	Critical Micelle Concentration
GPCR	G-protein coupled receptors
MSP	Membrane Scaffolding Protein
EPR	Electron Paramagnetic Resonance
DHPC	1,2-dihexanoyl-*sn*-glycero-3-phosphocholine

EM	Electron Microscopy
LCP	Lipidic Cubic Phase
PG	Phosphatidylglycerol
CL	Cardiolipin
AQP0	Aquaporin-0
DMPC	1,2-Dimyristoyl-*sn*-Glycero-3-Phosphocholine
DAGK	Diacylglycerol Kinase
AD	Alzheimer's Disease
Aβ	amyloid β-peptide
C83	83 residue C-terminal fragment of the amyloid precursor protein
AICD	APP-intracellular domain
BACE1	β-site APP cleavage enzyme 1
PNS	Peripheral Nervous System
CNS	Central Nervous System
CNP	2',3'-Cyclic-Nucleotide 3'-Phosphodiesterase
PLP	Proteolipid protein
P_0	Myelin Protein Zero
ECL1	Extracellular Loop 1

ECL2	Extracellular Loop 2
HNPP	Hereditary Neuropathy with Liability to Pressure Palsies
DSS	Dejerine-Sottas Syndrome
LMPG	lyso-myristoylphosphatidylglycerol
CHAPSO	3-[(3-cholamidopropyl)dimethylammonio]-2-hydroxy-1-propane-sulfonate
ESM	Egg Sphingomyelin
BSM	Brain Sphingomyelin
MSM	Milk Sphingomyelin
POPC	1-Pamitoyl-2-Oleoyl-Phosphatidylcholine
Ch	Cholesterol
DLS	Dynamic Light Scattering
TROSY	Transverse-Relaxation Optimized Spectroscopy
EDTA	Ethylenediaminetetraacetic acid
Gd-DTPA	Gd(III)-diethylenetriaminepentaacetic acid
CHAPS	3-[(3-cholamidopropyl)dimethylammonio]-1-propanesulfo-nate
POPG	1-palmitoyl-2-oleoyl-*sn*-glycero-3-phospho-(1'-rac-glycerol)
D_2O	Deuterium oxide

16-DSA	16-doxylstearic acid
GST	Glutathione *S*-transferase
ERAD	Endoplasmic Reticulum Associated Degradation
WT	Wild-type
IMLFs	Intracellular Myelin-Like Figures
LPR	Lipid-to-Protein Ratio
cys-PMP22	C42S,C53S-PMP22
cysless-PMP22	C42S,C53S,C85A,C109A-PMP22
TrJ	TremblerJ
TM1	Transmbrane Domain 1
TM2	Transmbrane Domain 2
TM3	Transmbrane Domain 3
TM4	Transmbrane Domain 4
ICL	Intracellular Loop
RMSD	Root Mean Square Deviation
HSQC	Heteronuclear Single Quantum Coherence
TROSY	Transverse-Relaxation Optimized Spectroscopy
PRE	Paramagnetic Relaxation Enhancement

TEM	Transmission Electron Microscopy
DDMB	n-Dodecyl-β-D-Melibiose
DOPC	1,2-Dioleoyl-*sn*-Glycero-3-Phosphocholine

CHAPTER I

INTRODUCTION TO MEMBRANES AND MEMBRANE PROTEINS

Statement of Purpose

The purpose of the following chapters is to elucidate the relationship between membrane environment and human membrane proteins, with a focus on two disease-linked human membrane proteins: the 99-residue C-terminal fragment of the amyloid precursor protein (APP), C99, which is involved in Alzheimer's disease (AD), and peripheral myelin protein 22 (PMP22), which is involved in Charcot Marie Tooth Disease (CMTD) and related peripheral neuropathies. The overall story of this dissertation can be considered as two sides of the same coin. One side of this coin focuses on the effects of membrane environment on a protein, using C99 as a case study, and the other side of this coin examines the effects of a protein on its membrane environment, using PMP22 as a case study. As there are two sets of relevant background information, two introductory chapters will be presented.

Chapter I will serve as an introduction to membranes, membrane proteins, and membrane mimetics, and will include a brief primer on C99. Chapter II will serve as a primer on peripheral myelin ultrastructure and the proteins contributing to the myelin organization, including PMP22. Follow the introduction, three data chapters will explore in detail these effects as examined experimentally. The first of these (Chapter III) will highlight how the hydrophobic width of the bicelle affects C99 structure and topology. It will be shown that C99 overall structure is unaffected by hydrophobic width of the bilayer components, demonstrating a remarkable example of protein tolerance to changes in lipidic environment. It will further be demonstrated that C99 adapts to changes in hydrophobic width asymmetrically relative to the bilayer normal. The implications for

disease will be discussed. The second story (Chapter IV) will focus on the reconstitution of PMP22 into a vesicular environment, a reconstitution that results in organized and layered assemblies of membranes reminiscent of myelin (myelin-like lipoprotein assemblies, MLAs). Considerations of possible PMP22 function and its implication in disease will be discussed. Finally, the last story (Chapter V) will highlight a computational model of PMP22 generated from the crystal structure of a homologous tetraspan membrane protein, claudin-15. This model was used to explore potential effects of disease mutations and the implications are discussed. These findings will support that PMP22 is likely destabilized in disease, highlight the need for determining the effects of various disease mutations on protein structure and stability via *in vitro* assays, and establish one such *in vitro* functional assay. Chapter VI will reflect upon the implications of Chapters I-V. Finally, Chapter VII will offer a brief primer on the methods employed in this work, and Chapter VIII will present some preliminary data on the future directions of these studies.

Membranes and Membrane Proteins

The eukaryotic cell is separated from its environment via a selectively permeable membrane composed of a bilayer of amphipathic lipids, including phospholipids, glycolipids, and sterols (Figure 1.1a). Membranes further divide cells into various compartments, called organelles, which perform precise functions. Residing within the membrane entities are the numerous intramembrane proteins, which variously act as transporters or channels to control the entry and exit of certain molecules, as receptors to outside ligands that stimulate intracellular signaling cascades, as structural proteins to facilitate cell shape and/or function, and/or as enzymes to catalyze specific, compartmentalized reactions (Figure 1.1a)(Chiu, 2001). The organization of the cell into compartments and the regulation of the contents of the cell and its organelles by the

membrane enable an individual cell to have a specific function within an organism, and thus allow for the existence of higher-ordered organisms. Because the cell membrane is composed of amphipathic molecules, it has unique chemical properties; as a result, the proteins that reside within the cell membrane are, in practice, difficult to study. However, approximately ~20-50% of the proteome is made up of membrane proteins, and more than 50% of drugs on the market today act on membrane proteins, making them important targets of research (Chiu, 2001). This dissertation focuses on (i) the development of membrane mimetics for the study of membrane proteins, (ii) the application of those membrane mimetics in nuclear magnetic resonance (NMR) studies of the Alzheimer's disease-related protein C99, and (iii) studies of a likely native function of PMP22 as a membrane-organizing protein and how this relates to its structure and role in heritable peripheral neuropathies.

Introduction to the fluid mosaic model and exceptions to the rule

The description of the eukaryotic cell membrane presented above generally depicts that of the fluid mosaic model (FMM, Figure 1.1a) of the biological membrane, developed by Singer and Nicholson (1972) (Singer, 2015). This model has largely persisted in the field for over forty years, though a number of complicating factors and exceptions have been discovered. In the FMM, the bilayer of lipids contains proteins residing within it and can be considered a two-dimensional liquid in which the resident lipids and proteins are free to laterally diffuse. While scientists still generally conceptualize membranes as a two-dimensional fluid, it is currently appreciated that this model is an oversimplification. Membrane lipids and membrane-associated proteins are anisotropically distributed, with a higher concentration of sterols and sphingolipids in the outer membrane leaflet, and a majority of the negatively charged phosphatidylserine (PS) and the polar but neutral phosphatidylethanolamine (PE) residing on the inner

leaflet (Fadeel and Xue, 2009). PS and PE are concentrated at the inner leaflet in an active process by membrane-resident enzymes that serve to facilitate membrane lipid "flipping" along the longitudinal axis (Fadeel and Xue, 2009). Phosphatidylcholines and sphingolipids, on the other hand, are largely distributed on the outer leaflet, which in turns creates a preferential association of sterols to the outer leaflet as well (Fadeel and Xue, 2009). Finally, proteins are inserted in the membrane during synthesis in an asymmetric fashion, having a preferred orientation as determined by the translocon—the channel through which endoplasmic reticulum (ER) proteins pass during synthesis and which recognizes and inserts transmembrane segments—and other factors such as membrane potential (Bogdanov et al., 2014; Cymer et al., 2015). Thus, while the FMM in its simplest form creates a physical model of the membrane as a two-dimensional fluid, already the picture is far more complex.

In addition to the asymmetric distribution of membrane components within the two-dimensional fluid, it is now appreciated that there are a number of limiters to free lateral diffusion, restricting the movement of certain molecules within membranes locally. For instance, a number of membrane proteins are more or less bound to the underlying cytoskeleton, meaning that they are relatively fixed within the membrane. These bound proteins, in addition to themselves not obeying the FMM, can create local disturbances, serving as "pickets" and "fences" to prevent the free diffusion of molecules that become temporarily trapped amongst a high concentration of fixed proteins (Figure 1.1c) (Kusumi et al., 2004). There also exist membrane domains often referred to as lipid rafts, which are in dynamic exchange with the bulk "fluid" membrane, but which are composed of preferentially associating lipids and proteins (Figure 1.1b) (Simons and Ikonen, 1997). Finally, some proteins may associate with a preferential "shell" of annular lipids, and proteins are highly concentrated in the biological membrane, leading to the so-called "shell model" (Figure 1.1d) (Jacobson et al., 2007). However, it should be noted that

none of these models are mutually exclusive, and an adapted model incorporating elements of the initially proposed FMM and the subsequent “exceptions” to this model, can be created (Figure 1.1e) (Kwiatek et al., 2014).

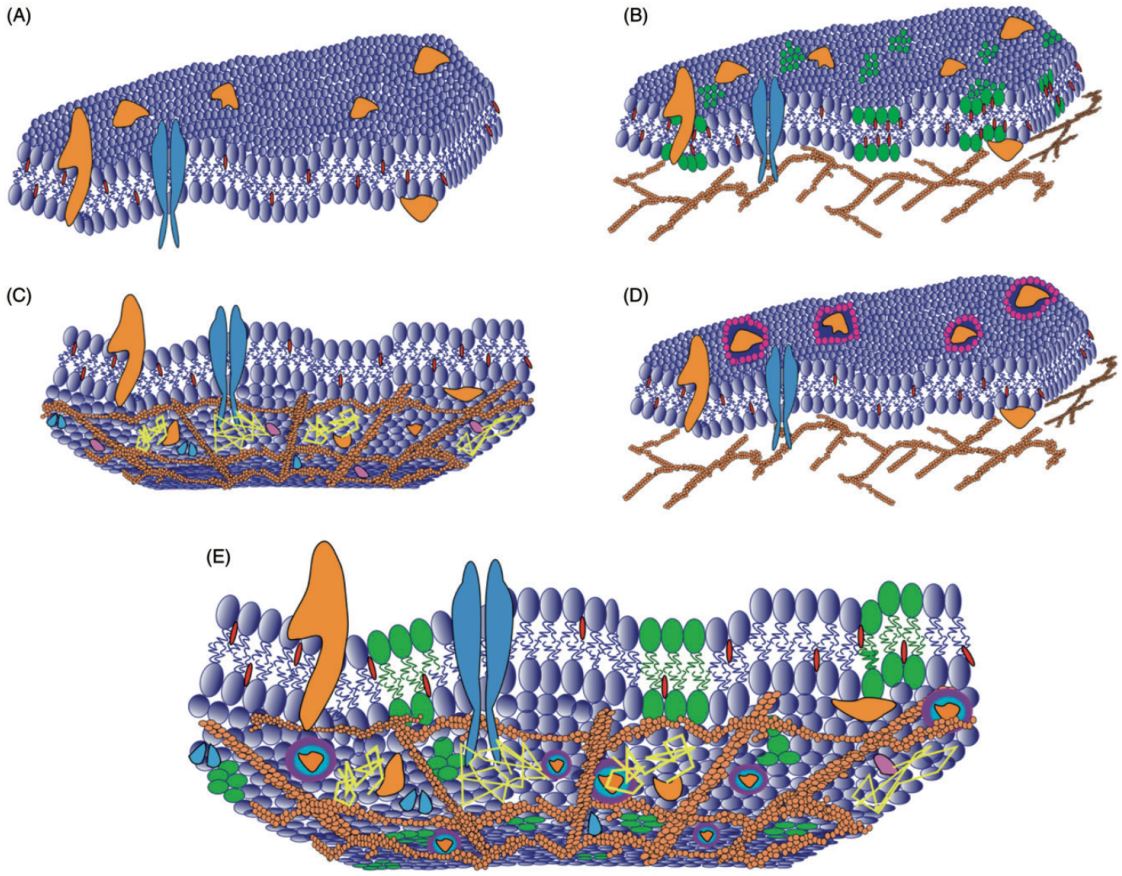

Figure 1.1. Membranes as two dimensional fluids: various models.
(A) A depiction of the Fluid Mosaic Model as proposed by Singer and Nicholson (1972) in which proteins (blue and orange shapes) and lipids and sterols (purple and red shapes, respectively) are free to diffuse in the lateral dimension. (B) A depiction of the raft hypothesis where small domains of sphingolipids and sterols form. (C) A depiction of the picket fence model where membrane proteins (blue and orange) and lipids are bound to the inner cytoskeleton (brown circles), creating diffusion traps where lipids can freely diffuse only within a section of membrane (diffusion tracks represented by yellow lines). (D) A depiction of preferentially associating annular lipid “shells”. (E) A model demonstrating that these principles are not mutually exclusive. Figure adapted from Kwiatek et al., 2014.

The “fluid” phase of the bulk—that is, non-raft—membrane is typically referred to as the liquid crystalline, or L_α, phase. In this phase, head groups are loosely packed and have rotational freedom, and acyl tails are not rigidly packed, instead “dancing” freely amongst their neighbors. This motion results in individual lipid molecules taking up more space in the lateral dimension but a decreased hydrophobic width as a result of freer tail motion. Because membranes are “liquids,” they can undergo a phase transition like any other molecular system. When cooled below their phase transition temperature, membrane lipids enter a phase called the “solid” gel phase, L_β. In the gel phase, the acyl tails are much more rigid and tightly packed and the head groups move less freely. This tight packing leads to a straightening of the lipid tails, which lends a larger hydrophobic width to gel-phase membranes, while the reduced lateral motion of the head groups results in a smaller per-molecule area in the lateral dimension (Niemelä et al., 2007; van Meer et al., 2008). It is largely appreciated that biological membranes under physiological conditions are not in the gel phase. While sphingolipids alone would, at physiological temperature, be in the gel phase, the addition of sterol groups renders these membranes fluid (Holthuis and Menon, 2014). But, within the bulk membrane there likely exist small, transient lipid domains composed of those sphingolipids and sterols that are potentially in another phase entirely, called the liquid-ordered, or L_O, phase. These domains are commonly referred to as “lipid rafts” and have properties distinct from either fluid or gel phase membranes (Figure 1.2 adapted from van Meer et al., 2008) (Simons and Ikonen, 1997; Contreras et al., 2011; Bagatolli, 2013; Holthuis and Menon, 2014; Nicolson, 2014; Richens et al., 2015).

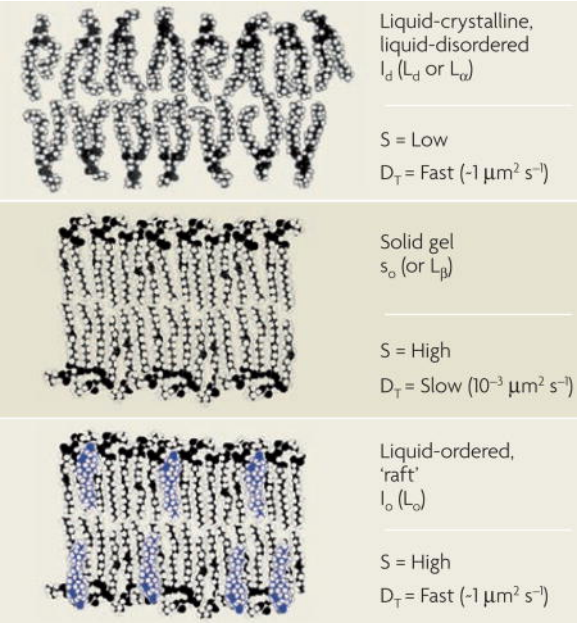

Figure 1.2. Lipid membranes can exist in one of three phases, L-alpha, or liquid-disordered, L-beta, or solid, and L_o, or liquid-ordered.
The three phases depicted have different parameters: S, defined as the order parameter of a segment of acyl chain, and D_T, defined as the translational diffusion coefficient of a single lipid molecule within the two-dimensional membrane plane. Adapted from van Meer et al., 2008.

The “raft hypothesis” has enjoyed lively debate about its physiological relevance and accuracy since its introduction nearly 20 years ago (Simons and Ikonen, 1997). At that time, it was suggested that functional microdomains formed in areas of the plasma membrane enriched locally with sphingolipids and cholesterol and that certain proteins, such as glycophosphatidylinositol (GPI)-anchored proteins, preferentially associated with these domains. This model explained the existence of the previously observed so-called “detergent-resistant membranes” (DRMs) that were sphingolipid- and cholesterol-enriched. However, this model was yet another oversimplification, as it implies long-lived raft-structures of protein and lipids floating amongst the bulk liquid-disordered phase because it calls to mind a stable “raft” floating amongst the dynamic “ocean” of bulk lipid. In this publication, the authors defined the formation of rafts as “preferential packing of sphingolipids and cholesterol in moving platforms, or rafts, onto which specific proteins attach within the bilayer” (Simons and Ikonen, 1997). Yet, the supporting evidence for the implied long-lived microdomains has been relatively slim (Owen et al., 2012) and as a result, the model has evolved to incorporate the probable dynamic, transient, and nanoscale nature of these domains. For the purposes of this dissertation, we will still use the term lipid raft. However, instead of implying a stable, long-lived microdomain, we set forth the definition of a lipid raft as a “small (10-200 nm), transiently-associating, heterogeneous, and ordered nanodomain assembly enriched in sphingolipids and cholesterol but in dynamic exchange with the disordered bulk membrane surroundings.” In our definition, then, some lipids and proteins may have a preferential association with these so-called rafts, which represent a more ordered lipid environment, but these lipids and proteins shall all be dynamically exchanged with the liquid-disordered phase. Thereby we depart from the FMM presented by Singer and Nicholson in that the fluidity of our membrane does not equate with randomness. Preferential, if only transient, association of protein and lipid components allows for the formation of small, ordered

domains. However, in contrast to the original raft model, our definition reincorporates the dynamics implied in the original FMM, and the exceptions to the FMM depicted in Figure 1.1e. And, it must be further noted that even this updated picture of membrane organization and dynamics likely does not capture the complex biophysical phenomena of the true plasma membrane. Because we invoke equilibrium thermodynamics in discussing lipid exchange between raft and non-raft phases, we ignore the constant flux and membrane turnover effected by the numerous physiological processes occurring within the cell. It is with caution, then, that conclusions about membrane protein behavior in a physiological environment can be drawn from this model.

Lipid rafts are important as a subject of intense scrutiny as the field of membrane protein biology evolves, as a number of key physiological processes have been shown to be affected by raft formation and trafficking (Nguyen and Hildreth, 2000; Carrasco et al., 2004; Gaus et al., 2005; 2006; Márquez et al., 2006; Gupta and DeFranco, 2007; Yang et al., 2010). However, the ability to study proteins in raft-domains has been limited (Owen et al., 2012; Kwiatek et al., 2014). As more imaging tools evolve for the study of rafts in membrane environments, it is requisite that the corollary tools in biophysics and membrane protein structure determination similarly evolve. Thus, the development of membrane mimetics suitable for structural and biophysical studies will be a key addition to this field. Because of their complex nature, it is difficult to replicate a true physiological "raft" in an *in vitro* system. As such, this remains a field of active mimetic development and one that remains a necessity for accurate biophysical characterization of membrane proteins under a variety of physiologically replicative conditions. However, a great many mimetic systems exist for the exploration of membrane proteins via a number of *in vitro* biophysical and structural techniques, and many of those membrane systems may well be adaptable to create mimetic systems with altered hydrophobic width or fluidity.

This dissertation discusses the development of novel isotropic bicelles suitable for NMR, crystallographic, biophysical, and biochemical studies with increased hydrophobic width. In the future directions section, it turns to focus on initial phases of the exploration of the development of heterogeneous bicelle mixtures containing both sphingolipid and cholesterol components that may one day be adapted to the study of membrane proteins in a more representative “raft-like” environment.

Introduction to membrane mimetics for biophysical and structural characterization of membrane proteins

As discussed above, membrane proteins are remarkably tolerant to gross changes in their membrane environment throughout their life-cycles. As such, it is no surprise that many membrane proteins can be fully reconstituted in terms of folding and function into a variety of membrane mimetics, including detergent micelles, bicelles, nanodiscs, amphipols, and lipid vesicles. However, each of these mimetics has its shortcomings in terms of (a) its ability to imitate the native membrane environment and (b) its applications to *in vitro* biochemical, biophysical, and structural studies.

Micelles (Figure 1.3a) are made of amphipathic detergents, typically consisting of a polar head group and an acyl chain of variable length depending on the detergent type. These detergents, at high enough concentrations, form aggregates in solution referred to as micelles, which are in equilibrium exchange with free detergent molecules in solution. The concentration at which detergents go from existing as only free detergent molecules to the aggregate micellar structures is known as the critical micelle concentration (CMC), and is determined by the detergent identity. At or above the CMC, detergent exists in equilibrium exchange with free detergent at the concentration of the CMC and all other detergent molecules being micelle bound. As a result of this free exchange, micelles are typically rather dynamic in nature and allow more water into the

hydrophobic region. As a result, micelles may not be a particularly good mimetic for more structurally unstable membrane proteins (Cross et al., 2014). However, a new class of detergent molecules, the neopentyl glycol detergents, deserves a special mention. These detergents have a CMC so low as to be nearly negligible, meaning that the free exchange of detergent molecules with those in solution is minimized. This stability may improve upon their use for membrane proteins, as has already been observed with the difficult class of membrane proteins G-protein coupled receptors (GPCRs) (Chae et al., 2010; Jastrzebska et al., 2013). Finally, it should be noted that detergent micelles, while offering an amphipathic environment for the protein, must be used at concentrations above the CMC to offer this environment—meaning that solutions cannot be infinitely diluted—and that the amphipathic environment provided by the micellar aggregate is only an approximate of the membrane, in that it is not a true bilayer. However, micelles are useful in a number of applications. They are relatively inexpensive and easy to work with, with many purifications of membrane proteins involving at least a transient purification into micelles (Popot, 2014). They are small and tumble isotropically, making them amenable to solution NMR (Warschawski et al., 2011). Many early crystal structures of membrane proteins were solved in micelles (Carpenter et al., 2008). Finally, many proteins retain their function in detergent micelles, making them useful for a number of biochemical, biophysical, and functional studies.

However, micelles do not accurately represent the bilayer of a physiological membrane. Bicelles (Figure 1.3b) seek to remedy this inaccuracy by offering a bilayered environment while still maintaining many of the useful properties of micelles. Bicelles are a two-component system containing a long-chain phospholipid molecule as well as a short-chain lipid or detergent molecule. The short-chain lipid or detergent component serves as an edge-cap to protect the hydrophobic chains of, and to solubilize the bilayer formed by, the long-chain phospholipids. Depending on the long-chain lipid to short-

chain lipid ratio (q ratio), the size of the bicelles ranges from mixed micelles (not depicted), to small, isotropically tumbling bicelles (Figure 1.3b), to large Swiss-cheese-like assemblies that align in a magnetic field (not depicted). The various sizes of bicelles have different applications. For instance small bicelles can be utilized in solution-NMR, biochemical and biophysical studies, electron paramagnetic resonance (EPR), and crystallization, whereas larger bicelles are applicable in crystallography, solid-state NMR, and, due to their property of aligning in a magnetic field, as a means of marginally aligning a soluble protein for the collection of residual dipolar coupling measurements in solution NMR. This thesis concerns the applications of small, isotropic bicelle mixtures, which have a number of the same benefits of micelles while still providing a bilayer environment. While bicelles "solve" the problem of micelles by adding a bilayer environment, they do have a number of limitations. First, bicelles are still subject to the requirements of remaining above the CMC of the short-chain lipid or detergent end-capping molecule, and thus cannot be infinitely diluted. During buffer exchange, for instance, the CMC of the detergent must be included in the new buffer, which is a costly enterprise, due to the relative expense and high CMC of the traditional bicelle detergent 1,2-dihexanoyl-*sn*-glycero-3-phosphocholine (DHPC). Finally, despite bicelles having been used in various biochemical and biophysical applications for over 20 years (Sanders and Schwonek, 1992), there has been a relative dearth of improvement upon small, soluble bicelle systems, with very little adaptation of bicelles with greater phospholipid profiles and development of this important membrane mimetic. Only recently have several laboratories set out to increase the diversity of available bicelle systems (Morrison and Henzler-Wildman, 2012; Yamaguchi et al., 2012), and this thesis focuses on contributing to these advances. Chapter III will explore the creation of novel bicelles with increased hydrophobic width, and Chapter VIII presents preliminary data for

the development of three-component bicelles containing phosphatidylcholine, sphingomyelin, and cholesterol.

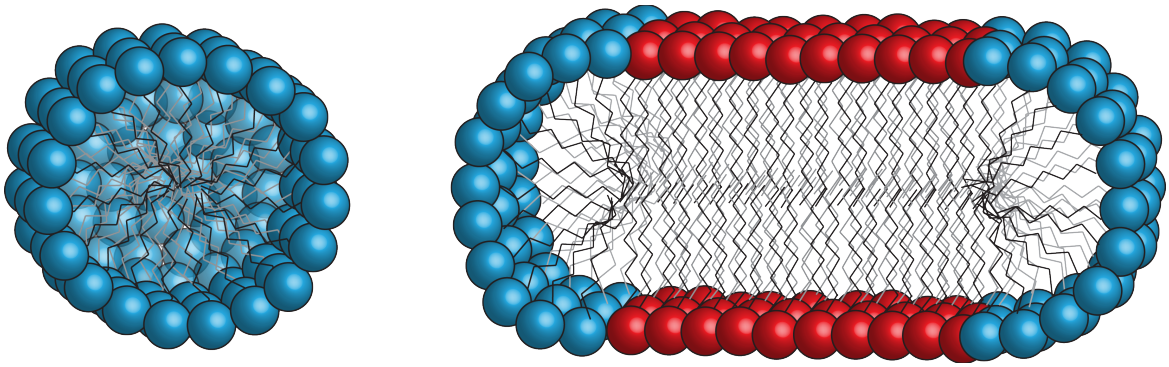

Figure 1.3. Micelles versus bicelles as isotropic membrane mimetics suitable for solution studies.
(Left) Micelles are composed of amphipathic detergent molecules (blue), which form approximately spherical assemblies around the hydrophobic portion of the protein. (Right) Bicelles are composed of a bilayer of phospholipid and/or other lipid components (red) that are edge-protected by a detergent component (blue).

Nanodiscs (Figure 1.4) are similar to bicelles in that they offer a small bilayer environment and tumble isotropically. However, the edge-capping molecule in this case is not a detergent, but rather an amphipathic protein known as a membrane scaffolding protein (MSP). The original MSP was designed based on human apoliprotein A-1 and wraps itself like an inner tube around the small bilayer disc (Denisov et al., 2004). While slightly larger than bicelles, they are still small enough to be applicable to solution NMR in some cases (Warschawski et al., 2011), and offer the advantage of being infinitely dilutable. They have found themselves applicable to a number of other techniques, such as electron microscopy, the successful reconstitution of membrane protein complexes, and localized surface plasmon resonance, to name a few (Bayburt and Sligar, 2010). Unfortunately, to use nanodiscs, one must recombinantly express and purify the amphipathic proteins used to solubilize the lipids, an additional undertaking to already difficult membrane protein preparations. A recent approach utilizing the same philosophy of nanodiscs has been the creation of so-called “lipodisqs”, which utilize a polymer, rather than a protein, to stabilize the hydrophobic lipids and which are formed through detergent-free methods (Orwick et al., 2012; Zhang et al., 2015). So far, this system has shown promise with functionally incorporating membrane proteins for biophysical studies (Orwick-Rydmark et al., 2012).

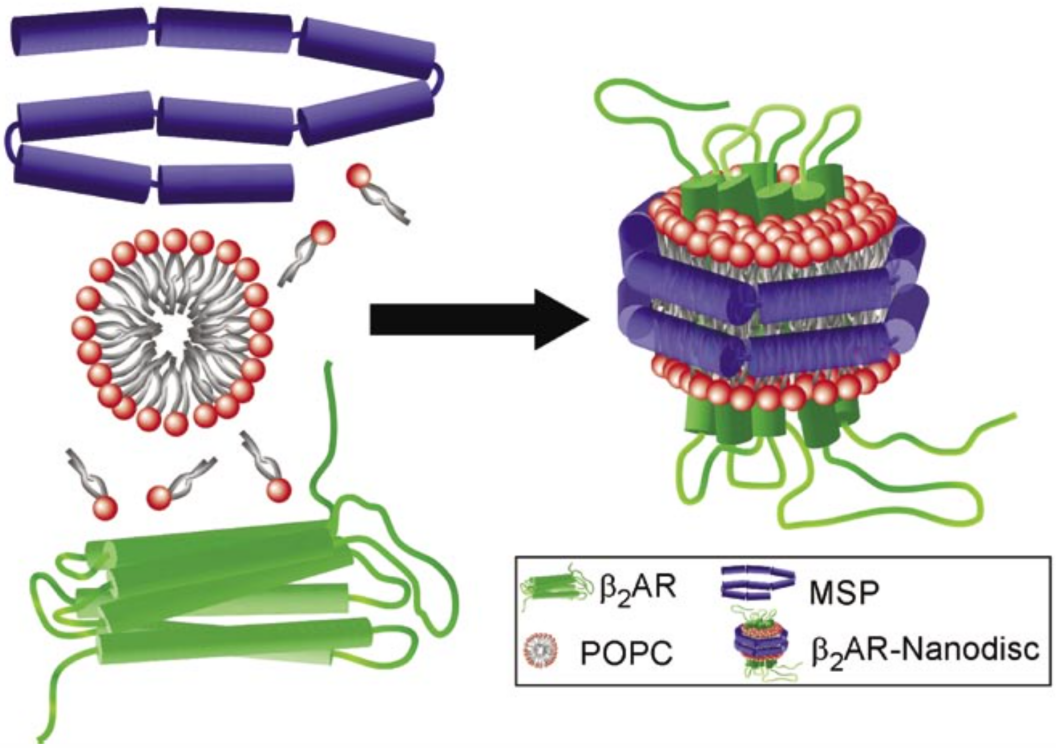

Figure 1.4. Nanodiscs are made up of a bilayer of phospholipids and/or other lipid components that approximate a cellular membrane.
These lipids are wrapped and edge-protected by an amphipathic peptide to create small, isotropic membrane systems. Adapted from Leitz et al., 2006.

Amphipols (Figure 1.5), developed by the laboratory of Jean Luc Popot in 1996 (Tribet et al., 1996), are a unique system in membrane protein solubilization. This mimetic, save being composed of amphipathic molecules, has very little in common with other membrane mimetics. Amphipols are amphipathic polymers, which contain various functional groups that alternate randomly in their nature: hydrophobic versus polar. These large functional groups (similar to amino acid side chains) then orient themselves in a preferential manner, with the hydrophobic groups facing the transmembrane regions of the protein, and the hydrophilic groups facing the aqueous buffer. While amphipols have had a few successes in NMR (Popot et al., 2011), (Kleinschmidt and Popot, 2014), their most important contribution did not come until recently, with the 3.4Å structure of the small, tetrameric ion channel TRPV1 (Liao et al., 2013) and the 4.5Å structure of the large, asymmetric membrane protein complex human γ-secretase (Lu et al., 2014), both determined using cryoelectron microscopy (cryo-EM). It may well be that amphipols will find their place amongst the membrane mimetics as a major tool in the soon-to-be massive enterprise of cryo-EM membrane protein structure determination.

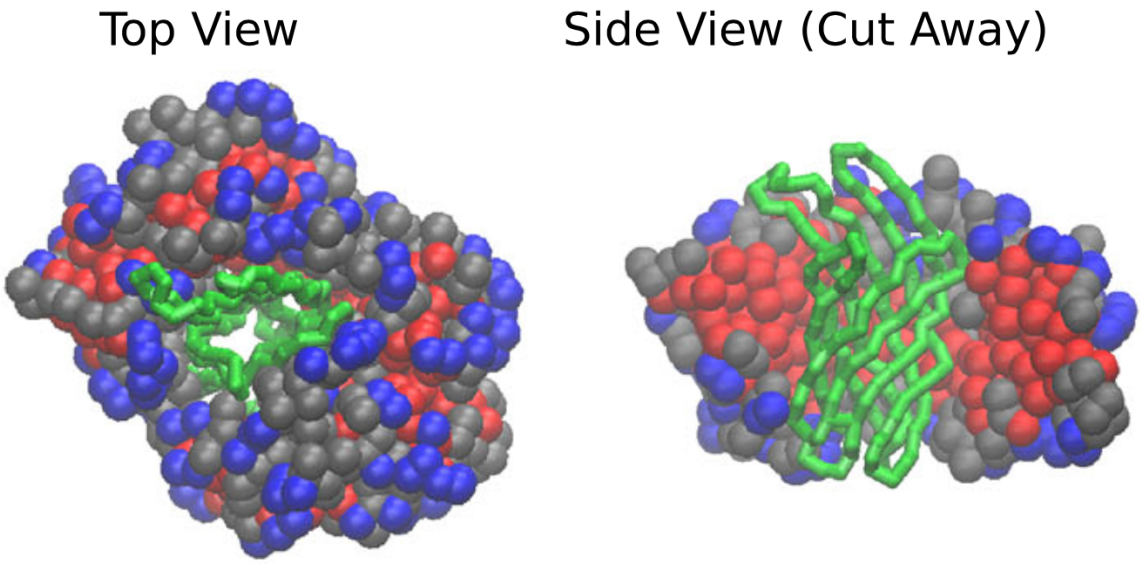

Figure 1.5. Amphipols are amphipathic polymers that provide a stabilizing environment for membrane proteins in the absence of detergent and lipids. Pictured here are snapshots from a molecular dynamics simulation of A10 amphipols surrounding the membrane protein OmpX (green). Octyl chains are depicted in red, isopropyl chains are depicted in grey, and carboxylates are depicted in blue. Figure and legend adapted from Perlmutter et al., 2014.

Vesicles (Figure 1.6) are perhaps the most native-like membrane environment, although they are still typically made from synthetic phospholipids. However, they can be derived from either lipids purified from native sources or be induced to "bleb off" from a cell (Sezgin and Schwille, 2012). Vesicles are small structures that resemble full cell membranes. They can be reconstituted by a variety of methods and can exist in both multilamellar and unilamellar forms. Vesicles are extremely useful in biochemical characterization of proteins, and also find uses in solid-state NMR, EPR, and EM. However, because of their large size, vesicles are not applicable to solution state NMR, which requires rapid, isotropic tumbling of the molecular assembly. It is often important to verify key functions and features observed using other mimetics via other methods using vesicles. For instance, if a helix is found to be curved after structure determination in micelles, EPR in vesicles could be used to verify that this curved nature is not an artifact of the micellar environment (Barrett et al., 2012). Vesicles can be multilamellar—consisting of multiple bilayers nested inside one another—or unilamellar (Kaurinovic and Popovic, 2012). A specialized application of vesicle reconstitution is in the application of 2-D electron crystallography. In this case, proteins are slowly reconstituted into a bilayer at high concentration, with the hope of producing a two-dimensional array suitable for the acquisition of an electron diffraction pattern and for imaging by EM. A small number of membrane protein structures have been determined using this method (Ubarretxena-Belandia and Stokes, 2012).

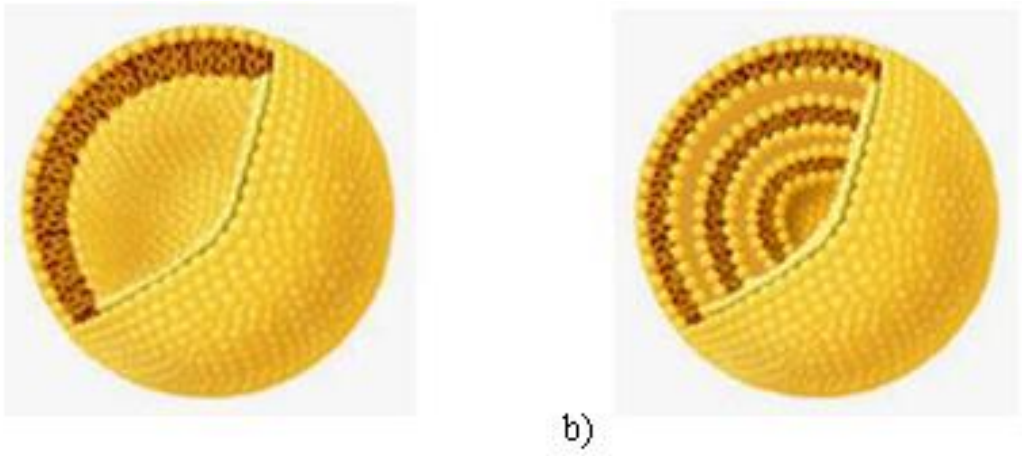

Figure 1.6. Vesicles, or liposomes, present the most physiological approximation of *in vitro* methods for the study of membrane proteins.
(A) A unilamellar vesicle; (B) a multilamellar vesicle. Adapted from Kaurinovic and Popovic, 2012.

Reverse micelles (Figure 1.7) have also found an application in solution state NMR (Kielec et al., 2009). In this case, a membrane protein is solvated with an organic solvent, such as pentane, but a micelle surfactant is added. The micelle surfactant maintains and protects a water layer around the exposed aqueous portions of the protein, while the transmembrane region is exposed to the organic solvent. Motivation for the development of this method stems from the potential to increase the size limit of proteins amenable to study by solution NMR.

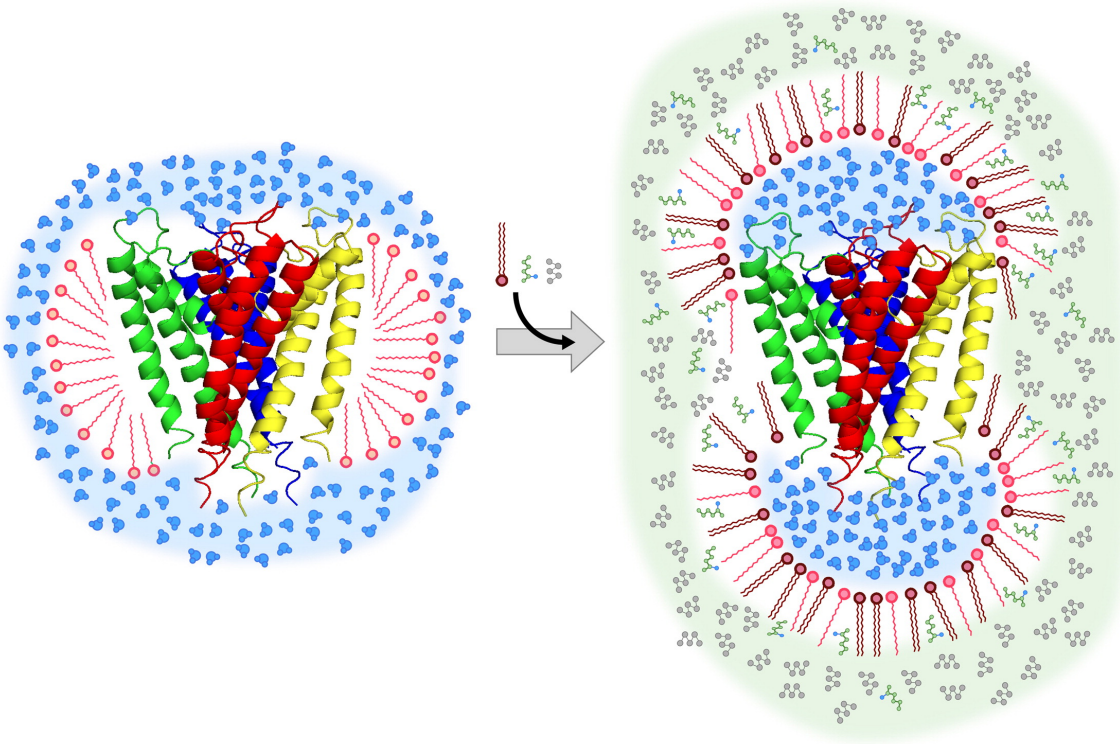

Figure 1.7. Reverse micelles represent another isotropic system for use with solution NMR.
This figure depicts the purification of a membrane protein (ribbon diagram) into an amphipathic micelle in the aqueous phase (left). Here, the versatile detergent depicted is cetyltrimethylammonium bromide. Addition of hexanol (green) and the accessory surfactant dihexadecyldimethylammonium bromide serve to convert the system to reverse micelles in the solvent pentane (grey). Figure and legend adapted from Kielec et al., 2009.

The lipidic cubic phase has been a breakthrough, especially for 3-dimensinoal X-ray crystallography of membrane proteins. In this method, the solubilized membrane protein is dispersed with an amphipathic lipid (e.g., monoolein) that simulates the phospholipids found in biological membranes and forms a viscous lipidic cubic mesophase (Caffrey and Cherezov, 2009). Adding the correct concentrations of protein and lipid will cause the lipidic cubic phase (LCP) to self-assemble (Caffrey and Cherezov, 2009).Then, a precipitant is added to trigger nucleation and crystal growth. The particular precipitant used varies based upon the protein and must be determined through a crystal screen. The LCP is a three- dimensional lipidic array (Figure 1.8) that provides crystal nucleation sites and support for lateral diffusion of the protein molecules as they come together to form stable crystals (Caffrey and Cherezov, 2009). The mechanism by which this occurs remains unclear, but it is speculated that the precipitant triggers a phase separation event, allowing a “lamellar portal” to form in the center (Figure 1.8). Diffusion within the bilayer allows additional protein molecules to join at the leading edge of the crystal (center of Figure 1.8).

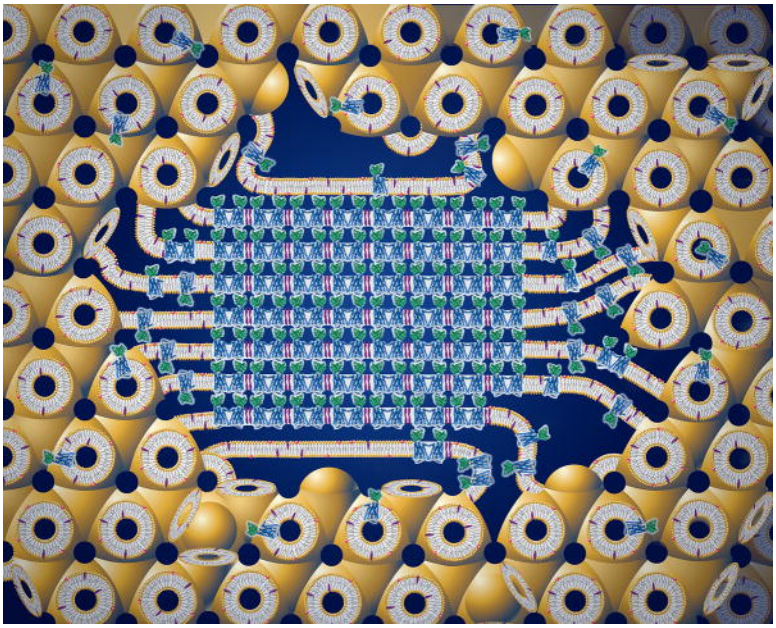

Figure 1.8. A depiction of a crystal forming from the lipidic cubic phase.
The process of crystal formation begins with addition of protein and lipid at appropriate concentrations to form the cubic phase. Added precipitants induce phase separation and the formation of a lamellar portal (center section of illustration). Adapted from Caffrey and Cherezov, 2009.

A variety of supported lipid membranes have been developed for the reconstitution of membrane proteins. These systems aim to link the biophysical surface investigative techniques that come with great analytical advantage to the study of the complex molecular architectures of membrane proteins and membrane protein complexes (Forming supported lipid membranes, 2003; Richter et al.); such techniques include fluorescence microscopy, surface plasmon resonance, atomic force microscopy, ellipsometry, Brewster angle microscopy, and quartz crystal microbalance. These supported membranes include lipid monolayers formed at an air-water interface, self-assembled monolayers, monolayers and multilayers formed or tethered on a solid support, and black lipid membranes formed in an aperture between aqueous phases (Figure 1.9). It is not yet clear how the properties of the solid support may influence the physical properties of the bound membrane.

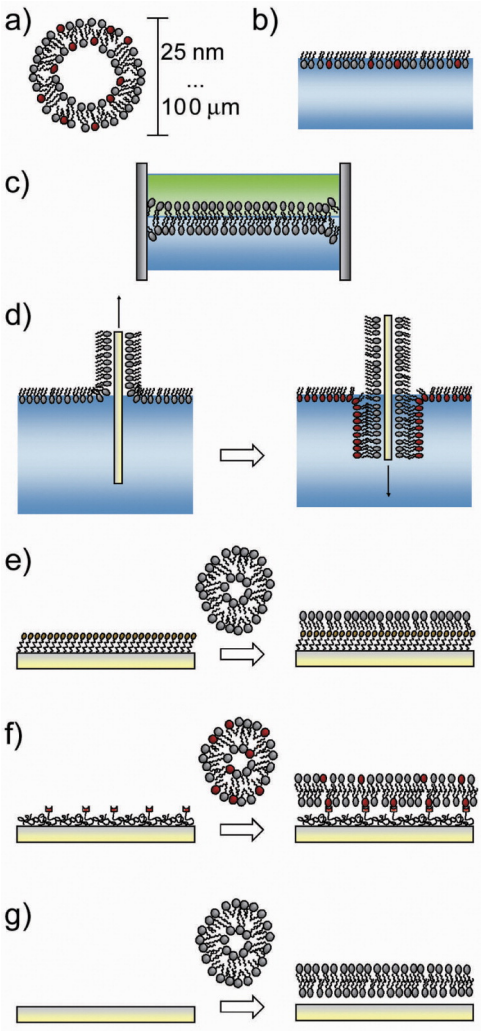

Figure 1.9. A variety of solid supported lipid membranes are available.
(A) unsupported liposomes, (B) lipid monolayers at the air-water interface; (C) black lipid membranes suspended over an aperture between two aqueous phases; (D) Langmuir-Blodgett method of transferring lipid mono- and multi-layers from the air-water interface to a solid support; (E) self-assembled monolayers (SAMs), where a second lipid layer can be deposited by spontaneous disruption of liposomes; (F) deposition of a polymer coating with tethers followed by the spontaneous spreading of liposomes, so that the polymer creates a cushion between support and bilayer; (G) spontaneous spreading of liposomes or membranes on mica, glass, and silica. Figure and legend adapted from Richter et al.

As is made clear in the next section, many membrane proteins may well tolerate a variety of membrane mimetic systems, retaining both structural and functional fidelity in many of these systems. However, there are well-documented exceptions to this rule (Opekarová and Tanner, 2003; Lee, 2004; Hunte, 2005; Nyholm et al., 2007; Qin et al., 2007; Hunte and Richers, 2008; Marsh, 2008; Ernst et al., 2010; Adamian et al., 2011; Lee, 2011). As such, exploration of useful mimetics is needed on a protein-by-protein basis, as no hard-and-fast rules exist for the choice of effective mimetic. The impetus to study membrane proteins far outweighs the varied drawbacks of each individual mimetic system, however, and thus care should simply be taken to ensure that the appropriate mimetic is selected for the protein and application at hand. As further mimetic systems are developed that more accurately represent the range of conditions found in the native cellular membranes, this problem will be partially mitigated.

Tolerance of Membrane Proteins to Changes in Their Environment as a Selected Trait of Membrane Proteins[1]

It has long been appreciated that membrane proteins are not always fully functional following purification into model membranes such as detergent micelles or lipid/detergent mixed micelles. Reduced functionality can reflect destabilization, misfolding, or perturbation of membrane protein structure in model membranes relative to native bilayer conditions. Loss or perturbation of membrane protein function can also reflect a requirement by certain membrane proteins to form specific complexes with lipids, which may play cofactor roles in promoting function and/or serve to buttress native structure (reviewed in Opekarová and Tanner, 2003; Lee, 2004; Hunte, 2005; Nyholm et al., 2007; Qin et al., 2007; Hunte and Richers, 2008; Marsh, 2008; Ernst et al., 2010;

[1] This section is adopted from the published manuscript by Sanders and Mittendorf in *Biochemistry*. Sanders, C.R. and Mittendorf, K.F. (2011). Tolerance to changes in membrane lipid composition as a selected trait of membrane proteins. *Biochemistry 50*, 7858-7867.

Adamian et al., 2011; Lee, 2011). Recent biophysical and structural studies of integral membrane proteins have also highlighted the degree to which some model membranes such as micelles or lipid/detergent mixed micelles can fail to fully support native membrane protein stability or structure. For example, homodimerization of single-span membrane proteins such as the receptor tyrosine kinases is sometimes weaker in detergent micelles than in bilayers (reviewed in MacKenzie and Fleming, 2008), reflecting a reduction in the free energy for dimerization in micelles relative to bilayers by as much as 5 kcal/mol (Bowie, 2011). Another example is provided by the initial high-resolution structure determined for a voltage-gated potassium channel, KvAP, which was crystallized from micelles (Jiang et al., 2003). KvAP was seen to have a distorted disposition of the voltage sensor domain relative to the channel domain, a fact that was appreciated later when a more native-like structure was crystallized from lipid-containing mixed micelles (Lee et al., 2005b).

Data such as those cited above have helped to drive the development of model membranes such as bicelles, lipidic cubic mesophases, and nanodiscs that capture some of the advantages of working with micelles and mixed micelles while at the same time providing a bilayer environment for membrane proteinss reconstituted therein (Sanders and Prosser, 1998; Faham and Bowie, 2002; Caffrey and Cherezov, 2009; Bayburt and Sligar, 2010). Moreover, techniques such as electron two-dimensional (2D) crystallography and solid state NMR are increasingly being used to directly probe membrane protein structure in actual bilayer lipid vesicles, sometimes to high resolution (see below).

In the laudable impetus to conduct quantitative structural and functional measurements under membrane conditions as close to native as possible, it can be tempting to view current and previous studies of membrane proteins conducted in model membranes with a skepticism that extends beyond well-justified caution regarding

extrapolating results obtained using model membranes to the situation in native membranes. However, we suggest that there are a number of reasons that an overly judgmental view of the relevance of model membrane-derived results is not well-justified. One reason is the tremendously useful body of information gleaned from the many dozens of high-resolution structures of membrane proteins determined in recent years, the vast majority of which employed detergent micelles as the model membrane medium. Structural advances have been matched by tremendous progress in studies of membrane protein folding and stability and of membrane protein function, work that has also relied heavily on results derived using nonbilayer model membranes. It can also be observed that “native membrane conditions” represent an ideal rather than a fixed reality in light of the facts that (i) a given membrane protein will often traffic through several different organelles, each with a distinct lipid composition, en route to its destination membrane, (ii) membrane lipid composition is dynamic even within a single plasma or organellar membrane, (iii) even within a single membrane, all components are not uniformly and randomly mixed, but some lipids and proteins will transiently form domains, the components of which are likely to also spend significant time in the bulk (unorganized) membrane domain, and (iv) there can be even more dramatic variations in lipid composition from organism to organism (see below for more on this topic). Even studies conducted directly on unpurified membrane proteins in natural membranes often rely on conditions under which the protein of study is highly overexpressed relative to normal physiological conditions.

Here, we explore a more fundamental reason why studies of membrane proteins in model membranes have been and are likely to continue to be informative. We propose that many membrane proteins are remarkably tolerant of significant variations in membrane composition, reflecting the outcome of strong evolutionary selective pressure to be so. In the following sections, we cite bodies of evidence showing that this is the

case. We emphasize that the purpose of this review is *not* in any way to either discount previous work documenting the specificity of membrane protein–lipid interactions or to encourage irresponsible use of model membranes. Rather, the purpose is to highlight evidence that shows that many membrane proteins appear to be quite tolerant of major variations in membrane composition and to reassure those pursuing structural or biochemical studies of membrane proteins in model membranes that good-faith efforts to conduct experiments using the best available model membrane medium compatible with a given experimental approach are likely to be rewarded by illuminating data.

Escherichia coli can survive knockout of all major classes of phospholipids

The tools of microbial genetics have been extensively used over the past 30 or more years to explore lipid metabolism and homeostasis in *Escherichia coli*, with mutations being used to knock out enzyme activities required for biosynthesis of various native lipid species (Shibuya, 1992; Matsumoto, 2001; Bogdanov et al., 2009). A major goal of these studies has been to discover specific roles for various phospholipid species in *E. coli* physiology and associated cellular biology, biochemistry, and biophysics. For example, elegant work from the Dowhan lab has established the fact that the presence of PE is required for certain transporters such as lactose permease to adopt their correct topology in the plasma membrane and to function normally (Dowhan and Bogdanov, 2011). A long-term focus of the genetic studies has been to unravel examples in which lipids play specific roles in regulating or sustaining normal structure and function. However, a largely overlooked outcome of these studies is a large body of evidence that shows that *E. coli* is remarkably tolerant of extensive remodeling of its phospholipid composition.

Figure 1.10 (adapted from (Shibuya, 1992)) illustrates the plasma membrane lipid compositions of wild-type and phospholipid biosynthesis knockout mutant strains of

E. coli at various stages of growth and/or under unusual culture conditions. Represented in this figure are wild-type *E. coli* (example 1) and strains in which its major phospholipids, phosphatidylethanolamine (zwitterionic), phosphatidylglycerol (PG, anionic), and cardiolipin (CL, anionic), have each been eliminated. Also represented is a strain in which both PG and CL have been removed. Very unusual plasma membrane lipid compositions have been observed. One strain has membranes that are almost exclusively zwitterionic (example 5). Some have lipids that are almost exclusively anionic (examples 2 and 4). One has membranes composed almost exclusively of cardiolipin (example 4), a lipid with a nonconventional architecture (see Figure 1.11). Yet another has membranes that are almost exclusively composed of lipids that are present only in very small quantities in wild-type cells (example 9). Despite such extreme differences in lipid composition, life persists, although the mutant strains often have more stringent growth requirements and are less robust than wild-type strains. It can also be pointed out that *E. coli* and its set of essential membrane proteins are also remarkably tolerant of the introduction of foreign lipids such as phosphatidylcholine (up to at least 70% of total lipid (Bogdanov et al., 2010)) or mono- or diglucosyldiacylglycerols (at 40% of total lipid (Wikström et al., 2004; Xie et al., 2006; Wikström et al., 2009)). Some foreign lipids can successfully substitute for PE to fulfill its role in facilitating adoption of the correct topology of lactose permease (Dowhan and Bogdanov, 2011), among which is glucosyldiacylglycerol, the headgroup of which resembles PE only in that both have a net charge of zero (Xie et al., 2006). The results summarized above strongly suggest that many of the of membrane proteins present in *E. coli* are tolerant of major changes in membrane lipid composition, remaining correctly threaded into the plasma membrane, reasonably stable, and functional despite the loss of their usual phospholipid neighbors.

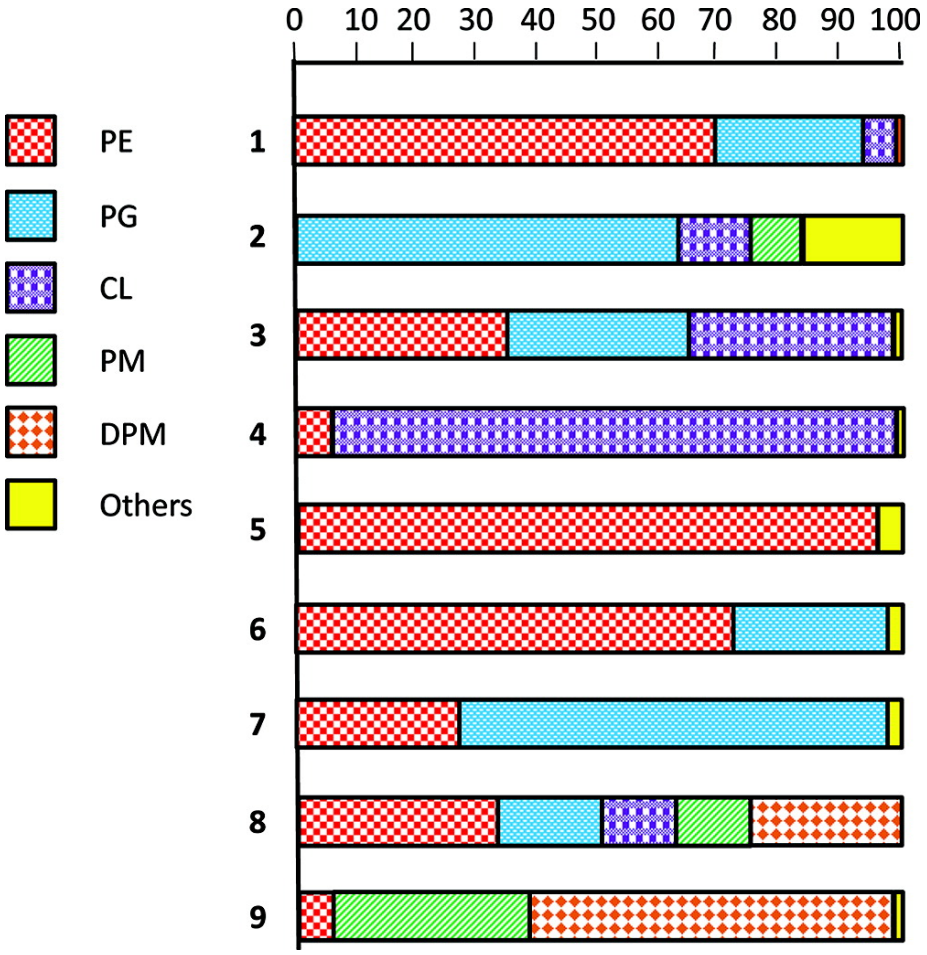

Figure 1.10. Phospholipid compositions observed for various strains of E. coli, as measured at various growth phases or following culturing in unusual media. Example 1 is wild-type strain SD12 during exponential growth. Example 2 contains an interrupted allele of PS synthase in strain AH930 during exponential growth. Example 3 is strain SD10, which contains a temperature sensitive PS synthase, during exponential growth. Example 4 is strain SD10 grown at the stationary phase. Example 5 is a double mutant of strain SD312 containing a mutated phosphatidylglycerophosphate synthase and a defective CL synthase during exponential growth. Example 6 is strain CB64-CLI with a knockout of CL synthase during exponential growth. Example 7 is strain SD9 containing a temperature sensitive PS synthase and a defective CL synthase during exponential growth. Example 8 is strain SD10 (see example 3) grown under high-d-mannitol conditions during exponential growth. Example 9 is strain SD10 grown under high-mannitol conditions during the stationary phase. This figure was adapted from Shibuya, 1992.

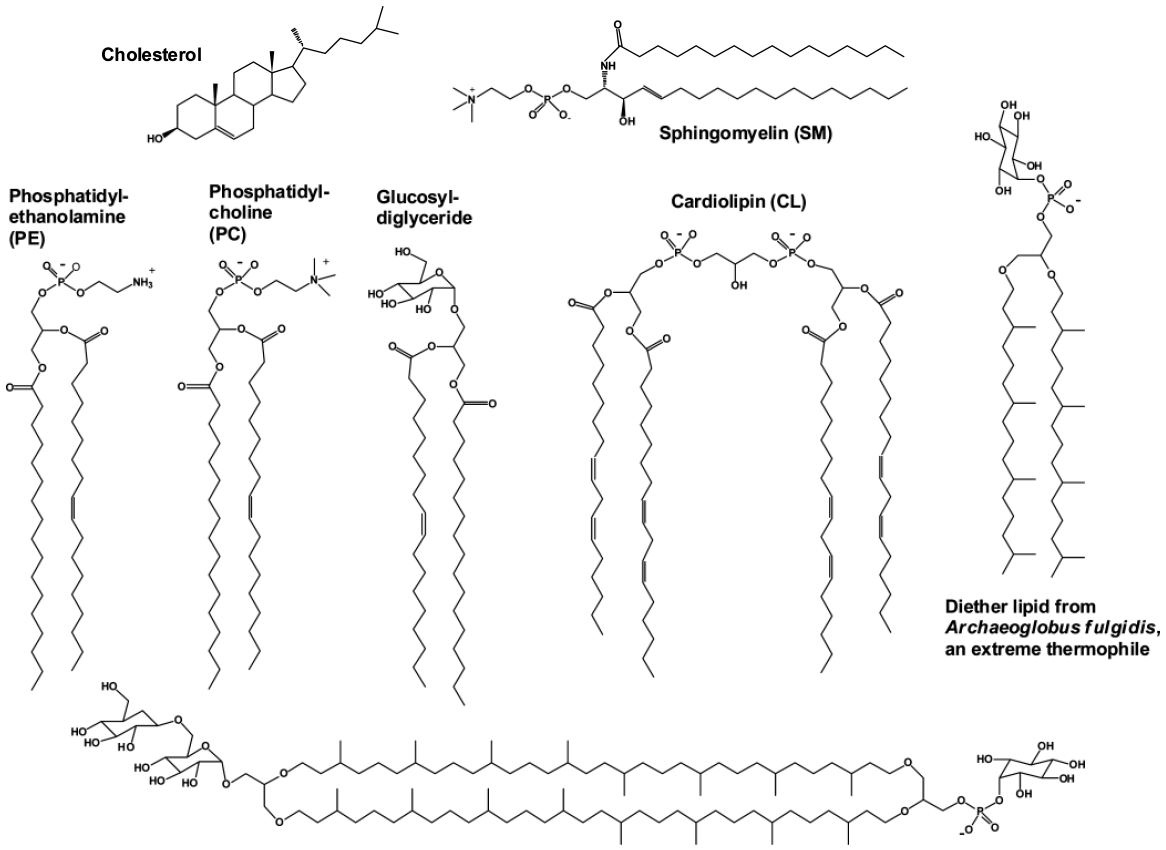

Figure 1.11. Structures of representative lipids from different domains of life. Cholesterol and sphingolipids such as sphingomyelin are found primarily in eukaryotes. Phosphatidylcholine is among the most common glycerophospholipids of higher eukaryotes but is less common in bacteria (and is absent in E. coli). Phosphatidylethanolamine is common in both bacteria and eukaryotes. Glucosyldiglyceride and related neutral glycoglycerolipids are often the most common lipids of plants. Cardiolipin is common in bacteria and in the mitochondria of eukaryotes. Ether-linked isoprenoid lipids such as those exemplified by the bottom and far right lipids dominate the membranes of thermophilic archaebacteria (Lai et al., 2008; Ulrih et al., 2009).

Membrane lipid composition is not static and can vary greatly during the cell lifetime

In addition to being asymmetrically and anisotropically distributed in the bilayer leaflet as discussed above, certain lipids are preferentially distributed to different organelles within the same cell. Proteins are also trafficked to their functional destination in a preferential manner post-synthesis, a process that, when disrupted, can result in disease. As a result of this preferential distribution, various organelles can have membranes that are wildly different in lipid and protein composition. Thus, any given membrane protein inhabits a variety of different lipidic environments during its lifetime. Eukaryotic membrane proteins destined to reside in the plasma membrane are first synthesized and inserted into the membrane of the ER, are transported to the Golgi body, and then finally make their way to the plasma membrane. Each of these organelles has a different lipid composition, with levels of cholesterol in the membrane varying from <15% in the ER to 20–50% in the plasma membrane of mammalian cells (Mitra et al., 2004; van Meer et al., 2008). The ratios of different phospholipids often vary greatly between the organelles (Zambrano et al., 1975; Henry, 1982; Daum, 1985; Allan, 1996; van Meer et al., 2008). For instance, sphingomyelin makes up a significant percentage of the phospholipids in the mammalian plasma membrane, while sphingolipid content is very low in the ER (van Meer et al., 2008). The PC:PE:PI:PS ratio in the plasma membrane of rat liver is 28:17:6:6, while in the Golgi and the rough ER, it is 44:19:7:2 and 54:20:9:3, respectively (Zambrano et al., 1975). Similarly, ergosterol:phospholipid ratios are greater at the plasma membrane (1:2) of yeast than in organelles, where they range from 1:50 in the outer mitochondrial membrane and 1:30 in the peroxisomes to 1:3 in lipid particles. Yeast inositol sphingolipids are greatly enriched at the plasma membrane (~25%) relative to other organelles (e.g., near 0% in the ER) (Schneiter et al., 1999; van Meer et al., 2008). Even more specific differences between organelles exist. For example, phosphatidylserine and phosphatidylethanolamine in the

plasma membrane have fatty acid compositions that are 40 and 30% saturated, respectively, whereas the corresponding degrees of saturation for these lipids at the whole cell level are 29 and 16%, respectively (Schneiter et al., 1999). On the basis of the observations outlined above, it can reasonably be inferred that most membrane proteins remain essentially folded in a variety of lipid environments as they move from the ER to their destination membranes, an inference that does not imply that the functions of these proteins are independent of environment. These environments may vary in their bilayer thickness and bilayer fluidity as a consequence of variations in sphingolipid and cholesterol content as well as acyl chain composition.

In addition to trafficking through the secretory pathway en route to their destination membranes, membrane proteins are subject to internalization by pinocytosis and endocytosis, and many are recycled from endosomes back to the plasma membrane (Wileman et al., 1985). Studies of cultured hepatocytes indicate that these cells turn over the equivalent of their plasma membrane surface areas approximately five times every hour (Scharschmidt et al., 1986). In plant cells, plasma membrane turnover rates can be as rapid as once every 10 min (STEER, 1988). Membrane proteins internalized and recycled back to the plasma membrane are likely experiencing rapid variations in the local lipid composition yet retain their essential fold and ultimately remain functional after these transitions.

Cellular lipid composition also changes in response to various developmental and environmental conditions. Alterations of the fluidity of the bilayer are evident from studies of hepatocytes as they progress through the cell cycle, with an increase in membrane fluidity due to decreased cholesterol:phospholipid ratios (dropping from a resting ratio of 3:4 to <2:4 during early regeneration) accompanying rapid cellular proliferation (Cheng and Levy, 1979). Neuroblastoma cells, which are often employed as a model for malignant cell differentiation, show significant increases in

cholesterol:phospholipid ratios during differentiation, from 1:3 to 1:2 in the whole cell (Gulaya et al., 1989). Human epidermal cells also show large changes in lipid composition during differentiation, such as an enrichment of sphingolipids (from 7% of the lipids of the strata basal and strata spinosum and 18% of the lipids of the stratum corneum) and neutral lipids (from 51% in the strata basal/spinosum to 78% in the stratum corneum) coupled with a decrease in the fraction of polar lipids (from 45% in the strata basal/spinosum to 5% in the stratum corneum) (Lampe et al., 1983). *E. coli*, too, demonstrates lipid remodeling during growth. For example, when *E. coli* is grown in minimal medium, only 5% of the lipids of strain K-12 contained cyclopropane-containing fatty acyl lipids in a 4.5 h culture, while at 17 h, this number increased to 32% (Cronan, 1968).

Studies of various plant species show that lipid composition is altered in response to environmental conditions such as mineral exposure, aluminum stress, temperature variation, and light exposure (Kuiper et al., 1974; Burkey et al., 1997; Zhang et al., 1997; LarkindaleHuang, 2004). Similarly, yeast show lipid composition alterations in response to nutrient source and temperature variation (Hunter and Thirkell, 1971; Wriessnegger et al., 2007). These alterations can range from changes in saturation levels, large changes in sterol:phospholipid ratios, and significant differences in the ratios of the most prevalent phospholipids. For instance, in soybean plants, heavily shaded leaves see a decrease in the level of 18:3 fatty acids coupled with an increase in the level of 18:1 and 18:2 fatty acids, with the level of the most desaturated 18:3 fatty acids decreasing by >40% in the most heavily shaded leaves (Burkey et al., 1997). Not surprisingly, heat-stressed plants experience an increase in the saturation levels of the fatty acyl tails of their membrane lipids to maintain appropriate membrane fluidity and stability under hot conditions (LarkindaleHuang, 2004). The peroxisomal membrane lipid composition of the yeast *Pichia pastoris* is altered by the carbon source, with 80% of

lipid fatty acyl groups becoming oleoyl when the yeast are cultivated with oleic acid as the major carbon source, relative to only 30% otherwise (Wriessnegger et al., 2007).

The sometimes large variations in lipid and fatty acid content surveyed above are representative of what likely is very common throughout all domains of life. Such variations in lipid composition will, of course, often be accompanied by alterations in membrane protein composition via changes in transcription, translation, and degradation as well as a result of altered protein trafficking. Such variations are also likely to alter the functions of many membrane proteins through specific protein–lipid interactions and/or by altering the bulk properties of the surrounding bilayer (fluidity, thickness, etc.). However, it can also be inferred that a great many membrane proteins must be fairly tolerant of swings in membrane composition, remaining membrane-integrated, correctly folded, and functional. Else, life would cease.

While membrane proteins are often highly conserved, lipid compositions across domains of life can vary spectacularly

Many membrane proteins have been conserved by evolution throughout all domains of life. On the basis of a limited body of high-resolution structural data (below), it appears that membrane proteins have generally similar three-dimensional (3D) structures throughout all domains. Such high levels of retention of protein structure across eons of evolutionary time are in stark contrast to membrane lipid architecture and composition. While the building block amino and nucleic acids used in proteins, DNA, and RNA are essentially invariant across the furthest extremes of terrestrial and marine life, the building block lipids of membranes can exhibit remarkable diversity from organism to organism (see reviews in Henry, 1982; Daum, 1985; van Meer et al., 2008 and goldfine, 1982; Prasad, 1985; Kaneshiro, 1987; Luzzati et al., 1987; Ulrih et al., 2009). The dominant lipids of hyperthermophilic archaebacteria, which include cyclical

ether-linked isoprenoid bolalipids (see Figure 1.11 and Ulrih et al., 2009), are vastly different from the glycerophospholipid mixtures that dominate *E. coli* and many other eubacteria, which in turn only partially overlap with the lipid compositions of vertebrates, the latter of which include not only glycerophospholipids but also abundant sphingolipids and cholesterol (see Figure 1.11). Plant chloroplast lipid compositions, on the other hand, are often rich in neutral glycolipids (Benning, 2009). Diversity is great even among Gram-negative bacteria: *E. coli* is dominated by the diglyceride phospholipids PE, PG, and CL, yet membranes of *Trepenoma pallidum* contain >50 mol % neutral glycolipid (galactosyl-diglyceride), while >75% of the lipids of *Megasphaera elsdenii* are plasmalogen-based (Goldfine, 1982).

Given the widely variant and distinctive membrane compositions that have arisen in different lineages, one might expect that this would place evolutionary pressure on lipid-exposed residues of protein transmembrane domains to diverge in an effort to adapt to relatively rapidly evolving changes in membrane composition. However, lipid-exposed surfaces of membrane proteins exhibit approximately the same degree of (relatively low) sequence conservation as water-exposed surfaces of both membrane and water-soluble proteins (Oberai et al., 2009; Mokrab et al., 2010). This is despite the fact that the molecular identities of the “solvent” lipid molecules within the membrane vary dramatically, in contrast to the constancy of water.

There are a few examples in which the same membrane protein from more than one organism has had its structure determined to high resolution. In some cases, the membranes of these organisms are widely divergent, yet the structures remain similar. Consider thermophilic eubacteria and hyperthermophilic archaebacteria, whose membrane lipid compositions are very different from those of mesophilic bacteria such as *E. coli* and eukaryotic membranes. One might expect that there would be substantial differences in membrane protein structure between thermophiles and mesophiles both to

confer thermostabilization and to reflect adaptation to the very significant differences in the structures of the lipids found in thermophiles relative to mesophiles. However, we can cite examples of membrane proteins from thermophiles that are very similar to those found in mesophilic bacteria or higher organisms, at least in terms of static structure.

The lipids of the eubacteria genus *Thermus* have been determined to have high proportions of glycolipids and glycophospholipids in their membranes, with the fatty acyl tails being mainly composed of branched chains (Heinen et al., 1970; Pask-Hughes and Shaw, 1982). A crystal structure of a β-barrel outer membrane protein TtoA from *Thermus thermophilus* HB27 (optimal growth temperature of 70 °C) shows no obvious structural differences from that of mesophilic β-barrel outer membrane proteins (Oshima and Yamakawa, 1974; Brosig et al., 2009). An alignment of TtoA's structure with that of OmpA from the *E. coli* outer membrane demonstrates a high degree of conservation of structure as well as some sequence similarity within the transmembrane regions (Figure 1.12) (Goldfine, 1982; Pautsch and Schulz, 2000; Rahman et al., 2000; Vandeputte-Rutten et al., 2003). Indeed, the overall root mean squared deviation (rmsd) for the corresponding α-carbon atoms in the two structures is only 1.1 Å.

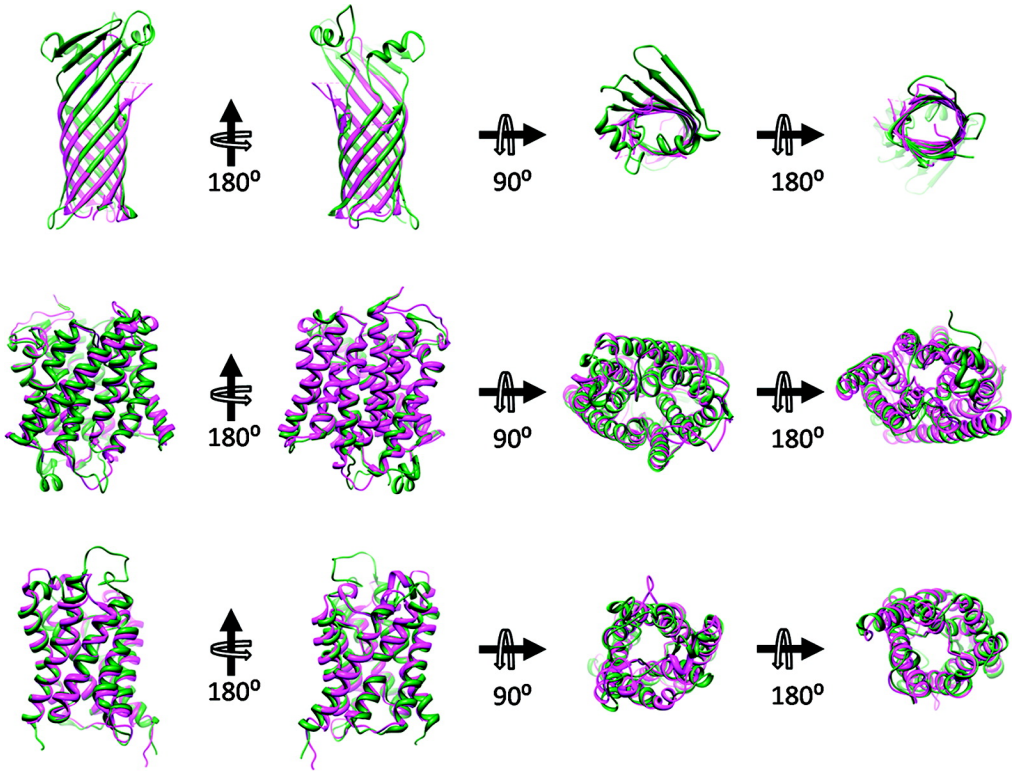

Figure 1.12. Superpositions of structures of thermophilic archaeal membrane proteins on those of mesophilic counterparts reveal a high degree of similarity. Views onto the membrane surface are from the extracellular space (second panel from right) and from the cytosol (far right): (top row) superposition of porins TtoA from *T. thermophilus* (green, PDB entry 3DZM(Brosig et al., 2009)) and OmpA from *E. coli* (magenta, PDB entry 1QJP (Pautsch and Schulz, 2000)), (middle row) superposition of ammonium transporters Amt-1 from the archaeal hyperthermophile *A. fulgidus* (green, PDB entry 2B2H (Andrade et al., 2005)) and AmtB from *E. coli* (magenta, PDB entry 1U77 (Khademi et al., 2004)), (bottom row) superposition of aquaporin from *A. fulgidus* (green, PDB entry 3NE2) and AqpZ from *E. coli* (magenta, PDB entry 1RC2 (Savage et al., 2003)).

To cite another example, *Archaeoglobus fulgidus* is an archaebacterial thermophile (optimal growth temperature of 83 °C) that has a very exotic lipid composition, with the two major lipid backbones being ether-linked diglycerides of either conventional (diether) or cyclical tetraether bolalipid architecture (Lai et al., 2008; Ulrih et al., 2009) (see Figure 1.11). The chains are composed of saturated isoprenoids. It has been shown that the ratio of the tetraether bolalipid to diether lipids increases with increasing growth temperature (1:1 ratio at 83 °C), indicating that the bolalipids are involved in imparting extreme thermostability (Bogdanov et al., 2008). Despite the differences in lipid structure between this organism and *E. coli*, the ammonium transporter Amt-1 from *A. fulgidus* is remarkably similar to that of the *E. coli* transporter AmtB, as illustrated by superposition of the two structures (Khademi et al., 2004; Andrade et al., 2005) (Figure 1.12), where the rmsd for the transmembrane domain α-carbons is 0.9 Å. The crystal structure of a second membrane protein from *A. fulgidus*, an aquaporin, was recently determined by the Stroud lab (PDB entry 3NE2). The sequence of this protein is ~30% identical with that of the *E. coli* aquaporin AqpZ, for which a crystal structure is also available (Savage et al., 2003). A superposition reveals very similar structures (see Figure 1.12), with an rmsd for the transmembrane domain α-carbons in the two structures of 0.94 Å.

The fact that lipid structure is so highly variable from organism to organism likely reflects a combination of both evolutionary selective pressure placed upon a successful membrane to adapt to changes in environment (temperature, energy and/or carbon sources, pH, hostile neighbors, etc.) and evolutionary drift. The fact that membrane proteins, in contrast, are often structurally well-conserved between evolutionarily distant organisms likely reflects the fact that all plasma membranes share some common structural and dynamic properties under organism-specific physiological conditions even though their lipids are highly divergent. At the same time, it appears equally likely that

widely retained membrane proteins have been selectively adapted so that they remain foldable, stable, and functional despite variations in membrane composition. It seems that in the development of new species evolution can substantially alter membrane lipid composition without at the same time having to dramatically alter the organismal complement of membrane proteins.

Aquaporin-0 has a tolerant lipid-exposed surface

Aquaporin-0 (AQP0) is a tetrameric helical membrane protein that serves as a water channel in the fiber cells of the vertebrate ocular lens and also forms intermembrane junctions between layers of flattened cells. Walz and co-workers conducted pioneering structural studies that provided atomic level details of the interaction of this protein with its annular layer of interacting lipids (for other examples of MP structures in which annular lipids have been observed, see (Bondar et al., 2009) and the references cited therein). 2D crystals of sheep AQP0 were prepared in lipid bilayers and then structurally characterized using electron crystallography. This led to a 1.9 Å structure of the protein in dimyristoylphosphatidylcholine (DMPC) bilayers (Gonen et al., 2005) and to a 2.5 Å structure in bilayers composed of *E. coli* phospholipids (Hite et al., 2010) (see Figure 1.13). In both structures, the annular lipids interacting directly with the exposed surface of the transmembrane domains of the tetramer are observed, revealing specific modes of direct interaction with the protein surface. The annular lipid:protein subunit stoichiometry is in each case 7:1. There are a number of interesting observations that can be made about these structures.

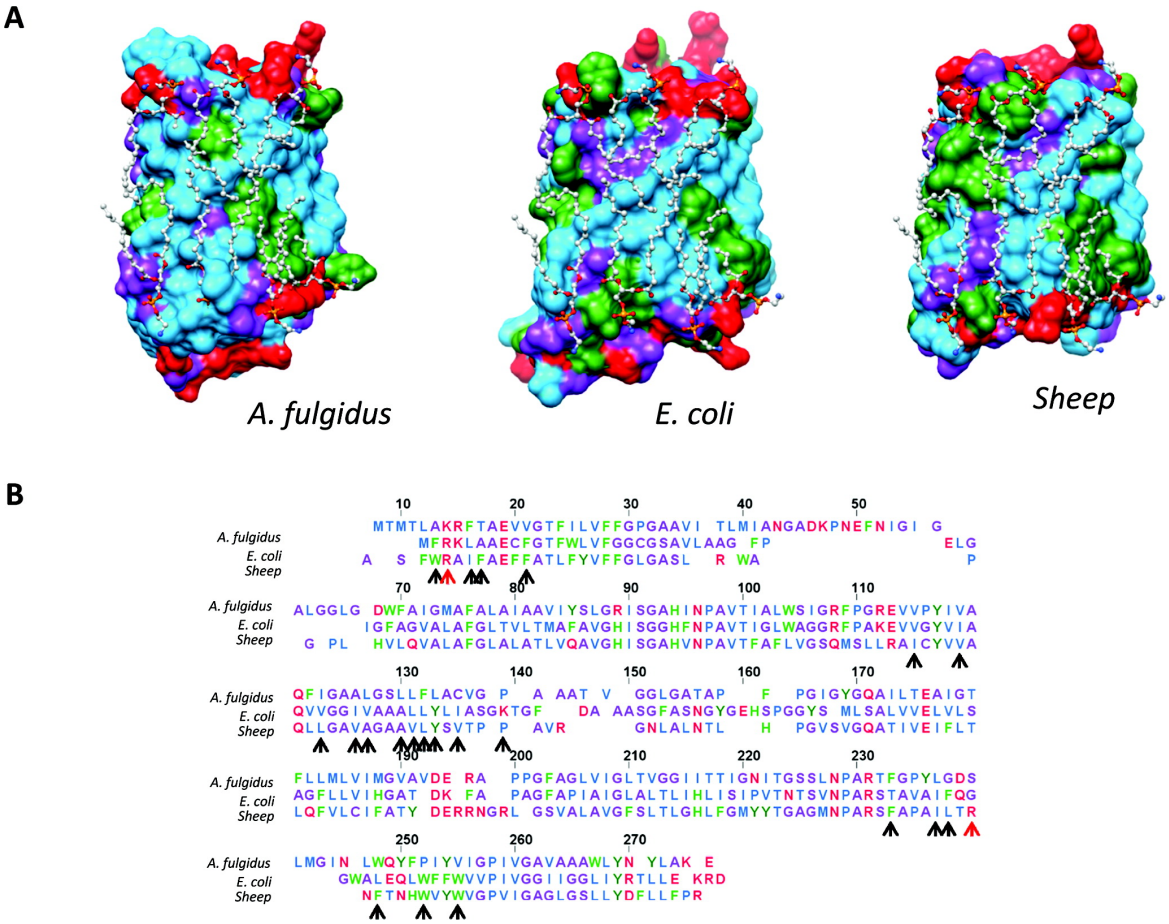

Figure 1.13. Lipid-contact faces of aquaporins from three domains of life show some common features.

(A) Depiction of the lipid-contact faces of aquaporins from a hyperthermophilic archaebacterium, *A. fulgidus* (PDB entry 3NE2), E. coli (PDB entry 1RC2 (Savage et al., 2003)), and *O. aries* (sheep) (PDB entry 3M9I (Hite et al., 2010)). Residues are colored as follows: red for polar residues, blue for large hydrophobic residues, green for aromatic or His residues, and purple for small residues (Gly, Ala, Ser, and Cys). In all three cases, the structures have been overlaid with the annular E. coli lipids as found in the structure of sheep aquaporin crystallized in the Walz laboratory (PDB entry 3M9I). (B) Structure-based sequence alignment of the aquaporins depicted in panel A. Arrows denote residues that were in direct contact with the lipid aliphatic chains in the sheep AQP0 structure. Red arrows depict residues in contact with the headgroups. The color-coding of residues is the same as that in panel A.

First, even though both structures reveal preferred modes of acyl chain–AQP0 interactions, neither pure DMPC nor *E. coli* phospholipids reflect compositions that are similar to the lipid composition of native lens fiber membranes. Those membranes are extremely rich in both cholesterol and sphingolipids, to the extent that they can be considered to be homogeneously raftlike in composition and biophysical properties (Tong et al., 2009; Borchman and Yappert, 2010). It is remarkable that AQP0 exhibits specific and preferred modes of interactions with its surrounding lipids even when those lipids are very different from its neighboring lipids under physiological conditions.

Second, while both DMPC and *E. coli* lipids exhibit preferred modes of interaction with the sheep AQP0 surface, the set of binding modes for the seven annular DMPC molecules is distinctly different from the set for seven *E. coli* lipids (Hite et al., 2010). DMPC differs from the *E. coli* lipids by having two relatively short and fully saturated acyl chains, whereas *E. coli* lipids usually have both a saturated chain and an unsaturated chain, both of which are typically longer than the C14 chains of DMPC. In both cases, the acyl chains fit into grooves on the surface of the transmembrane domain. It is notable that these grooves are able to accommodate multiple (alternative) modes of acyl chain interactions to suit the properties of its lipid neighbors in terms of chain length and possible sites of *cis* double bonds, even when these lipid neighbors are non-native.

While *E. coli* lipids form fluid phase bilayers that are significantly thicker than liquid crystalline phase DMPC, the structure of the protein is seen to be nearly identical regardless of which lipids were used during 2D crystallization (see Figures 1.10D and 1.13) (Hite et al., 2010). Indeed, the X-ray crystal structure of bovine AQP0 determined in alkylglycoside micelles is nearly identical to that determined via electron crystallography (see Figure 4 in (Harries et al., 2004)).

While we do not yet know the degree to which AQP0 can be regarded as a typical MP in terms of its interactions with lipids, the observations described above

suggest a structural basis for membrane protein tolerance. The hydrophobic grooves on the lipid-exposed surface of AQP0s transmembrane domain are compatible with participation in multiple alternative modes of intimate interaction with lipid chains, even involving chains that may be rare or completely absent in native membranes. It is as if the surface of AQP0 is similar to a “master key” with one defined set of notches that can nevertheless open many different locks. This surface appears to reflect the Scouting imperative “Always be Prepared” in terms of being able to accommodate a wide range of surrounding lipid compositions.

Despite being from organisms with very different membrane compositions (see Figure 1.11) from each other and from *O. aries*, the lipid-exposed surfaces of the *E. coli* and hyperthermophilic *A. fulgidus* AQPZ proteins exhibit structural properties surprisingly similar to those of the lipid-contact face of AQP0 (Figure 1.13). In all three structures, a tract of large nonpolar residues crisscrosses the lipid-contact surface found in the AQP0 structure (see Figure 1.13). In addition, the aquaporins presented here have a similar pattern of aromatic residues on the lipid-contact face. When the *E. coli* lipids from the *Ovis aries* (sheep) AQP0 structure are overlaid across the *E. coli* and *A. fulgidus* crystal structures (as shown in Figure 1.13), it appears that these structures may similarly be able to accommodate these lipids with only minor adjustments in acyl chain and headgroup positions. In fact, in the *E. coli* structure, which was crystallized in micelles of *n*-octyl glucoside, the detergent molecules are found on the natively lipid-exposed face, with the hydrophobic tails lying along grooves similar to the *E. coli* lipid niches in the lens AQP0 structure (PDB entry 1RC2 (Savage et al., 2003)). This conservation would imply that the aquaporins did not need to drastically alter their lipid-contact surface properties over the course of evolution, despite the large changes in lipid composition of the evolving membranes. This observation provides further support for the notion that the

lipid-exposed surfaces of aquaporins are capable of accommodating multiple modes of lipid–protein interactions.

The AQP0 protein was seen to be resistant to structural changes induced by either differing modes of lipid interactions in membranes of different compositions or differing preferred bilayer thicknesses for the mixtures of lipids in the membrane surrounding the protein. AQP0's tolerance is apparently rooted in a healthy intrinsic structural stability.

Final observations and conclusions regarding the apparent tolerance of membrane proteins to variations in their lipid solvent environment

Numerous additional examples of tolerance are provided by MPs that have been purified and then functionally reconstituted in model membranes that often are very different in composition from their native membranes. To cite an extreme example, *E. coli* diacylglycerol kinase (DAGK) is a homotrimer with three transmembrane helices per subunit that catalyzes an interfacial reaction between a lipid and a water-soluble substrate (Van Horn et al., 2009). More than 50% of DAGK's residues lie within the membrane, and its active site is partially membrane-submerged. DAGK is active in a variety of different types of detergent micelles provided that lipid is present, with full activation usually being observed at 10–20 mol % lipid (Bohnenberger and Sandermann, 1983; Walsh and Bell, 1986; Badola and Sanders, 1997). However, the lipid specificity is low; full activation can be accomplished even using lipids not found in *E. coli*, such as saturated phosphatidylcholine or hexadecyl sulfate (Bohnenberger and Sandermann, 1983; Walsh and Bell, 1986; Badola and Sanders, 1997). More recently, using a water-soluble form of diacylglycerol, it has also been shown that DAGK is fully active in certain lysophospholipid micelles even in the complete absence of any nonsubstrate lipid (Koehler et al., 2010). Indeed, DAGK has been shown to be fully active in lipid- and

detergent-free amphipathic polymers known as “amphipols”(Gorzelle et al., 2002), in CHAPSO/DMPC bicelles (Czerski and Sanders, 2000), and in LCPs composed of monoolein (Li and Caffrey, 2011). *E. coli* DAGK has also been shown to retain function following expression in mammalian COS cells (Ramer and Bell, 1990). DAGK is highly active following reconstitution in lipid vesicles, with maximal activity being observed in vesicles composed of dioleoylphosphatidylcholine (not present in *E. coli* membranes), with somewhat lower activity being observed in vesicles composed of lipids chosen to mimic the lipid composition of the plasma membrane of *E. coli* (Pilot et al., 2001a; 2001b). The fact that DAGK is so exceedingly tolerant of extreme variations in its membrane milieu may be closely related to the extremely high thermal stability of this protein in native membranes (cf., (Russ et al., 1988)). Indeed, the fact that *E. coli* membranes can be boiled for several minutes without any loss of DAGK activity suggests that DAGK’s thermal stability may have been “overdetermined” by evolution. Perhaps this trait represents a “reserve” of intrinsic stability that is not normally essential to DAGK or its host during the normal life span of an *E. coli* bacterium but could facilitate evolutionary membrane remodeling under conditions of selective pressure. While most membrane proteins are much less stable than DAGK, this enzyme illustrates the extreme degree to which evolution can sometimes confer tolerance to membrane proteins.

In addition to numerous examples of reconstituting membrane proteins into non-native model membranes, there are also examples of functionally expressing a membrane protein from one organism in another organism that has a very different membrane composition. A revealing example is provided by a number of mammalian G protein-coupled receptors that have been expressed in the plasma membrane of *E. coli* and shown to remain functional, at least to the extent that they retain the ability to specifically bind antagonists with high affinity.(Breyer et al., 1990; Stanasila et al., 1999;

Furukawa and Haga, 2000; Grisshammer et al., 2005; Berger et al., 2010) Such function is retained despite the fact that cholesterol is thought to be important for the stability and function of some of these receptors but is not present in *E. coli* (reviewed in ref (Opekarová and Tanner, 2003)).

Finally, we note that there are a number of membrane proteins that have now been crystallized from both detergent micelles and bilayer model membrane media (bicelles or lipidic cubic phases). These proteins, which include AQP0 (see above), the rhomboid protease (Bondar et al., 2009), bacteriorhodopsin (Faham and Bowie, 2002), and VDAC (Ujwal et al., 2008), have been seen to adopt similar structures in both detergents and bilayer model membranes, again supporting the notion that membrane proteins are often remarkably tolerant of their membrane or membrane-mimetic environment. There are, of course, relatively rare exceptions such as the KvAP potassium channel, whose flexibly linked multidomain architecture makes it particularly susceptible to micellar distortion (see the introductory section). Also, we acknowledge that at least some membrane proteins that have yielded to high-resolution structural analysis represent “low-hanging fruit” in terms of being relatively stable and rigid membrane proteins. It should also be noted that even for proteins that exhibit the same static structure when determined in both detergent micelles and lipid-containing model membranes it has been seen that the conformational flexibility of the protein in micelle-derived crystals is higher than in crystals with lipids present (Hite et al., 2008).

To conclude, we emphasize that it is abundantly clear (Opekarová and Tanner, 2003; Lee, 2004; Hunte, 2005; Nyholm et al., 2007; Qin et al., 2007; Hunte and Richers, 2008; Marsh, 2008; Ernst et al., 2010; Adamian et al., 2011; Lee, 2011) that many membrane proteins require specific lipid cofactors for proper folding, structure, and/or function. Some membrane proteins also have rather specific requirements with regard to membrane fluidity, thickness, lateral surface pressure, or other membrane properties.

However, the data highlighted here suggest that some degree of fundamental tolerance to variations in membrane lipid composition is also a trait that has been conferred in varying degrees by evolution to many, if not all, membrane proteins. In this regard, we should note that there is no inherent contradiction between this property and the notion that many membrane proteins also have specific lipid or membrane requirements. For example, a given membrane protein might be generally tolerant of a wide range of membrane compositions yet still have a specific lipid cofactor requirement to function, both of these traits having been evolutionarily selected. Here, we have suggested a couple of structural and biophysical mechanisms that may have been used by evolution to help confer tolerance to some membrane proteins: protein stabilization and the generation of grooved master key-like lipid-exposed surfaces. There likely are others. Tolerance is an intrinsic property shared by many membrane proteins that helps to explain the spectacular success of the reductionist approach to membrane biology, which has relied heavily on the assumption that illuminating and biologically relevant information can be gleaned from carefully controlled studies of membrane protein structure, folding, and function under model membrane conditions. Such studies should, of course, always employ the most realistic model membranes that are consistent with a given experimental approach and should also include verification of protein functionality, when possible.

The C-terminal fragment of the Amyloid Precursor Protein, C99, and Its Applications to the Investigation of Novel Bicelles

Alzheimer's disease (AD) is a progressive neurodegenerative disorder and is the most common form of dementia (Alzheimer's Association, 2014). AD, the 6th most common cause of death in the US (the 5th leading cause of death for people over age 65), affects 5.2 million people in the US alone, costs $214 billion per year, and has no

cure (Alzheimer's Association, 2014). The risk of AD increases with increasing age. Due to medical, environmental, and social factors, the population of American elderly is rapidly increasing, with 6 million Americans aged 85 or older in 2010 and that number projected to reach 21 million by 2050 (Alzheimer's Association, 2011). As a result of the aging population, AD is increasing in prevalence, even as many other common causes of death are decreasing, and is expected to affect 11-16 million people by 2050 if no new preventative measures or effective treatments are developed (Alzheimer's Association, 2014). Consequently, it is expected that the annual cost of AD will reach $1.2 trillion by 2050 (Alzheimer's Association, 2014). Current drug treatments are aimed at managing or delaying the onset of various symptoms but do not directly target the underlying causes of AD.

The prevailing hypothesis in the AD field is that amyloidal oligomers/aggregates formed from amyloid β-peptide (Aβ) are neurotoxic. AD is characterized pathologically by the formation of these Aβ oligomers/aggregates, both soluble and insoluble. The insoluble aggregates are responsible for formation of Aβ plaques that serve as histological markers of the disease, but it is the soluble oligomers/aggregates of Aβ that are thought to be the molecular species responsible for neurotoxicity and AD progression (Walsh and Selkoe, 2007). Aβ is generated through processive cleavage of the Aβ precursor protein (APP). APP can enter one of two pathways: a non-amyloidogenic pathway that produces the soluble p3 peptide and an amyloidogenic pathway that leads to production of toxic Aβ (see Figure 1.14) (Nunan and Small, 2000). In the non-amyloidogenic pathway, APP is initially processed by an α-secretase metalloprotease to form the 83-residue, membrane-integrated C-terminal fragment C83, and is then further processed by γ-secretase to produce the APP-intracellular domain (AICD) and the p3 peptide, which is thought to have neuroprotective and neuroproliferative properties (Konietzko, 2012).

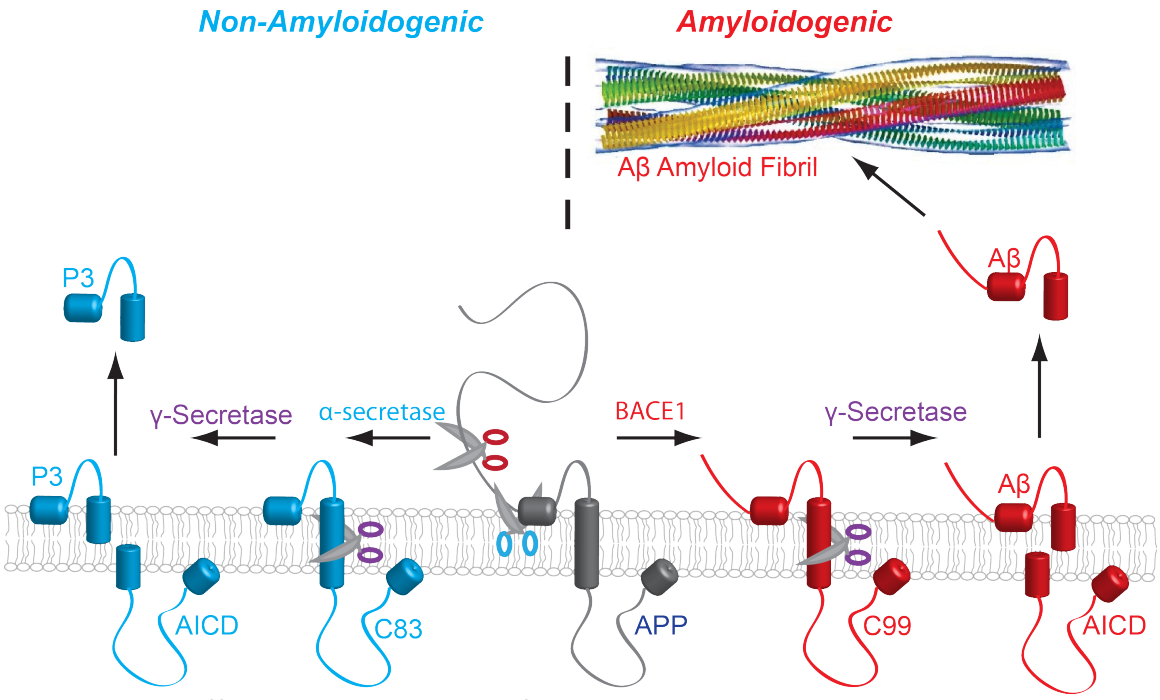

Figure 1.14. Differential processing of amyloid precursor protein.
Amyloid precursor Protein (APP; grey) can be differentially cleaved to enter a benign, non-amyloidogenic pathway (blue products) or a pathological, amyloidogenic pathway (red products). In the non-amyloidogenic pathway (left), APP is first processed by an α-secretase (blue scissors) to generate the 83-residue C-terminal fragment C83, which is then further processed by γ-secretase (purple scissors) to generate the amyloid precursor protein intracellular domain (AICD) and the P3 peptide, which may play neuroprotective roles. In the amyloidogenic pathway, APP is first cleaved by a β-secretase (BACE1; red scissors) to generate the 99-residue C-terminal fragment C99, which is then further processed by by γ-secretase (purple scissors) to generate the amyloid precursor protein intracellular domain (AICD) and the Aβ peptide, which can form toxic oligomers, aggregates, and ultimately, the amyloid fibrils that are characteristic of an Alzheimer's diagnosis. Figure modified from Mittendorf et al., 2012.

On the other hand, in the amyloidogenic pathway APP is instead initially processed by β-site APP cleavage enzyme 1 (BACE1) to form the 99-residue, membrane-integrated C-terminal fragment C99, followed by progressive processing by γ-secretase to produce the AICD, which is thought to participate in nuclear signaling (Konietzko, 2012), and the Aβ peptide involved in amyloidogenesis (Nunan and Small, 2000). Because this amyloidogenic pathway is thought to be responsible for the pathogenesis of AD, it is an attractive therapeutic target. Evidence supports that blocking the amyloidogenic pathway through reduction of BACE1 levels shuttles APP instead through the non-amyloidogenic pathway (initiated by an α-secretase metalloprotease instead of BACE1) and prevents Aβ secretion and AD pathogenesis (Dislich and Lichtenthaler, 2012). The attractiveness of BACE1 as a therapeutic target is bolstered by evidence that sporadic AD may be in part due to increases in BACE1 activity (Stockley and O'Neill, 2007). Unfortunately, due to the inherent difficulty of direct pharmacological targeting of the BACE1 enzyme, this treatment option has not yet been realized (Dislich and Lichtenthaler, 2012). Additionally, targeting γ-secretase activity has not been a viable strategy thus far, as gamma secretase is involved in a number of other important regulated intramembrane proteolysis events, such as cleaving the important developmental protein Notch (Zhang et al., 2014). Because it is difficult to develop substrate-selective inhibitors for gamma secretase, a number of therapeutic attempts have halted mid-trial due to the toxic effect of non-selective inhibition of the enzyme complex. Learning about the regulatory mechanisms for the cleavage of APP by BACE1 and also the cleavage of C99 is thus an important step in developing viable new therapeutic strategies targeting either APP or C99 specifically.

As a number of papers (Lichtenthaler et al., 2002; Holmes et al., 2012; Winkler et al., 2012) have shown that C99 cleavage is regulated by membrane thickness and

identity, the development of membrane mimetics with a broad and adjustable lipid profile for the study of this protein is imperative. Our laboratory already has a good handle on the biochemical, biophysical, and structural characterization of C99, with a number of NMR investigative studies behind us (Beel et al., 2008; 2009; 2010; Barrett et al., 2011; Pester et al., 2013; Song et al., 2013) and having published a structure of C99 using solution-state NMR in 2012 (Barrett et al., 2012) that also characterizes its binding to membrane cholesterol. Because we can easily purify ^{15}N-labeled C99, reconstitute it into bicelles, and study it by solution NMR, and because membrane identity is known to affect C99 cleavage, C99 is an ideal test-case for novel membrane mimetics for use with solution NMR. In this thesis, we outline a number of new bicelle membrane mimetics and test those novel bicelle mixtures for their application to solution NMR using C99.

Summary

This introductory chapter has focused on one side of the coin—how do membranes influence membrane proteins? It is clear from this overview that membrane proteins may be remarkably tolerant to a variety of environments. However, it is also clear that there may be subtle modulation of membrane proteins based on the properties of these environments. Chapter III of this thesis will focus on the exploration of the development of membrane mimetics that have a range of lipid profiles for the investigation of these modulations as it relates to the membrane protein C99.

The other side of the coin—how membrane proteins may influence their membrane environment—is explored with a case study protein, peripheral myelin protein 22 (PMP22). The next chapter introduces what is known about PMP22 and its relation to human pathology.

CHAPTER II

INTRODUCTION TO MYELIN AND PERIPHERAL MYELIN PROTEIN 22

Myelination is perhaps the best example of a membrane being influenced by cellular processes. In the peripheral nervous system, Schwann cells compress and wrap in a large number of spirals around nerve axons to provide an insulation for nerves that allows for rapid nerve conduction velocities, making higher forms of life as we know it possible. The various molecular mechanisms that underlie the shaping of the Schwann cell into this complex architecture remain poorly understood, but it is clear that several membrane proteins, including peripheral myelin protein 22 (PMP22), play important roles. This dissertation focuses on studies of how PMP22 reconstituted into a membrane environment profoundly shapes the ultrastructure of those membranes.

Myelin: A Nerve Conduction Enhancer

Nerves in healthy vertebrates are encased in a lipid-rich (70 to 85% lipids by weight compared to ~50% in other biological membranes) (Morell and Quarles, 1999a), segmented membranous structure called myelin. This structure acts as a dielectric material (Min et al., 2009) to prevent the leakage of ions. It enhances nerve conduction velocities by allowing conduction to occur in a saltatory, or “jumping,” manner between the unmyelinated segments of axons, termed Nodes of Ranvier, and by decreasing the capacitance in the myelinated regions with each added “wrap” of membrane from a myelinating glial cell (Morell and Quarles, 1999b). In the central nervous system (CNS), myelin is produced from the glial cells known as oligodendrocytes, while in the peripheral nervous system (PNS), this role is played by Schwann cells (Morell and Quarles,

1999b). The proteome of these two cell-types are very different. However, a great deal is known about the process of myelination and the roles of the proteins therein and many parallels can be drawn between the two systems. Because this dissertation is focused on the peripheral myelin protein 22, a component of the PNS, this chapter will most heavily focus on the process of myelination and the relevant components of the PNS.

In the PNS, a number of Schwann cells line up along the axon, wrapping it in a segmented fashion, with each Schwann cell unit being termed an "internode" because it myelinates the areas of nerve between the Nodes of Ranvier, the latter being the segments of the axon where the ion channels responsible for propagating the action potential are located (Figure 2.1). A myelinating Schwann cell spirals tightly around the axon, squeezing out the Schwann cell cytoplasm, such that the compact myelin is a dense multilamellar proteolipid structure composed of repeating bilayer-protein units. The average repeat distance in CNS myelin as observed by negative stain electron microscopy is 107 Å, while that observed for PNS myelin is 119 Å (Morell and Quarles, 1999b). The spiraling of myelin is thought to occur from growth at the inner tongue (Bunge et al., 1989) in a "carpet crawler" or "jelly roll" model (Snaidero and Simons, 2014) that is fairly accepted for the PNS. It wasn't until recently that a similar model of inner tongue growth was firmly established for the oligodendrocytes of the CNS (Snaidero et al., 2014) (Figure 2.2). The number of lamellae or "spirals" directly correlates to nerve conduction velocity, with more lamellae producing faster velocities due to further decreases in capacitance (Armati and Mathey, 2013). Around some large diameter sensory axons, up to 100 spirals of compact myelin lamellae may form(Armati and Mathey, 2013). Because each internode distance may be up to 2 mm, highly lamellar Schwann cells may produce up to 20 mm^2 of membrane—nearly 2000 times the membrane surface area of a typical cuboid epithelial cell (Armati and Mathey, 2013).

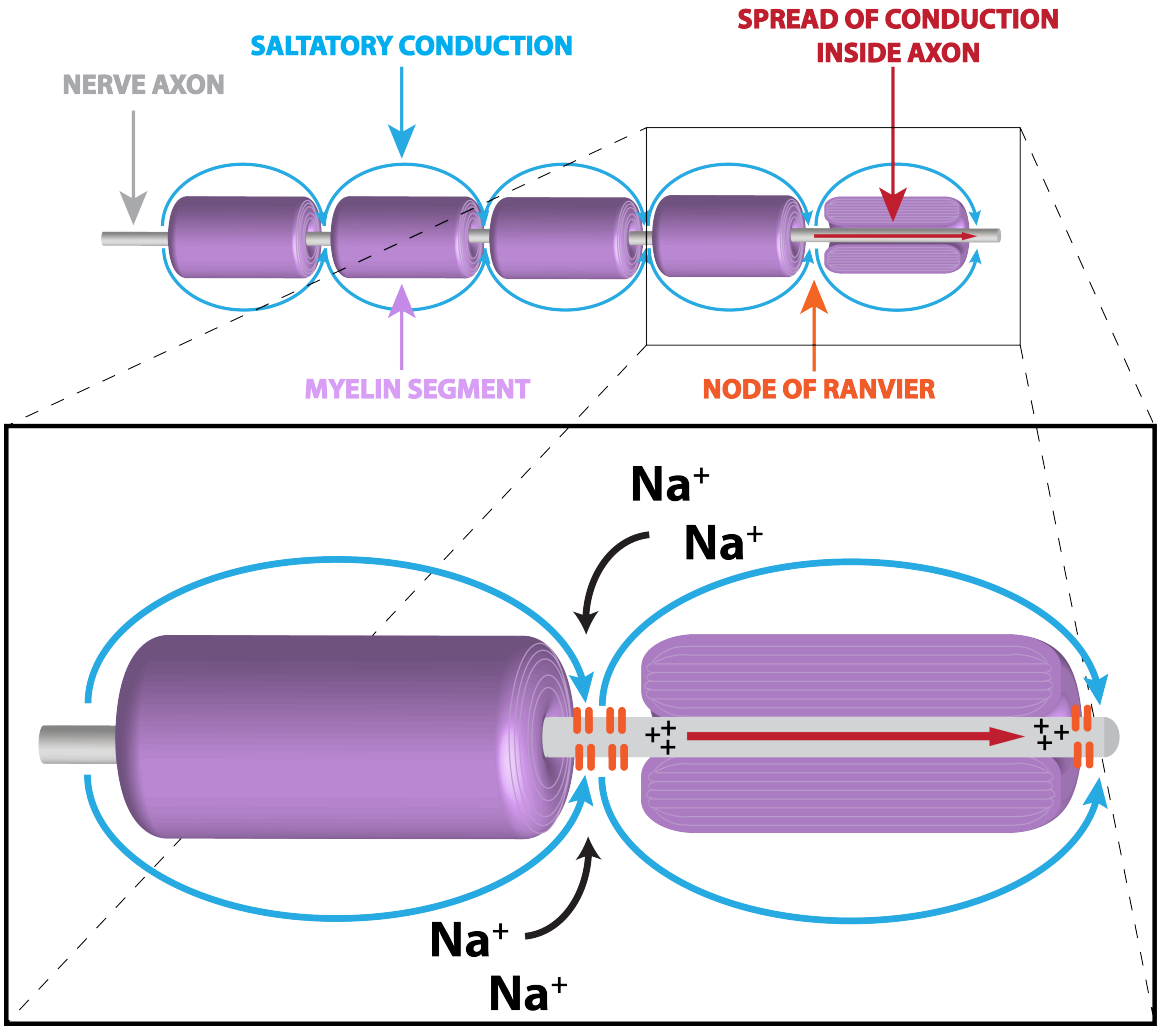

Figure 2.1. Diagram of myelinated axon.
(Top) A myelinated axon depicted myelin segments (purple) along an axon (grey). Saltatory conduction (blue arrow) spreads allows the charge influx to occur only at the Nodes of Ranvier (orange arrow), which spreads outward inside the myelinated regions (red arrows). (Bottom) Sodium ion channels (orange) allow for the influx of sodium ions that depolarize the axon.

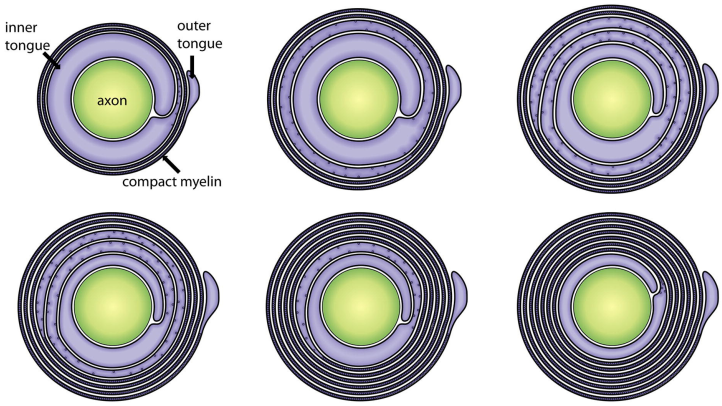

Figure 2.2. Model of growth and compaction of myelin membranes in the CNS. The growth and extension of the inner tongue provides the increased number of lamellae. The level of compaction is determined by the MBP concentration. A similar model has been established for the PNS, though the role of MBP in PNS myelination is less clear. Figure adapted from Snaidero et al., 2014.

Myelin ultrastructure is complex

The ultrastructure of a myelinating Schwann cell internode is intricate and complex (see Figure 2.3). The Schwann cell can be conceived of as consisting of three regions: the adaxonal Schwann cell (adjacent to the axon), the myelin sheath (consisting of compact and non-compact myelin lamellae), and the abaxonal Schwann cell (furthest from the axon). Both the abaxonal and adaxonal Schwann cell contain cytoplasm, and the Schwann cell nucleus is located in the abaxonal region (King, 2013). The compact multilammelar structure described above is known as the *compact myelin* and makes up the majority of the internode. The proteins located in compact myelin are described in greater detail below. Interspersed within compact myelin are regions of *noncompact myelin* or *Schmidt−Lanterman incisures*, which contain pockets of cytoplasm and may provide metabolic support to the distal parts of the Schwann cell. The proteins located in these regions are not the same as those found in compact myelin, instead consisting of a number of junctional complexes (Kidd et al., 2013). In addition to regions of noncompact myelin interspersed throughout the compact myelin, there also lie regions of non-compact myelin called *paranodal loops* bordering the internodes. These are also populated by junctional complexes that adhere them tightly to one another and to the axon (Kidd et al., 2013). As the name implies, the juxtaparanode lies immediately adjacent to the paranode and contains mitochondria-rich cytoplasm and the potassium channels that rectify membrane potential after depolarization (King, 2013).

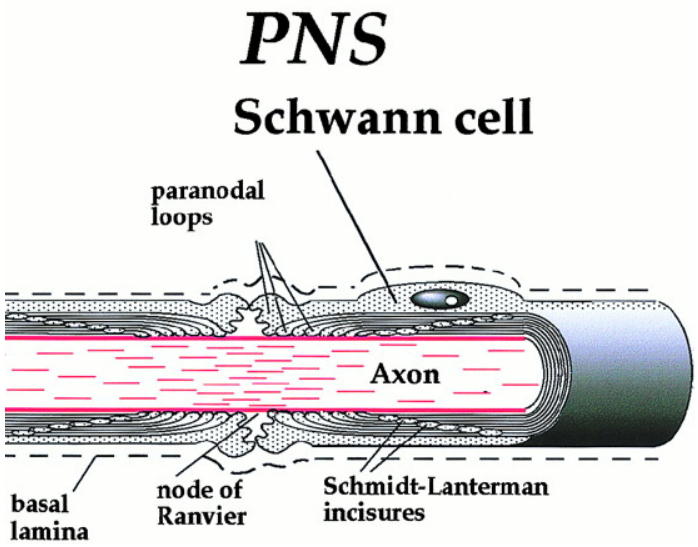

Figure 2.3. Diagram of myelinating Schwann cell morphology.
Two partial Schwann cell internodes are depicted, interrupted by a node of Ranvier. The Schmidt-Lanterman incisures are regions of non-compact myelin that interrupt the compact myelin (shown as tight lamellae). Figure adapted from Baumann and Pham Dinh, 2001.

The Proteins of Compact CNS Myelin

The focus of Chapters IV and V of this dissertation is on the PMP22 protein of PNS compact myelin. For comparison, we will consider the proteins of CNS compact myelin and PNS compact myelin in greater detail.

Myelin basic protein

Early estimates suggested that myelin basic protein (MBP) makes up 22-35% of the myelin proteome (Morell et al., 1972; Norton and Poduslo, 1973; Banik and Smith, 1977; Deber and Reynolds, 1991), though newer quantifications by mass spectrometry suggest a much lower (8%) abundance (Jahn et al., 2009). Still, MBP is the second-most abundant individual protein in CNS myelin (although present at much lower levels in the PNS myelin), and is likely responsible for myelin compaction on the cytosolic surface of the myelin membranes, self-assembling to edge out bulky proteins and cytosol (Bakhti et al., 2014).

MBP is so named for the its high proportion of polar and positively charged amino acid residues, which contributes to the fact that MBP exists as an intrinsically disordered protein in solution (Krigbaum and Hsu, 1975). However, in membrane mimetics, MBP takes on significant α-helical structure,(Farès et al., 2006; Ahmed et al., 2010; Wang et al., 2011a) and single particle EM reveals significant tertiary structure in membrane-bound MBP (Beniac et al., 1997; Ridsdale et al., 1997). Additionally, zinc induces significant secondary structure in solution or membrane-bound MBP (Smith et al., 2010; Wang et al., 2011a) and stabilizes MBP-membrane interaction (Earl et al., 1988). Given the potential role of zinc or copper in PMP22 folding and stability in PNS myelin (discussed below), and the fact that dietary zinc or copper depletion results in neuropathy (Terril-Robb et al., 1996; Kumar et al., 2004; Unal et al., 2005). it seems

reasonable that zinc ions may be an important co-factor in myelin biogenesis and maintenance.

2',3'-Cyclic-nucleotide 3'-phosphodiesterase

Early estimates suggested that 2',3'-Cyclic-nucleotide 3'-phosphodiesterase (CNP) made up 4-15% of the CNS myelin proteome, while newer mass spectrometry-based quantification suggest that number lies closer to 4% (Jahn et al., 2009). The role of CNP has remained ambiguous, but recent studies on the process of oligodendrocyte-mediated myelination show that CNP, a bulky protein (47 kDa), plays a role in preventing the premature compaction of myelin at the inner tongue as myelin growth proceeds (Snaidero et al., 2014). Corresponding evidence exists for the interaction of CNP with components of the cytoskeleton, further hinting at a role for CNP in the mediation of the myelin growth (Lee et al., 2005a).

Proteolipid protein

Early estimates suggested PLP made up 30-45% of the CNS myelin proteome (Morell et al., 1972; Norton and Poduslo, 1973; Banik and Smith, 1977; Deber and Reynolds, 1991), though newer quantifications by mass spectrometry suggest a much lower (17%) abundance (Jahn et al., 2009). Still, it is the most abundant individual protein in myelin. PLP is a tetraspan membrane protein (Popot et al., 1991) and is expressed in oligodendrocytes as two alternatively spliced isoforms: PLP and the shorter isoform DM20, which lacks 35 residues in the intracellular loop (Figure 2.4) (Greer and Lees, 2002). PLP is highly acylated, with up to six covalently bound palmitic acid moieties, contributing to its already highly hydrophobic nature (Greer and Lees, 2002). Two of the acylated cysteine residues of the long isoform of PLP are not present in the DM20 isoform (see Figure 2.4). Importantly, two intramolecular disulfide bonds are

present in the second extracellular loop (between C183 and C227 and between C200 and C219) that are crucial for protein folding and trafficking (Dhaunchak and Nave, 2007). Evidence also exists for an intermolecular disulfide bond at C108 that mediates covalent dimerization of the PLP isoform but not the DM20 isoform (Daffu et al., 2012).

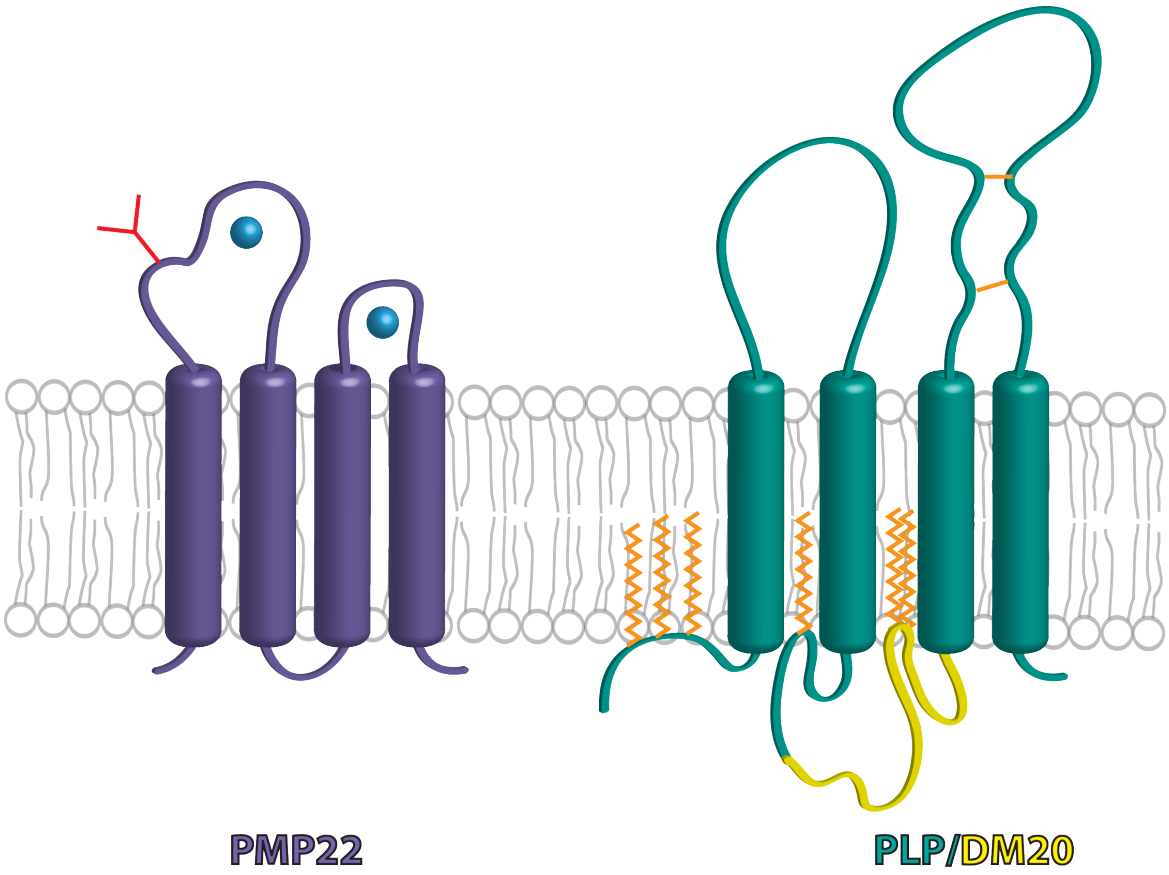

Figure 2.4. Comparison of PMP22 and PLP structure.
PMP22 (purple) is the tetraspan membrane protein found in peripheral myelin, which is the focus of Chapters IV and V of this dissertation. PMP22 has a known glycosylation site (red Y) at Asn41. Addditionally, PMP22 appears to be capable of coordinating up to two divalent metal cations (blue spheres) and this binding appears relevant to PMP22 folding and stabilization (Myers et al., 2008; Schlebach et al., 2015). Residues that might be involved in these binding events include His34, Asp37, Cys42, His51, His52, Cys53, and Glu60, all of which are located in the extracellular loop 1 (ECL1) and His121, Glu123, His125, and Asp129, all of which are located in the extracellular loop 2 (ECL2). PLP (green) and its alternatively spliced isoform, DM20, which lacks the region depicted in yellow (residues V115-K150 of PLP), are also tetrapsan membrane proteins, but are found in the CNS myelin. PLP contains 6 potential acylation sites, depicted as orange zig-zags, (Cys5, Cys6, Cys9, Cys108, Cys137, and Cys139, numbered according to PLP) and 2 sites of intermolecular disulfide bonds, depicted as orange bars (Cys183 to Cys227 and Cys200 to Cys219). A complete review of these modifications is presented in Han et al., 2013.

The major role for PLP is believed to be in the formation of a molecular zipper that promotes the sliding and adhesion of oligodendrocyte cell membranes along one another (Bakhti et al., 2014). The mechanism by which PLP may do this is unclear, though it could be through *trans*-homophilic interactions with other PLP molecules on apposing membrane surfaces or interactions with galactolipids on those apposing membrane surfaces (Coetzee et al., 1999). In any case, it would appear that these interactions are transient and weak and are enhanced upon the reduction of repulsive forces between juxtaposed membranes (Bakhti et al., 2013). The extracellular domains of PLP are the protein component of the interperiod line (the extracellular protein density) visualized in compact CNS myelin. A model for how PLP and MBP assemble CNS myelin is presented in Figure 2.5 (adapted from Bakhti et al., 2014). Intriguingly, when reconstituted into liposomes, native PLP creates assemblies reminiscent of the myelin-like assemblies formed by PMP22 that we report and characterize in Chapter IV, where the PLP appears to roll up vesicles into multilayered assemblies visible by negative-stain electron microscopy. This is one line of evidence for the role of PLP in the shaping of the oligodendrocyte membrane and the initiation of myelination (Palaniyar et al., 1998). Additionally, like PMP22 in the PNS (discussed below), a variety of mutations of PLP, which seem to impair its folding and trafficking, can result in dysmyelinating disorders of the CNS (Gow et al., 1994; Jung et al., 1996; Dhaunchak and Nave, 2007; Dhaunchak et al., 2011). It is feasible that these two sequence-unrelated tetraspan proteins may share at least some functions in common in the genesis of myelin in the CNS and PNS.

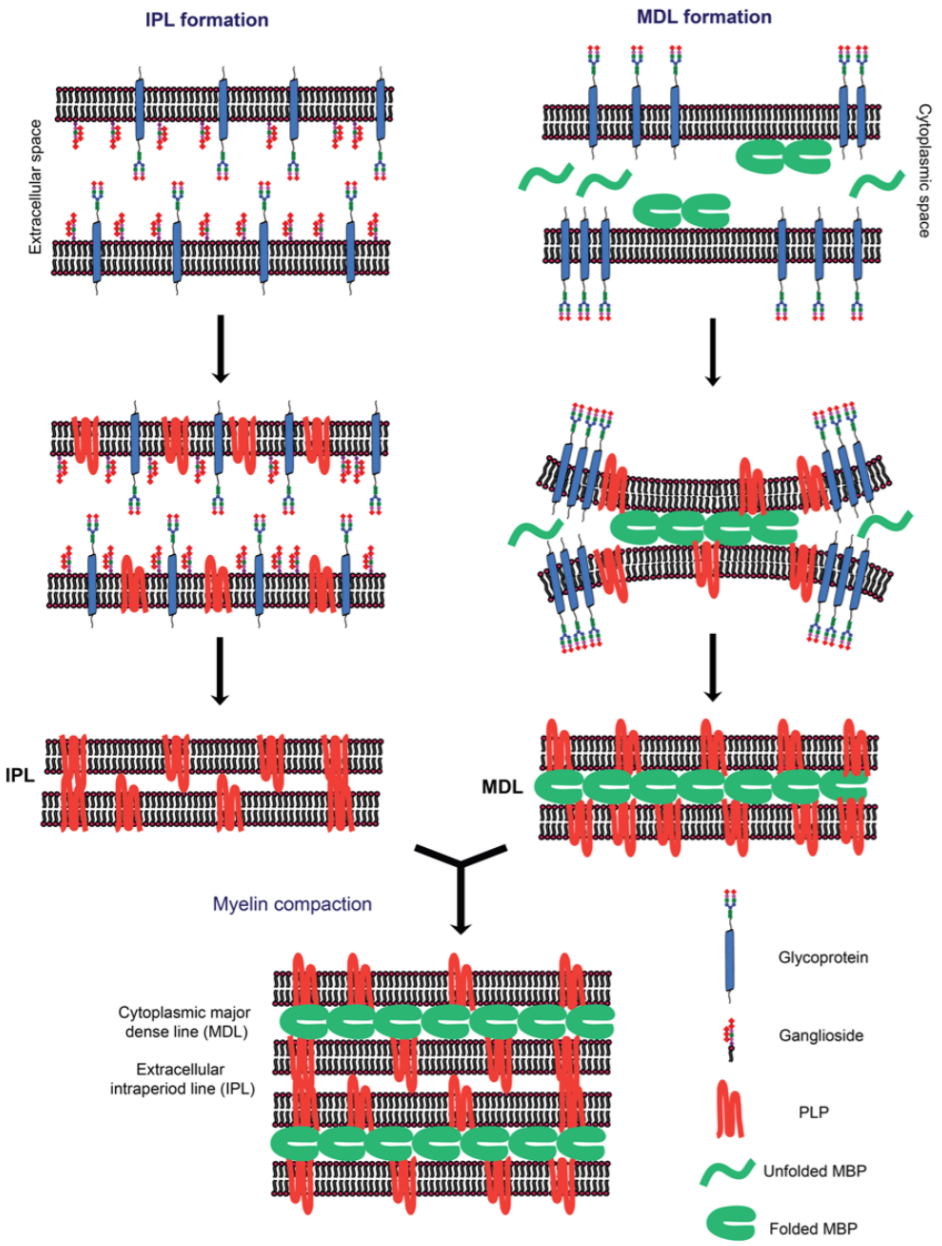

Figure 2.5 Schematic model of possible mechanisms of CNS myelin assembly. Removal of glycosylated components that generate repulsive forces in combinations with PLP-mediated weak adhesive forces facilitates the formation of the extracellular interperiod line (IPL). In the cytosol, MBP assembles into a tight meshwork to compress the cytosol and extrude larger proteins, facilitating formation of the cytosolic major dense line (MDL) of myelin. In this model, the IPL and MDL formation are independent processes that together result in myelin compaction. Figure obtained from Bakhti et al., 2014.

The Proteins of Compact PNS Myelin

The predominant proteins of PNS myelin, myelin protein zero (P_0) and peripheral myelin protein 22 (PMP22), likely play analogous roles to MBP and PLP in the CNS, but they share no homology. MBP is present in the PNS myelin, but at such low levels that it likely does not play the same role of myelin compaction on the cytosolic side of Schwann cells. Indeed, in the *Shiverer* murine mutant, which does not properly synthesize MBP, the PNS myelin is nearly normal (Morell and Quarles, 1999a). It was originally thought that PLP replaced P_0 in the CNS myelin during vertebrate evolution, because fish express P_0 in their central nervous system. However, recent evidence shows that fish co-express proteolipid proteins as major components of their CNS myelin, and a new theory of parallel evolution and coexpression is beginning to arise (Yoshida and Colman, 1996). As such, it is difficult from expression profiles in vertebrates to tease out which proteins play which functions in peripheral myelin, and how they are related to the CNS counterparts.

P_0 protein

Myelin protein zero (P_0), a type I transmembrane glycoprotein protein of 28 kDa (Eichberg, 2002), is the most abundant protein of peripheral myelin, with some estimates putting it as high as 50% of the protein composition by weight (Meuleman et al., 2000). However, more recent estimates by quantitative mass spectrometry suggest a more modest abundance of ~21% of the total protein by weight (Patzig et al., 2011). The protein is glycosylated at a single site (Asn93) and this glycosyl group is necessary for the adhesive properties of P_0 (Griffith et al., 1992; Filbin and Tennekoon, 1993; Filbin et al., 1999; Eichberg, 2002). Some have suggested that P_0 plays adhesive roles on both the extracellular side and the cytosolic side of the membrane, potentially mediated by an extraordinarily basic cytoplasmic domain, which may interact with apposed membrane

leaflets in much the same manner as MBP in the CNS (Ding and Brunden, 1994; Wong and Filbin, 1994; Kursula, 2008; Han et al., 2013). P_0 also contains a large extracellular immunoglobulin (Ig) domain. One crystal structure of the extracellular domain has suggested a tetrameric assembly that contains two molecules each from two juxtaposed membranes, whereby these *cis*- and *trans*-interacting P_0 molecules might mediate myelin compaction and membrane-membrane adhesion.(Shapiro et al., 1996) However, another crystal structure is monomeric.(Liu et al., 2012) A number of other lines of evidence, though, suggest that P_0 can function as a cell adhesion molecule and may exist as a tetramer (D'Urso et al., 1990; Filbin et al., 1990; Schneider-Schaulies et al., 1990; Inouye et al., 1999; Thompson et al., 2002).

In addition to the glycan modification, P_0 contains a number of other modifications crucial for its adhesive properties and/or stability: (1) a disulfide bond between Cys21 and Cys28 (Zhang and Filbin, 1994; 1998), (2) acylation at Cys153 (Bizzozero et al., 1994; Gao et al., 2000), and (3) phosphorylation by Protein Kinase C (PKC) at S181 and S204 (Brunden and Poduslo, 1987; Agrawal and Agrawal, 1989; Suzuki et al., 1990; Ding and Brunden, 1994; Rowe-Rendleman and Eichberg, 1994; Eichberg and Iyer, 1996; Lanwert and Jeserich, 2001). Further, P_0 may undergo tyrosine phosphorylation, though this appears to have no effect on adhesion or P_0 stability and may instead play a role in signaling (Xu et al., 2000; 2001). Due to the high number of critical post-translational modifications, it will be difficult to obtain physiologically relevant P_0 in high yield from *E. coli*-based recombinant means. Perhaps this contributes to the lack of structural information on the full-length protein, which also contains a transmembrane domain. Because of its extensive adhesive properties on both the extracellular and cytoplasmic faces and its high levels of expression, P_0 has been proposed to be the molecular “glue” of peripheral myelin (Figure 2.6) (Eichberg, 2002).

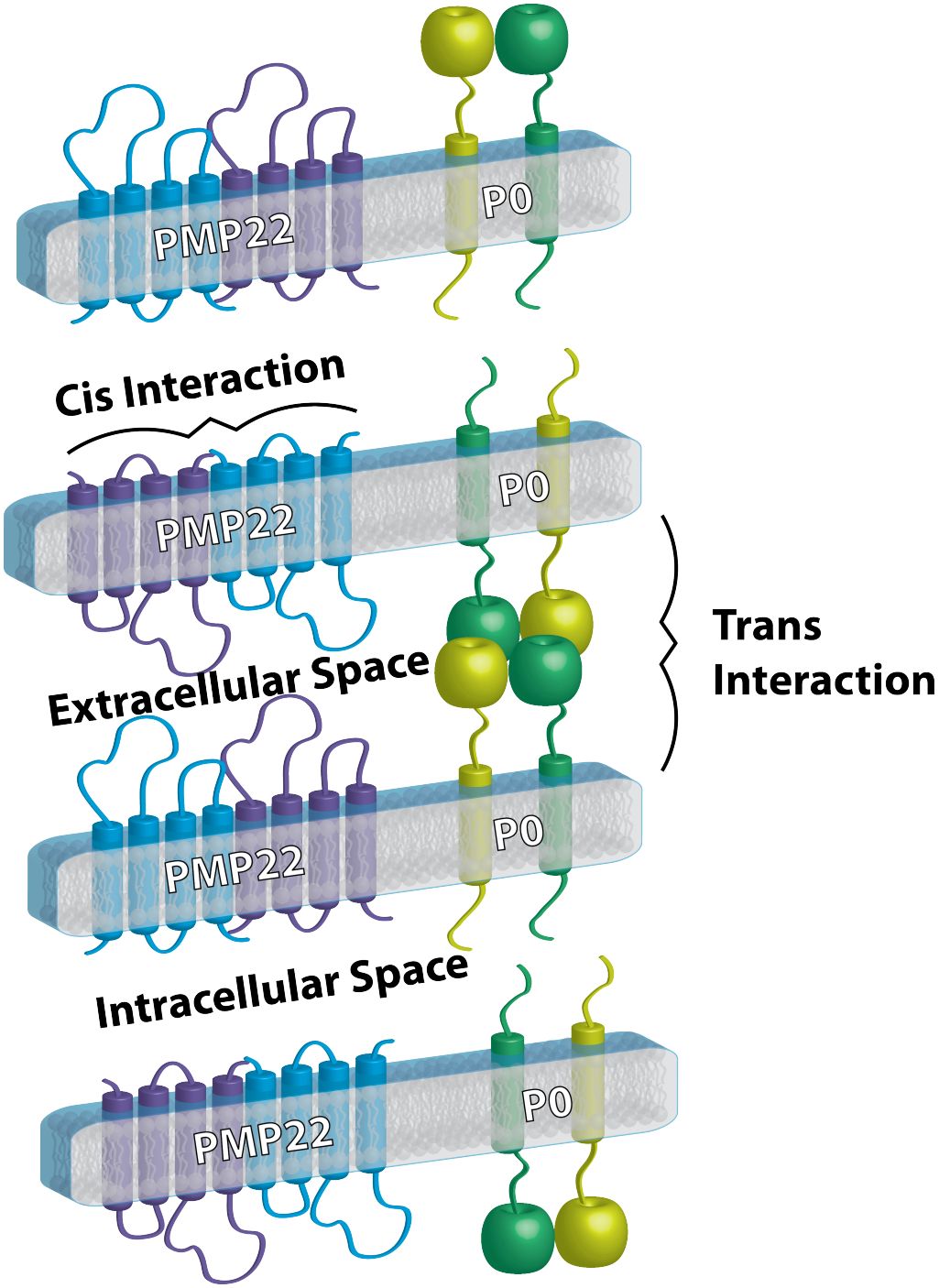

Figure 2.6. A model for the interactions of P_0 and PMP22 in myelin.
PMP22 is known to form dimers, though it is unclear if these interactions are in a *cis*- and/or in a *trans*-mannerism. P_0 has been shown to form a tetramer consisting of two molecules from one membrane bilayer face and two molecules from the apposing membrane bilayer. PMP22 and P_0 are also known to associate and the cytosolic domain of P_0 is thought to associate with lipids on the apposing membrane face; for simplicity these interactions are not pictured. See main text for references.

Peripheral myelin protein 22

Peripheral myelin protein 22 (PMP22) has been suggested to make up 2-5% by weight of the protein in peripheral myelin (Snipes et al., 1992). Unfortunately, PMP22 remains elusive in more robust detection and quantification methods employing mass spectrometry (Patzig et al., 2011), owing to technical difficulties of performing mass spectrometry on the smaller, highly hydrophobic multispan membrane proteins. As such, all proteomic profiles generated by mass spectrometry of PNS and CNS myelin must be taken with a grain of salt, due to the high abundance of small, hydrophobic tetraspan proteins in these tissue. PMP22 possesses no sequence homology to PLP, but does possess a topological similarity (see Figure 2.4 above). PMP22 is the focus of the work presented in Chapters IV and V, and as such will be considered in detail in the following section.

Peripheral Myelin Protein 22: An Important Regulator of Normal PNS Myelination

The focus of Chapters IV and V of this dissertation are on the function and structure of PMP22, respectively. As such, a more detailed review of what is known about PMP22 structure and function outside of this dissertation work is presented below.

PMP22 is a tetraspan integral membrane protein of unknown structure

Low-resolution structural information showed that PMP22 has a tetraspan topology (Sakakura et al., 2011), which aligns well with TM predictions based upon the fact that PMP22 has four very hydrophobic domains. The native protein is an 18 kDa protein that is modified with a lone N-linked oligosaccharide (on Asn41) to make the final product 22 kDa (Sedzik et al., 2015). The limited data on this modification suggests that it is *not* crucial for structure or function (Ryan et al., 2000; Hasse et al., 2004; Fontanini et al., 2005). PMP22 is known to associate with itself in cells in what is at least a dimeric

complex (Tobler et al., 1999; Brancolini et al., 2000; Ryan et al., 2000; Tobler et al., 2002). Recent structures of homologous claudins indicate that the conserved cysteine residues in the first extracellular loop may be involved in a disulfide bridge and that the predicted tetraspan topology is correct (Suzuki et al., 2014; Saitoh et al., 2015). Additionally, PMP22 contains two divalent metal cation coordination sites that are capable of coordinating Cu(II), Zn(II), or Ni(II) (Myers et al., 2008; Schlebach et al., 2015). These sites are likely mediated by a cluster of negatively-charged, cysteine, and histidine residues in the first and second extracellular loops (see Figure 2.4 and Figure 2.6). Residues that might be involved in these binding events include His34, Asp37, Cys42, His51, His52, Cys53, and Glu60, all of which are located in the extracellular loop 1 (ECL1), and His121, Glu123, His125, and Asp129, all of which are located in the extracellular loop 2 (ECL2).

PMP22 is involved in disease

Precise gene dosage of PMP22 is required for healthy myelination. Both gene deletion (one copy of PMP22) and gene duplication (three copies of PMP22) result in disease. Gene duplication of PMP22 is the most common cause of dysmyelinating disorders associated with PMP22, and is responsible for Charcot Marie Tooth Disease (CMTD) Type 1A. CMTD is the most common inherited neurodegenerative disorder of the peripheral nervous system, afflicting 1:3000 people (Pareek et al., 1997; Nelis et al., 1999; Young and Suter, 2001; Suter and Scherer, 2003; Young and Suter, 2003; Bertorini et al., 2004; Berger et al., 2006; Nicholson, 2006; Li et al., 2013). The etiology of PMP22-associated peripheral neuropathies includes dysmyelination, hypomyelination, and resultant axonal degeneration. These are accompanied by loss of reflexes and sensation and eventual atrophy (Li et al., 2013). This disease phenotype is more severe than the phenotype associated with heterozygous gene deletion, Hereditary Neuropathy

with Liability to Pressure Palsies (HNPP). Mutations throughout PMP22 result in diseases of varying phenotypes, including CMTD, HNPP, and the most severe Dejerine-Sottas Syndrome (DSS). Additionally a number of mutations that result in PMP22 truncation or amino acid deletion also cause disease (see Figure 2.7 for a full depiction of the PMP22 modifications resulting in disease; for a review of the genetic modifications of PMP22 causing disease see Li et al., 2013). A table of mutations causing disease, their nerve conduction velocities, and relevant references, along with a figure mapping the disease severity on the topology diagram of PMP22, can be found in Chapter V (Table 5.1 and Figure 5.1). Because these mutations are located throughout the protein (see Figure 2.7), rather than being concentrated in one domain, it is not surprising that evidence indicates that a number of these mutations are involved in protein misfolding and mistrafficking (Naef and Suter, 1999; Tobler et al., 1999; Colby et al., 2000).

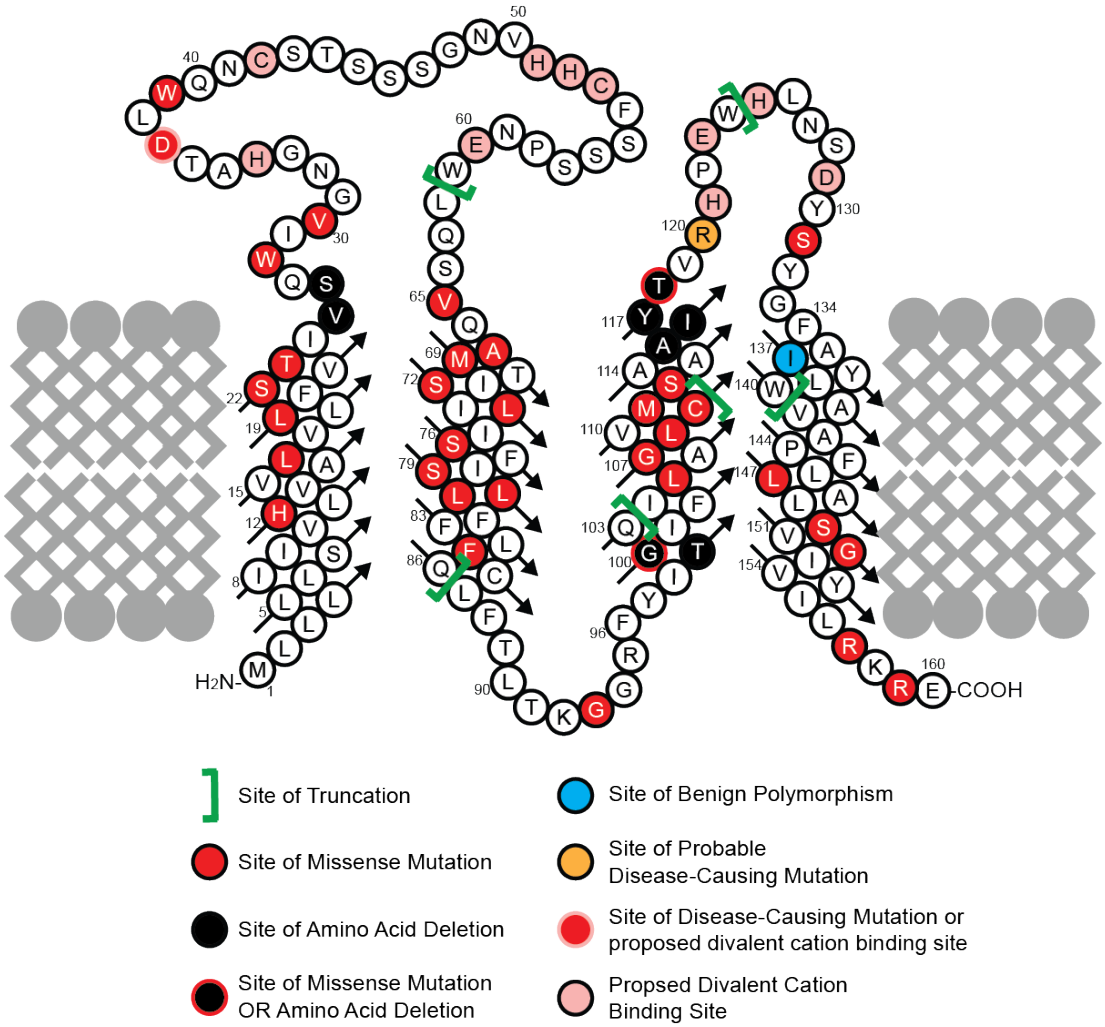

Figure 2.7. Topology map of PMP22 depicting genetic modifications resulting in peripheral neuropathy.
Sites of protein truncation are demarcated by green brackets. Sites of missense mutations are denoted by red circles. Sites of amino acid deletion are represented by black circles, except where they overlap with missense mutations, where they are depicted as black circles with red outline. A site of a known benign polymorphism is represented by a blue circle, and a probable disease-causing mutation is depicted by an orange circle. The site of potential divalent metal cation binding site residues are depicted by pink circles, except where they overlap with a missense mutation, where they are depicted as a pink outlined red circle. For a complete discussion of all of the disease-causing genetic modifications see Li et al., 2013.

PMP22 is misfolded and mistrafficked in disease

Only a portion of wild-type protein is transported to the plasma membrane. PMP22 has a very short half-life (30-60 minutes in cultured Schwann cells) (Pareek et al., 1993), and only around 20% of WT protein makes it to the plasma membrane (Pareek et al., 1993; 1997). Indeed, attempts to structurally characterize WT PMP22 by solution NMR found that at mildly elevated temperature (45 °C) WT PMP22 populates a folding intermediate state, with the helical first transmembrane domain (TM1) transiently dissociating from the TM2-TM4 bundle, which exists in a molten globular state (See Figure 2.8) (Sakakura et al., 2011). Additionally, recent analysis of the folding energetics of WT PMP22 *in vitro* showed that it exhibits only marginal conformational stability (Schlebach et al., 2013). Intriguingly, the high turnover rate of PMP22 and the low efficiency with which functional PMP22 is made must result in a high energetic cost for the cell. This hints that PMP22 conformational flexibility may be important for PMP22 function. Indeed, if PMP22 functionally mirrors PLP, a conformationally flexible protein may be useful for creating weak interactions that help to initiation myelination and perform a “molecular zipper” role.

Most pathogenic mutations greatly reduce the trafficking of PMP22 from this already marginal WT efficiency (Naef and Suter, 1999; Tobler et al., 1999; Colby et al., 2000). NMR and circular dichroism analyses of the L16P *TremblerJ* form of PMP22, a severe mutant, suggest that disease mutations might contribute to PMP22 instability. In the case of L16P PMP22, the substitution of a proline residue in the middle of the TM1 promoted the dissociation of TM1 from TM2-TM4 even at 25 °C (Figure 2.8) (Sakakura et al., 2011). Importantly, this folding intermediate state might be relevant, because it has been demonstrated that calnexin recognizes L16P PMP22 in a glycan-independent manner through TM1 and retains it in the ER for degradation, suggesting that the

aberrant overabundance of this intermediate leads to retention/degradation and loss-of-function (Fontanini et al., 2005).

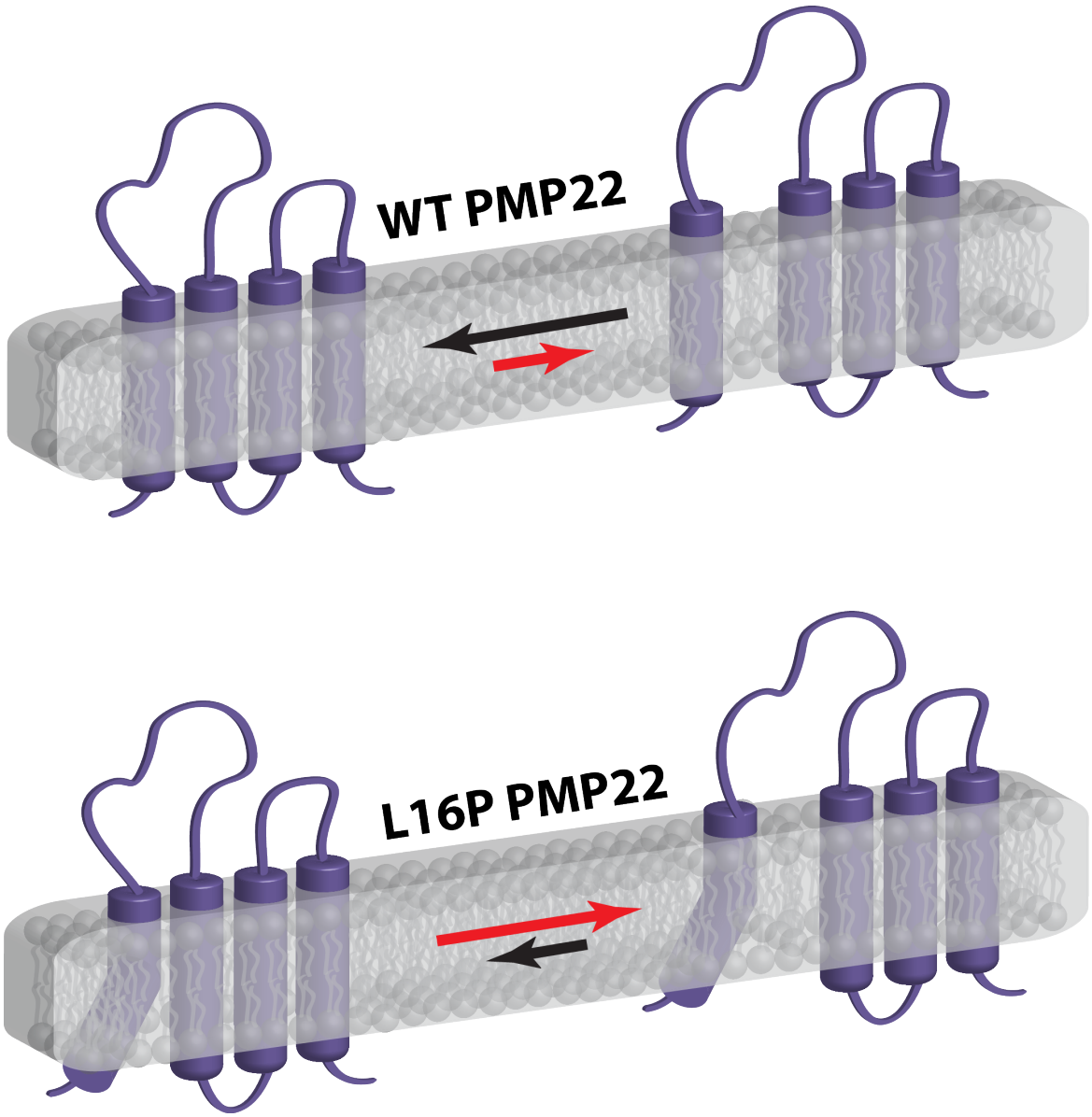

Figure 2.8. Model of the effects of the folding intermediate state of WT-PMP22 and the effects of the L16P mutation.
WT PMP22 already has the tendency for the first TM to dissociate from the helical bundle. L16P introduces a kink in the first TM, which promotes dissociation from bundle, further destabilizing the protein. Model adapted from (Sakakura et al., 2011).

Recent analysis has demonstrated that the severity of PMP22 disease mutations correlates with their trafficking efficiency (Schlebach et al., 2015). Further, this work found that these mutations variably disrupted the ability of PMP22 to fold in the absence or presence of Zn(II), an abundant metal ion in myelin and an ion known to bind PMP22 (Frederickson, 1989; Myers et al., 2008), and demonstrated that PMP22 folding and ion binding are thermodynamically coupled (Schlebach et al., 2015). The coupled energetics of binding and folding also correlated to disease severity. It is tempting to propose a mechanism whereby the first Zn(II) binding event serves the function to "lock down" the first TM through stabilization of the ECL1 flexible loop and the second binding even further stabilizes the helical bundle through ECL1 and ECL2 interaction. Future work should focus on mapping the Zn(II) binding site and either determining or modeling of the structure of PMP22 in the presence and absence of Zn(II) ions.

The function of PMP22 is not well established

The function of PMP22 is not well established. It has been shown to interact with a number of partners, including P_0 and α6β4 integrin (Hasse et al., 2004; Amici et al., 2006). The interaction between P_0 and PMP22 has been suggested to be mediated by PMP22-ECL2, while the PMP22-ECL1 has been suggested to mediate homophilic PMP22-PMP22 interactions (Hasse et al., 2004). These interactions may contribute to establishing the myelin architecture. Indeed, early mouse studies with $PMP22^{-/-}$ mice demonstrate that these mice have excess immature Schwann cells that fail to initiate myelination, and observations from mice deficient in both PMP22 and P_0 further indicate a role for PMP22 in the initiation of myelin wrapping (Adlkofer et al., 1995; Carenini et al., 1999). Further roles for PMP22 have been implicated in Schwann cell survival, differentiation, proliferation, and death (for a thorough review, see Li et al., 2013). Gene deletion, gene duplication, and all disease mutants investigated have been found to

increase Schwann cell apoptosis (see Table 1 in Li et al., 2013). Finally, there is new evidence for interaction of PMP22 with junctional proteins in myelin (Guo et al., 2014). The absence of PMP22 in these junctions contributes to "leaky" myelin.

Summary

It is clear that myelination is a complex process. Despite its importance in a number of neuropathies, the full process of myelination is not fully understood at the histological, cellular, and molecular levels. It is likely that a complex and ordered set of interactions between proteins, the bilayer, and the extracellular matrix all contribute to the organization and maintenance of the myelin ultrastructure, though these interactions are not yet defined. The analogous functional relationships between CNS and PNS myelin proteins have not yet been elucidated, and for both PNS and CNS myelin proteins there exists very little high-resolution structural data. It is tempting to compare PLP and PMP22 based upon their topological similarity, the similar effects of mutations on protein stability and animal phenotype, and their potential weak homophilic interactions with one another. Ultimately, understanding these interactions and the mechanisms by which they contribute to the formation of myelin ultrastructure represents the other side of the coin—that is, how do membrane proteins shape their bilayer milieu? Chapters IV of this dissertation will explore the ability of PMP22 to promote formation of MLAs, structures that resemble the layered assemblies observed for PLP reconstituted into liposomes. Chapter V will explore the structure of PMP22 through homology modeling. We think this work sheds insight on the function of PMP22 and the effects of disease mutations. New hypotheses about PMP22 folding and function will be discussed in Chapter VI.

CHAPTER III

IMPACT OF BILAYER LIPID COMPOSITION ON THE STRUCTURE AND TOPOLOGY OF THE TRANSMEMBRANE AMYLOID PRECURSOR C99 PROTEIN[2]

Introduction

The transmembrane (TM) C99 protein is a critical intermediate on the amyloidogenic pathway associated with the genesis of Alzheimer's disease. C99 is the product of β-secretase cleavage of the full-length amyloid precursor protein and is the substrate for cleavage by γ-secretase to release the amyloid-β polypeptides. The structure of monomeric C99 in anionic lyso-myristoylphosphatidylglycerol (LMPG) detergent micelles was determined by NMR (Barrett et al., 2012) and was seen to be composed of a disordered N-terminus (NTD, 672–687), followed by a surface-associated N-helix extending from 688 to 694, a flexible "N-loop" (695–699), a helical transmembrane domain (700–723), a disordered intracellular "C-loop", and finally a surface associated "C-helix" (CTD, 762–770). The NMR structural work was followed by both EPR (Barrett et al., 2012) and computational (Pester et al., 2013; Dominguez et al., 2014; Lemmin et al., 2014) studies of the protein under membrane conditions.

However, the dependence of the C99 structure and membrane interactions as a function of variations in lipid composition has not been investigated. Here, we provide insight into this issue and illuminate previous studies showing that alteration of either the transmembrane span of C99 or of the bilayers in which it is solubilized impact cleavage of the protein by γ-secretase (Murphy et al., 1999; Lichtenthaler et al., 2002; Marenchino et al., 2008; Osenkowski et al., 2008; Miyashita et al., 2009; Uemura et al., 2011;

[2] This section is adopted from the published manuscript by Song, Mittendorf, Lu, and Sanders in *JACS*. Song, Y., Mittendorf, K.F., Lu, Z., and Sanders, C.R. (2014). Impact of bilayer lipid composition on the structure and topology of the transmembrane amyloid precursor C99 protein. *JACS 136*, 4093-4096.

Holmes et al., 2012; Winkler et al., 2012; Ousson et al., 2013). For this purpose we used solution NMR to examine monomeric C99 in a series of detergent edge-stabilized lipid bilayers (bicelles), using the same detergent in all samples, but varying the lipid compositions.

Results and Discussion

We screened more than 40 potential bicelle compositions using either dihexanoylphosphatidylcholine (DHPC) or 3-[(3-cholamidopropyl)dimethylammonio]-2-hydroxy-1-propane-sulfonate (CHAPSO) as the detergent component mixed with a variety of neutral (cholesterol) and zwitterionic (phosphatidylcholine and sphingomyelin) lipids (Table 3.1). Sixteen of the mixtures appear to form bicelles. For this study we focused on DHPC-based bicelles, which yield better solution NMR spectra than CHAPSO-based bicelles. In addition, because C99 forms a 1:1 complex with cholesterol (Barrett et al., 2012), which would complicate interpretation of results, we excluded all cholesterol-containing mixtures.

Table 3.1. Potential bicelle compositions tested for this work.
MSM = milk sphingomyelin, BSM = brain sphingomyelin, ESM = egg sphingomyelin.
Mixtures for which it was possible to achieve complete solubilization of all components are indicated in bold font.

Lipids	Detergent	q ratio	Observations
4:1 POPC:POPG + 15mol% Ch	**DHPC**	**0.5**	**Quickly solubilized upon adding detergent solution and a few rounds of freeze-thaw; final solution clear at room temperature.**
1:1 Ch:ESM	DHPC	0.5	Did not solubilize upon adding detergent solution, freeze-thaw, or hot-sonication; further, did not solubilize upon reducing q to q = 0.3 or q = 0.15. Final solution thick and densely cloudy.
1:1:1 Ch:ESM:DMPC	DHPC	0.5	Did not solubilize upon adding detergent solution, freeze-thaw, or hot-sonication; further, did not solubilize upon reducing q to q = 0.3 or q = 0.15. Final solution thick and densely cloudy.
6:2:2 Ch:ESM:POPC	DHPC	0.5	Did not solubilize upon adding detergent solution, freeze-thaw, or hot-sonication; further, did not solubilize upon reducing q to q = 0.3 or q = 0.15. Final solution thick and densely cloudy.
4:1 POPC:POPG + 15mol% Ch	**CHAPS**	**0.5**	**Quickly solubilized upon adding detergent solution and a few rounds of freeze-thaw; final solution clear at room temperature.**
1:1 Ch:ESM	CHAPS	0.5	Did not solubilize upon adding detergent solution, freeze-thaw, or hot-sonication; further, did not solubilize upon reducing q to q = 0.3 or q = 0.15. Final solution thick and densely cloudy.
1:1:1 Ch:ESM:DMPC	CHAPS	0.5	Did not solubilize upon adding detergent solution, freeze-thaw, or hot-sonication; further, did not solubilize upon reducing q to q = 0.3 or q = 0.15. Final solution thick and densely cloudy.
6:2:2 Ch:ESM:POPC	CHAPSO	0.5	Did not solubilize upon adding detergent solution, freeze-thaw, or hot-sonication; further, did not solubilize upon reducing q to q = 0.3 or q = 0.15. Final solution thick and densely cloudy.
70:15:15 POPC:Ch:ESM	DHPC	0.5	Somewhat clarified upon adding detergent, upon several freeze thaws and hot sonication, left with clear solution containing several white particulates; reduction to q = 0.2 did not improve solubility.
85:15 ESM:Ch	DHPC	0.5	Somewhat clarified upon several freeze thaws and hot sonication but still slightly cloudy; reduction to q = 0.2 did not improve solubility.
10:4 POPC:ESM	**DHPC**	**0.5**	**Clarified completely upon detergent addition and vortexing.**
9:1 ESM:Ch	DHPC	0.5	Slightly clarified upon detergent addition; after continuous hot sonication for one hour, solution became mostly clear but some particulates remained.
9:1 BSM:Ch	DHPC	0.5	Slightly clarified upon detergent addition; after continuous hot sonication for one hour, solution became mostly clear but some particulates remained.
10:4:1 ESM:Ch	**DHPC**	**0.5**	**Slightly clarified upon detergent addition; after continuous hot sonication for one hour, solution became completely clear; solution remained clear at room temperature.**
6:3:1 DMPC:ESM:Ch	DHPC	0.5	At first clarified during freeze thaw but returned to cloudy at room temperature
3:3:1 DMPC:ESM:Ch	DHPC	0.5	Milky solution after addition of detergent. Did not improve with freeze-thaw, hot-sonication, or boiling.
8:1 ESM:Ch	DHPC	0.5	Milky solution after addition of detergent. Did not improve with freeze-thaw, hot-sonication, or boiling.

3:1 ESM:Ch	DHPC	0.5	Milky solution after addition of detergent. Did not improve with freeze-thaw, hot-sonication, or boiling.
Lipids	**Detergent**	**q ratio**	**Observations**
1.7:1 ESM:Ch	DHPC	0.5	Milky solution after addition of detergent. Did not improve with freeze-thaw, hot-sonication, or boiling.
1:1 POPC:BSM	**DHPC**	**0.5**	**Solubilized slowly upon addition of detergent.**
2:1 POPC:BSM	**DHPC**	**0.5**	**Solubilized slowly upon addition of detergent and short sonication**
1:1 POPC:MSM	**DHPC**	**0.5**	**Milky solution after addition of detergent. Improved to clear after cycles of hot sonication and freeze-thaw.**
2:1 POPC:MSM	**DHPC**	**0.5**	**Milky solution after addition of detergent. Improved to clear after cycles of hot sonication and freeze-thaw.**
2:1 BSM:Ch	DHPC	0.5	Milky solution after addition of detergent. Did not improve after sonicating, freeze/thaw, or boiling.
2:1 MSM:Ch	DHPC	0.5	Milky solution after addition of detergent. Did not improve after sonicating, freeze/thaw, or boiling.
ESM	**DHPC**	**0.5**	**Solubilized slowly upon addition of detergent.**
BSM	**DHPC**	**0.5**	**Solubilized slowly upon addition of detergent and short sonication.**
MSM	**DHPC**	**0.5**	**Solubilized slowly upon addition of detergent.**
6:3:1 DMPC:ESM:Ch	CHAPSO	0.5	Clear solution with white solids present. Did not improve with hot sonication, freeze/thaw, or boiling.
3:3:1 DMPC:ESM:Ch	CHAPSO	0.5	Milky solution after addition of detergent. Did not improve with freeze-thaw or hot-sonication. Slight improvement with boiling, although still cloudy.
8:1 ESM:Ch	CHAPSO	0.5	Milky solution after addition of detergent. Did not improve with freeze-thaw, hot-sonication, or boiling.
3:1 ESM: Ch	CHAPSO	0.5	Milky solution after addition of detergent. Did not improve with freeze-thaw, hot-sonication, or boiling.
1.7:1 ESM:Ch	CHAPSO	0.5	Milky solution after addition of detergent. Did not improve with freeze-thaw, hot-sonication, or boiling.
1:1 POPC:BSM	**CHAPSO**	**0.5**	**Solubilized slowly upon addition of detergent and short sonication.**
2:1 POPC:BSM	**CHAPSO**	**0.5**	**Solubilized slowly upon addition of detergent and short sonication.**
1:1 POPC:MSM	**CHAPSO**	**0.5**	**Solubilized slowly upon addition of detergent and short sonication.**
2:1 POPC:MSM	**CHAPSO**	**0.5**	**Solubilized slowly upon addition of detergent and short sonication.**
2:1 BSM:Ch	CHAPSO	0.5	Milky solution after addition of detergent. Did not improve with freeze-thaw, hot-sonication, or boiling.
2:1 MSM:Ch	CHAPSO	0.5	Milky solution after addition of detergent. Did not improve with freeze-thaw, hot-sonication, or boiling.
MSM	**CHAPSO**	**0.5**	**Dissolved slowly to clear on benchtop.**
4:1 DPPC:Ch	DHPC	0.5	Milky solution after addition of detergent. Did not improve with freeze-thaw, hot-sonication, or boiling.
2:1 DPPC:Ch	DHPC	0.5	Milky solution after addition of detergent. Did not improve with freeze-thaw, hot-sonication, or boiling.
1:1:1 DPPC:ESM:Ch	DHPC	0.5	Milky solution after addition of detergent. Did not improve with freeze-thaw, hot-sonication, or boiling.
4:1 DPPC:ESM	CHAPSO	0.5	Milky solution after addition of detergent. Did not improve with freeze-thaw, hot-sonication, or boiling.
2:1 DPPC:ESM	CHAPSO	0.5	Milky solution after addition of detergent. Did not improve with freeze-thaw, hot-sonication, or boiling.
1:1:1 DPPC:ESM:Ch	CHAPSO	0.5	Milky solution after addition of detergent. Did not improve with freeze-thaw, hot-sonication, or boiling.

We then selected a cross-section of five bicelle lipid compositions. Two of the chosen compositions have been previously reported: DHPC-dimyristoylphosphatidylcholine (DMPC) bicelles (Sanders and Schwonek, 1992), which have a relatively thin transbilayer span due to the C14 chains of DMPC, and DHPC-POPC (1-pamitoyl-2-oleoyl-phosphatidylcholine) bicelles (Chou et al., 2004; Triba et al., 2006) ,which have an intermediate transbilayer span that includes an unsaturated acyl chain. The other three bicelle systems are novel but resemble previously described brain (mostly C18) sphingomyelin bicelles (Yamaguchi et al., 2012) in that they are sphingolipid-based: DHPC-egg sphingomyelin (ESM) bicelles, in which the fatty amide chain composition is of intermediate (mostly C16) chain length (http://avantilipids.com), DHPC-milk sphingomyelin (MSM) bicelles, which have a fatty amide chain composition dominated (~60%) by very long C22–C24 chains, and finally a DHPC-POPC/MSM (1:1 POPC:MSM) mixture. All bicelles used in this work contained a mole ratio of 2:1 DHPC:lipid (q = 0.5). Light scattering measurements confirmed that each of these five bicelle compositions form monodisperse assemblies of similar dimensions (Table 3.2).

Table 3.2. Results of Dynamic Light Scattering (DLS) measurements for selected 4% (w/v) bicelle mixtures in water at 24 °C.

R_h values were calculated from a globular (spherical) model and thus are only approximations of a discoidal bicelle shape. *It is recognized that the bicelle samples of this work are almost certainly not spherical aggregates, so we emphasize that the calculated R_h and aggregate molecular weights are only apparent—useful for qualitatively comparing the relative sizes from bicelle to bicelle, but not quantitatively accurate.*

Bicelle Composition	D_T (10^{-9} cm^2/s)	R_h (nm)	MW (kDa)	PolyD (nm)	% PolyD	PolyD Index
DMPC-DHPC q = 0.5	1016±51	2.44 ±0.1	27.2±1.4	0.336±0.017	13.7±0.7	0.020±0.01
POPC-DHPC q = 0.5	952±48	2.57±0.1	30.6±1.5	0.351±0.018	13.6±0.7	0.020±0.01
2:1 POPC:MSM- DHPC q = 0.5	955±48	2.57±0.1	30.5±1.5	0.353±0.018	13.7±0.7	0.020±0.01
MSM-DHPC q = 0.5	972±49	2.53±0.1	29.6±1.5	0.356±0.018	14.0±0.7	0.020±0.01
ESM-DHPC q = 0.5	962±48	2.58±0.1	31.0±1.6	0.358±0.018	13.9±0.7	0.020±0.01

C99 was reconstituted into the selected bicelles at a concentration low enough (<1:800 C99:{lipid+detergent}) to ensure that the protein is monomeric.(Song et al., 2013) $^{1}H,^{15}N$-TROSY NMR was acquired (Figure 3.1 and 3.2). Because peak positions in all cases were similar to those seen in LMPG micelles (Figure 3.2), it was possible to assign the bicelle spectra of C99 based on correlating peaks to the previously assigned(Beel et al., 2008) peaks in LMPG. Based on these assignments, we then measured site-specific variation of backbone amide ^{1}H and ^{15}N chemical shifts from random coil values.

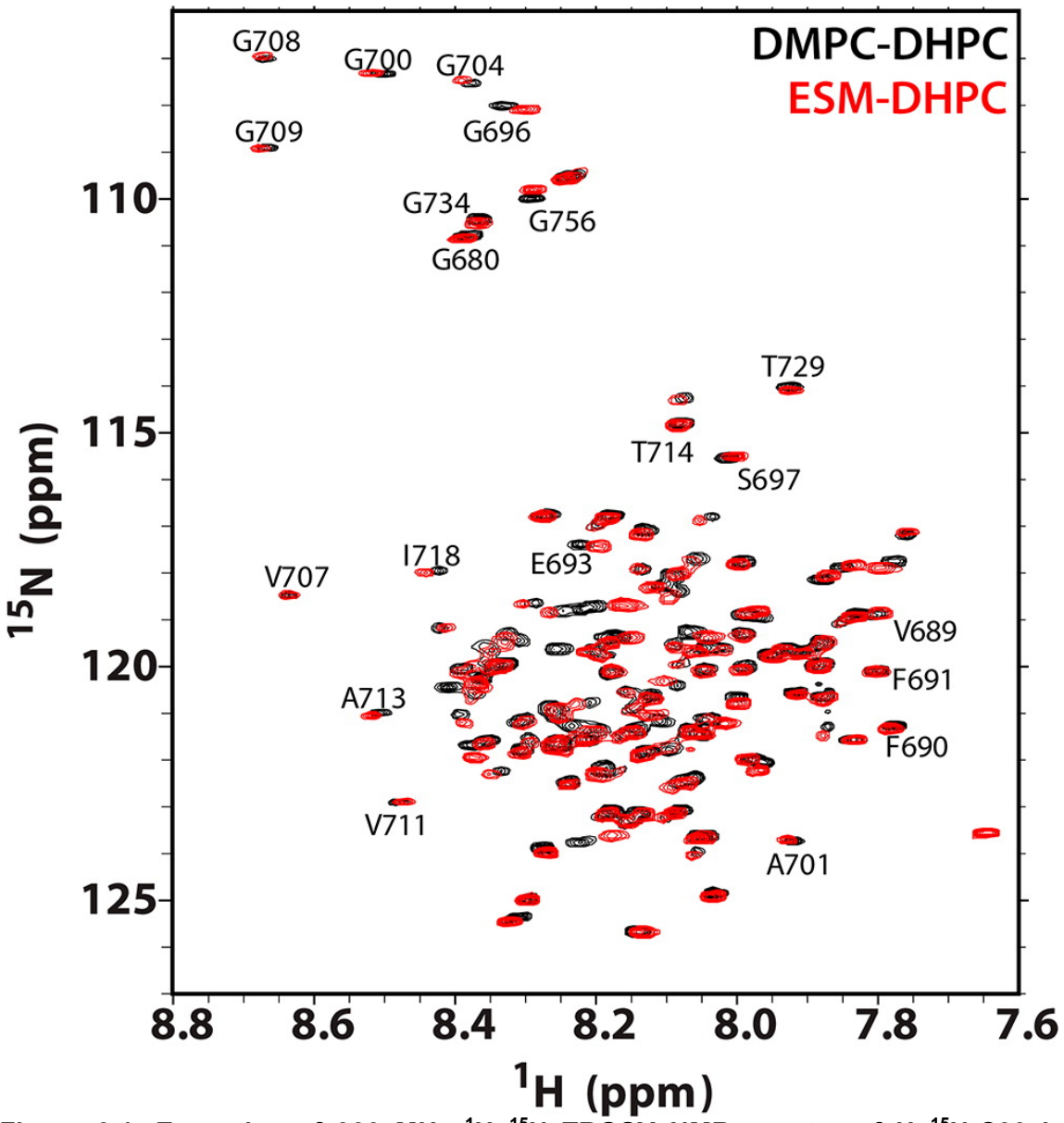

Figure 3.1. Examples of 900 MHz ^{1}H–^{15}N TROSY NMR spectra of U–^{15}N-C99 in bicelles at 45 °C.

Shown are spectra of the protein in ESM-DHPC bicelles (red) and the corresponding spectrum from conventional DMPC-DHPC bicelles (black). Bicelle samples contained 0.2–0.3 mM C99, 20% w/v bicelles, 250 mM imidazole, 1 mM EDTA, 10% D_2O, and pH 4.5. In all cases the bicelle *q* ratio (lipid-to-detergent mol/mol) was 0.5. Selected resonance assignments are illustrated.

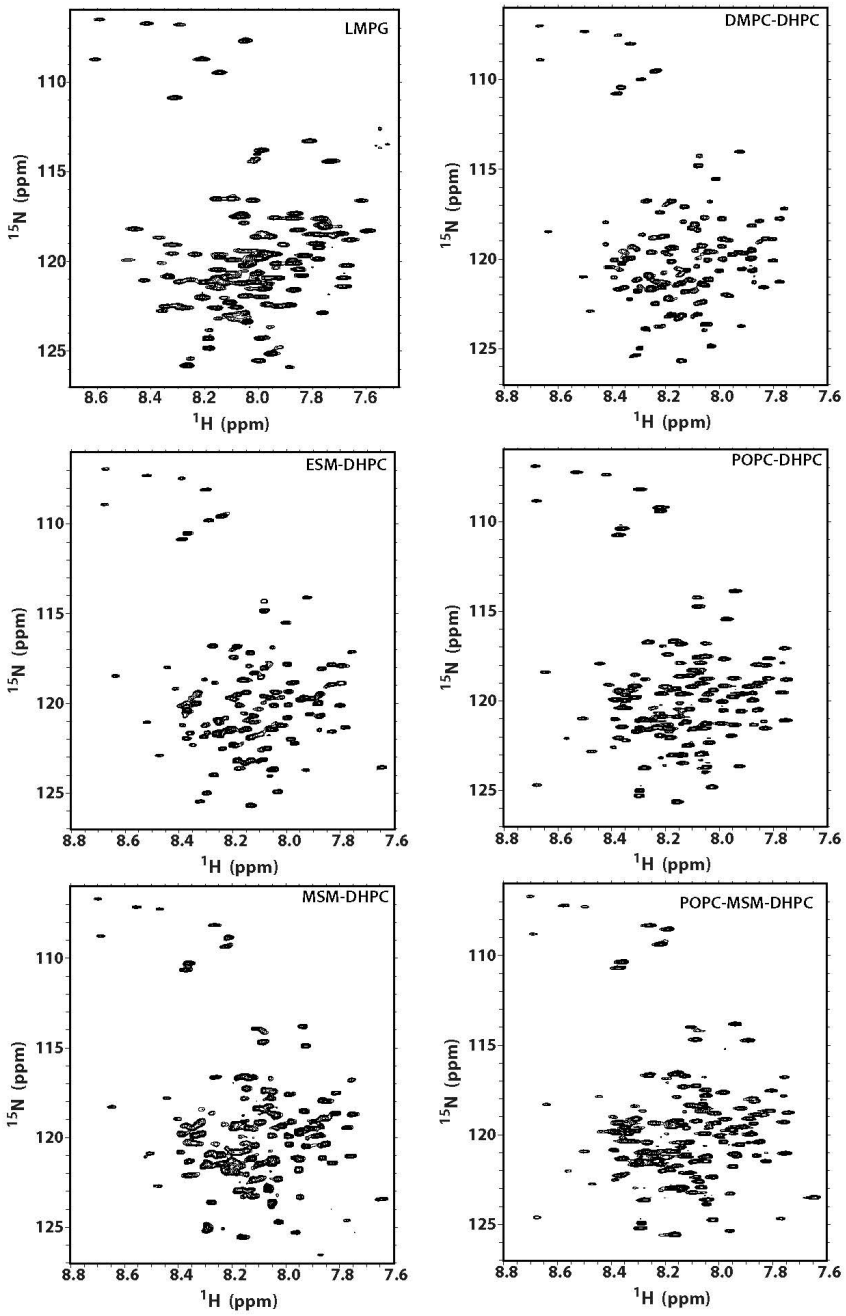

Figure 3.2. 900 MHz 1H-15N TROSY spectra of C99 in LMPG and in the 5 different bicelle compositions used in this work.

All samples contained 0.2-0.3 mM C99, 20% w/v bicelles, 250 mM imidazole, 1 mM EDTA, 10% D2O and pH 4.5. In all cases the bicelle q ratio (lipid-to-detergent mol/mol) was 0.5. The temperature was 45 °C. The data for LMPG micelles were previously reported(Barrett et al., 2012) and represents pH 6.5 conditions.

Results for the ^{15}N chemical shifts are shown in Figure 3.3 and 3.4, while results for ^{1}H shifts are shown in Figure 3.5 and 3.6. For both data sets it can be seen that there are only very minor differences in site-specific shifts between LMPG micelle conditions and any of the five bicelle mixtures tested. This indicates that C99 has a very similar backbone conformation in all six mixtures. This is despite the facts that (i) micelles are morphologically distinct from bicelles, (ii) LMPG is anionic, whereas all the bicelles tested contained only zwitterionic lipid and detergent, and (iii) the lipid acyl chain lengths in the various mixtures varied dramatically, from C14 to C24 carbons. The similarity of the NMR data for C99 from such very different model membrane hosts suggests that the conformational and dynamic features of C99 are robust and tolerant of changes in membrane environment. Variations in cleavage of C99 by γ-secretase as a function of changes in lipid composition are unlikely to be due to composition-dependent changes in C99 conformation. We also repeated these measurements under reduced salt conditions (Figures 3.3 and 3.6-3.8) and obtained nearly identical results, indicating that the C99 structure is also largely independent of ionic strength.

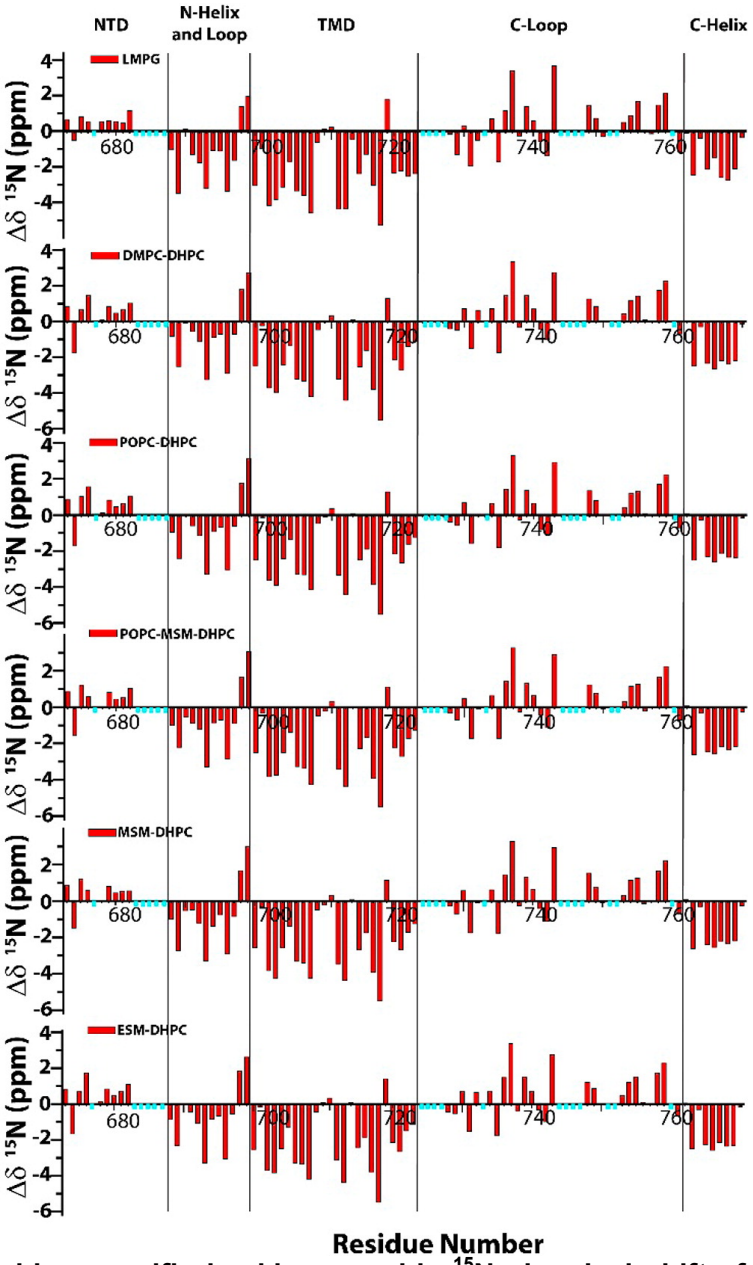

Figure 3.3. Residue-specific backbone amide ^{15}N chemical shifts for C99 in 10% LMPG micelles and in various DHPC-based bicelles.

The values reported here represent the difference between the measured chemical shift and the random coil chemical shift (estimated as described in the Materials and Methods). The residues marked with cyan bars are either too broad to observe (even in the absence of a paramagnet) or lack peak assignments. The four vertical lines represent the boundaries of the disordered N-terminal cytosolic domain (NTD, 672–687), the combined N-helix and N-loop (688–699), the transmembrane domain (TMD, 700–723), the C-loop (724–761), and the distal C-terminal domain (C-helix, 762–770).(Barrett et al., 2012) All samples contained 0.2–0.3 mM C99, 20% w/v bicelles (q = 0.5), 250 mM imidazole, 1 mM EDTA, 10% D_2O, and pH 4.5 (except for LMPG, which was pH 6.5). The temperature was 45 °C. The data for LMPG micelles were previously reported in Beel et al., 2008.

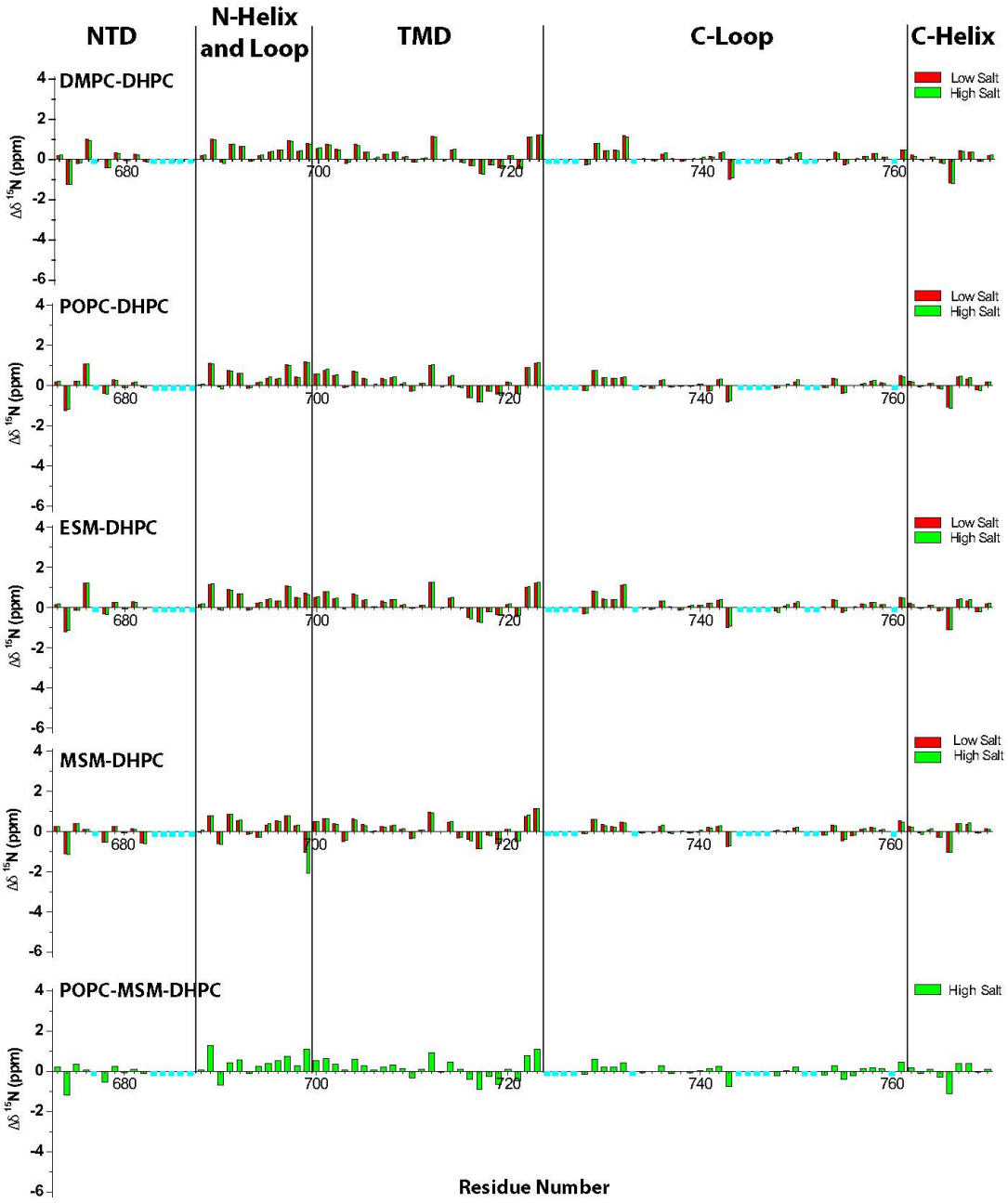

Figure 3.4. Backbone amide ^{15}N chemical shift differences between C99 in LMPG micelles versus C99 in various bicelles in both high salt (green bars) and low salt (red bars) conditions.

POPC-MSM-DHPC bicelle experiments were not performed in low salt conditions. The vertical lines demarcate boundaries of C99 domains defined according to the C99 structure determined in LMPG micelles.(Barrett et al., 2012) The residues marked with cyan bars are either invisible or lack peakassignments. The y-axis scale is the same as in Figure 3.3.

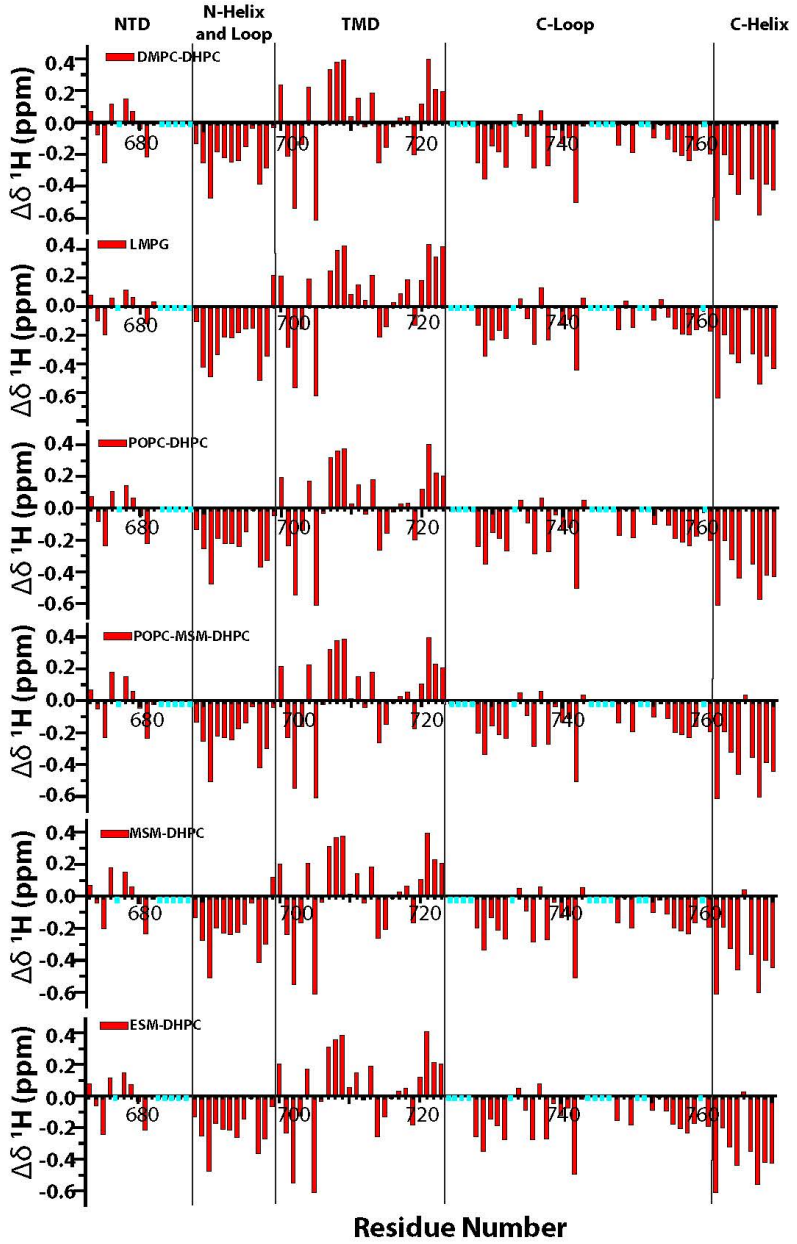

Figure 3.5. Residue-specific backbone amide ^{1}H chemical shifts for C99 in various bicelles.

The values reported here represent the difference between the reported chemical shift and the random coil chemical shift. The residues marked with cyan bars are invisible (even in the absence of a paramagnet) or lack peak assignments The four vertical lines represent the boundaries of the N terminal cytosolic domain (NTD, 672-687), the combined N-helix and Nloop (688-699), the transmembrane domain (TMD, 700-723), the C-loop (724-761), and the distal C-terminal domain (C-helix, 762-770).1 All samples contained 0.2-0.3 mM C99, 20% w/v bicelles, 250 mM imidazole, 1 mM EDTA, 10% D2O and pH 4.5. In all cases the bicelle q ratio (lipid-to-detergent mol-to-mol ratio) was 0.5. The temperature was 45 °C. The data for LMPGmicelles were previously reported in Beel et al., 2008, and represents pH 6.5 conditions.

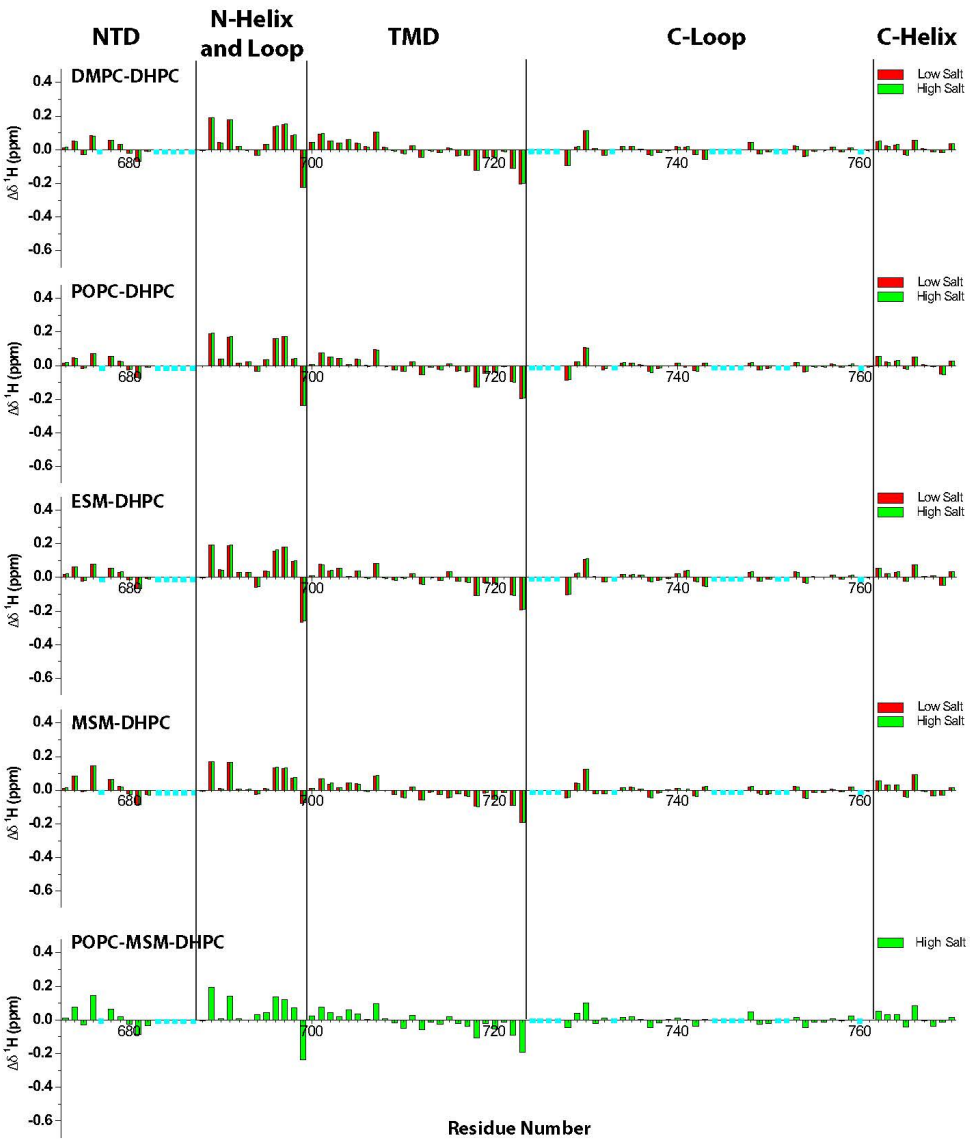

Figure 3.6. Backbone amide 1H chemical shift differences between C99 in LMPG micelles versus C99 in various bicelles in both high salt (green bars) and low salt (red bars) conditions.

POPC-MSM-DHPC bicelle experiments were not performed in low salt conditions. The vertical lines demarcate boundaries of C99 domains defined according to C99 structure determined in LMPG micelles (Barrett et al., 2012). The residues marked with cyan bars are either invisible or lack peak assignments. The y-axis scale is the same as in Figure 3.5.

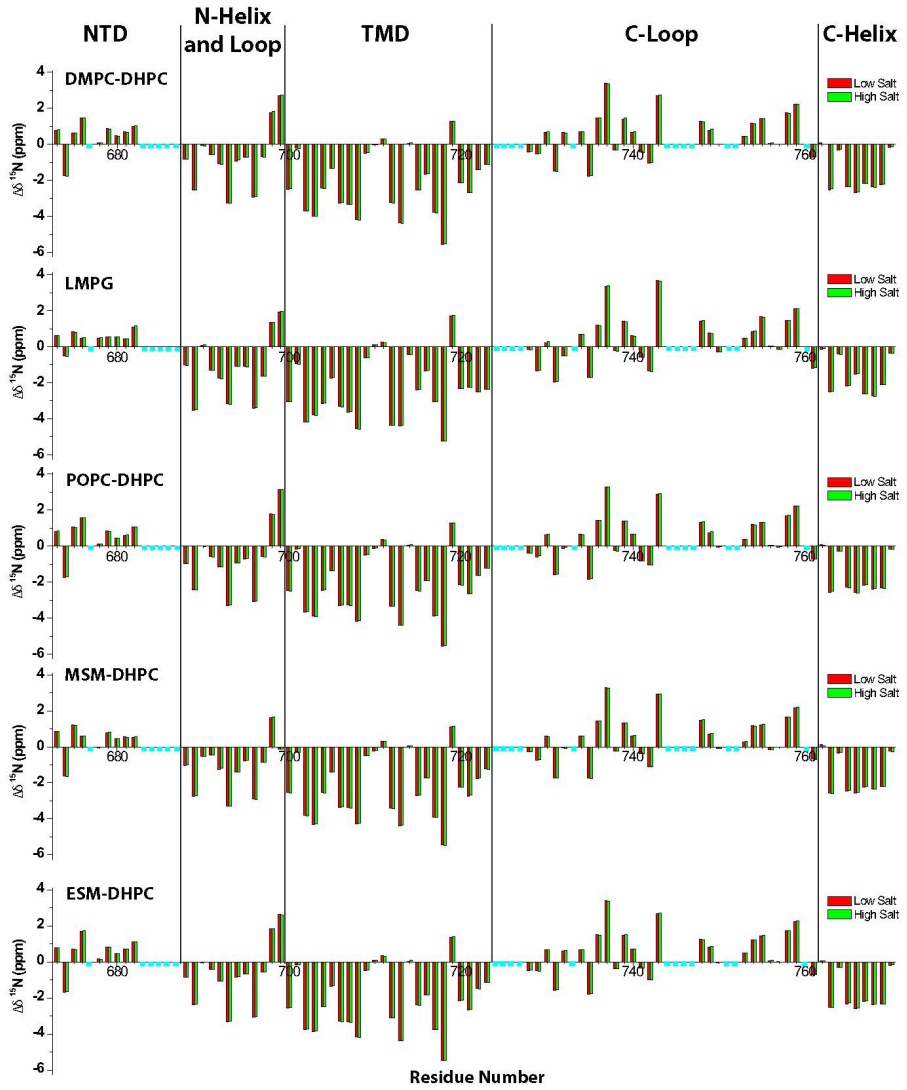

Figure 3.7. Comparison of residue-specific backbone amide ^{15}N chemical shifts for C99 in LMPG micelles and in various DHPC-based bicelles under reduced salt conditions (red bars) versus high salt (green bars) conditions.

The high salt data is the same that is presented in Figure 3.3. The values reported here represent the difference between the measured chemical shift and the random coil chemical shift (estimated as described in the Methods section). The residues marked with cyan bars are either too broad to observe (even in the absence of a para-magnet) or lack peak assignments. The four vertical lines represent the boundaries of the disordered N terminal cytosolic domain (NTD, 672-687), the combined N-helix and N-loop (688-699), the transmembrane domain (TMD, 700-723), the C-loop (724-761), and the distal C-terminal domain (C-helix, 762-770) (Barrett et al., 2012). Comparison of residue-specific backbone amide 15N chemical shifts for C99 in LMPG micelles and in various DHPC-based bicelles under reduced salt conditions (red bars) versus high salt (green bars) conditions. The high salt data is the same that is presented in Figure 3.3. All reduced salt samples except for the LMPG sample contained 0.2-0.3 mM C99, 20% w/v bicelles (q =0.5), 5 mM imidazole, 35 mM sodium acetate 1 mM EDTA, 10% D_2O and pH 4.5. The reduced salt LMPG sample was identical except that it contained 50 mM imidazole, no sodium acetate, and was pH 6.5. The temperature was 45 °C.

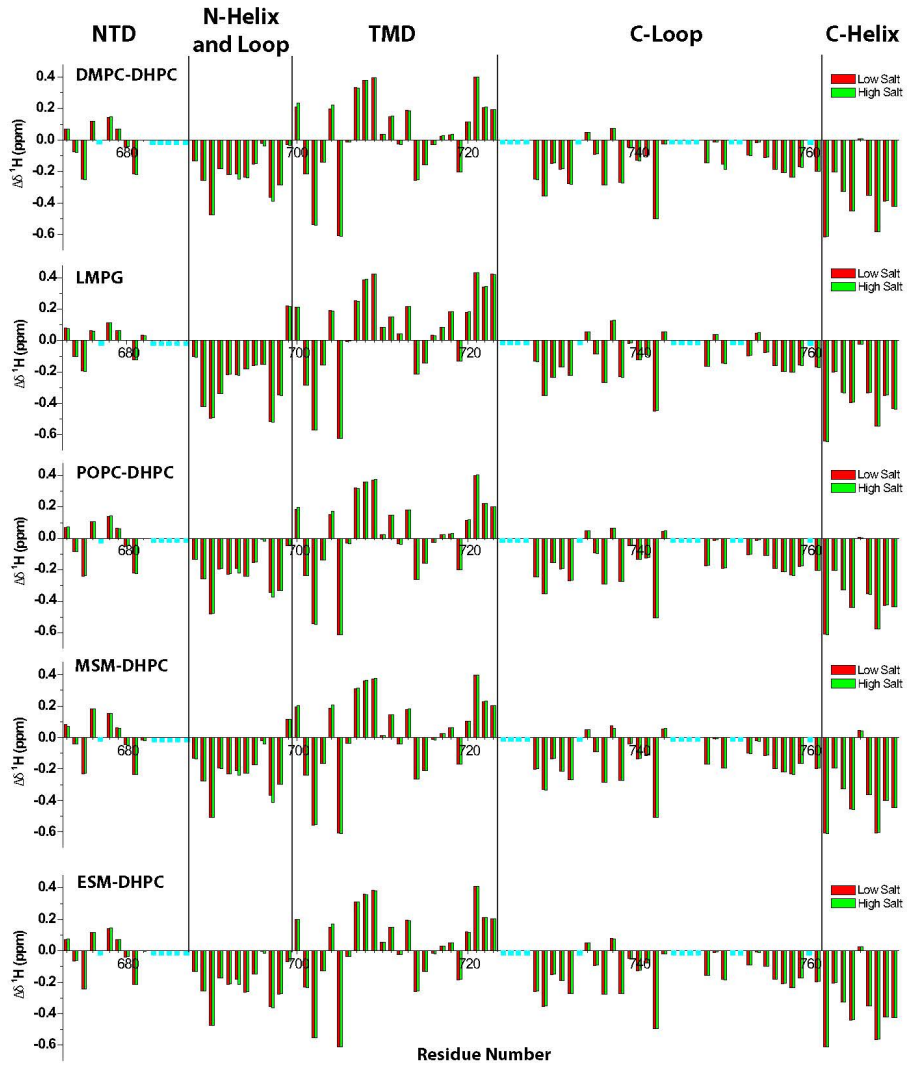

Figure 3.8. Comparison of residue-specific backbone amide ^{1}H chemical shifts for C99 in LMPG micelles and in various DHPC-based bicelles under reduced salt conditions (red bars) versus high salt (green bars) conditions.

The high salt data is the same that is presented in Figure 3.3. The values reported here represent the difference between the reported chemical shift and the random coil chemical shift (estimated as described in the Methods section). The residues marked with cyan bars are invisible (even in the absence of a paramagnet) or lack peak assignments. The four vertical lines represent the boundaries of the N terminal cytosolic domain (NTD, 672-687), the combined N-helix and N-loop (688-699), the transmembrane domain (TMD, 700-723), the C-loop (724-761), and the distal C-terminal domain (C-helix, 762-770).(Barrett et al., 2012) The composition of the high salt samples is given in the caption to Figure 3.3. All reduced salt samples except for the LPMG sample contained 0.2-0.3 mM C99, 20% w/v bicelles, 5 mM imidazole, 35 mM sodium acetate, 1 mM EDTA, 10% D2O and pH 4.5. The reduced salt LMPG sample was identical that except it contained 50 mM imidazole, no sodium acetate, and was pH 6.5. In all cases the bicelle q ratio (lipid-to-detergent mol-to-mol ratio) was 0.5. The temperature was 45 °C.

We next used water-soluble Gd(III)-diethylenetriamine-pentaacetate (Gd-DTPA) and lipophilic 16-doxylstearate (16-DSA) paramagnetic probes to examine whether the membrane topology of C99 varies as a function of host model membrane type and composition (cf. Figure 3.9). Figures 3.10 and 3.11 reveal no gross changes in membrane topology for C99 in all six mixtures tested: In all cases the three membrane-associated domains of C99 (the N-helix, TMD, and C-helix) remained membrane associated. Moreover, no new membrane interacting structural elements formed.

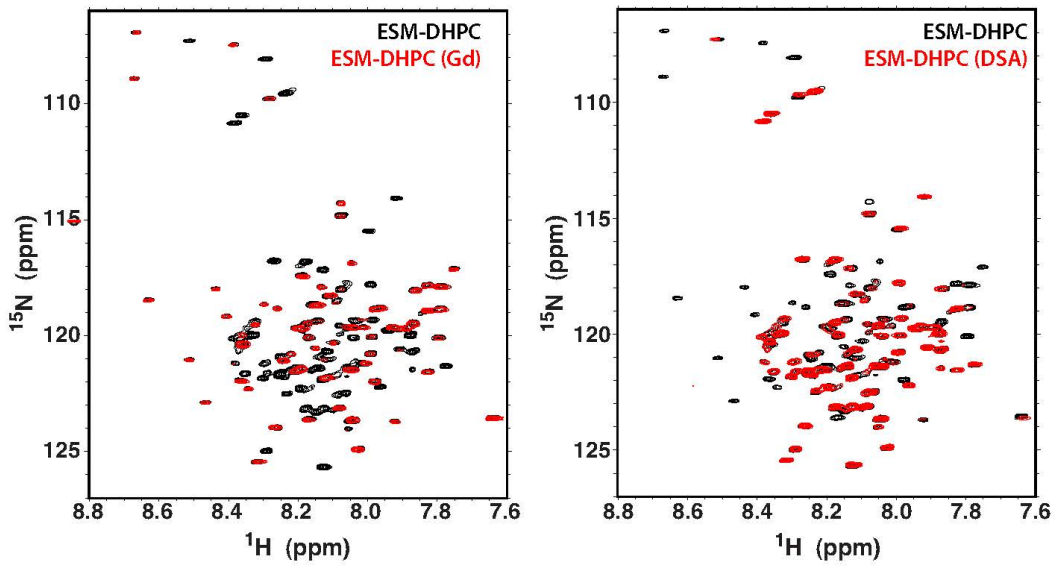

Figure 3.9. Example of data used to measure accessibility of C99 backbone amide sites in bicelles to the water soluble paramagnetic chelate Gd(III)-DTPA (left panel) or to the lipophilic nitroxide spin-labeled 16-doxylstearate (16-DSA, right panel). The black spectrum is a diamagnetic reference spectrum, while the red spectrum is from a matched sample except that it also contains the paramagnetic probe. NMR acquisition parameters were also matched for each pair of spectra. These 900 MHz ^{1}H,^{15}N-TROSY spectra were acquired at 45°C and are for q = 0.5 DHPC-ESM bicelles.

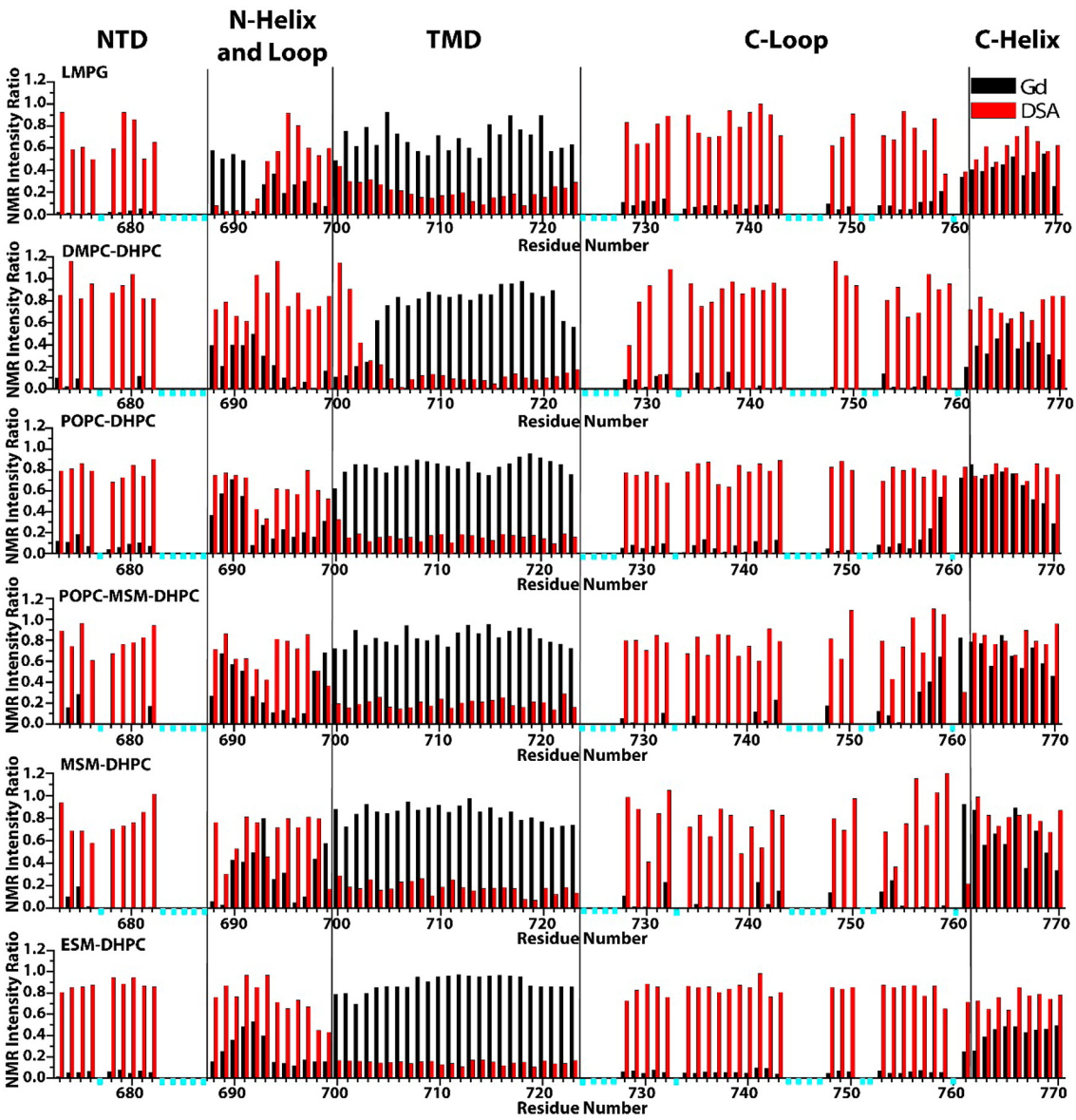

Figure 3.10. Paramagnetic probe-induced reductions in TROSY NMR peak intensities for backbone amide sites of C99 in LMPG micelles and in the five bicelle compositions examined in this work.

Data were collected at 900 MHz and 45 °C as described in the Methods Section and as exemplified by Figure 3.9. The reported intensity ratios are for peak height in a paramagnetic probe-containing sample divided by the corresponding peak intensity observed in a matched control sample. The water-soluble paramagnetic probe was Gd(III)-DTPA (black bars), while the lipophilic paramagnetic probe was 16-DSA (red bars). The residues marked with cyan bars are either invisible (even in the absence of a paramagnet) or lack peak assignments. Data were also collected for samples with low-salt content, yielding data very similar to that shown here (Figure 3.11).

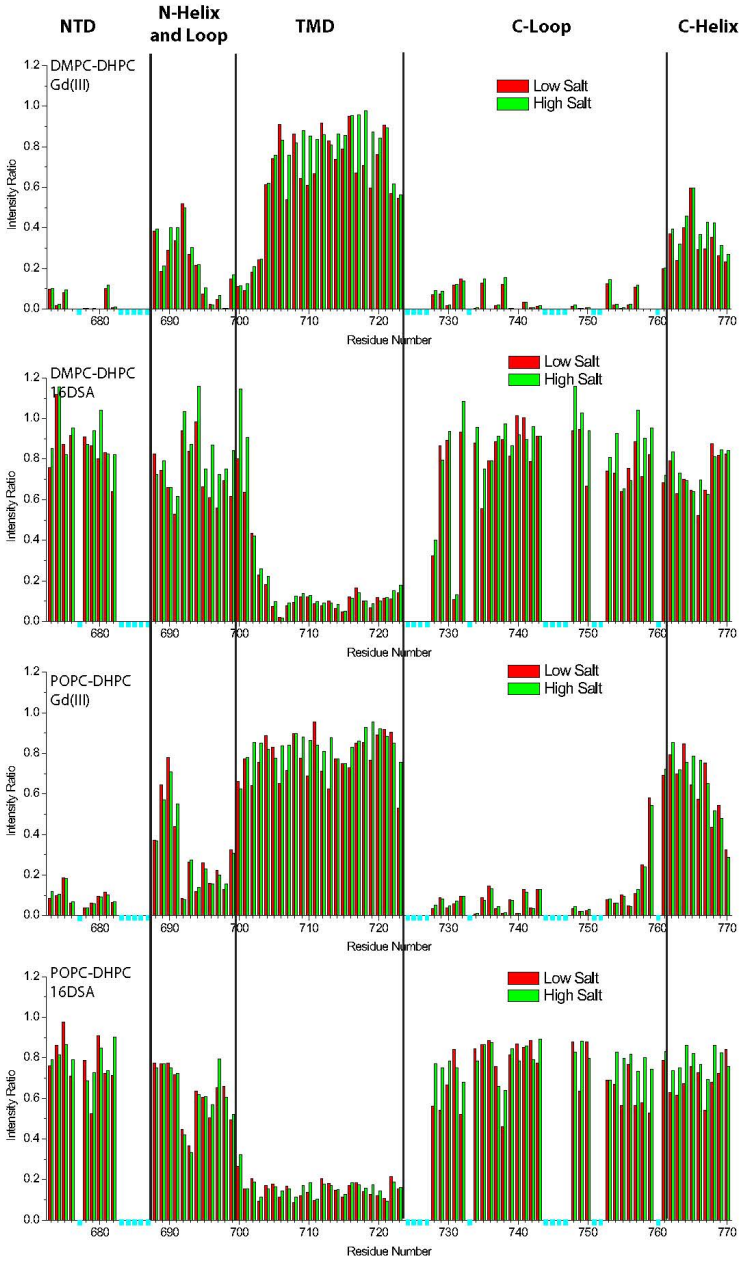

Figure 3.11 (Page 1 of 3). Comparison of paramagnetic probe access NMR data for C99 in bicelles and LMPG micelles under reduced salt (35-50 mM) versus high salt (250 mM) conditions.

The high salt data is the same that is presented in Figure 3.10 and is represented as green bars in these plots. The low salt data (red bars) is for samples of composition as given in Figures 3.7 and 3.8 plus the added 16-DSA and Gd(III)-DTPA paramagnetic probes (at the same concentrations as given in the caption to Figure 3.10). We did not collect low salt data for the POPC-MSM-DHPC bicelles. These data document both the general insensitivity of the C99 topology to salt concentration and also the generally high reproducibility of the probe access data.

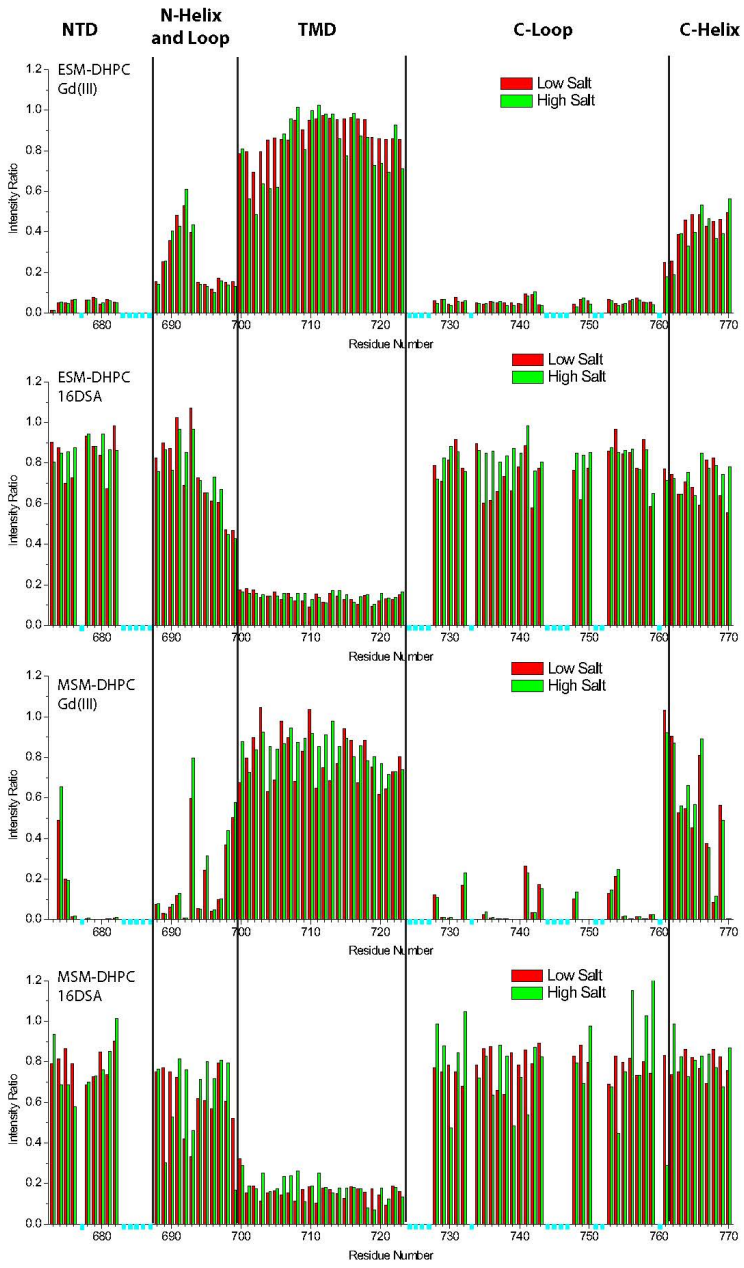

Figure 3.11 (Page 2 of 3). Comparison of paramagnetic probe access NMR data for C99 in bicelles and LMPG micelles under reduced salt (35-50 mM) versus high salt (250 mM) conditions.

The high salt data is the same that is presented in Figure 3.10 and is represented as green bars in these plots. The low salt data (red bars) is for samples of composition as given in Figures 3.7 and 3.8 plus the added 16-DSA and Gd(III)-DTPA paramagnetic probes (at the same concentrations as given in the caption to Figure 3.10). We did not collect low salt data for the POPC-MSM-DHPC bicelles. These data document both the general insensitivity of the C99 topology to salt concentration and also the generally high reproducibility of the probe access data.

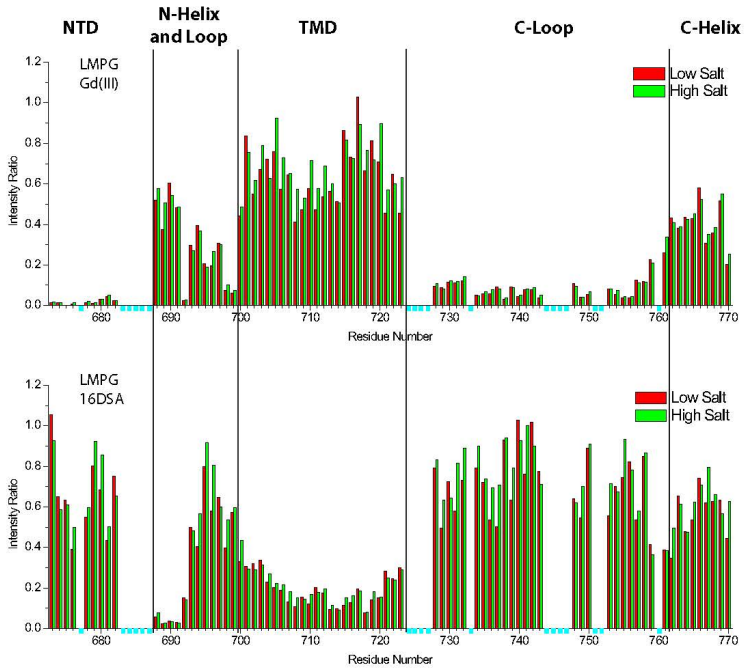

Figure 3.11 (Page 3 of 3). Comparison of paramagnetic probe access NMR data for C99 in bicelles and LMPG micelles under reduced salt (35-50 mM) versus high salt (250 mM) conditions.

The high salt data is the same that is presented in Figure 3.10 and is represented as green bars in these plots. The low salt data (red bars) is for samples of composition as given in Figures 3.7 and 3.8 plus the added 16-DSA and Gd(III)-DTPA paramagnetic probes (at the same concentrations as given in the caption to Figure 3.10). We did not collect low salt data for the POPC-MSM-DHPC bicelles. These data document both the general insensitivity of the C99 topology to salt concentration and also the generally high reproducibility of the probe access data.

However, some changes of a more modest nature are evident from Figure 3.10: (i) LMPG micelles are unique in that the N-helix peaks were completely broadened by the lipophilic probe, 16-DSA. This indicates that the N-helix is more deeply buried in the surface of LMPG micelles than in any of the five bicelle mixtures. This observation does not apply to the C-helix, which is protected to a similar degree from both probes in all mixtures examined. (ii) The N-terminal end of the TMD for C99 in DMPC-DHPC micelles is much more exposed to the polar Gd-DTPA probe than in either LMPG micelles or the other bicelle mixtures. This suggests that the C14 acyl chains of DMPC do not provide an adequate bilayer span to accommodate the 24 residue TM helix of C99. It is notable that the C-terminus of the C99 TMD remains largely protected from Gd-DTPA and exposed to 16-DSA in DHPC-DMPC bicelles. This means that adjustment of the TM span of C99 to thinner bilayers is not symmetric but is localized to the N-terminal end, probably because the C-terminal end is flanked by three consecutive Lys residues (724–726), which serve as a TMD termination motif (Figure 3.12). This implies that the γ-secretase cleavage sites in C99 are shifted in position with respect to center of the bilayer when bilayer thickness varies. This observation may shed light on previous results showing that the Aβ42:Aβ40 production ratio decreases as bilayer thickness increases(Holmes et al., 2012; Winkler et al., 2012) and increases when additional hydrophobic residues are inserted to extend the C-terminal end of the TMD (Murphy et al., 1999; Lichtenthaler et al., 2002; Ousson et al., 2013). Of course, bilayer composition and properties may also impact cleavage of C99 through other mechanisms, such as direct modulation of γ-secretase activity. (iii) The transmembrane span of C99 is longer by two N-terminal residues in the MSM-containing bicelle mixtures than in LMPG micelles and ESM bicelles. In POPC bicelles the TMD span is intermediate between the MSM-containing bicelles and ESM bicelles. (iv) The YEN segment (residues 757–759) that precedes the surface-associated C-helix of C99 is more deeply membrane buried

(protected from Gd(III)-DTPA-induced line broadening) in POPC-containing bicelles than in the two sphingomyelin-only bicelles or in DMPC bicelles. This is possibly the consequence of the *cis* double bond present in the *sn*-2 chain of POPC, which will expand the bilayer surface area relative to bilayers with only saturated acyl chains (Lewis and Engelman, 1983). The YEN segment leads into the $NPTY_{762}$ sequence, a known trafficking motif that is subject to tyrosine phosphorylation (Radzimanowski et al., 2008; Tamayev et al., 2009; Schettini et al., 2010). One wonders whether access of this motif by tyrosine kinases and/or by trafficking adaptor proteins is dependent on the lipid composition-dependent degree of membrane association of the preceding YEN segment.

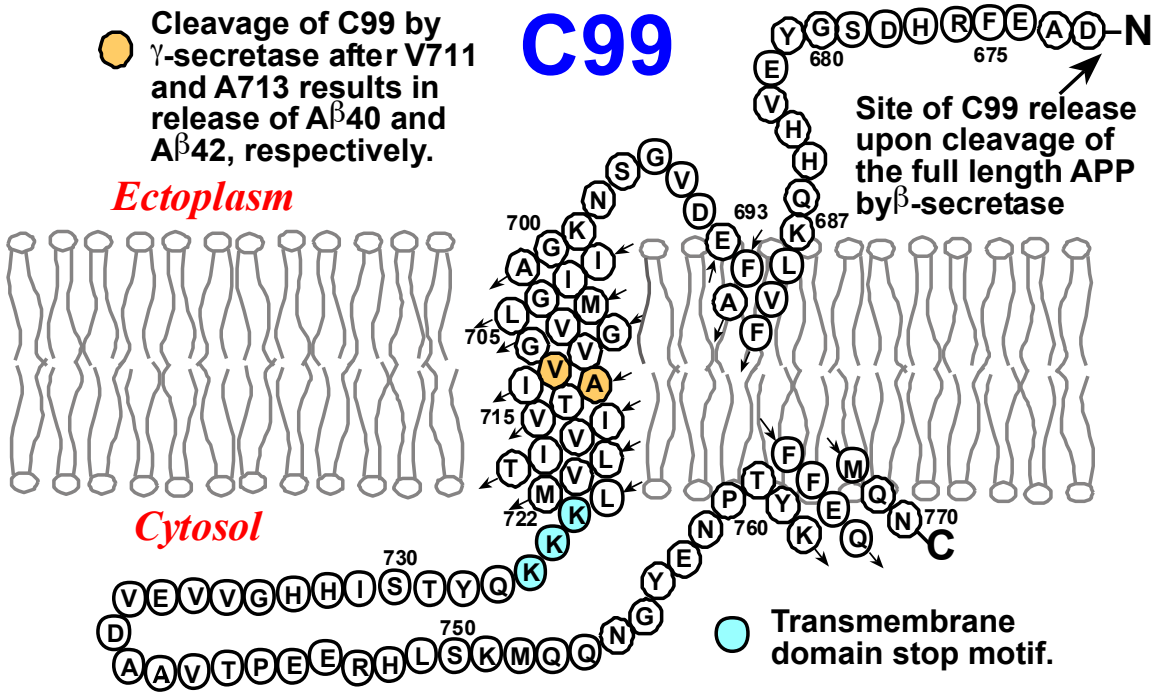

Figure 3.12. C99 contains a Lys-Lys-Lys TMD stop-motif that causes a non-uniform shift of C99 with respect to the bilayer normal with altered hydrophobic width.

Depicted is the topology diagram of C99. γ-secretase cut sites that generate Aβ40 and Aβ42 are highlighted in yellow, and the proposed TMD stop motif is highlighted in blue. Based on the results presented in this section and in figure 3.10 and 3.11, it is apparent that the N-terminal region of the TM helix of C99 becomes more buried in bicelles of increased hydrophobic width, while the C-terminal region of the helix does not become more buried. This observation may explain previous observations about altered γ-secretase cleavage behaviors in various model membranes and when the length of the C99 TM domain is adjusted (see text).

The results of this work show C99 appears to have a robust conformational structure, a property that it potentially shares with many other membrane proteins (Sanders and Mittendorf, 2011). These results are interesting in light of considerable current interest in the question of to what degrees membrane protein structures determined under micellar conditions can be assumed to be native-like (Matthews et al., 2006; Sanders and Mittendorf, 2011; Warschawski et al., 2011; Zhou and Cross, 2013). While the C99 structure seems to vary little, it is significant that modest membrane topological adjustments were seen when C99 was reconstituted in bicelles containing lipids with very different chemistries (glycerol- vs sphingosine-based) or acyl chains of dramatically different lengths. These changes in topology may provide insight into how the cleavage sites of C99 by γ-secretase depend on membrane thickness (Lichtenthaler et al., 2002; Holmes et al., 2012; Winkler et al., 2012). Because the Aβ42:Aβ40 ratio decreases upon thickening the bilayer, it is possible that shifting the entire helix down with the respect to the bilayer normal results in a shift of γ-secretase access from the cut-site position (A713) for Aβ42 generation to give it preferential access to the cut-site position (V711) for the production of Aβ40 (see Figures 3.12 and 3.13). It will be interesting in future work to see if the known complex formation of C99 with cholesterol (Barrett et al., 2011) or dimerization of the protein (Miyashita et al., 2009; Sato et al., 2009; Botev et al., 2011; Wang et al., 2011b; Nadezhdin et al., 2012; Pester et al., 2013; Song et al., 2013) alters the membrane topology of the protein (although the physiological relevance of dimerization has been questioned Song et al., 2013). Importantly, we also determined that the triple-lysine motif flanking the C-terminal end of C99 likely serves as a transmembrane domain “stop motif.” Because many membrane proteins have highly basic residues on the cytosolic/membrane interface, these observations may be generalizable to a number of other important membrane proteins. This may be an evolved mechanism to insure reproducible access of proteins inside the

cell to the cytosolic domains of these membrane proteins (for which spacing with respect to the membrane surface may be key). Many membrane proteins engage in signaling or scaffolding that relies on the interaction of membrane proteins with peripheral membrane proteins and soluble proteins at the cytosol-membrane interface. Finally, we note that this work also provides over a dozen new bicelle compositions that may be used in future studies of other membrane proteins.

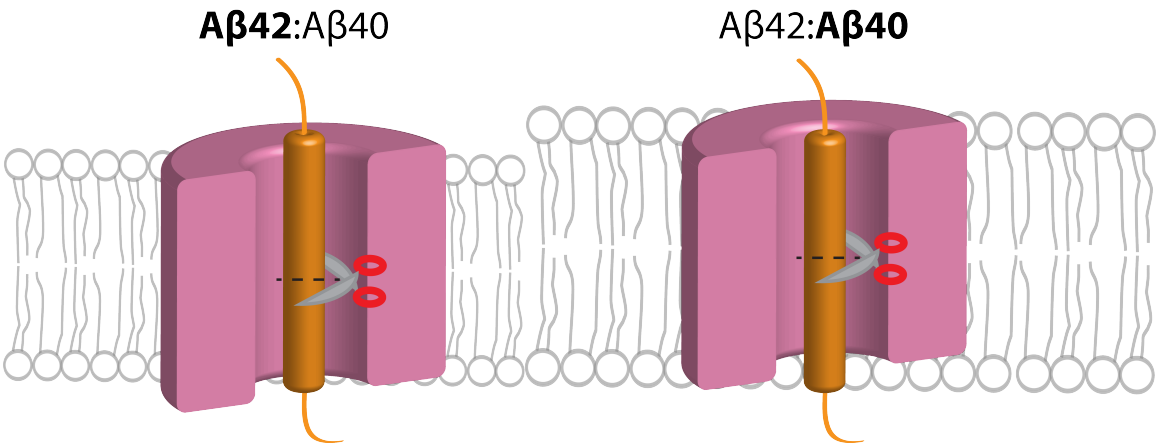

Figure 3.13. Model demonstrating how the shift of C99 with respect to the bilayer normal results in altered access to cleavage sites.
(Left) In thinner membranes, γ-secretase has better access to the cut-site position that generates the longer N-terminal C99 fragment. (Right) In thicker bilayers, C99 does not uniformly adjust, instead becoming more buried in the N-terminal. If γ-secretase does not adjust in such a manner (or adjusts to a lesser degree), instead remaining "central" within the bilayer, it would have preferential access to the more N-terminal cleavage site, generating a shorter Aβ fragment, thus decreasing the Aβ42:Aβ40 ratio.

Material and Methods

Chemicals

The following chemicals and abbreviations were used, as detailed below: 16-doxylstearic acid (16-DSA; Sigma), Gd(III)-diethylenetriaminepentaacetic acid (Gd-DTPA; Sigma), lyso-myristoylphosphatidylglycerol (LMPG; Avanti Polar Lipids), bovine milk sphingomyelin (MSM; Avanti Polar Lipids, Alabaster Alabama), chicken egg sphingomyelin (ESM; Avanti Polar Lipids), cholesterol (Ch, Sigma, St. Louis, Missouri), 1,2-dihexanoyl-*sn*-glycero-3-phosphocholine (DHPC; Avanti Polar Lipids), 3-[(3-cholamidopropyl)dimethylammonio]-2-hydroxy-1-propanesulfonate (CHAPSO, Affymetrix- Anatrace), 3-[(3-cholamidopropyl)dimethylammonio]-1-propanesulfonate **(**CHAPS), 1,2-dimyristoyl-*sn*-glycero-3-phosphocholine (DMPC; Avanti Polar Lipids), 1,2-dipalmitoyl-*sn*-glycero-3-phosphocholine (DPPC; Genzyme, Cambridge, Massachusetts), 1-palmitoyl-2-oleoyl-*sn*-glycero-3-phosphocholine (POPC; Avanti Polar Lipids), 1-palmitoyl-2-oleoyl-*sn*-glycero-3-phospho-(1'-rac-glycerol) (POPG; Avanti Polar Lipids); porcine brain sphingomyelin (BSM; Avanti Polar Lipids), Deuterium oxide (D_2O, Sigma-Aldrich).

Bicelle screening

DMPC, DPPC, POPC, POPG, MSM, BSM and ESM were weighed out as solids and mixed in glass vials at the molar ratios indicated in Table 4.1. The lipid mixtures were solubilized with 95:5 benzene:ethanol to homogenize the components and then freeze-dried overnight to yield white powders. Aqueous detergent stock solutions in 50 mM PIPES buffer pH 7.0 of DHPC, CHAPS, or CHAPSO, were added to the lipid powders to reach the indicated molar q ratio where q = moles lipid/moles detergent, with the final lipid+detergent w/v percentage being set to 10% (w/v). Bicelle mixtures were allowed to equilibrate at room temperature for one hour. Solubility was recorded. Freeze-

thaw rounds were then performed on samples showing incomplete solubility. The glass vials were frozen in liquid nitrogen and then thawed in room temperature water. After five rounds of freeze-thawing, solubility was recorded. Incompletely soluble samples were then treated to bath sonication for up to one hour. Incompletely soluble samples were sometimes subjected to additional freeze-thaw cycles, with thawing in the presence of bath sonication at 55-60°C. As a last resort, samples that remained insoluble were heated briefly in boiling water followed by vortexing.

Dynamic light scattering

Dynamic light scattering measurements were conducted at room temperature (24 °C) using the DynaPro instrument (Protein Solutions, Inc. Charlottesville, VA) and data were analyzed by *Dynamics V5* software (Protein Solutions, Inc.). Selected bicelles were prepared in water at 4% total bicelle concentration (lipid plus detergent) in addition to the critical micelle concentration of free DHPC. For each sample three independent experiments were performed, with at least 40 light scattering scans on 100 µL samples per experiment. The 100% mass peak was chosen for analysis. *Dynamics V5* software was used to calculate molecular translational diffusion coefficients, DT, by fitting the data to an exponential autocorrelation function. The program then used the Stokes-Einstein equation for an isotropic globular assembly to calculate the hydrodynamic radius, Rh: $D\mathrm{T} = kT/6\pi\eta R\mathrm{h}$, where k is the Boltzmann constant, T is the experimental temperature, and η is the solvent viscosity*. It is recognized that the bicelle samples of this work are almost certainly not spherical aggregates, so we emphasize that the calculated Rh and aggregate molecular weights are only apparent— useful for qualitatively comparing bicelle to bicelle, but not quantitatively accurate.*

Bicelles for protein purification

DMPC, POPC, MSM, and ESM were weighed in solid form and mixed in glass vials at the desired molar ratio. The lipid mixtures were then solubilized with 95:5 benzene:ethanol and freeze-dried overnight to yield a white powder. After the solvent was completely removed, stock solutions of 10% DHPC in water were added to reach the indicated molar q 0.5. Bicelle solutions were brought to final volume with water and concentrated imidazole buffer to reach final conditions with a bicelle concentration of 2%, 250 mM imidazole and pH 7.8.

Protein expression and purification

The C-terminal domain of the human amyloid precursor protein (C99) was expressed essentially as described previously.1,2 In brief, cDNA encoding human C99, tagged with a hexa-histidine purification tag –QGRILQISITLAAALEHHHHHH at its C-terminus, was integrated into a modified pET-21a vector. The protein was expressed in BL21DE3 E coli cells in 15N-labeled M9 media. Three grams of cells were lysed in 60 ml lysis buffer (20 mM Tris, 300 mM NaCl, pH 7.8) with lysozyme solution (0.2 mg/ml) and sonication (5 s on and 5 s off at a power of 40 W), followed by centrifugation to isolate the inclusion bodies, with 3 times washing in the lysis buffer. The inclusion bodies were then solubilized in 30 ml SDS-urea solution (8M urea, 20 mM Tris, 150 mM NaCl, pH 7.8, and 0.2% SDS). The solution was subjected to centrifugation at 15000 x g to remove insoluble debris and the supernatant, containing SDS/urea-solubilized C99, was incubated with 5 ml of the SDS-urea solution pre-equilibrated with Ni-NTA-Superflow metal ion affinity chromatography resin (Qiagen, Valencia, CA) at room temperature for 90 min. The resin was extensively washed with 200 mL of Tris-buffered saline (20 mM Tris, 150 mM NaCl, pH 7.8) containing 0.2% SDS and then washed with 7.5 mL of a 1% bicelle (w/v) solution (containing 20 mM imidazole and pH 7.8) in a gravity column at

room temperature. C99 was eluted with 10 mL of a 2% bicelle buffer containing 250 mM imidazole at pH 7.8. A chart recorder coupled with a UV detector was used to monitor the elution at 280 nm. Typically, the C99 was eluted in 5 mL. The typical concentration of purified C99 in 5 mL of the 2% bicelle elution solution was 20–30 μM (calculated with A280 and ε280 = 5960 M−1 cm−1).

Preparation of NMR samples

The ca. 5 ml C99 solution in 2% bicelles was concentrated to 0.5 ml with an Amicon Ultra centrifugal filter cartridge (molecular weight cut-off = 10 kDa). The pH of the concentrated sample was then adjusted to 4.5 with acetic acid. D2O and EDTA were then added to 10% and 1 mM, respectively, before running NMR experiments. The concentrated C99 sample (200 μl) was transferred into a 3 mm NMR tube for the paramagnet- free control NMR spectrum acquisition. After the control spectrum acquisition, an aliquot of a stock solution of 200 mM Gd(III)-DTPA in water at pH 4.5 was added directly to the NMR tube (200 μL C99 NMR sample) to a final concentration of 0.8 mM. The spectrum with Gd-DTPA was then acquired using identical NMR acquisition parameters as the diamagnetic control. When 16-DSA was the paramagnetic probe, a different method was used to add this compound to the control sample. A stock solution of 16-DSA in methanol (74 μl) with a concentration of 2.5 mg/ml (6.5 mM) was dispensed into a 1 ml glass vial and then dried in a fume hood overnight. The concentrated C99 NMR solution (200 μl) was added to the glass vial. The sample became clear after vigorously vortexing. The final concentration of 16-DSA in the NMR sample was then 2.4 mM. This sample was then subjected to NMR spectral acquisition using the same parameters as used for the diamagnetic control sample. All NMR experiments were conducted at 45°C on a 900 MHz NMR spectrometer using the

standard Bruker 1H,15N-TROSY pulse sequence. The TROSY spectra from LMPG and the bicelle mixtures are shown in Figures 2.1 and 2.2.

Preparation of reduced salt NMR samples

C99 protein was purified as above, but was eluted from the gravity NTA column with an elution buffer containing 2% bicelle, 500 mM imidazole. The sample was concentrated to 0.5 mL using an Amicon Ultra Centrifugal filter with a MWCO of 10 kDa. The concentrated C99 sample (0.5 mL) in high salt concentration (500 mM imidazole) was then diluted with 4.5 mL 15 mM (the CMC of DHPC) DHPC solution and concentrated back to 0.5 mL. The imidazole concentration was reduced to 5 mM by repeating the buffer exchange step twice. D2O and EDTA were added to the sample to 10% and 1 mM, respectively. Acetate buffer was added to 35 mM and pH was adjusted to 4.5. The sample was then transferred to an NMR tube as described above. The LMPG samples was prepared slightly differently in that C99 was eluted from the NTA column using a solution containing 0.5% LMPG instead of 2% bicelles. Also, this sample was buffer exchanged only once and no sodium acetate was added. The final imidazole concentration in the LMPG sample was 50 mM.

Chemical shift analysis

Amide ^{1}H and ^{15}N chemical shifts were measured for C99 in each bicelle mixture. $^{1}H,^{15}N$-TROSY peak assignments for C99 spectra in the novel types of bicelles examined in this work were completed based on correlating peaks to the previously-assigned peaks in DMPC-DHPC bicelles (Barrett et al., 2012). Backbone amide chemical shifts in both ^{1}H and ^{15}N dimensions for each residue in different bicelle conditions were compared to the reference chemical shift for that residue in a random coil structure, with the sequence-dependent correction based on its preceding and

following residues (Figures 2.3 and 2.5) (Schwarzinger et al., 2001). Specifically, the reference chemical shift of the residue i in a random coil structure is determined by averaging the statistical value for the residue i (from http://www.bmrb.wisc.edu/published/Ikura_cs_study/part2_rc_aa_cs_stats.pdf), with the neighboring effect from the residue i-1 (from http://www.bmrb.wisc.edu/published/Ikura_cs_study/part2_dipep_NH-.pdf for 1H and http://www.bmrb.wisc.edu/published/Ikura_cs_study/part2_dipep_N-.pdf for 15N), and the statistical value of the residue *i* corrected with the neighboring effect from the residue *i+1* (from http://www.bmrb.wisc.edu/published/Ikura_cs_study/part2_dipep_NH+.pdf for 1H and http://www.bmrb.wisc.edu/published/Ikura_cs_study/part2_dipep_N+.pdf for 15N). All statistical values used in this study were accessed in Oct 2013. The chemical shift differences were plotted as a function of the residue number using Origin 8.0 (OriginLab Corp, Northampton, MA).

Examination of the topology of C99 in bicelles

In each bicelle condition, the NMR spectrum with Gd-DPTA or 16-DSA was overlaid with the control NMR spectrum (see examples in Figure 3.9). The intensity ratio for each assigned peak in the presence of either Gd-DPTA or 16-DSA relative to its corresponding peak in the control spectrum was determined using Sparky (T. D. Goddard and D. G. Kneller, SPARKY 3, University of California, San Francisco). The intensity ratio of each peak was plotted (Figure 3.10) as a function of its residue number using Origin 8.0 (OriginLab Corp, Northampton, MA).

CHAPTER IV

PURIFIED, RECOMBINANT PMP22 INCORPORATED INTO A BILAYER FORMS MYELIN-LIKE LIPOPROTEIN ASSEMBLIES[3]

Introduction

Peripheral myelin protein 22 (PMP22), a tetraspan helical integral membrane protein highly expressed (2-5% by weight of protein) in the Schwann cells of the peripheral nervous system, has been extensively studied at the genetic and cellular levels. Expression of PMP22 is essential for the development and maintenance of normal myelin (Adlkofer et al., 1995; Carenini et al., 1999). A series of heritable neuropathies of varying severities are associated with aberrations in the *PMP22* gene. These disorders, Charcot Marie-Tooth disease (CMTD), hereditary neuropathy with liability to pressure palsies (HNPP), and Djerine-Sottas syndrome (DSS), collectively affect 1/3000 individuals (Pareek et al., 1997; Nelis et al., 1999; Young and Suter, 2001; Suter and Scherer, 2003; Young and Suter, 2003; Bertorini et al., 2004; Berger et al., 2006; Nicholson, 2006; Li et al., 2013). The most common cause of CMTD is duplication of the PMP22 gene. Deletion of one copy of PMP22 causes HNPP. Point mutations throughout the PMP22 sequence result in a variety of phenotypes (Li et al., 2013). These mutations alter the trafficking of the protein away from the plasma membrane, causing it to be targeted by the endoplasmic reticulum associated degradation (ERAD) system for disposal (Naef et al., 1997; Naef and Suter, 1999; Colby et al., 2000; Dickson et al., 2002; Fontanini et al., 2005) and may cause the accumulation of PMP22 in aggresomes (Ryan et al., 2002; Tobler et al., 2002). Many of the point mutations result in

[3] This work will be submitted after the completion of this dissertation. Several other people contributed to this work: Dr. Mariena Silvestry, Arina Hadziselimovic, Cheryl L. Law, Dr. Jonathan Schlebach, Dr. Melanie Ohi, and Dr. Charles Sanders, all of Vanderbilt University, and Dr. Cheri M. Hampton, Dr. Elizabeth R. Wright, of Emory University.

the most severe form of neuropathy, DSS (Li et al., 2013). Thus, it may be by a combination of a loss-of-function at the plasma membrane and a toxic gain-of-function that lends the severity to these point mutation phenotypes. All disease forms are characterized by dysmyelination and/or demyelination, highlighting the importance of PMP22 in normal myelin formation and function.

Recent studies in our lab have focused on characterizing the structure of the PMP22 protein, its binding properties, and the stability of the wild-type (WT) and mutant forms (Myers et al., 2008; Sakakura et al., 2011; Schlebach et al., 2013; 2015). However, no data has shed definitive light on the function of PMP22 at the Schwann cell plasma membrane. Evidence suggests that PMP22 has adhesive properties (Notterpek et al., 2001; Hasse et al., 2004), which is perhaps not surprising considering that it shares ~25% sequence identity with the tight-junction protein family of claudins (see Chapter V). Additional data demonstrates that diseased forms of PMP22 are retained within the early secretory pathway of Schwann cells and organize the ER membrane into ultrastructures termed intracellular myelin-like figures (IMLFs) (Niemann et al., 2000; Dickson et al., 2002). These figures resemble the ER whorls known to form by overexpressed membrane proteins with tendencies to weakly associate in *trans* (Snapp et al., 2003; Volkova et al., 2011; 2012). Together, these studies suggest that PMP22 may play a role in the advanced organization of the Schwann cell membrane into the spiraled, wrapped ultrastructure of myelin.

During routine reconstitution of purified PMP22 into lipid vesicles, we discovered that the lipid-protein assemblies formed were not classical vesicles, but rather that PMP22 shapes membranes into complex structures resembling myelin, which we have termed myelin-like lipoprotein assemblies (MLAs). We document these results here along with efforts to characterize these assemblies and to determine how PMP22 promotes and stabilizes their formation.

Results

Negative Stain EM of Reconstituted PMP22-Lipid Assemblies

PMP22 was reconstituted into vesicles and visualized via negative stain electron microscopy (EM), which allows visualization of the outer shell of the lipoprotein assemblies through the use of an electron dense stain that coats the outside of particles. Because the stains employed (*i.e.*, uranyl formate in this study) cannot penetrate the membrane, it is impossible to determine by negative-stain EM if a vesicle is unilamellar or multilamellar. Reconstitution of PMP22 into vesicles composed of 4:1 (mole:mole) ratios of POPC:ESM (lipid-to-protein weight ratio = 1.0, mole ratio = 25.6) via the dialysis method resulted in the formation of organized assemblies that resemble myelin (myelin-like lipoprotein assemblies; MLAs) visible by negative-stain EM (Figure 4.1A-C). When vesicles are prepared by the dialysis method in absence of PMP22, these assemblies are not visible (Figure 4.1D). Because of the aforementioned properties of negative-stain EM, the MLAs cannot simply be multilamellar vesicles. To confirm, we prepared multilamellar vesicles by dispersing the same lipids in water, and found that only the outer vesicle was visible (Figure 4.1E). Finally, to confirm that the ordered assemblies are specific to PMP22, we used the same method to reconstitute another tetraspan membrane protein, the voltage sensor domain of the of the KCNQ1 potassium channel into the same lipid compositions. While the vesicles are misshapen, we do not see evidence of MLAs (Figure 4.1F).

We measured the apparent “interperiod repeating distance” from a number of different MLAs and in a variety of locations within the MLAs (~200 measurements), and found an average (119 ± 13 Å), very similar to that reported for negative stain cross-sections of PNS myelin (119 Å) (See Figure 4.2) (Morell and Quarles, 1999b).

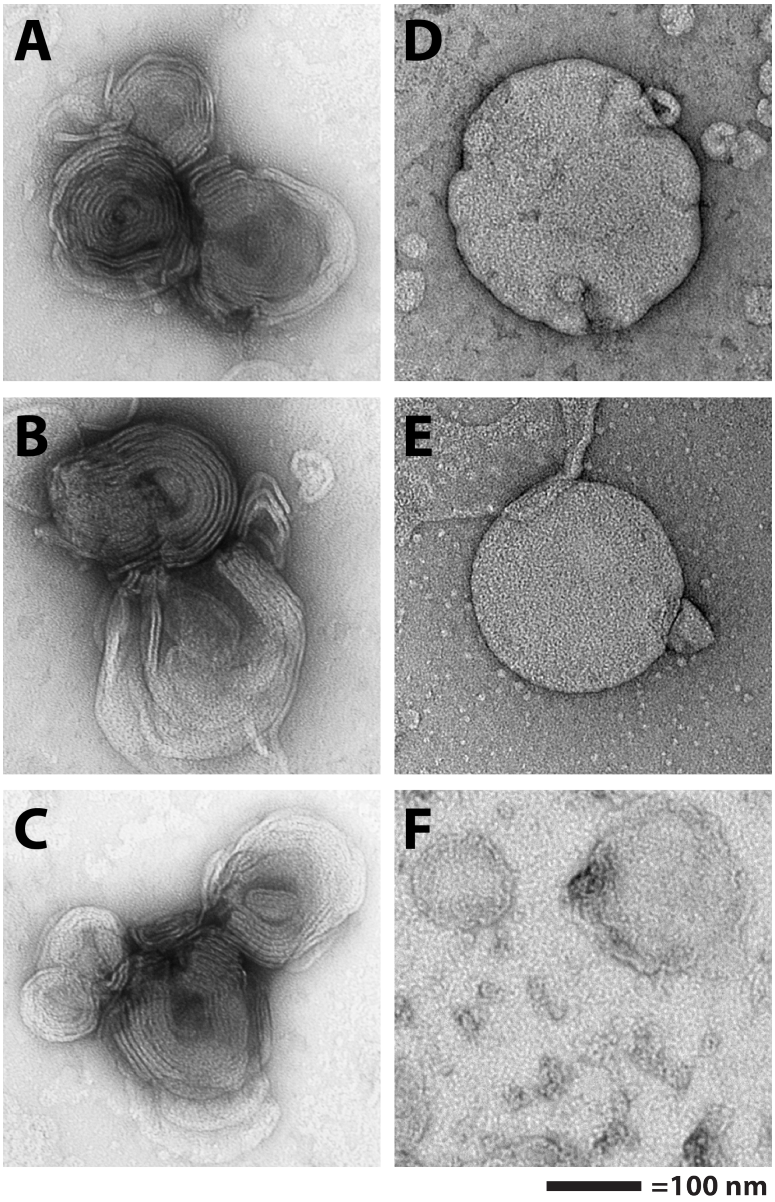

Figure 4.1. Peripheral myelin protein 22 forms ordered assemblies upon reconstitution into vesicles.
(A-C) examples of "myelin like assemblies" created when PMP22 is reconstituted into vesicles via the dialysis method; (D) multilamellar vesicles prepared in the absence of protein via the dialysis method; (E) multilamellar vesicles prepared by spontaneous bilayer formation through hydration of lipids with water; (F) proteolipid assemblies containing 4:1 POPC:ESM and the voltage sensor domain (VSD) of KCNQ1 prepared using the same method as used in (D) and (A-C).

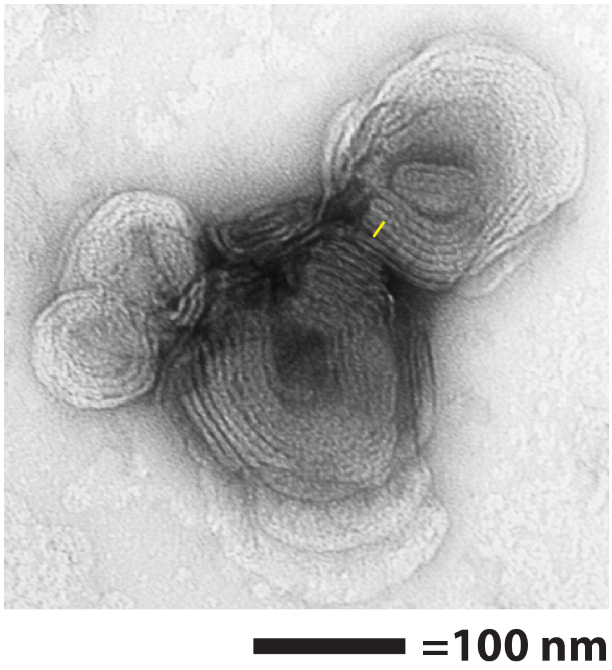

Figure 4.2. Example of "Interperiod Distance" Measurement Taken on MLA.
Yellow line depicts the distance measured to approximate a myelin interperiod distance.

Cryo-EM of PMP22-Containing MLAs

To confirm that MLAs are not an artifact of the negative staining protocol and to gain further insight into MLA ultrastructure, we froze the MLAs and control vesicles in vitrified ice and performed cryo-EM. These results indicated that control vesicles—both those formed via dialysis and those formed the traditional way—are multilamellar assemblies (Figure 4.3A-B), but that PMP22-containing vesicles formed assemblies resembling the MLAs seen in negative stain (Figure 4.3C-D).

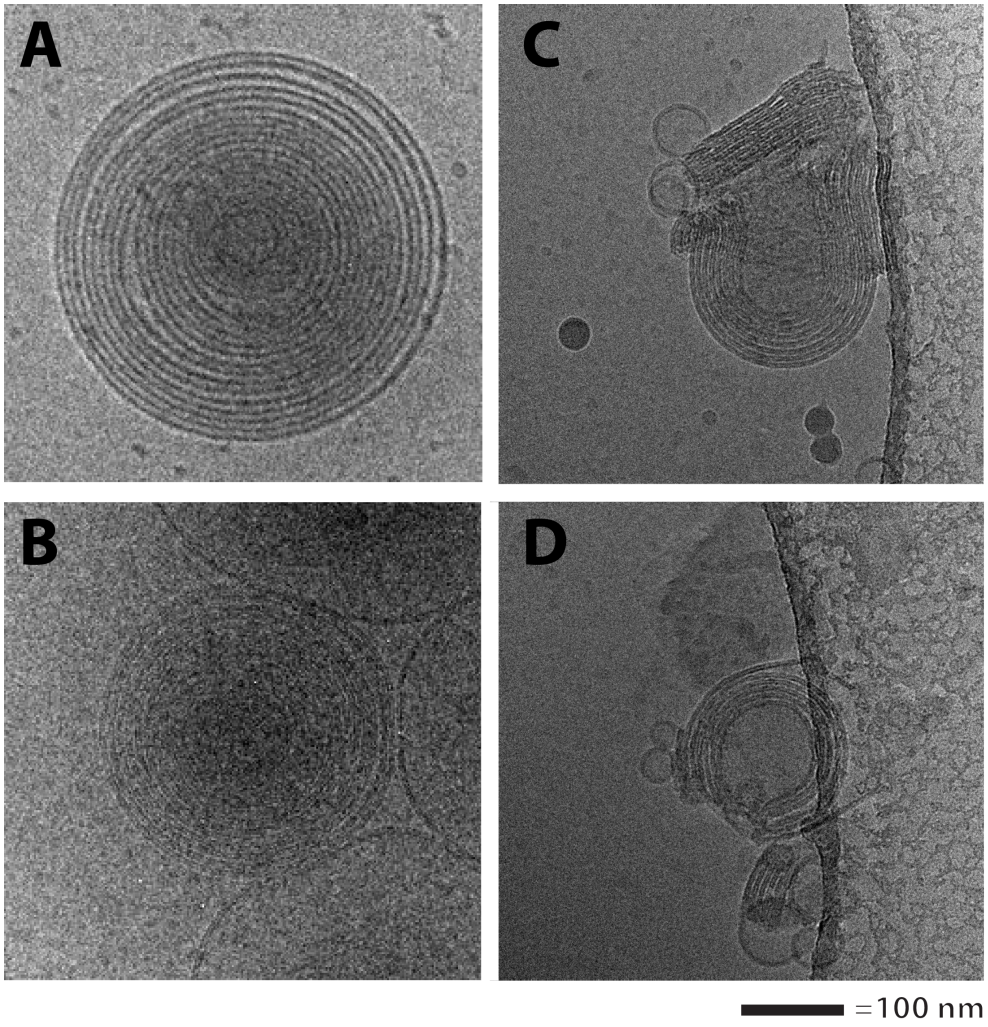

Figure 4.3. Ordered assemblies are visible by cryo-EM.
(A) Multilamellar vesicles prepared in the absence of protein via the dialysis method; (B) multilamellar vesicles prepared by spontaneous bilayer formation through hydration of lipids with water; (C-D) examples of MLAs created when PMP22 is reconstituted into vesicles via the dialysis method. Note that MLAs often are attracted to the carbon, so it is difficult to obtain cryo-EM images of MLAs in the center of the holes of the carbon film.

Tomography suggests that MLA morphology is that of compressed, wrapped vesicles

While the negative-stain and cryo-electron microscopy experiments indicate that MLAs are *not* composed of nested vesicles like MLVs, a number of remaining non-mutually exclusive morphological possibilities remain for MLAs. They could be composed of (i) a single, compressed spiraled vesicle, very akin to Schwann cells, (ii) a series of individual compressed, wrapped vesicles, and/or (iii) single spiraling bilayers. To more closely examine the morphology of MLAs, cryo-electron tomography was performed, whereby a tilt-series of images is acquired in 2° increments from (ideally) -65° to +65°. These images are then aligned using colloidal gold fiducials included within the frozen sample, and then backprojected to reconstruct a three-dimensional volume that is representative of the original density. Initial efforts to perform cryo-electron tomography on PMP22-induced MLAs have resulted in low-resolution tomograms that allow for preliminary construction of 3D models (Figure 4.4). These models indicate that MLAs seem to be composed of compressed, wrapped vesicles, a morphology that does not precisely recapitulate that of Schwann-cell myelination (compressed, spiraling cell membranes). However, this morphology does have some similarities to myelin in that there is compression and wrapping.

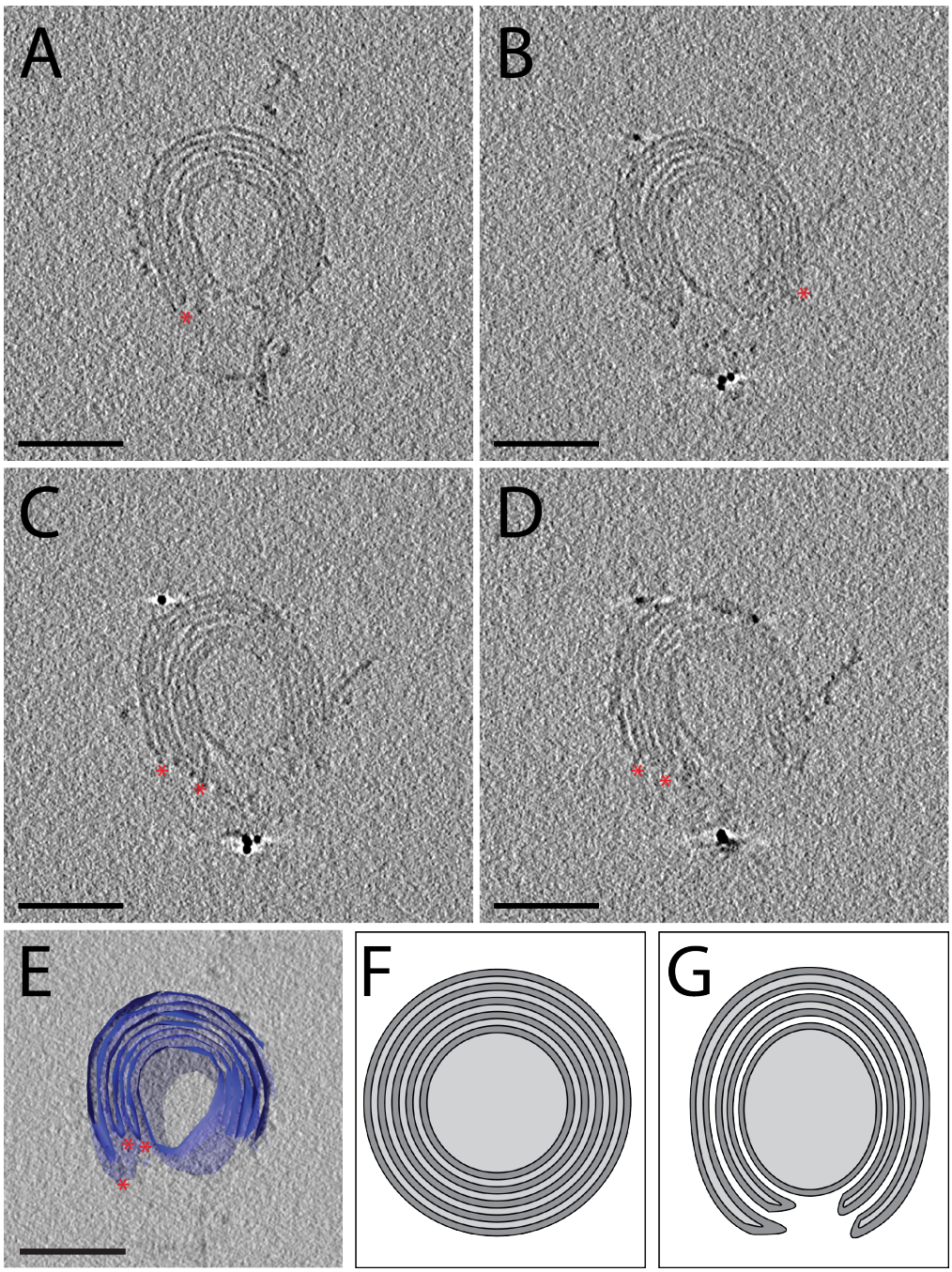

Figure 4.4 Representative z-sections from four depths in the 3-D tomogram and a 3-D tomographic model reveal that MLAs are composed of compressed wrapped vesicles.

Z slices (8 pixels deep) from 1/8, 1/4, 1/2, 3/4 of the tomogram depth (A-D), respectively. Red arrows mark sites where the edges of the compressed vesicles are visible. All tilt series acquired in vitrified ice on Tecnai™ (F-30) Transmission Electron Microscope operating at 300 keV. Scale bars = 100 nm. (E) Preliminary 3D tomographic model constructed from the tomogram depicted in (A-D). (F) Model demonstrating the nesting vesicles of a MLV and (G) model demonstrating the compressed, wrapped vesicles of a MLA.

Formation of MLAs is dependent on the lipid-to-protein ratio

PMP22 lipid to protein ratio (LPR) is important for the formation of MLAs. A decrease in the LPR (more protein) to 0.5 (mass-to-mass; mole to mole = 12.8) results in the formation of many types of clustered vesicles and disordered MLAs (Figure 4.5A and 4.5B; Figure 4.6; Table 4.1). MLAs are most prevalent at LPRs of 1.0 (mole-to-mole = 25.6) (Figure 4.5C and 4.5D; Figure 4.6; Table 4.1). Conversely, increasing the overall LPR (reduced protein) (w/w) in the dialysis button to 10 (mole-to-mole = 256.2) results in near abrogation of MLA formation, although a small number of disordered MLAs still form (Figure 4.5E and 4.5F; Figure 4.6; Table 4.1). These studies suggest that specific LPR ranges are required for the formation of MLAs and confirm a role for PMP22 in MLA formation. This is reminiscent of the fact that dysmyelination under disease conditions can be cause by either overdosage or underdosage of the *PMP22* gene, resulting either in too much or too little PMP22 protein.

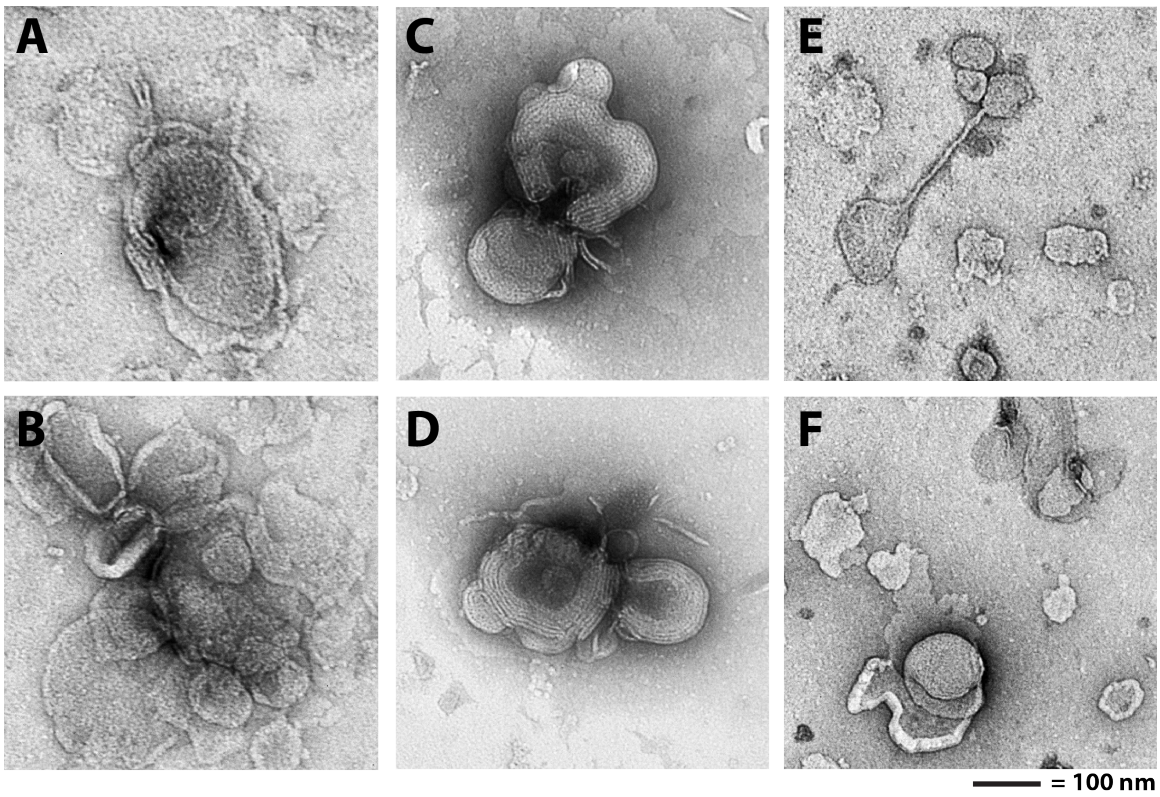

Figure 4.5. Altered PMP22:lipid ratios and disease-causing mutations disrupt MLA formation.
(A and B) LPR 0.5 displays disordered MLAs and clustered vesicles; (C and D) LPR 1.0 displays MLAs; (E and F) LPR 10.0, displays empty and clustered vesicles.

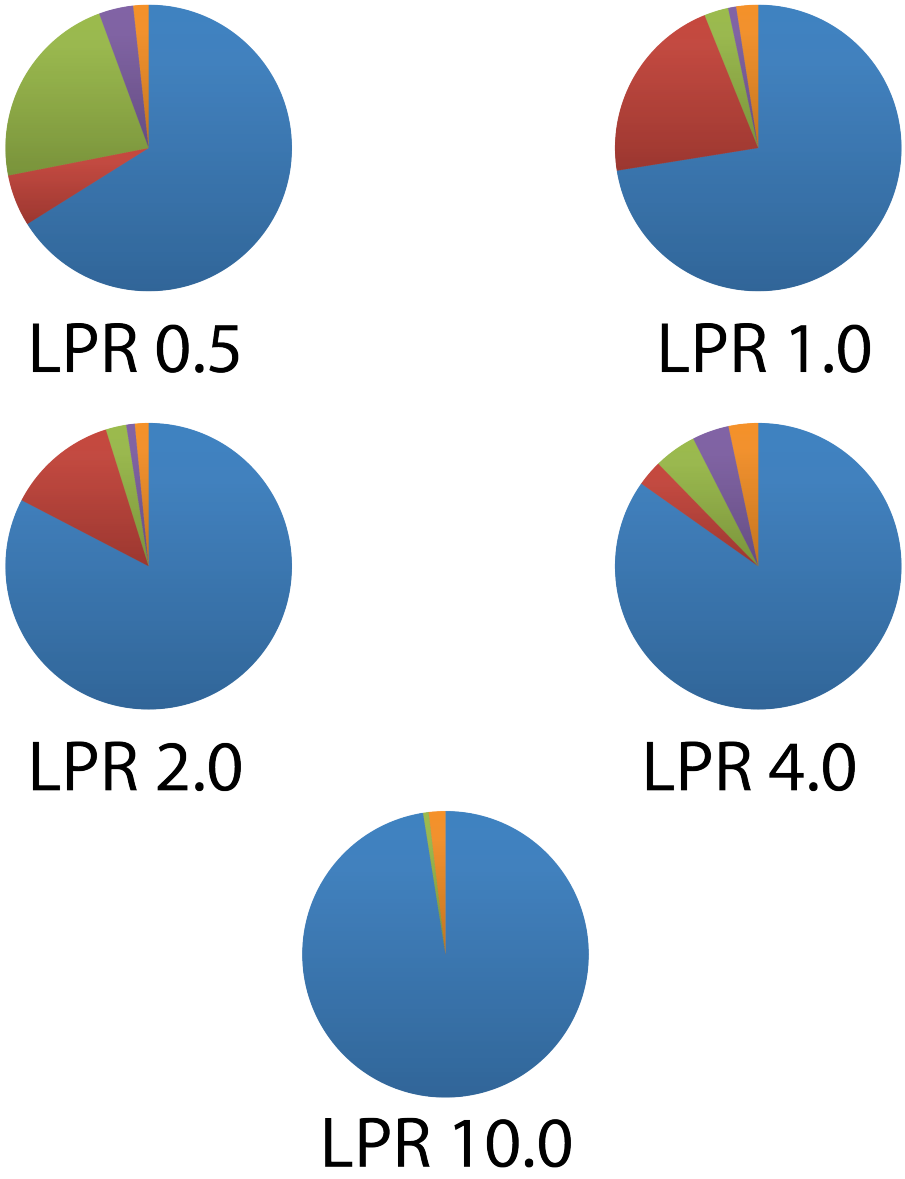

Figure 4.6. Altered PMP22:lipid ratios and disease-causing mutations disrupt MLA formation.
Counts from 40 images of WT PMP22 reconstitutions taken at 14,000x magnification for each of 5 different LPRs (weight-to-weight). Key: (Red): MLAs, (Blue): Vesicles; (Green): Disordered MLAs; (Purple): Clumped Vesicles; (Light blue): Sheet formation, (Orange) Aggregation.

Removal of cysteine residues does not abrogate MLA formation

Preliminary efforts to directly visualize PMP22 in MLAs have not, thus far, been successful. We have therefore explored the role of PMP22 in MLA formation using structure-function studies. We first tested whether disulfide bond formation in PMP22 might be related to MLA formation. PMP22 contains four native cysteine residues (Figure 4.7). Two of these residues are found in the extracellular loop and may be involved in an intramolecular disulfide cross-link based on the observation of a disulfide bond involving the corresponding Cys pair in claudin-15 (see chapter V). While DTT is present in the dialysis buffer during reconstitution at low levels (0.5 mM), it is possible that high local concentrations of PMP22 in vesicular assemblies could overcome the DTT and form non-native intermolecular cross-links that contribute to MLA formation. To verify that the MLAs were not dependent on intramolecular or intermolecular PMP22 cross-linking, we removed both cysteine residues in the loops (cys-PMP22) and confirmed that MLAs still form (Figure 4.8). Additionally, removal of all cysteine residues to create a cysless construct (cysless-PMP22) does not abrogate MLA formation (Figure 4.8).

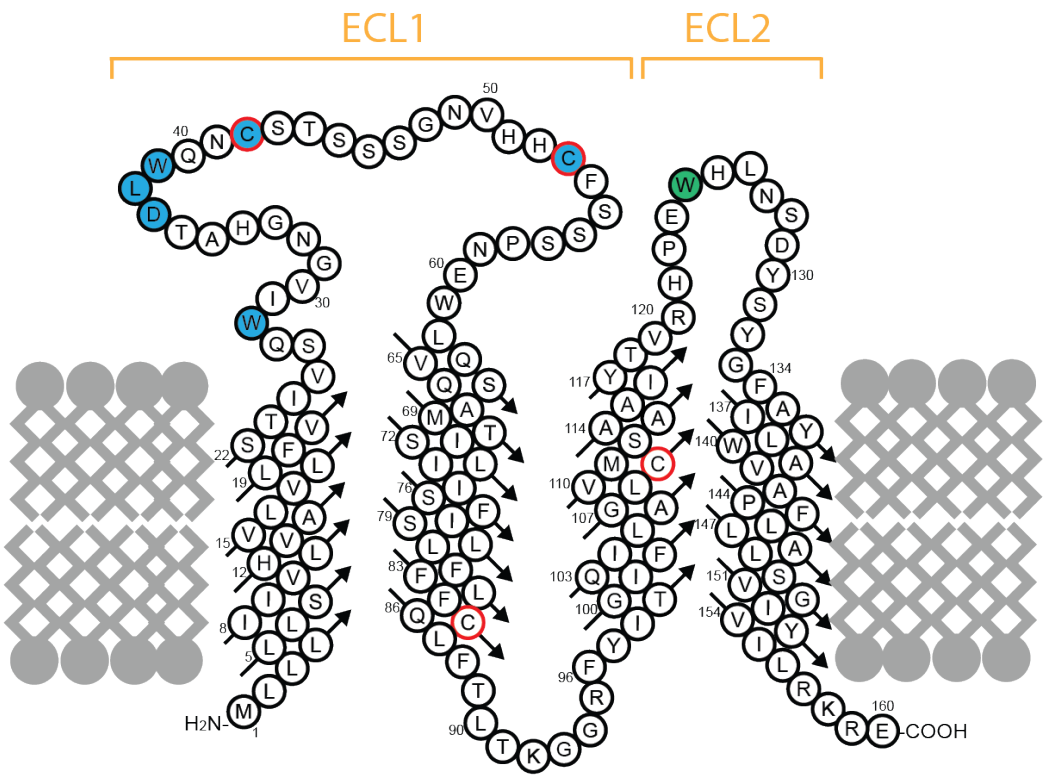

Figure 4.7. Topology Diagram of PMP22.
Blue residues are conserved residues from the claudin motif. The green residue is a conserved tryptophan in ECL2 in PMP22s. Cysteine residues are highlighted by a red ring.

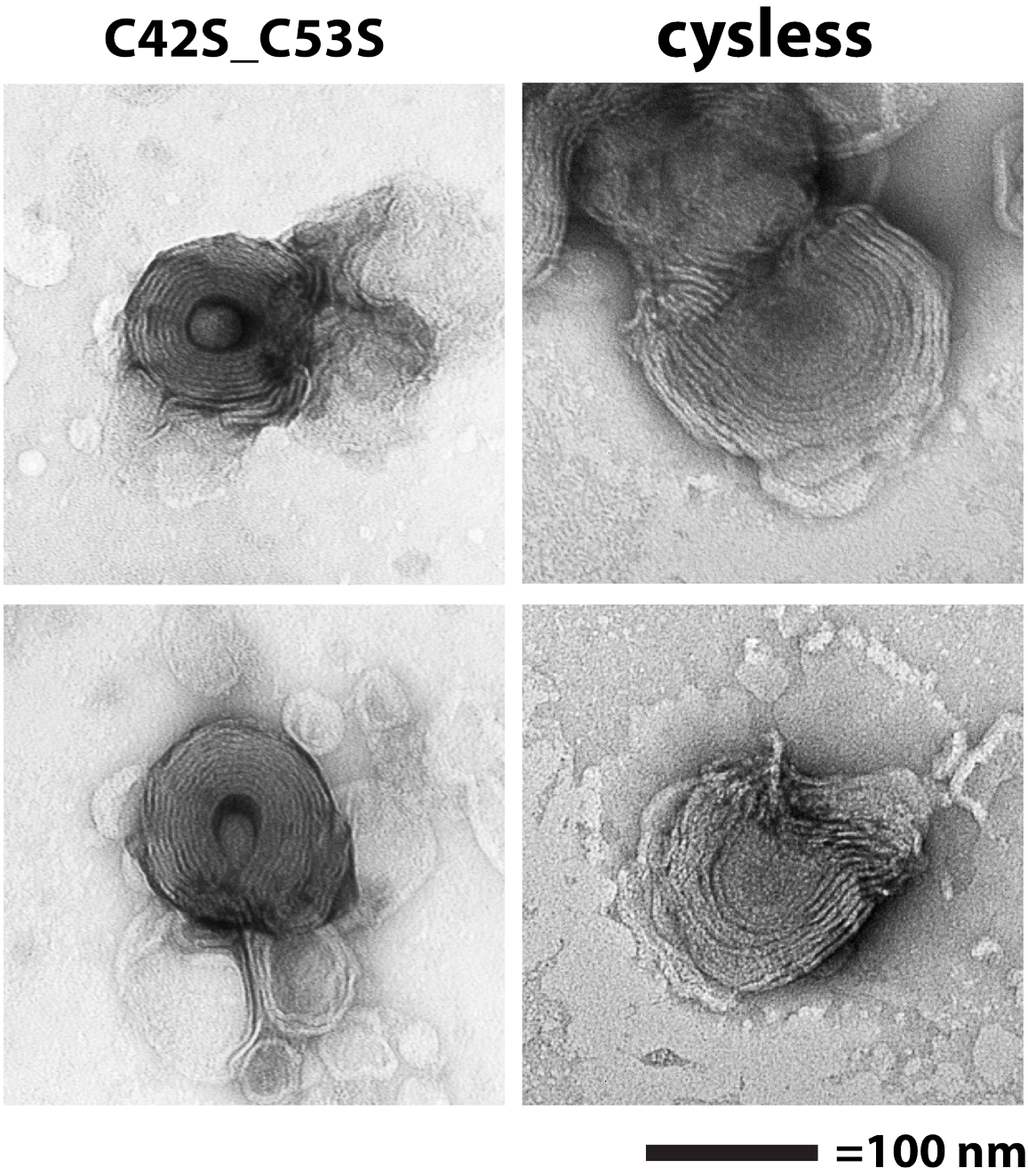

Figure 4.8. MLA formation is not dependent upon intermolecular disulfide linkage. (Left column) Mutation of the cysteine residues in ECL1 does not abrogate MLA formation. (Right column) Mutation of all of the cysteine residues does not abrogate MLA formation.

Formation of MLAs is disrupted by the inclusion of peptides from extracellular loop 2

Previous research had indicated a role for the extracellular loop 1 (ECL1) of PMP22 in the *trans* homophilic adhesive properties of PMP22 (Hasse et al., 2004). ECL2-mediated homophilic interactions, while still present, were less strong than interactions of ECL2 with P0 or than ECL1 with PMP22 (See Figure 3 of Hasse et al., 2004). Thus, we hypothesized that incubating PMP22 with a GST-ECL1 fusion protein, but not with a GST-ECL2 fusion protein, during dialysis would cause the disruption of MLA formation. We found instead a surprising role for ECL2 in MLA formation. In addition to disrupting the MLA formation, it was found that ECL2 promoted the formations of mosaic, extended membrane sheets and small vesicles (Figure 4.9 and 4.11). ECL1 seemed to have a lesser effect in reducing the MLA formation overall, although MLA prevalence was reduced (Figure 4.11).

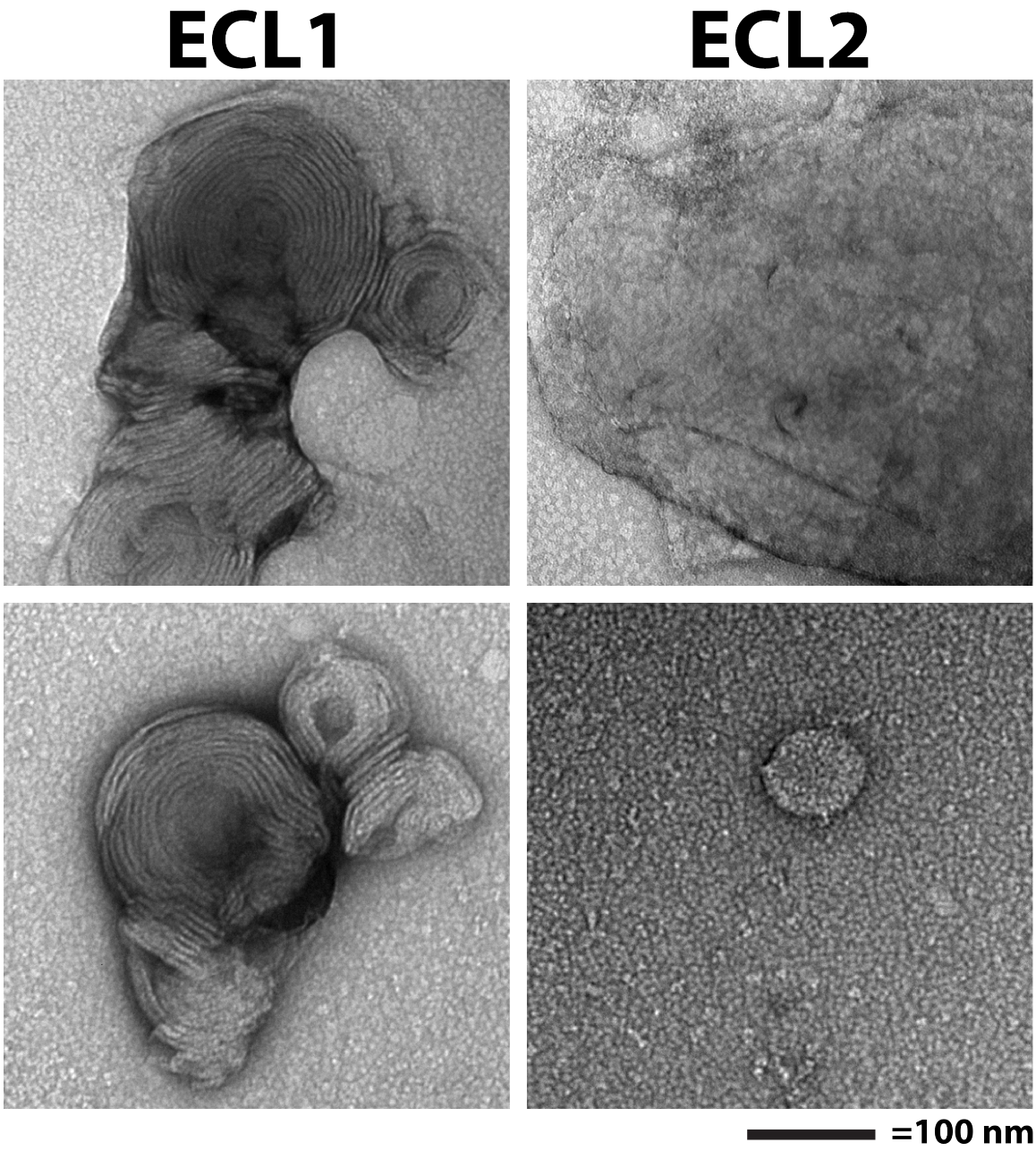

Figure 4.9. Addition of ECL2 GST-fusion peptides alters morphology.
(Left column) While MLA formation is reduced but still present when ECL1 peptides are added to the dialysis solution; (Right column) MLA formation is disrupted when ECL2 peptides are added to the dialysis solution and large membrane sheets (top image) and small vesicles are seen (bottom image).

To further confirm a role for ECL2, we mutated a highly conserved tryptophan residue (W124) to alanine (Figure 4.10 and 4.11; Table 4.1). We found that this mutation completely disrupted MLA formation, and resulted in the formation of a small number of similar flat sheet structures as found in the ECL2 peptide experiments as well as significant aggregation. Alanine mutations of the individual residues from the conserved claudin motif in ECL1, on the other hand, did not result in disruption of MLA formation (Figure 4.12).

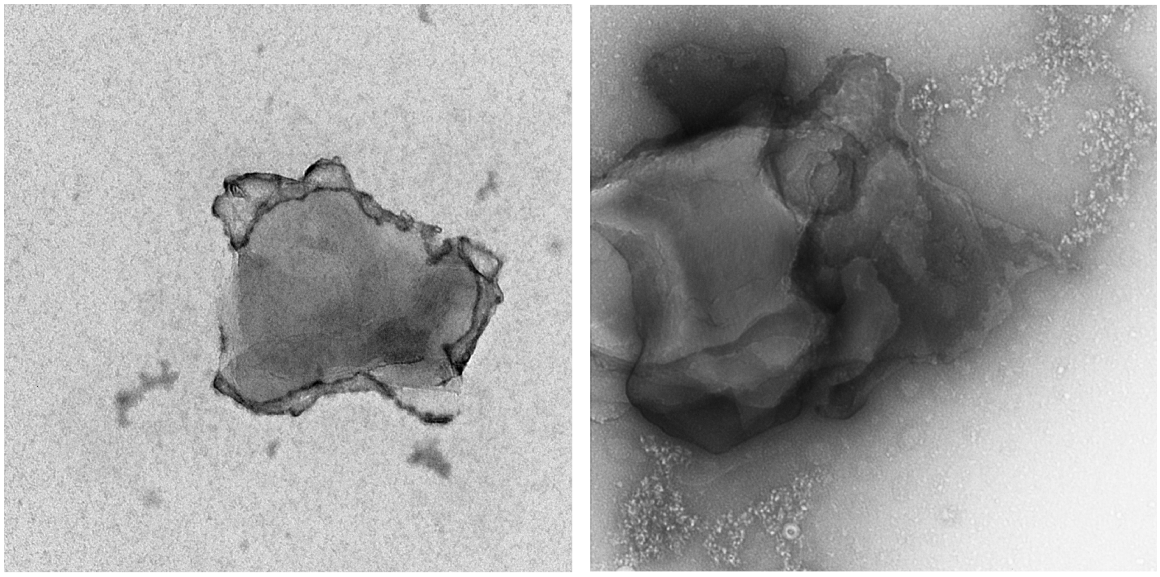

Figure 4.10. W124A Mutation of ECL2 Disrupts MLA Formation.
(A) Example image of the large sheets created by the W124A mutation. (B) Example image of a large sheet and the aggregates seen in the W124A mutation preparation.

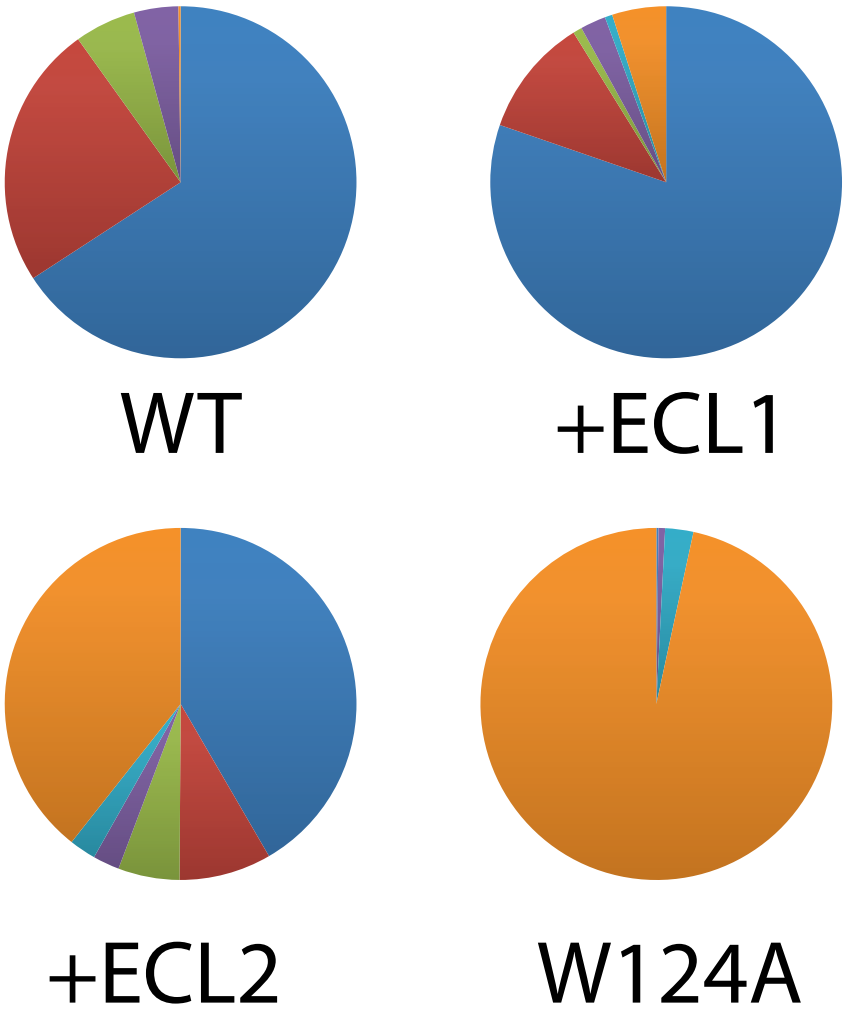

Figure 4.11. GST-peptides and ECL2 mutants reduce MLA formation and induce Aggregation and Sheet formation; ECL1 peptides reduce MLA formation to a lesser degree.
(Top left) Counts from 40 images of WT PMP22 reconstitutions taken at 14,000x magnification. (Top right) Counts from 40 images of PMP22 reconstitutions with GST-ECL1 peptides at 2.9 uM, taken at 14,000x magnification. (Bottom left) Counts from 40 images of PMP22 reconstitutions with GST-ECL2 peptides at 2.7 uM taken at 14,000x magnification. (Bottom right) Counts from 40 images of W124A-PMP22 reconstitutions taken at 14,000x magnification. Key: (Red): MLAs, (Blue): Vesicles; (Green): Disordered MLAs; (Purple): Clumped Vesicles; (Light blue): Sheet formation, (Orange) Aggregation.

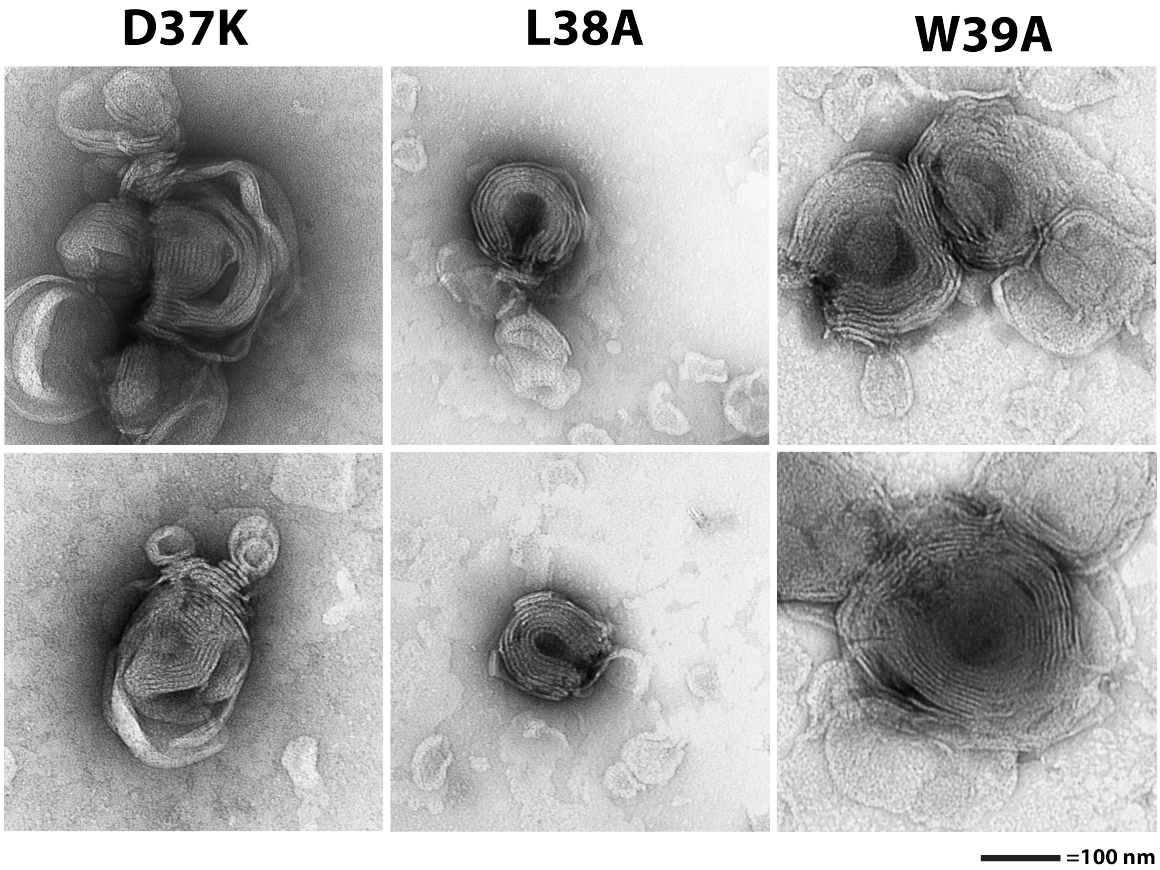

Figure 4.12. Mutations in the Claudin Motif of ECL1 Do Not Disrupt MLA Formation.

Examples of (A and B) D37K mutations, (C and D) L38A mutations, (E and F) W39A mutations. See also Figure 4.5, which shows that the double mutant containing C42S and C53S is also not disruptive to MLA formation, indicating that any disulfide bonds are not critical to MLA formation.

The L16P (TremblerJ) Mutation Disrupts MLA Formation

Reconstitution of the L16P *TremblerJ* (*TrJ*) disease mutant form of PMP22 into vesicles still results in layered assemblies, but these assemblies appear to be unstable or incomplete (Figure 4.13 and 4.14; Table 4.1). The L16P form of the protein does not have a grossly different overall tertiary structure from WT protein, but the mutation does induce more subtle structural changes and reduces the thermodynamic stability of the protein, increasing its propensity to misfold (Fontanini et al., 2005; Sakakura et al., 2011).The fact that the TrJ PMP22 mutant leads to both defective MLA formation and defective myelination in vivo is consistent with the notion that the formation of MLAs is potentially reflective of one possible function of PMP22 in Schwann cells.

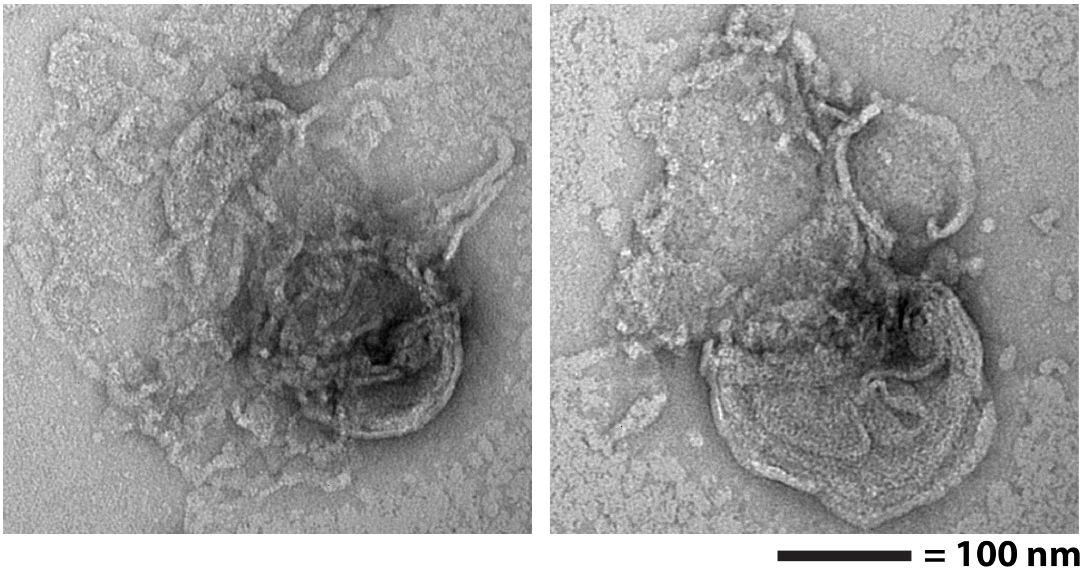

Figure 4.13. L16P (*TremblerJ*) mutation disrupts MLAs.
Disordered MLAs (pictured) and aggregates are present in L16P PMP22 reconstitutions.

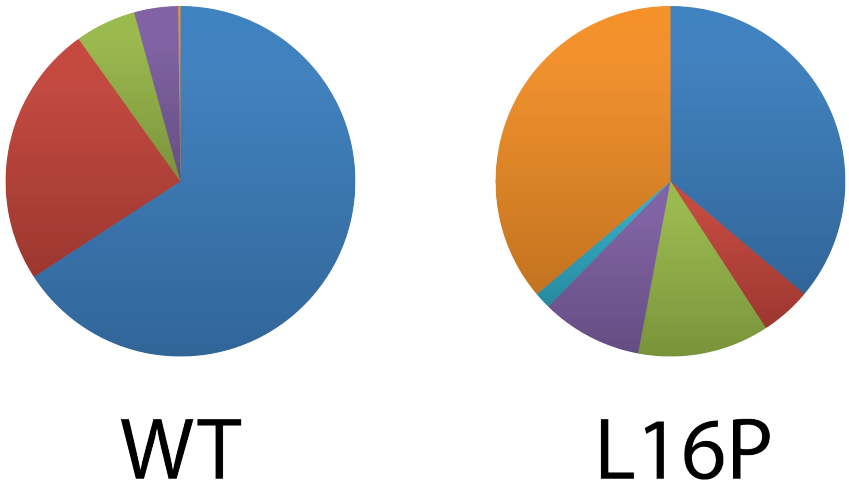

Figure 4.14*. TremblerJ* mutation disrupts MLAs.
(Left) Counts from 40 images of WT PMP22 reconstitutions taken at 14,000x magnification. (Right) Counts from 40 images of L16P PMP22 reconstitutions taken at 14,000x magnification. Key: (Red): MLAs, (Blue): Vesicles; (Green): Disordered MLAs; (Purple): Clumped Vesicles; (Light blue): Sheet formation, (Orange) Aggregation.

Table 4.1. Total counts from images of PMP22 reconstitutions.

	WT		L16P		W124A		ECL1		ECL2	
	raw counts	%	raw counts	%	raw counts	%	raw counts	%	raw counts	%
Vesicle	339	66	116	36	1	0	582	80	267	70
MLA	125	24	15	5	0	0	79	11	69	18
Disordered MLA	29	6	39	12	0	0	6	1	3	1
Clumped vesicles	21	4	30	9	3	1	17	2	19	5
Sheet	0	0	5	2	13	3	5	1	2	1
Aggregation	1	0	116	36	484	97	36	5	21	6
Total	515	100	321	100	501	100	725	100	381	100

	WT LPR 0.5		WT LPR 1.0		WT LPR 2.0		WT LPR 4.0		WT LPR 10.0	
	raw counts	%	raw counts	%	raw counts	%	raw counts	%	raw counts	%
Vesicle	306	66	558	72	428	83	407	85	467	97
MLA	27	6	165	21	65	13	14	3	0	0
Disordered MLA	104	22	21	3	12	2	23	5	3	1
Clumped vesicles	18	4	7	1	5	1	20	4	0	0
Sheet	0	0	0	0	0	0	0	0	0	0
Aggregation	8	2	19	2	8	2	16	3	9	2
Total	463	100	770	100	518	100	480	100	479	100

Discussion

These experiments suggest a role for PMP22 in the formation of the myelin ultrastructure. Because purified, recombinant-PMP22 reconstituted into lipids causes the formation of higher-ordered myelin-like lipoprotein assemblies (MLAs), it suggests that at least one role of PMP22 at the Schwann cell plasma membrane may be to initiate or support the compression, spiraling, and/or adhesion of the myelin membrane. This role of PMP22 has been previously suggested (Hasse et al., 2004) and is in agreement with the observation that PMP22-null mice see strong retardation of correct initiation of myelin spiraling (Adlkofer et al., 1995). On the other hand, P0-null mice see a reduction of myelin compaction, dysmyelination, and a lack of myelination (Giese et al., 1992). P0/PMP22 deficient mice show an enhanced retardation of myelin formation compared to either single deficient mutant, suggesting that both P0 and PMP22 are involved in the initiation of Schwannn cell spiraling around the axons (Carenini et al., 1999). From these observations, it is thought that PMP22 plays either a structural or signaling role in the formation of myelin.

Similarity of MLA Ultrastructure to That of PNS Myelin

It is clear that the MLAs formed are not multilamellar vesicles (MLVs) because (i) MLVs are indistinguishable from unilamellar vesicles under negative stain conditions while MLAs are clearly layered lipoprotein assemblies and (ii) MLAs are visible as distorted structures under cryo-conditions which are still distinct from MLVs. Preliminary tomography experiments suggest that MLAs are composed of compressed, wrapped vesicles. While this is not a replica of myelin, in which each internode is composed of one Schwann cell that has compressed and wrapped tightly around itself, it is not dissimilar, in that the vesicles are compressing and wrapping. A role for PMP22 in the formation of MLAs is in agreement with the observation that PMP22 retained in the ER *in*

vivo organizes the ER membrane into assemblies that are termed intracellular myelin-like figures (IMLFs) (Niemann et al., 2000; Dickson et al., 2002). Thus, the accumulation of PMP22 in a membranous structure may result in the formation of myelin-like assemblies. Importantly, because PMP22 forms IMLFs *in vivo*, one can postulate from our results that the lipid-organizing properties of PMP22 might, when unregulated, be one toxic feature of this protein. Furthermore, it is important to note that the "interperiod distances" observed in MLAs are consistent with true interperiod distances in PNS myelin (Figure 4.2). This observation lends further credence to a role for PMP22 in myelin ultrastructure formation and/or maintenance.

How Does PMP22 Promote and/or Stabilize MLA formation?

Because (i) PMP22 is homologous to the claudins (see Chapter V), a family of tight-junction proteins, (ii) other proteins prone to weakly dimerizing form higher-architecture of ER whorls resembling IMLFs when retained in the ER (Snapp et al., 2003; Volkova et al., 2011; 2012) and (iii) PMP22 ECL1 had been previously been shown to mediate homophilic PMP22 interactions, we hypothesized that ECL1 may be responsible for MLA formation via PMP22 dimerization in *trans*. However, we were surprised to find that ECL2 mediated MLA formation (Figures 4.7-4.9). ECL1 peptides did seem to also disrupt MLAs, but an ECL2 mutation completely abrogated MLA formation. However, the previous study by (Hasse et al., 2004) demonstrated that both ECL1 and ECL2 are capable of homophilic interactions, but concluded that the ECL1 interaction was likely more important. Thus, we update this model. We postulate that ECL2 mediates MLA formation by one of two mechanisms: (i) low-affinity transient ECL2-mediated *trans*-interactions, as described for ER whorl formation (Snapp et al., 2003; Volkova et al., 2011; 2012), thus allowing for MLA formation but the interperiod distance observed, or (ii) ECL2-mediated *cis*-interactions, which would potentially result

in a wedging mechanism to deform and/or compress the vesicle, allowing for wrapping (Hu et al., 2011). There is evidence that weakly *trans*-interacting proteins can induce the formation of organized smooth ER whorls, which resembles the IMLFs see in ER-retention of PMP22, so this mechanism cannot be ruled out by the experiments conducted in this study. Additionally, because GST-ECL1 peptides seem to somewhat disrupt MLA formation relative to control, it is possible that both loops are involved. This mirrors recent studies of claudin-15 that suggest both ECL1 and ECL2 are involved in both *cis*- and *trans*-homophilic interactions responsible for forming tight junctions (Suzuki et al., 2015).

Efforts to localize PMP22 within the MLAs have not yet met with success. The majority of localization methods rely upon antibodies or the addition of gold particles, which so far seems to disrupt MLA formation when added prior to formation. Adding antibodies or gold particles after MLA formation also did not meet with success, presumably because the space between layers is too small to accommodate these tags and labels. Future efforts to localize PMP22 in MLAs may rely on affixing and sectioning the MLAs prior to labeling.

MLA Formation, Like Myelin, Is Highly Dependent on the LPR and CMTD Mutations Disrupt MLA Formation

It is also clear that MLAs are dependent on PMP22 for formation, as varying the PMP22 dosage abrogates MLA formation, which is consistent with the observation that either possession of a third copy of the PMP22 gene (increased gene dosage) or the absence of one copy of PMP22 (decreased gene dosage) results in disease formation (Li et al., 2013). Further, a known severe disease mutation, L16P, which exerts its deleterious effects by disrupting PMP22 stability (Fontanini et al., 2005; Sakakura et al., 2011), results in the formation of aggregates and deformed MLAs (Figure 4.6).

Conclusions

In this work, we demonstrate that reconstitution of PMP22 into vesicles results in the formation of assemblies that resemble myelin, which we have termed myelin-like lipoprotein assemblies (MLAs). We further demonstrate that MLA formation is affected by PMP22 dosage, is dependent upon the PMP22 ECL1 *and* ECL2, and is disrupted by disease forms of PMP22. Thus, we update the model of PMP22 interactions presented in previous papers to include *cis*- and/or transient *trans*-homophilic interactions mediated by the ECL2 of PMP22 (Figure 4.12). Further, we suggest that at least one function of PMP22 may be to play a direct structural role in the formation and maintenance of myelin architecture. This model resembles that of the role of PLP, a tetraspan protein in CNS myelin unrelated by homology. Importantly, PLP resembles PMP22 topologically in that it contains four TM segments and shows a similar formation of higher-ordered lipoprotein assemblies when reconstituted into vesicles and examined by negative stain TEM (Palaniyar et al., 1998). Myelin basic protein, the other major component of CNS myelin, also creates higher-ordered lipoprotein assemblies reminiscent of the MLAs shown in this work (Mac Millan et al., 2000). No studies have been performed yet on the incorporation of purified P0 protein, possibly owing to the difficulty of obtaining purified and well-folded full-length P0 protein, as it has a large extracellular domain containing a number of disulfide bonds and important modifications as well as a single membrane-spanning segment (Eichberg, 2002).

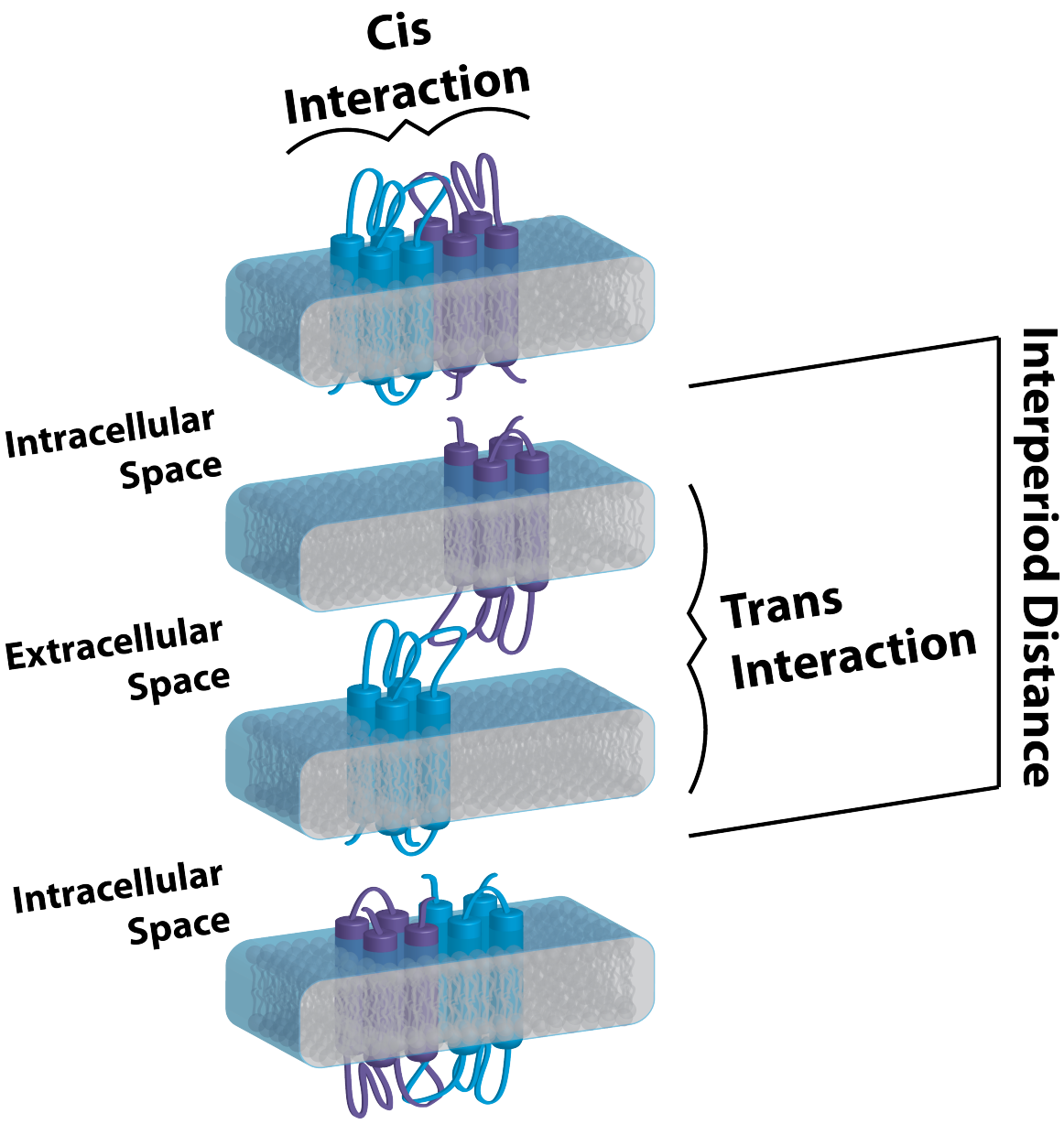

Figure 4.12. Model of Potential Homophilic PMP22 Interactions Involved in Myelin Formation.
Note that both *cis*- and *trans*-interactions mediated by ECL2 are possible with the data presented herein, and may not be mutually exclusive. ECL1 may also participate in either or both of these interactions, but ECL1-mediated interactions were not pictured for simplicity.

Lastly, the authors note that the formation of MLAs could be used as an assessment of PMP22 functionality. Combined with recent studies on the altered stability and trafficking of PMP22 (Schlebach et al., 2015), this assay could be used to estimate the efficacy of pharmacological chaperones that improve PMP22 trafficking to the plasma membrane. Because a number of mutants are recognized by the cell as folding-defective and are targeted for destruction by the ER-associated degradation system, many of these mutants never make it to the plasma membrane where they may perform initiation of myelination. Screening mutants for their ability to form MLAs in the presence and absence of any pharmacological chaperones discovered to be effective at enhancing PMP22 delivery to the plasma membrane represents on avenue of evaluating the potential efficacy of these molecules in treating neuropathy.

Materials and Methods

Expression and Purification of PMP22

PMP22 was expressed and purified as previously described,(Mobley et al., 2007; Myers et al., 2008; Sakakura et al., 2011; Schlebach et al., 2013) with minor adjustments. Briefly, PMP22 was expressed in one-shot BL21 Star (*DE3*) *E. coli* (Life Technologies) as a fusion protein construct consisting of an N-terminal 76-amino acid segment of the lambda repressor, which serves to drive the protein into inclusion bodies, (Mobley et al., 2007) followed by a 10x-histidine tag, a 7 amino-acid linker, a thrombin cleavage site, an 11 amino acid strep-tag and, finally, the human-PMP22 sequence. The fusion protein was solubilized initially from inclusion bodies using the zwitterionic Empigen BB detergent (Sigma-Aldrich) and purified using Ni(II)-NTA Superflow resin (Qiagen) (0.5 ml/1g of original cell pellet) packed into a gravity column. While bound to the Ni-NTA resin, the detergent was exchanged for decyl maltoside (DM), a mild, uncharged detergent, by repetitive washing of the column (20 column volumes) with 25

mM phosphate buffered saline, pH 7.5, containing 0.5% DM. The fusion construct was cleaved by incubation with Recothrom® Thrombin (The Medicines Company) overnight. This cleavage reaction was followed by a second purification over Ni-NTA resin. Cleaved PMP22 has a mild affinity for divalent metal cations, including Ni(II) (Myers et al., 2008). As a result, PMP22 was eluted in a stepwise fashion using 10-30 mM imidazole (Sigma-Aldrich) in a 50 mM Tris pH 8.0 buffer. The uncleaved PMP22 and the His_{10}-tag containing fusion cleavage product remain bound to the resin at these imidazole concentrations. Protein purity was assessed via LDS gel electrophoresis and the most pure fractions were pooled. Depending on the construct of PMP22 purified (wild-type versus the various mutants), the purified fractions varied.

Cleaved and purified PMP22 was concentrated to 1.0 mg/ml as determined by A_{280} using a molecular weight of 19.2 kDa and an extinction coefficient of 44,900 $M^{-1}cm^{-1}$ prior to reconstitution into vesicles.

Reconstitution of PMP22 into vesicles

PMP22 was mixed at the lipid-to-protein mass ratios described in the results section with mixed micelles containing 8.33% DM and pipetted into dialysis buttons (Hampton Research). These buttons were covered by hydrated dialysis membrane with a molecular weight cutoff of 20 kDa (Biotech RC Tubing, SpectraPor) that had been pretreated by boiling in 1 mM EDTA for 5 minutes to remove metal ions. Buttons were dialyzed for 10 days at room temperature against a buffer containing 10 mM Tris pH 8.0, 150 mM NaCl, and 0.5 mM fresh DTT, which was changed daily. Protein-free vesicle controls were prepared by mixing mixed micelles and PMP22 elution buffer together at the same volume-to-volume ratio as the experimental conditions and dialyzed in the same buffer. Alternatively, multilamellar vesicle controls were prepared by mixing dry lipids and water and agitating.

Expression, Purification, and Addition of GST-ECL1 and GST-ECL2 to MLA Preparations

The following methods were adapted from Hasse et al., 2004. The first extracellular loop (ECL1, residues 32-64) and second extracellular loop (ECL2, residues 120-133) of PMP22 and ECL2 were PCR amplified using the following primers: 5'-TCCGCGTGGATCCCCAGGAATTccCAATGGACACGCAACTGATCTC-3' (ECL1-forward), 5'- GCCGCTCGAGTCGACTCAAGACTGCAGCCATTCGTTTGG-3' (ECL1-reverse), 5'-TCCGCGTGGATCCCCAGGAATTccCAGGCACCCGGAGTGGCATCTC-3' (ECL2-forward), 5'-GCCGCTCGAGTCGACTCAACCGTAGGAGTAATCCGAGTT-3' (ECL2-reverse). PCR products were restriction digested using BamHI-HF and SalI-HF enzymes (NEB) and ligated into a similarly digested pGEX-4T-1 vector (GE Healthcare Life Science). The final product of the ligation reaction was transformed into XL1-Blue *E. coli* cells and plasmid DNA purified with QIAprep Spin Miniprep Kit (Qiagen). The final constructs were verified by sequencing and were then transformed into BL21(*DE3*) *E. coli* cells. A single colony was used to grow an overnight starter culture in LB containing 0.1 mg/ml ampicillin. The starter culture was then added to a 1L LB and grown for 3 hours at 37°C shaking at 230 rpm to an $OD_{(600nm)}$=0.9. Cultures were transferred to 25°C and induced over 5 hours with 1 mM IPTG. Cells were harvested by centrifugation, flash frozen, and stored at -80°C until use.

To purify the GST-fusion peptides, cells were thawed on ice. Each cell pellet from one liter of growth was resuspended in 30 ml Buffer NETN (50 mM Tris pH 7.5, 150 mM NaCl, and 0.5% NP40), containing 2 mM DTT and 1 mM PMSF and 1 mg/ml lysozyme. This mixture was tumbled for 30 minutes at 4°C. Cells were sonicated at a 20% duty cycle (30 seconds on, 2 minutes off) for 1.5 minutes of total process time on ice at 4°C. The lysate was centrifuged in a JA 25.5 rotor at 20,000 rpm for 20 minutes and the

supernatant was collected and filtered in a 0.2 µm filter. Glutathione sepharose resin (GE Lifesciences) was prepped by washing with 2 column volumes (CVs) of water and 10 CVs of Buffer NETN. For each liter of cells, 2 ml bed volume of glutathione resin was added. The resin-binding reaction was allowed to proceed for 2 hours at 4°C with tumbling. The resin was washed with 24 CVs of NETN containing 0.2 mM DTT and 24 CVs of 50 mM Tris pH 8.0 containing 0.2 mM DTT. Protein was eluted with 50 mM Tris pH 8.0 containing 0.2 mM DTT and 10 mM glutathione. Elution was monitored by a UV (BioRad) and the elution volume was collected in fractions. Purity was assessed by SDS-PAGE, and fractions containing pure PMP22 were combined. To these purified peptides, we added 10% glycerol, and the flash froze the sample in liquid nitrogen. Samples were stored at -80°C until use. Fusion peptides were added to the PMP22 dialysis conditions at final concentrations of 2.9 µM and 2.7 µM for GST-ECL1 and GST-ECL2, respectively. In this case, the final concentrations for PMP22 and the ECL peptides were the same in each preparation. For control conditions, buffer was added at the same volumetric ratio.

Expression and Purification of KCNQ1-VSD

KCNQ1-voltage sensor domain was purified as previously described (Peng et al., 2014). Briefly, Q1-VSD containing an N-terminal hexahistidine tag was overexpressed in C43(DE3) *E. coli* cells modified by the addition of a pRARE plasmid. Cells were harvested by centrifugation, lysed by tumbling with lysozyme followed by sonication, and the inclusion bodies collected by centrifugation. Q1-VSD was solubilized overnight using DPC and insoluble debris was removed by centrifugation. The supernatant was incubated with Ni(II)-NTA Superflow Resin (Qiagen), and purified into DPC using gravity flow. Q1-VSD was then mixed with mixed micelles containing 4:1 POPC:ESM in 6.1% DPC and dialyzed alongside PMP22.

Electron Microscopy

For negative-stain EM, 2 µL of resuspended PMP22 lipoprotein assemblies were added to 400 mesh copper grids (Electron Microscopy Sciences) that had been glow-discharged at 25 mA for 2 minutes, washed, and stained with 0.7% uranyl formate as previously described (Ohi et al., 2004). These grids were then imaged using an FEI Morgagni equipped with a 1Kx1K CCD camera. Measurements to determine the "interperiod distance" were taken using the associated Advanced Microscopy Techniques (AMT) software. For quantification purposes, images were acquired at 14,000x magnification and were quantified using Nikon Elements software. In the case of cryoelectron microscopy, 3 µL PMP22 lipoprotein assemblies were pipetted directly onto glow-discharged (25 mA for 20 seconds) Quantifoil R2/2 Holey Carbon (200 Mesh Copper) grids (Electron Microscopy Sciences) and plunge-frozen in vitrified ice using a Vitrobot. Grids were plunged within a chamber set to 60% humidity, 22 °C, a blot time of 3.5 seconds, an offset of -1, and a drain time of 1 second. These grids were imaged (Figures 4.3C and 4.3D) using a Tecnai F20 electron microscope (FEI) equipped with a field emission gun at an acceleration voltage of 200 kV under low-dose conditions at a magnification of 68,661x using a defocus value of 2.0-4.0 µm underfocus and recorded on a 4k × 4k Gatan CCD camera or using (Figures 4.3A and 4.3B) a Tecnai F30 Polara electron microscope (FEI) equipped with a field emission gun at an acceleration voltage of 300 kV under low-dose conditions at a magnification of 35654x using a defocus value of 5.0-8.0 µm underfocus and recorded on a 4k × 4k Ultrascan CCD camera (Gatan).

In the case of electron tomography, prior to plunge-freezing, 10 nm colloidal gold partilcles were added as fiduciary markers so that tilted images could be aligned. To add gold particles, 1.5 µL of sample were pipetted directly onto a grid as described above, and 1.5 µL of 10 nm colloidal gold were then pipetted directly onto the same grid prior to

plunge freezing. Tilt series (-65° to +65°) were acquired in two degree increments on the F30 Polara using SerialEM (Mastronarde, 2005) and a 4Kx4K Ultrascan CCD Camera (Gatan) at a magnification of 35654x using a defocus value of 5.0-8.0 µm underfocus. The total electron dose for each tilt-series was approximately 100 $e^-/Å^2$. Tomograms were assembled and segmented using the IMOD software package (Kremer et al., 1996; Mastronarde, 1997).

CHAPTER V

THE HOMOLOGY MODEL OF PMP22 SUGGESTS MOST MUTATIONS RESULTING IN PERIPHERAL NEUROPATHY DISRUPT TRANSMEMBRANE HELIX PACKING[4]

Introduction

Peripheral myelin protein 22 (PMP22) is a member of the claudin/EMP/PMP22 tetraspan membrane protein family and is strongly expressed in the myelinating Schwann cells of the peripheral nervous system (Jetten and Suter, 2000; Li et al., 2013). Among its functions, PMP22 is critical to the formation and maintenance of the myelin ultrastructure (Jetten and Suter, 2000; Amici et al., 2007; Li et al., 2013), including possible roles in the tight junction-like assemblies therein (Notterpek et al., 2001; Guo et al., 2014). A number of genetic aberrations, including more than 40 different missense mutations that encode single-amino acid changes in PMP22 distributed throughout its sequence (Li et al., 2013), result in mild to severe peripheral neuropathy and disability (Figure 5.1).

These peripheral neuropathies include heritable neuropathy with liability to pressure palsies (HNPP, mild neuropathy), Dejerine Sottas syndrome (DSS, severe), and Charcot-Marie-Tooth disease (CMTD, moderate to severe) (Li et al., 2013). It is believed that most disease mutant forms of PMP22 induce misfolding of the protein, leading to loss of function and possible toxicity from accumulated misfolded protein (Naef et al., 1997; Pareek et al., 1997; Naef and Suter, 1999; Colby et al., 2000; Notterpek et al., 2001; Sanders et al., 2001; Liu et al., 2004; Guo et al., 2014).

[4] This section is adopted from the published manuscript by Mittendorf, Kronke, Meiler and Sanders in *Biochemistry*. Mittendorf, K.F., Kroncke, B.M., Meiler, J., and Sanders, C.R. (2014). The Homology Model of PMP22 Suggests Mutations Resulting in Peripheral Neuropathy Disrupt Transmembrane Helix Packing. *Biochemistry 53*, 6139–6141.

Previous work indicates at least some PMP22 disease mutants are considerably destabilized; even wild-type (WT) PMP22 is only marginally stable (Myers et al., 2008; Sakakura et al., 2011; Schlebach et al., 2013), being transported to cell plasma membranes with an efficiency of only ~20% (Pareek et al., 1997). This inherent instability is among the reasons an experimental high-resolution structure of PMP22 has thus far proved elusive.

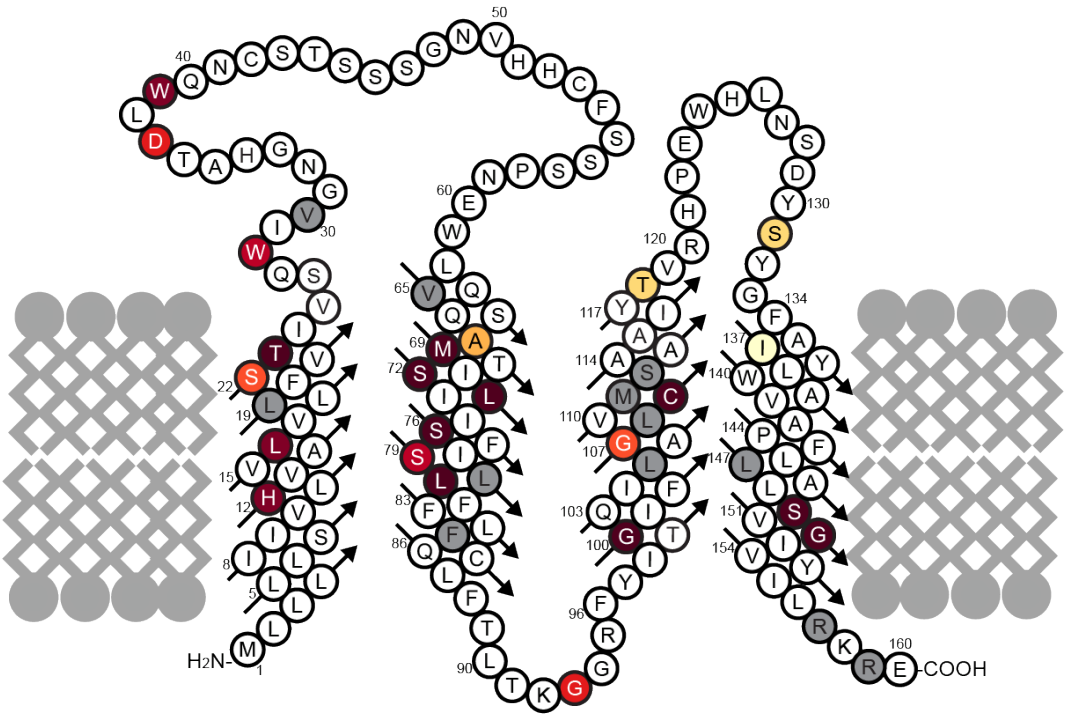

Figure 5.1. Topology diagram of PMP22.
Known missense mutation sites are highlighted in red. Blue outlines represent disease mutations for which conduction velocities known (Figure 3, Table 5.1). The sequential spans of the helices match those of the model developed in this work. The extracellular loops (ECL1 and ECL2) are at the top and the intracellular loop (ICL1) is at the bottom of this figure.

In this study, we utilized the recently published 2.4 Å crystal structure of claudin-15 (Protein Data Bank entry 4P79; Suzuki et al., 2014) the first high-resolution structure of a claudin/EMP/PMP22 family member, as a template for building a homology model of PMP22. The model presented here provides a step toward the goal of discriminating mechanisms of disease-inducing mutations.

Results and Discussion

Briefly, we employed BCL::Align, an alignment program that accounts for sequence identity and similarity as well as secondary structure and transmembrane region predictions (Dong et al., 2008), to generate an alignment of PMP22 (NP_696997.1) with claudin-15 (NP_068365.1). The alignment was truncated to cover only portions of the protein present in the crystal structure (Figure 5.2), and the confidence of this alignment was evaluated (Figure 5.3). In the final alignment, sequences were 25% identical and ~60% similar. Interestingly, TM1 was much more divergent (only 13% identical) than the other transmembrane helices (TM2–TM4 being 36, 50, and 38% identical, respectively). Extracellular loop 1 (ECL1) was relatively well conserved (30% identity), while there was limited conservation in the intracellular loop (ICL, 7%) and ECL2 (14%).

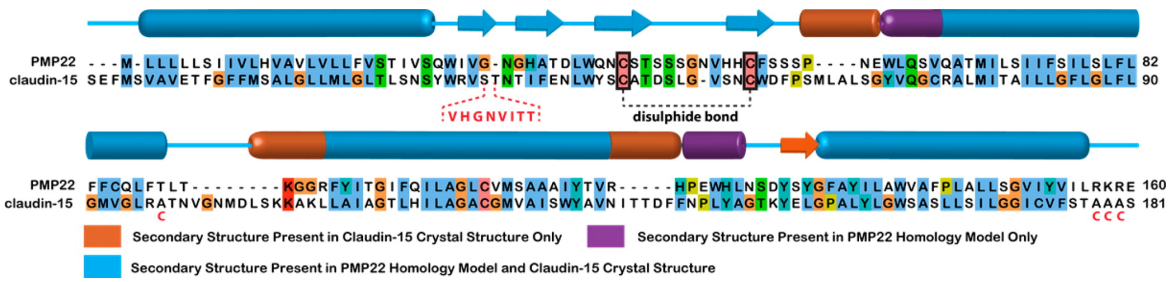

Figure 5.2. Final alignment of human PMP22 with murine claudin-15 utilized for homology modeling, with secondary structure indicated.
Orange secondary structure elements are observed in the claudin-15 crystal structure, but not in the final top-scoring models; purple elements are observed in the final model but not in claudin-15. The sequence in ECL2 that was unresolved in the crystal structure and was removed in the final alignment is colored red within the dashed lines; the claudin-15 disulfide bond is denoted in black, and the C-to-A mutations in the claudin-15 crystal construct are depicted below the sequence in red.

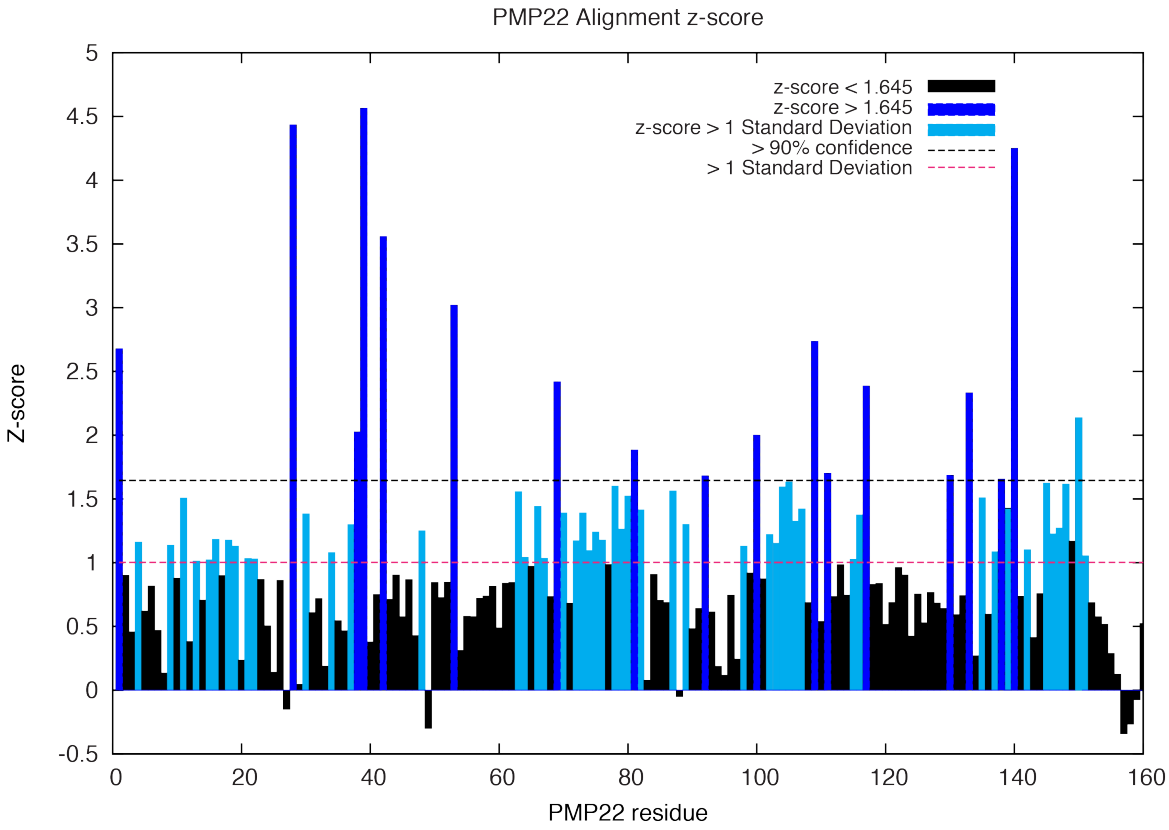

Figure 5.3. Per-residue z-scores generated by BCL::Align, depicting the confidence of the alignment.
Note that residues with z-scores greater than 1.645 (>90% confidence) are spread throughout the sequence. Residues are numbered according to PMP22 residue number.

Using the loop rebuilding utility within Rosetta 3.5, a starting set of homology models of PMP22 was constructed. Knowledge-based potentials included within the calculation utilized secondary structure predictions as well as transmembrane residue lipid-facing propensity (so-called “lipophilicity”) generated within the Rosetta *membrane ab initio* utility (Yarov-Yarovoy et al., 2006; Barth et al., 2007; 2009). These models were scored by Rosetta (Das and Baker, 2008), and the top models were relaxed iteratively (see Figures 5.4-5.6).

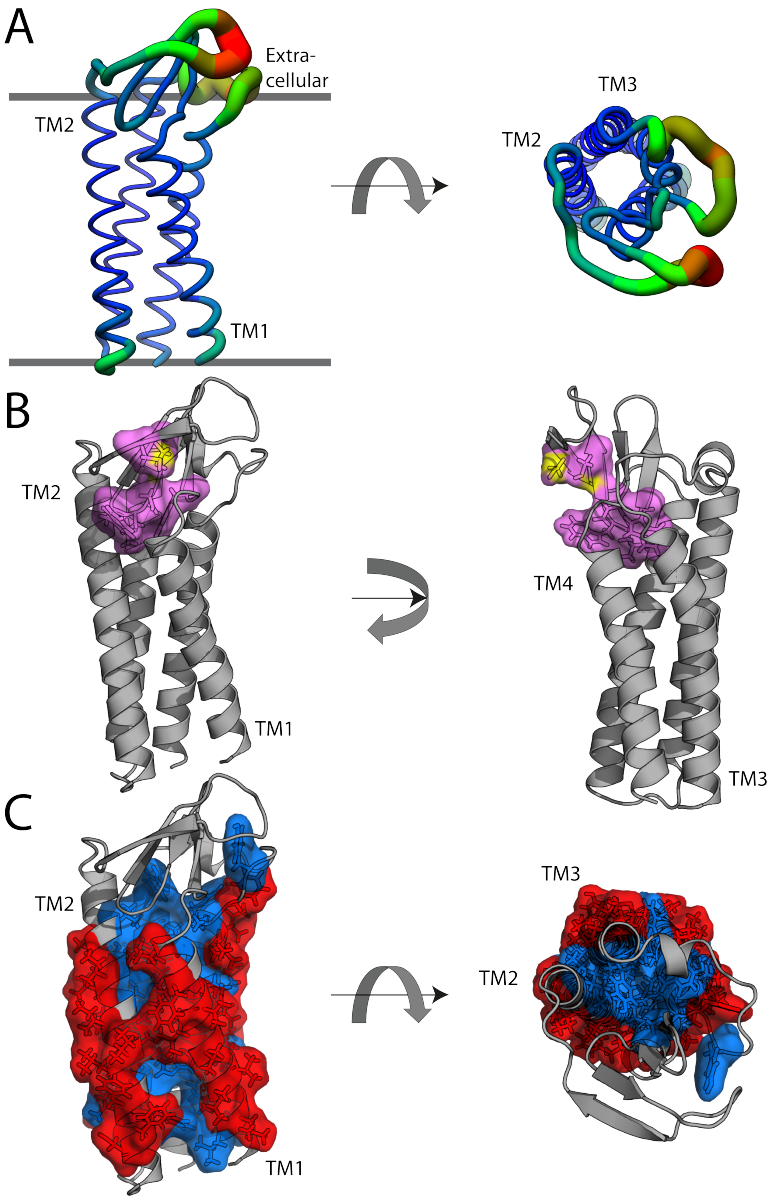

Figure 5.4. PMP22 homology model derived from claudin-15.
(A) Top-scoring PMP22 model color-coded according to the average chain root-mean-square deviation (rmsd) in the top 10 scoring models. The rmsd ranges from 0.6 Å (blue, thin backbone trace) to >10 Å (red, thick backbone trace). (B) Top-scoring model with the claudin motif residues highlighted in cyan as stick and surface view. Sulfur atoms are colored yellow. (C) Top-scoring model showing the most (red) and least (blue) "lipophilic" sites as determined by the LIPS algorithm.(Adamian and Liang, 2006) The extracellular face of the protein is at the top in the left panels. PDB coordinates of this file are available in the Supporting Information of the original manuscript online (Mittendorf et al., 2014).

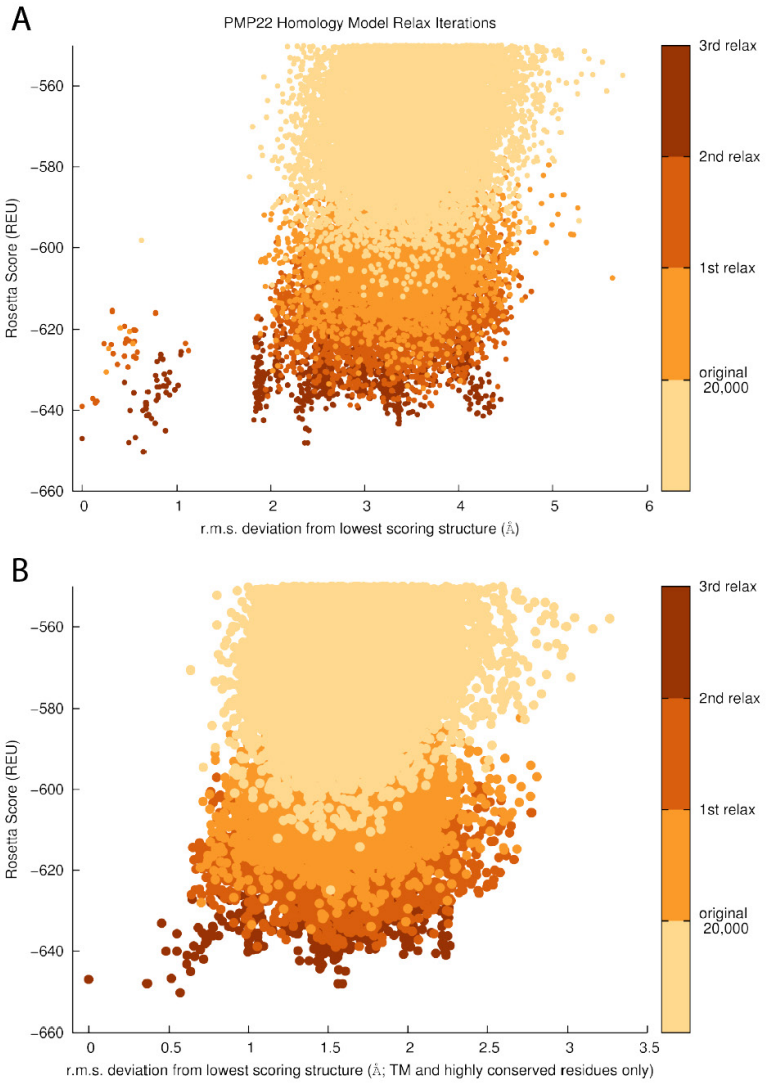

Figure 5.5. Rosetta energy score vs. RMSD from cluster center of final top 10 scoring PMP22 homology models for each iteration (see color key at right).
(A) RMSD calculated using C_α positions from all residues in the PMP22 models. (B) RMSD calculated using C_α positions from all TM and highly conserved residues only in the PMP22 models.

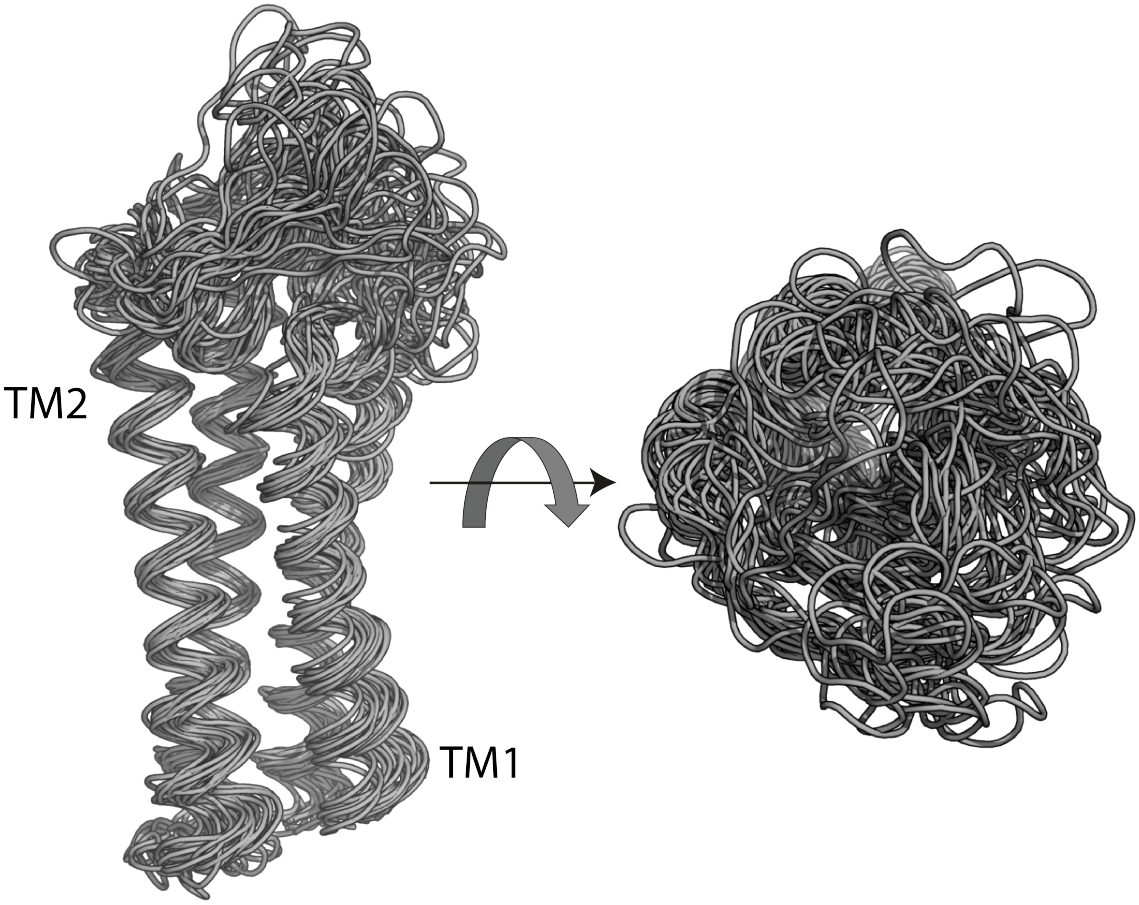

Figure 5.6. Overlay of the top scoring wild type PMP22 family member from each of 25 end-branch families with >20 members.

The top-scoring PMP22 model was evaluated with MolProbity (Chen et al., 2010). After energy minimization, only the first four of five extracellular β-strands present in the claudin-15 template were retained (Figure 5.4A); these strands are all in ECL1. On the basis of the root-mean-square deviation (rmsd) from the top 10 models (Figure 5.4A), Rosetta most confidently predicts the TM1–TM4 region with slight uncertainty at the TM1 N-terminus. The predictions for ECL1 appear to be relatively uniform within the β-strands but have very weak convergence in the loop of the first β-hairpin.

Additionally, there is conformational heterogeneity among high scoring models present in both ECL2 and the ICL. It is observed that a portion (W-DLW) of the conserved claudin motif (W-[N/G/D]LW-C-C)(Krause et al., 2008) dips back into the membrane to stabilize the helical packing on the extracellular side of the helical bundle (Figure 5.4B). While claudins have an extracellular disulfide bond, it is unclear whether a bond forms between the corresponding Cys pair in PMP22. This bond was therefore not enforced in the generation of this model (3.6 Å between sulfur atoms). Repeating model generation with a forced disulfide bond did not require gross alterations in the structure (overall rmsd to the reduced-form structure of 1.96 Å), suggesting that this model may be accurate in either case (Figure 5.7). We also note that the computed “lipophilicity” (Adamian et al., 2011) predicts transmembrane helix–helix contacting faces that are fully consistent with what is seen in the model (Figure 5.4C).

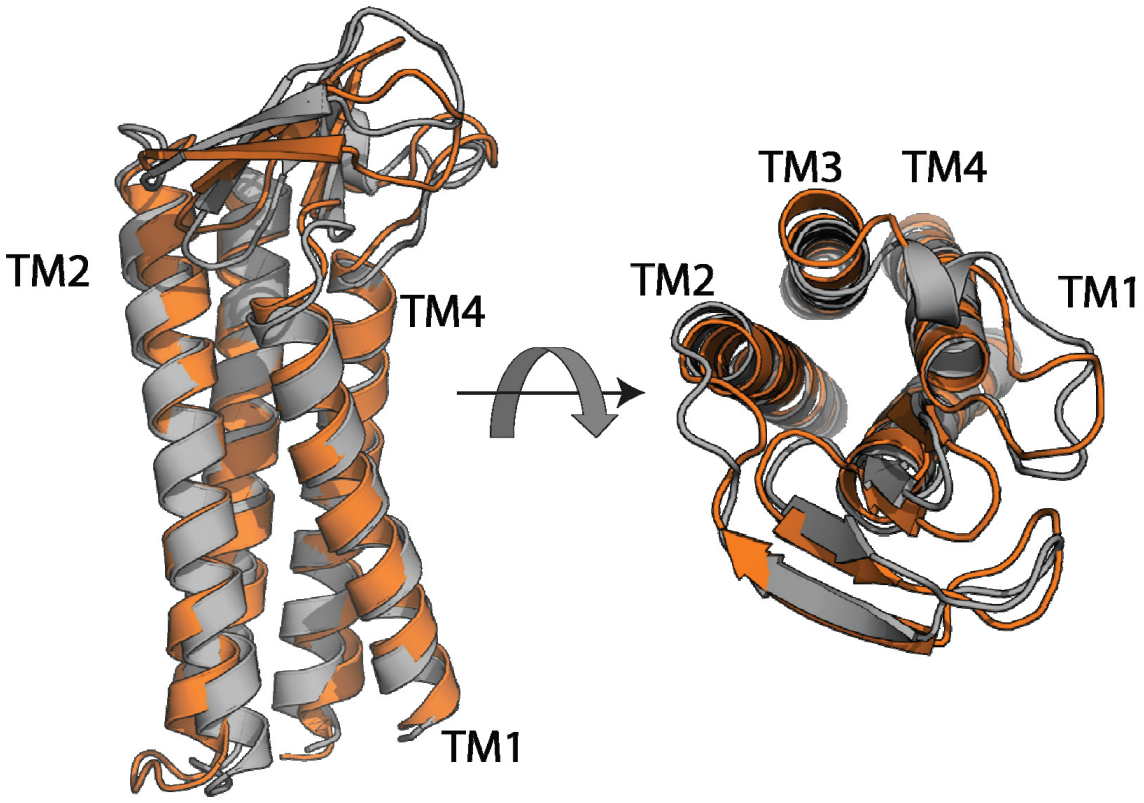

Figure 5.7. Overlay of Final WT homology model and the nearest top-scoring model containing a forced disulfide bond.
Final WT PMP22 homology model (grey) aligned to the nearest model (orange) from the top-scoring model containing a forced disulfide bond (see Methods section), demonstrating the minimal changes (in the SS- free model) necessary to accommodate a disulfide bond (overall RMSD 1.955 Å). This suggests that our models are essentially the same whether or not a disulfide bond is present in PMP22 (a question that has not been addressed experimentally for native PMP22).

Previous studies indicate that even WT PMP22 is only marginally stable (Myers et al., 2008; Sakakura et al., 2011; Schlebach et al., 2013), and nuclear magnetic resonance (NMR) studies indicate that under micellar conditions at 45 °C WT PMP22 occupies a folding intermediate in which TM1 dissociates from the rest of the transmembrane domain, with TM2–TM4 forming a molten globule-like bundle (Sakakura et al., 2011). The TrJ disease mutant (L16P in TM1) increases the propensity of this helix to dissociate. Interestingly, Rosetta found the initial conformation of TM1 in the WT protein to be unfavorable; consequently, the loop rebuilding and side chain repacking algorithms readjusted the position of the packing of the bundle in nearly every case. In our final WT model, TM1 of PMP22 is packed much less tightly to TM2–TM4 than the corresponding helices of claudin-15 (Figure 5.8). Additionally, the L16 residue, along with several other disease mutation sites, appears to be involved in TM1 packing with the helical bundle (Figure 5.9A and 5.10).

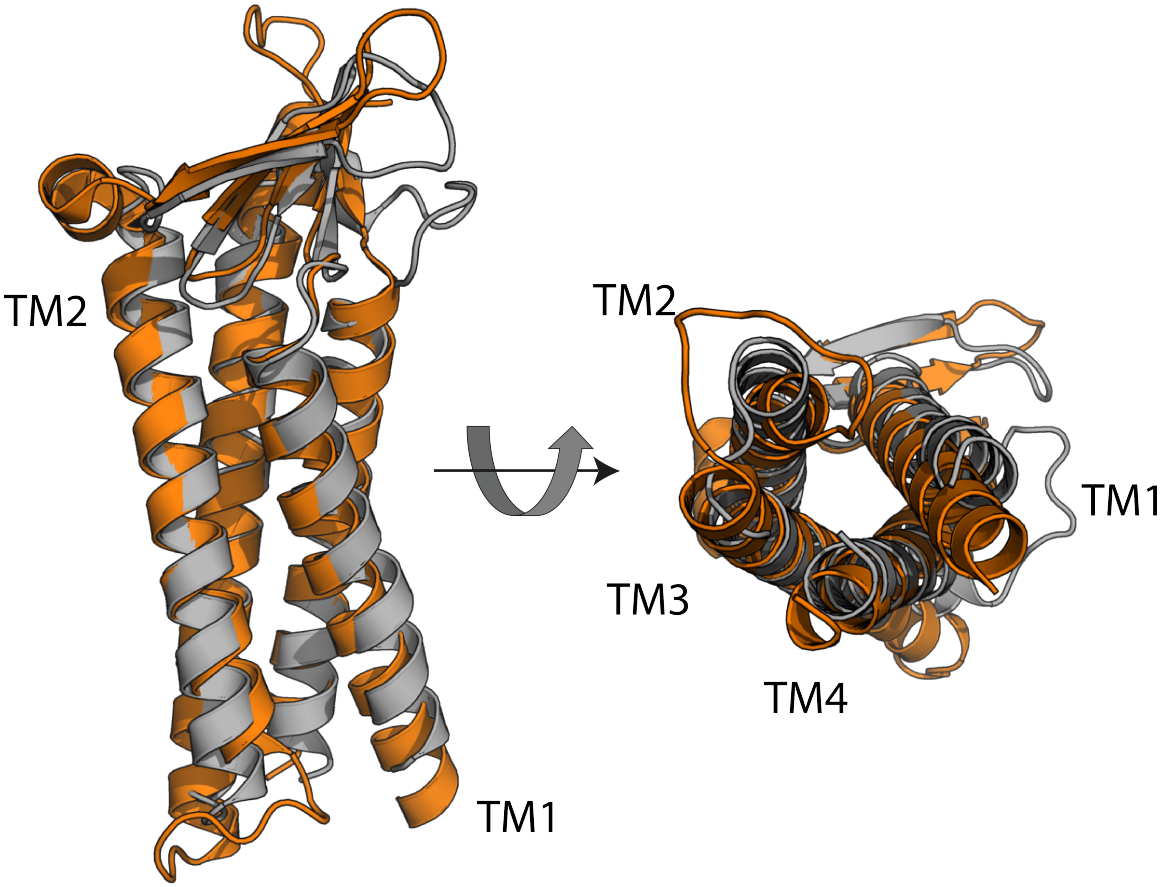

Figure 5.8. The TM helices of WT PMP22 are less tightly packed than the helices of claudin-15.
Final WT PMP22 homology model (grey) aligned to the crystal structure of murine claudin-15 (orange), demonstrating the slight outward rotation of TM1 and slight repacking of the TM interfaces that is seen in the final top scoring PMP22 models.

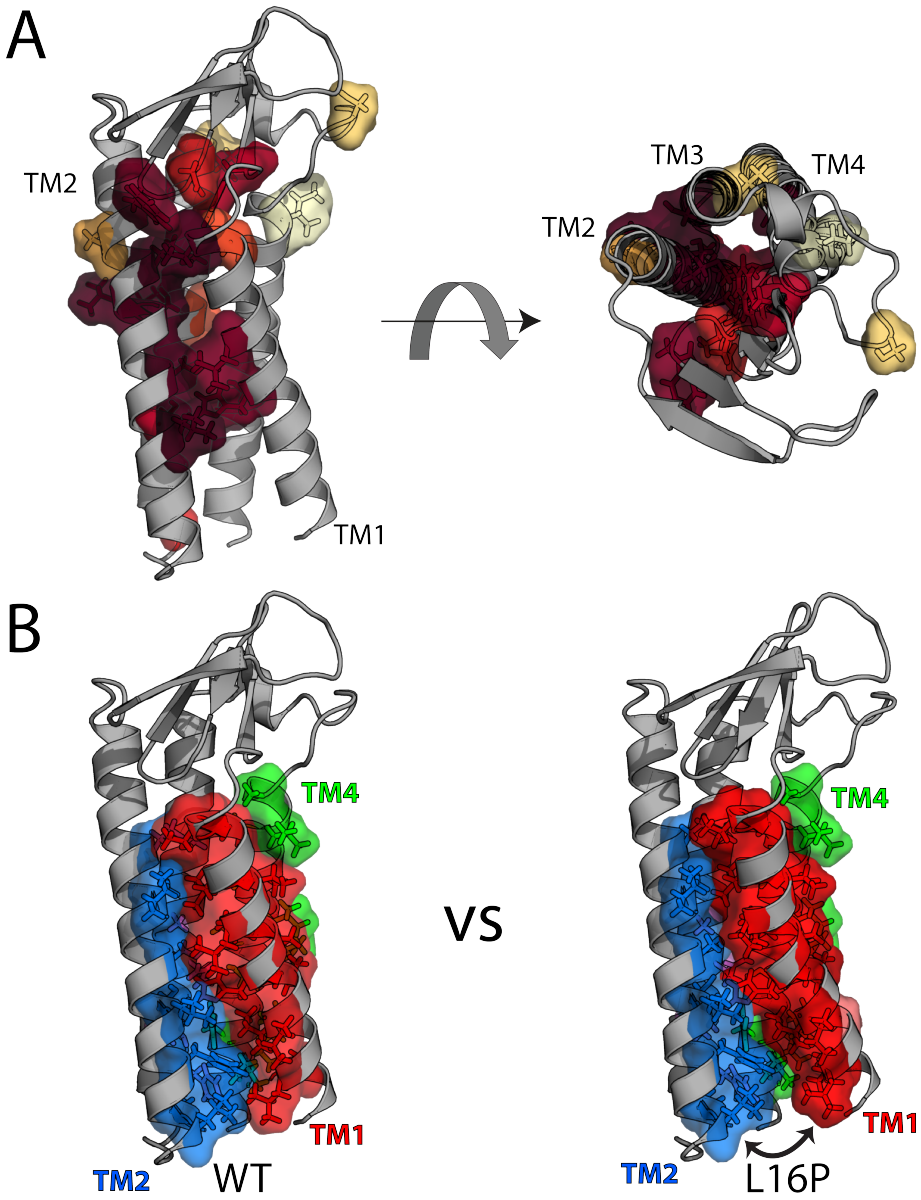

Figure 5.9. Assessment of disease mutation locations in the PMP22 model.
(A) PMP22 homology model with color coding of wild-type residues mutated in neuropathies according to patient motor nerve conduction velocities (NCVs), with maroon having the lowest NCVs and cream representing a benign polymorphism (see Table 5.1). Note that for a number of known disease mutations, patient nerve conduction velocities have not been reported, such that the associated sites are not highlighted in this figure. Note also that the lone site of a severe mutation facing the lipid environment is a proline substitution (L71P) in the middle of a TM2, which is expected also to disrupt helical packing. (B) Comparison of the packing interface between the WT model and the top two L16P models, showing a reduced interface for L16P between TM1 and the rest of the bundle: red for TM1, marine for TM2, violet for TM3, green for TM4, and salmon for the additional contacting residue on L16P TM1.

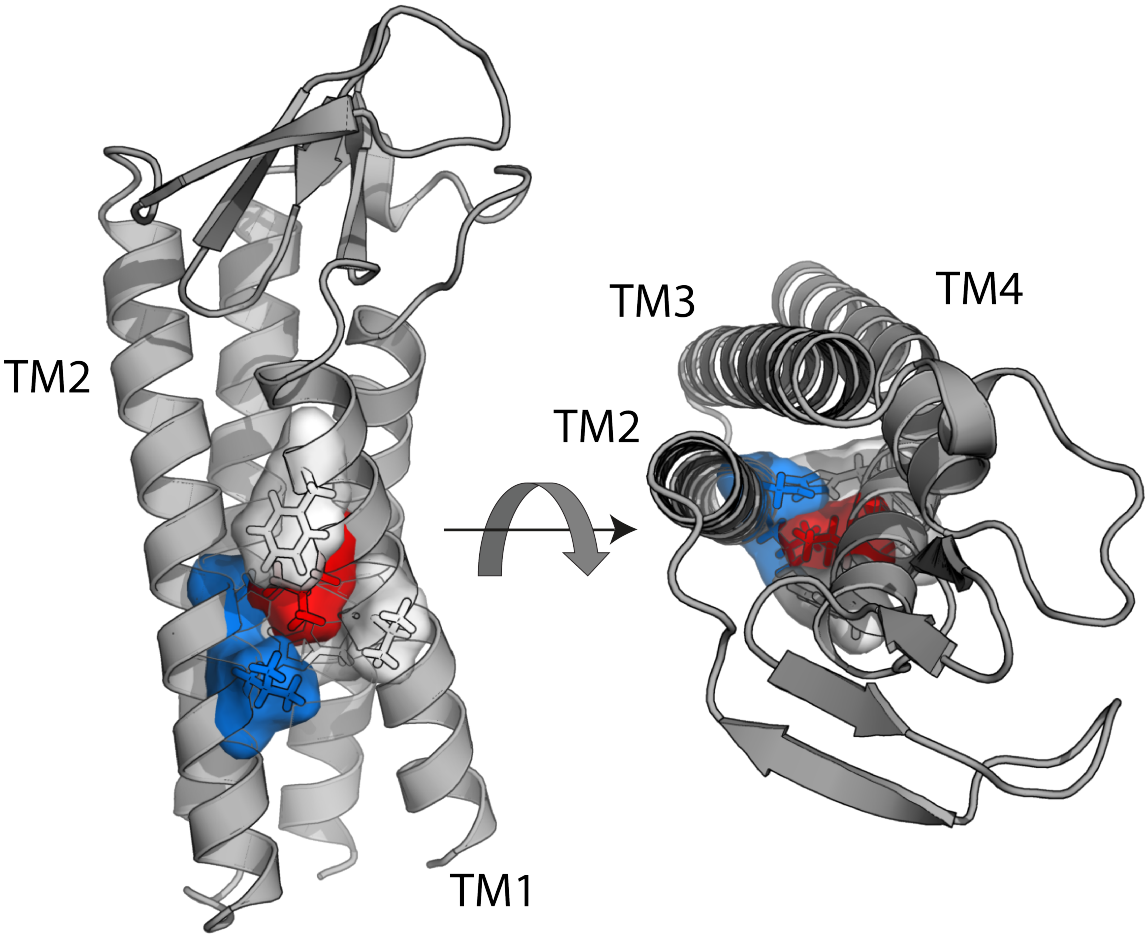

Figure 5.10. The WT PMP22 homology model indicates that L16 is essential for packing interactions of TM1 with TM2.
L16 is displayed as sticks/surface and is colored red. The TM2 and TM1 residues in contact are displayed as sticks/surface and colored blue and white, respectively.

A number of the most severe disease mutations (associated with patients presenting nerve conduction velocities of <10 m/s), including L16P, are at residues located along the helix-packing interface between TM1 and TM2/TM4, while less severe mutation sites tend to either face the lipid or “cap” the helices (Figure 5.9A and Table 5.1). Modeling of the L16P mutation with Rosetta generates structures with a significantly higher Rosetta energy ($p < 0.0001$). These models conform to the predictions made by the NMR data; the size of the TM1 interface with TM2–TM4 is reduced, with predicted structures sharing an interface with either the N- or C-terminal side of L16P TM1, but not both (Figure 5.9B and Figure 5.11).

Table 5.1 (3 pages). Patient motor nerve conduction velocities and literature references for each mutation depicted in Figure 5.9.

PMP22 Mutation	Phenotype	Average Reported Motor Nerve Conduction Velocity (m/s)	Reference
H12Q	DSS	7	Déjérine-Sottas neuropathy is associated with a de novo PMP22 mutation.Valentijn LJ, Ouvrier RA, van den Bosch NH, Bolhuis PA, Baas F, Nicholson GA. *Hum Mutat.* (1995) 5:76-80.
L16P	CMT1	10	Identical point mutations of PMP-22 in Trembler-J mouse and Charcot-Marie-Tooth disease type 1A. Valentijn LJ, Baas F, Wolterman RA, Hoogendijk JE, van den Bosch NH, Zorn I, Gabreëls-Festen AW, de Visser M, Bolhuis PA. *Nat Genet.* (1992) 2:288-91 Allelic heterogeneity in hereditary motor and sensory neuropathy type Ia (Charcot-Marie-Tooth disease type 1a).Hoogendijk JE, Janssen EA, Gabreëls-Festen AA, Hensels GW, Joosten EM, Gabreëls FJ, Zorn I, Valentijn LJ, Baas F, Ongerboer de Visser BW, et al. *Neurology.* (1993) 43:1010-5.
S22F	HNPP/CMT1	25	A novel PMP22 mutation Ser22Phe in a family with hereditary neuropathy with liability to pressure palsies and CMT1A phenotypes. Kleopa KA1, Georgiou DM, Nicolaou P, Koutsou P, Papathanasiou E, Kyriakides T, Christodoulou K. *Neurogenetics.* (2004) 5:171-5. Variable phenotypes are associated with PMP22 missense mutations. Russo M, Laurá M, Polke JM, Davis MB, Blake J, Brandner S, Hughes RA, Houlden H, Bennett DL, Lunn MP, Reilly MM. *Neuromuscul Disord.* (2011) 21:106-14.
T23R	CMT1 and deafness	0	Variable phenotypes are associated with PMP22 missense mutations. Russo M, Laurá M, Polke JM, Davis MB, Blake J, Brandner S, Hughes RA, Houlden H, Bennett DL, Lunn MP, Reilly MM. *Neuromuscul Disord.* (2011) 21:106-14.
W28R	Severe CMT1 and deafness	13.7	Charcot-Marie-Tooth disease and related neuropathies: mutation distribution and genotype-phenotype correlation. Boerkoel CF, Takashima H, Garcia CA, Olney RK, Johnson J, Berry K, Russo P, Kennedy S, Teebi AS, Scavina M, Williams LL, Mancias P, Butler IJ, Krajewski K, Shy M, Lupski JR. *Ann Neurol.* (2002) 51:190-201.
D37V	Atypical CMT1	16.6	Myelin uncompaction in Charcot-Marie-Tooth neuropathy type 1A with a point mutation of peripheral myelin protein-22. Fabrizi GM, Cavallaro T, Taioli F, Orrico D, Morbin M, Simonati A, Rizzuto N. Neurology. (1999) 53:846-51.
W39C	CMT1	8.7	Parental mosaicism of a novel PMP22 mutation with a minimal neuropathic phenotype.Taioli F, Bertolasi L, Ajena D, Ferrarini M, Cabrini I, Crestanello A, Fabrizi GM. *J Peripher Nerv Syst.* (2012) 17:414-7.
A67T*	HNPP	39.9	HNPP due to a novel missense mutation of the PMP22 gene.Nodera H, Nishimura M, Logigian EL, Herrmann DN, Kaji R. *Neurology.* (2003) 60:1863-4.
A67P*	CMT1 and deafness	24	A unique point mutation in the PMP22 gene is associated with Charcot-Marie-Tooth disease and deafness. Kovach MJ, Lin JP, Boyadjiev S, Campbell K, Mazzeo L, Herman K, Rimer LA, Frank W, Llewellyn B, Jabs EW, Gelber D, Kimonis VE. *Am J Hum Genet.* (1999) 64:1580-93.
M69R	CMT1	<1	Variable phenotypes are associated with PMP22 missense mutations. Russo M, Laurá M, Polke JM, Davis MB, Blake J, Brandner S, Hughes RA, Houlden H, Bennett DL, Lunn MP, Reilly MM. *Neuromuscul Disord.* (2011) 21:106-14.
M69K	DSS	3.3	Dejerine-Sottas syndrome associated with point mutation in the peripheral myelin protein 22 (PMP22) gene. Roa BB, Dyck PJ, Marks HG, Chance PF, Lupski JR. *Nat Genet.* (1993) 5:269-73.
L71P	CMT1/DSS + vestibular hearing loss	2-3	Charcot-Marie-Tooth disease and related neuropathies: mutation distribution and genotype-phenotype correlation. Boerkoel CF, Takashima H, Garcia CA, Olney RK, Johnson J, Berry K, Russo P, Kennedy S, Teebi AS, Scavina M, Williams LL, Mancias P, Butler IJ, Krajewski K, Shy M, Lupski JR. *Ann Neurol.* (2002) 51:190-201.
S72L	CMT1/DSS (+deafness)	4.3	Dejerine-Sottas neuropathy and PMP22 point mutations: a new base pair substitution and a possible "hot spot" on Ser72. Marques W Jr, Thomas PK, Sweeney MG, Carr L, Wood NW. Ann Neurol. (1998) 43:680-3.

			Dejerine-Sottas syndrome associated with point mutation in the peripheral myelin protein 22 (PMP22) gene. Roa BB, Dyck PJ, Marks HG, Chance PF, Lupski JR. *Nat Genet.* (1993) 5:269-73. Congenital hypomyelination neuropathy with Ser72Leu substitution in PMP22. Simonati A, Fabrizi GM, Pasquinelli A, Taioli F, Cavallaro T, Morbin M, Marcon G, Papini M, Rizzuto N. *Neuromuscul Disord.* (1999) 9:257-61. Infantile demyelinating neuropathy associated with a de novo point mutation on Ser72 in PMP22 and basal lamina onion bulbs in skin biopsy. Ceuterick-de Groote C, De Jonghe P, Timmerman V, Van Goethem G, Löfgren A, Ceulemans B, Van Broeckhoven C, Martin JJ. *Pathol Res Pract.* (2001) 197:193-8. Charcot-Marie-Tooth disease and related neuropathies: mutation distribution and genotype-phenotype correlation. Boerkoel CF, Takashima H, Garcia CA, Olney RK, Johnson J, Berry K, Russo P, Kennedy S, Teebi AS, Scavina M, Williams LL, Mancias P, Butler IJ, Krajewski K, Shy M, Lupski JR. *Ann Neurol.* (2002) 51:190-201. The range of chronic demyelinating neuropathy of infancy: a clinico-pathological and genetic study of 15 unrelated cases. Planté-Bordeneuve V, Parman Y, Guiochon-Mantel A, Alj Y, Deymeer F, Serdaroglu P, Eraksoy M, Said G. *J Neurol*. (2001) 248:795-803. Dejerine-Sottas' neuropathy caused by the missense mutation PMP22 Ser72Leu. Marques W Jr, Neto JM, Barreira AA. *Acta Neurol Scand.* (2004) 110:196-9. Dejerine-Sottas disease with de novo dominant point mutation of the PMP22 gene. Ionasescu VV, Ionasescu R, Searby C, Neahring R. *Neurology.* (1995) 45:1766-7. Dejerine-Sottas disease with sensorineural hearing loss, nystagmus, and peripheral facial nerve weakness: de novo dominant point mutation of the PMP22 gene. Ionasescu VV, Searby C, Greenberg SA. *J Med Genet.* (1996) 33:1048-9.
S72W	DSS	0	Hereditary demyelinating neuropathy of infancy. A genetically complex syndrome. Tyson J, Ellis D, Fairbrother U, King RH, Muntoni F, Jacobs J, Malcolm S, Harding AE, Thomas PK. Brain. (1997) 120 (Pt 1):47-63.
S76I	DSS+deafness	3	Variable phenotypes are associated with PMP22 missense mutations. Russo M, Laurá M, Polke JM, Davis MB, Blake J, Brandner S, Hughes RA, Houlden H, Bennett DL, Lunn MP, Reilly MM. *Neuromuscul Disord.* (2011) 21:106-14. Hereditary demyelinating neuropathy of infancy. A genetically complex syndrome. Tyson J, Ellis D, Fairbrother U, King RH, Muntoni F, Jacobs J, Malcolm S, Harding AE, Thomas PK. *Brain.* (1997) 120 (Pt 1):47-63.
S79C	CMT1	13.9	Charcot-Marie-Tooth disease type 1A. Association with a spontaneous point mutation in the PMP22 gene. Roa BB, Garcia CA, Suter U, Kulpa DA, Wise CA, Mueller J, Welcher AA, Snipes GJ, Shooter EM, Patel PI, Lupski JR. *N Engl J Med.* (1993) 329:96-101.
L80p	DSS	0	Hereditary demyelinating neuropathy of infancy. A genetically complex syndrome.Tyson J, Ellis D, Fairbrother U, King RH, Muntoni F, Jacobs J, Malcolm S, Harding AE, Thomas PK. *Brain.* (1997) 120 (Pt 1):47-63.
G93R	CMT1	17	HNPP due to a novel missense mutation of the PMP22 gene. Nodera H, Nishimura M, Logigian EL, Herrmann DN, Kaji R. *Neurology.* (2003) 60:1863-4.
G100E	DSS	<1	Variable phenotypes are associated with PMP22 missense mutations.Russo M, Laurá M, Polke JM, Davis MB, Blake J, Brandner S, Hughes RA, Houlden H, Bennett DL, Lunn MP, Reilly MM. *Neuromuscul Disord.* (2011) 21:106-14.
G107V	CMT1	22.7	A novel point mutation in the peripheral myelin protein 22 (PMP22) gene associated with Charcot-Marie-Tooth disease type 1A. Marrosu MG, Vaccargiu S, Marrosu G, Vannelli A, Cianchetti C, Muntoni F. *Neurology.* (1997) 48:489-93.

C109R	DSS	3.6	PMP22 related congenital hypomyelination neuropathy. Fabrizi GM, Simonati A, Taioli F, Cavallaro T, Ferrarini M, Rigatelli F, Pini A, Mostacciuolo ML, Rizzuto N. *J Neurol Neurosurg Psychiatry.* (2001) 70:123-6.
T118M	HNPP	37.9	Variable phenotypes are associated with PMP22 missense mutations. Russo M, Laurá M, Polke JM, Davis MB, Blake J, Brandner S, Hughes RA, Houlden H, Bennett DL, Lunn MP, Reilly MM. *Neuromuscul Disord.* (2011) 21:106-14. Evidence for a recessive PMP22 point mutation in Charcot-Marie-Tooth disease type 1A. Roa BB, Garcia CA, Pentao L, Killian JM, Trask BJ, Suter U, Snipes GJ, Ortiz-Lopez R, Shooter EM, Patel PI, Lupski JR. *Nat Genet.* (1993) 5:189-94.
S131C	HNPP/CMT1	37.3	Variable phenotypes are associated with PMP22 missense mutations. Russo M, Laurá M, Polke JM, Davis MB, Blake J, Brandner S, Hughes RA, Houlden H, Bennett DL, Lunn MP, Reilly MM. *Neuromuscul Disord.* (2011) 21:106-14.
I137V	Healthy poly-morphism	*Assumed 50+	Mutational analysis of the MPZ, PMP22 and Cx32 genes in patients of Spanish ancestry with Charcot-Marie-Tooth disease and hereditary neuropathy with liability to pressure palsies. Bort S, Nelis E, Timmerman V, Sevilla T, Cruz-Martínez A, Martínez F, Millán JM, Arpa J, Vílchez JJ, Prieto F, Van Broeckhoven C, Palau F. *Hum Genet.* 1997 99:746-54.
S149R	DSS	0	Dejerine-sottas disease with a novel de novo dominant mutation, Ser 149 Arg, of the peripheral myelin protein 22. Ohnishi A, Yamamoto T, Izawa K, Yamamori S, Takahashi K, Mega H, Jinnai K. *Acta Neuropathol.* (2000) 99:327-30.
G150D	DSS	<5	Dejerine-Sottas neuropathy in mother and son with same point mutation of PMP22 gene. Ionasescu VV, Searby CC, Ionasescu R, Chatkupt S, Patel N, Koenigsberger R. *Muscle Nerve.* (1997) 20:97-9.

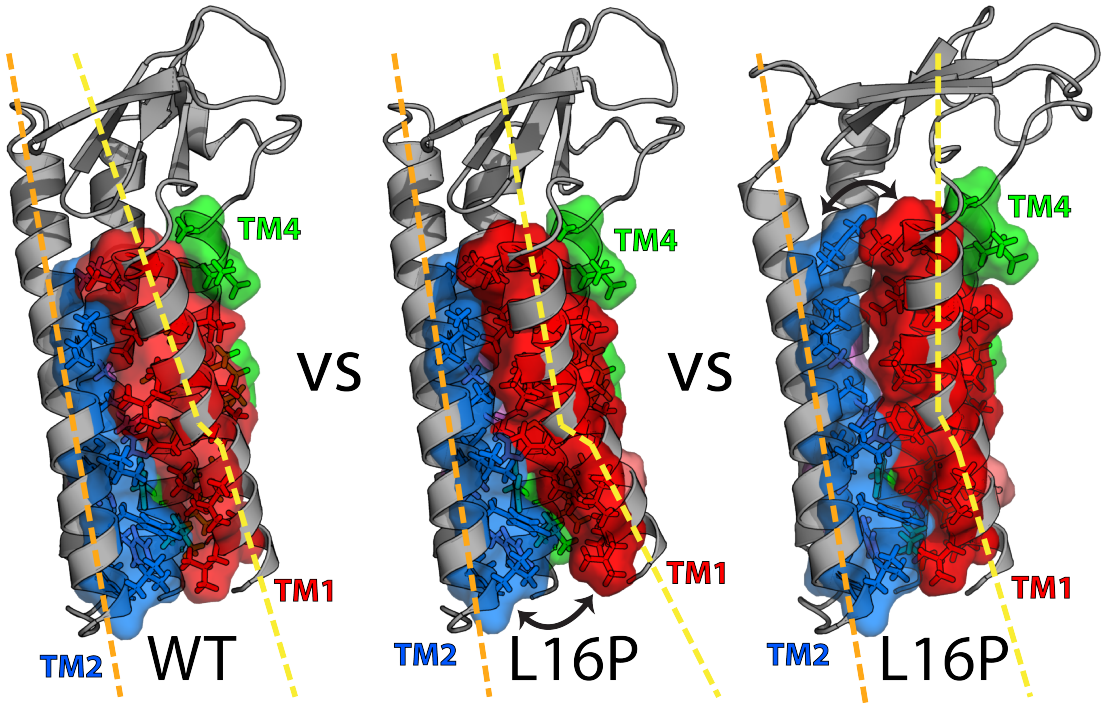

Figure 5.11. L16P mutation causes a reduced interface between TM1 and the rest of the helical bundle and a kink in the helix, consistent with reported experimental results.
The WT model (left) shows a relatively straight TM1 that forms an interface with all TM helices. Two representative L16P models from the lowest scoring clusters (middle, lowest scoring model overall; right) demonstrate the kink in the helix (see line) and the reduced helical interface. Contacting residues of WT are colored red = TM1, marine = TM2, violet = TM3, and green = TM4 on all structures. Additional residues from TM1 on L16P making contacts are colored salmon.

This study provides the first high-resolution working model for PMP22 and will be used as a springboard for future work through its potential predictive power. Future studies will focus on verifying which disease mutations are indeed destabilizing as well as providing experimental restraints for refinement of this computational model. Additionally, molecular dynamics simulations of WT and mutant PMP22 in membranes of different compositions may shed light on whether the unique lipid composition of the Schwann cell plasma membrane may contribute to PMP22 stability (See Figure 5.12), with a focus on the behavior and interactions of disease-linked residues between TM1 and the rest of the helical bundle.

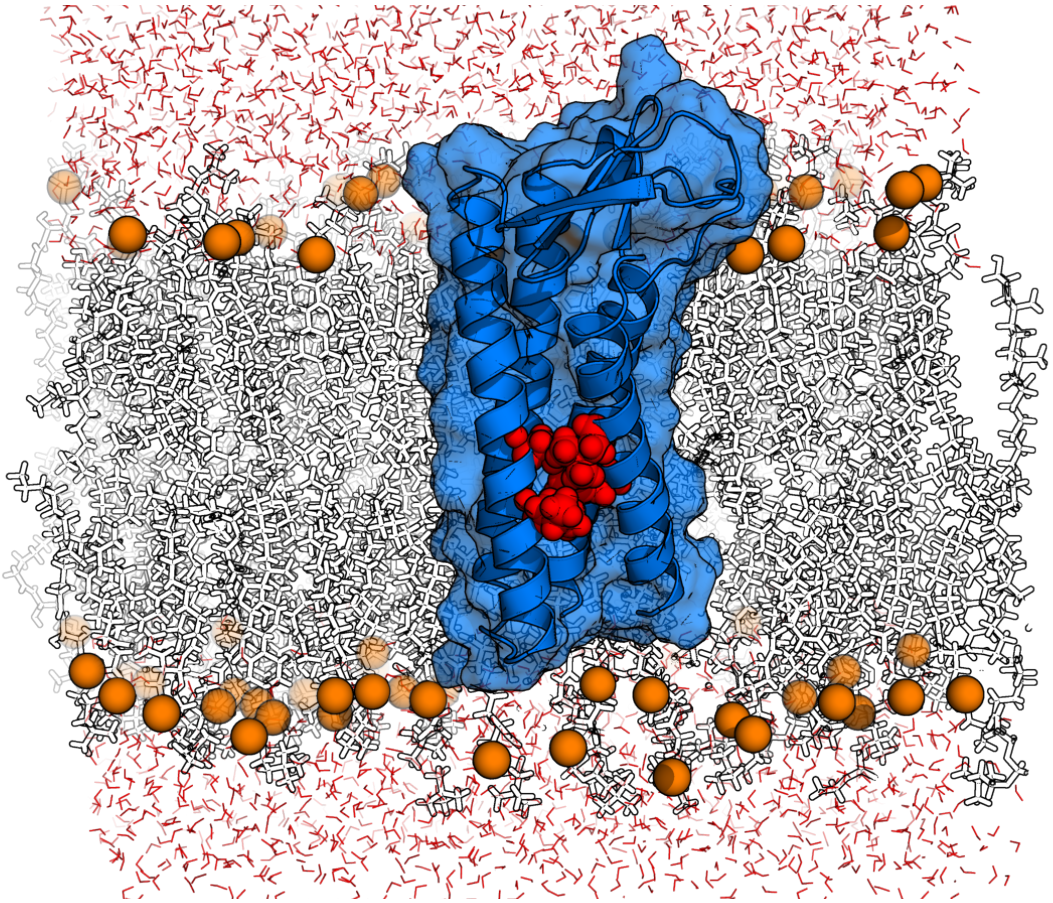

Figure 5.12. Model of PMP22 inserted into a CHARMM membrane containing sphingomyelin and cholesterol components.
Water molecules are represented as red lines, lipids are represented as white sticks, with phosphate groups highlighted as orange balls. The PMP22 model is depicted in blue as a cartoon with a transparent surface, with disease-associated residues responsible for TM1-helical bundle contacts depicted as solid red spheres. Note that the loops of PMP22 dip significantly back into this membrane.

Methods

Alignment

In this study, we used BCL::Align to generate an alignment of PMP22 (NP_696997.1) and the full sequence of murine claudin-15 (NP_068365.1). Following a previously published protocol, we weighted the PAM250 mutation matrix (Barker et al., 1978), PSIBLAST sequence profiles (Altschul et al., 1997), PSIPRED secondary structure prediction (Jones, 1999), JUFO secondary structure prediction (Meiler and Baker, 2003), and TMHMM transmembrane prediction (Kahsay et al., 2005) at 0.25, 0.25, 0.15, 0.15, and 0.30, respectively. The gap opening and gap extension penalties were set to -3.0 and -0.3, respectively. The resulting alignment was trimmed to remove the cytosolic C-terminus of claudin-15 and the stretch of extracellular loop 1 (ECL1) residues (VHGNVITT) that was unresolved in the crystal structure (see Figure 5.2). The sequence of claudin-15 was also altered to include the cysteine-to-alanine mutations in the crystallized construct of claudin-15. The PMP22 TM regions and conserved "claudin motif" (W-[N/G/D]LW-C-C) in ECL1 aligned as expected with claudin-15 in light of the structure. To further verify the accuracy of the alignment generated by BCL::Align, the final alignment was compared to the results of HHPred, another alignment program that has proven successful for the alignment of membrane proteins (Söding, 2005; Söding et al., 2005; Remmert et al., 2012), which predicts the exact same alignment for the TM regions, lending greater confidence to our initial model. The BCL::Align alignment guided the population of atoms into an initial PMP22 structure drawn from the claudin-15 coordinates using an in-house script (Jens Meiler, unpublished).

Loop rebuilding

Following building of the initial model, the following PMP22 residues were completely rebuilt using the loopmodel utility within Rosetta 3.5: 23-28, 30-33, 36-41, 44-

51, 55-62, 86-93, and 119-134. These residues represent all elements not containing secondary structure as well as one flanking residue on each side of each secondary structure element. Fragment files were generated using the Rosetta server (Kim et al., 2004). The loop building took place in two stages: (1) a low resolution "centroid" method that closes the loop and performs an initial relaxation (we used the default score4L centroid score function for soluble proteins at this stage since all loop-rebuilt residues reside in the soluble segment of PMP22 and since the soluble score function has been much more extensively benchmarked compared to the membrane-specific score function) (Wang et al., 2007), and (2) an all-atom refinement that allows side-chain and backbone conformational sampling of all loop residues, employing a membrane protein-specific scoring function; the score function used at this stage has been benchmarked with several membrane proteins and has recently performed well in discriminating native-like GPCR homology models (Nguyen et al., 2013). The resulting conformation is then subjected to an energy minimization protocol that allows side-chain and backbone conformational sampling across the entire protein and is scored with a membrane protein-specific score function.

Relaxation, clustering, and evaluation of models

The lowest scoring 1000 models, as evaluated by the full atom membrane protein-specific scoring function of Rosetta 3.5, were subjected to an additional round of relaxation—an energy minimization through iterative side-chain repacking and gradient-based minimization with a ramping repulsive potential ten times—each model producing 5 new structures for a total of 5000 new models. Of these 6000 total models, the top 1000 models were further relaxed, generating another 5000 new models. The final top-scoring 1000 models of all rounds were then clustered into structurally similar families using BCL::Cluster (Alexander et al., 2011). The top scoring models from the largest

clusters (>20 members and having no further branchpoints) were chosen as the representative models; 26 in total. These top models were mutated to L16P, using the fixbb application within Rosetta, or left as wild type and further relaxed, generating 1000+ new models (40+ new models per starting model) for each variant. The best scoring 10 models for each variant were selected to generate the p-value. To calculate RMSD, all structures were compared to the most average/center model out of the 10 best scoring WT models. To generate Figure 5.4A and Figure 5.6, the final top-scoring 1000 models for WT were clustered into families as described above. These structures were aligned in Chimera (Figure 5.4A) or Pymol (Figure 5.6) and the RMSD to the top-scoring structure was calculated in UCSF Chimera (Figure 5.4A). The top-scoring structure represented in these clusters was utilized in all remaining figures of WT-PMP22 and is the structure described by the PDB file (for both wild type and the L16P mutant).

The top-scoring WT model was subjected to MolProbity analysis, which reported 152/160 (96.20%) residues were in favored regions of the Ramachandran plot, and 160/160 (100%) residues occupied allowed regions. Molprobity also reported a clashscore of 2.35 (99th percentile), 1 poor rotamer (0.71%), no Cβ deviations, 0/1300 bad backbone bonds, and 4/1775 (0.23%) bad backbone angles. The MolProbity score was 1.27 (99th percentile). Subsequent analysis presented in this paper, including the generation of all figures from a single model, was performed using this model. The pdb coordinates for this model are available for download as a part of the supporting information of this manuscript.

Similarly, the top-scoring L16P model was subjected to MolProbity analysis, which reported 152/160 (96.20%) residues were in favored regions of the Ramachandran plot, and 160/160 (100%) residues occupied allowed regions. Molprobity reported a clashscore of 3.92 (96th percentile), 1 poor rotamer (0.71%), no Cβ

deviations, 0/1300 bad backbone bonds, and 4/1775 (0.23%) bad backbone angles. The MolProbity score was 1.44 (96th percentile). This model was then used as the basis for subsequent analysis presented in this paper, and is available for download as a part of the supporting information of this manuscript.

Because the above final models did not contain a disulfide bond, we repeated the analysis for WT to verify that adding a forced disulfide bond did induce gross alterations of predicted protein structure. The protocol followed to generate the disulfide-bonded models was identical to the above mentioned process with the addition of the fix_disulf flag and accompanying file listing the residues to be locked in a disulfide bond. After two relax iterations, clustering, and final relax step of the lowest energy cluster representative structures; the best scoring models had comparable values to those generated without the disulfide bond enforced--between -650 and -640 Rosetta energy units. To generate Figure 5.7, the overall backbone RMSDs between our original model and the top-scoring structure in each of these clusters were calculated. The nearest model, which is depicted in Figure 5.7, had an overall backbone RMSD of only 1.955 Å, indicating very little changes are necessary to accommodate a disulfide bond restraint. This model was subjected to MolProbity analysis, which reported 151/160 (95.57%) residues were in favored regions of the Ramachandran plot, with 160/160 (100%) residues occupying allowed regions. Molprobity reported a clashscore of 2.35 (99th percentile), no poor rotamers, no Cβ deviations, 0/1300 bad backbone bonds, and 4/1775 (0.23%) bad backbone angles. The MolProbity score was 1.32 (98thpercentile). This model was then used as the basis for subsequent analysis presented in this paper, and is available as a Protein Databank file for download in the original version of the manuscript (Mittendorf et al., 2014).

Figure generation

All protein structure figures were generated with The PyMOL Molecular Graphics System, Schrödinger, LLC, except Figure 5.4A, which was generated using UCSF Chimera version 1.9 (Pettersen et al., 2004).

CHAPTER VI

DISCUSSION AND FUTURE DIRECTIONS

Summary of This Work

This dissertation is focused on the understanding the cross-talk between membrane proteins and their membrane environments. This has been a focus of the membrane field for many years. We have utilized two important human membrane proteins involved in neurological disorders, the 99-residue C-terminal fragment of the amyloid precursor protein (C99) and peripheral myelin protein 22, as model systems for the study of these interactions. Specifically, we utilized C99 as a model system for studying the influence of membrane composition on structure utilizing solution state NMR. This part of the project was largely focused on methods development and the improvement of current bicelle systems to create more physiologically relevant bicelle compositions with an expanded hydrophobic width profile. Future efforts will focus on expanding the compositions of these bicelles to contain multiple components, including cholesterol. Additionally, we have investigated the influence of PMP22 on its membrane environment, exploring the hypothesis that PMP22 is capable of shaping membranes into complex structures *in vitro* that resemble myelin. This project sheds light on one potential function of PMP22 and sets up an assay for studying the influence of disease mutations on one aspect of PMP22 function. Future efforts will focus on understanding how PMP22 shapes these MLAs—whether it be through *cis*- or *trans*-homophilic interactions or some other mechanism, and whether these are transient or stable oligomeric structures.

Novel Bicelle Mixtures and C99

On the Development of Novel Membrane Mimetics

The most ideal membrane mimetic is native-like in composition and behavior. However, because the techniques to effectively study the structure, function, dynamics, and biophysical properties of membrane proteins in native environments are limited, it is also important to improve the mimetics available for other biophysical techniques. As noted in Appendix A, solution state NMR has particular power in biophysical investigations, because many biological processes occur on the NMR timescale. Consistent improvement of solution NMR techniques to adapt them to the study of membrane proteins can be expected as the membrane protein field continues to develop. Bicelles were applied to biological problems over 20 years ago (Sanders and Prestegard, 1991; 1992; Sanders and Schwonek, 1992), and yet isotropic bicelles with expanded lipid profiles have only just begun to be explored (Morrison and Henzler-Wildman, 2012; Yamaguchi et al., 2012).

The work outlined in Chapter III, as well as that in Appendix B, sets forth to contribute more physiologically relevant bicelle mixtures that are compatible with solution state NMR. As demonstrated by their application to the study of C99, discussed below, these bicelles can provide insight into interesting properties of membrane proteins and even contribute to an understanding of disease mechanisms. In this work, we outlined 16 new mixtures that appear to form bicelles, and employed four of them in our studies of C99. In Appendix B, several additional novel mixtures containing mixtures of sphingomyelin and cholesterol that appear to form isotropic bicelles are outlined; these mixtures are in the initial stages of application-based screening.

On the Implications of the Influence of Membranes on C99 in Alzheimer's Disease

The effects of model membrane thickness on C99 cleavage by γ-secretase are well established, with increased hydrophobic width resulting in a decreased product Aβ42:Aβ40 ratio. This result has positive implications for Alzheimer's disease, where higher Aβ42:Aβ40 ratios are linked to disease. As discussed in Chapter III, our results may explain this interesting finding as being due to a shift in the topology of C99 with respect to the bilayer normal. Assuming that γ-secretase does not similarly shift, this would shift the position of the cleavage site with respect to both the center of the bilayer and the γ-secretase recognition/cleavage site(s) (see Figures 3.12 and 3.13). However, this hypothesis is complex when considered in light of other hypotheses regarding C99 trafficking into rafts. C99 is known to bind cholesterol (Barrett et al., 2012), and it has been postulated that this binding may promote trafficking of C99 and/or APP into rafts, where both β- and γ-secretase reside (see Figure 1.14). As discussed in Chapter I, lipid rafts have an increased hydrophobic width relative to bulk membrane. Because raft-association is thought to be correlated with adverse cleavage outcomes—resulting in C99 generation by β-secretase over C83 generation by α-secretase—it is clear that the complexities of these implications have not yet been fully explored. While it would initially seem beneficial that thick membranes lower the Aβ42:Aβ40 ratio, this benefit may be offset by overall increased Aβ production when either APP or C99 are dragged into (thick) rafts, where both β- and γ-secretase are thought to preferentially reside. Future work will need to examine C99 in bilayers that are raft-like in nature to determine if this shift still exists, what structural or biophysical differences may be observed in those bicelles, and if these bicelles affect dynamics. Preliminary progress toward this goal is described in Appendix B. Importantly, this progress includes the development and preliminary characterization of isotropic three-component bicelles containing

phosphatidylcholine, sphingomyelin, and cholesterol. As of yet, small membrane mimetics containing lipid raft components have not been developed. These bicelles will likely have important applications in crystallographic, biophysical, biochemical, and solution-NMR studies of membrane proteins.

PMP22 Structure and Function

On the homology model of PMP22: implications and future directions

Chapter V presents a homology-based Rosetta model for PMP22 from the recently determined claudin structure (Suzuki et al., 2014). In this model it was apparent that the TM1 of WT-PMP22 was tilted outward with respect to the TM1 of claudin, suggesting a less-tightly associating helical bundle. This model is in agreement with the previous observation that TM1 has a propensity to dissociate from the bundle (Fontanini et al., 2005; Sakakura et al., 2011). Further, our homology-based Rosetta model of the L16P-PMP22 agrees with low-resolution NMR data that suggests that this mutation introduces a kink in the helix and promotes dissociation of the TM1 from the helical bundle. I hypothesize from the combination of the work presented in this dissertation and the experimental data regarding TM1 dissociation and Zn(II) binding, that Zn(II) binding serves the function to “lock down” the first TM to the rest of the helical bundle through stabilization of the ECL1 structure (Fontanini et al., 2005; Sakakura et al., 2011; Schlebach et al., 2015). Experimental testing of this hypothesis seems well-merited. Ultimately, understanding structurally and mechanistically how Zn(II) binding contributes to PMP22 stability and folding may provide the basis for development of a pharmacological chaperone, a reasonable treatment strategy that is being explored in other diseases of misfolding (Sampson et al., 2011).

In the absence of an experimental high resolution structure of PMP22, the Cys-less construct, which retains the ability to form MLAs, created during the course of this

project (see Chapter IV) could be exploited in labeling-dependent techniques such as EPR to add restraints to the computational model obtained in Chapter V. Other important future work may focus on mapping the Zn(II) binding site in the extracellular loops of PMP22 via alanine scanning mutagenesis through the proposed divalent cation coordinating sites, and adding zinc coordination in future renditions of the homology module, a task for which there already exists a Rosetta module that should be adaptable to this task (Wang et al., 2010). This work could provide mechanistic insight into how Zn(II)-binding may act to stabilize the folded structure of PMP22.

The structure of claudin-15 as determined by X-ray crystallography was monomeric in nature (Suzuki et al., 2014). However, claudins exist as complex oligomers *in vivo* as part of tight junctions. As such, it is probable that there is an important element of quaternary structure missing in the monomeric model of PMP22 presented in Chapter V. Indeed, the results we outline in Chapter IV indicate that PMP22 participates in homophilic interactions via the ECL2. Because of its monomeric nature, our structure does not illuminate how these interactions might occur. Since mutation of the conserved residue W124 to alanine disrupts the formation of MLAs, from our structure it is possible to postulate that this residue may be directly involved in the ECL2-mediated quaternary interactions. This residue is located in a small helix within a flexible loop that faces the interior of the structure in our model (see Figure 6.1), but it is easy to imagine that the flexibility of the loop might allow for an outward rotation of W124 that would result in π-stacking interactions between the W124 residue on one molecule and the W124' or Y132', both conserved aromatic residues, on a *cis*- or *trans*-interacting neighbor PMP22.

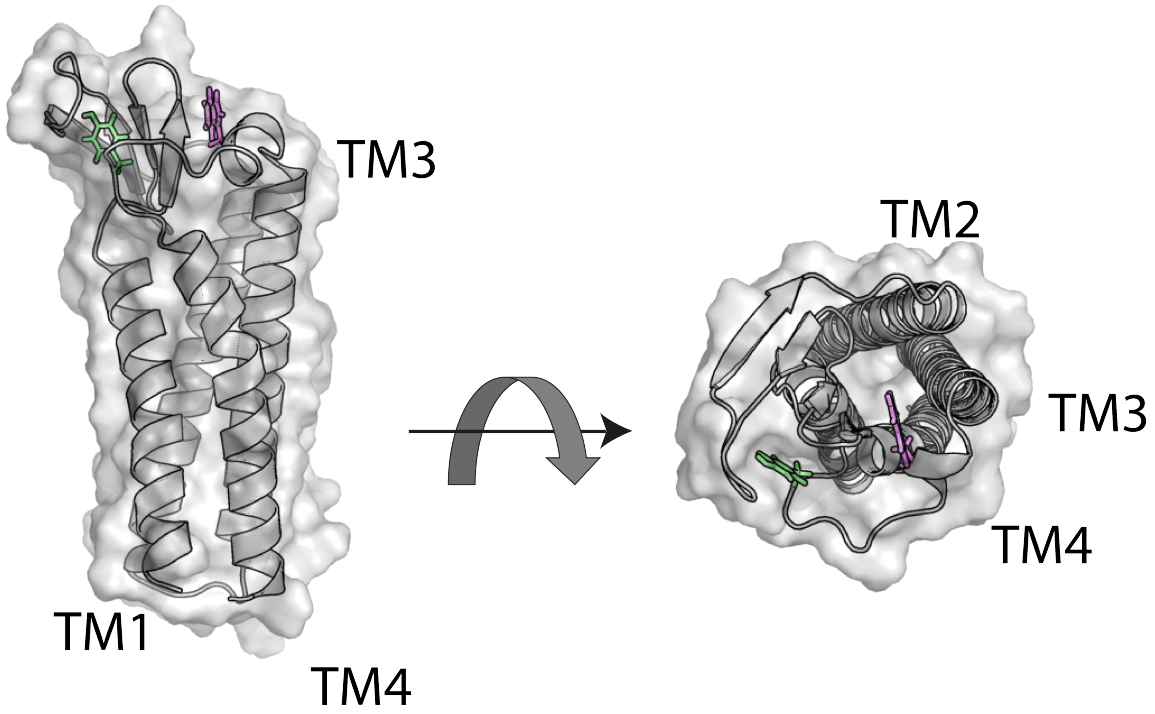

Figure 6.1. PMP22 model with conserved aromatic residues W124 (purple) and Y132 (green) highlighted and the surface displayed.
The mutation W124A has been shown to disrupt MLAs. It is conceivable that outward rotation ECL2 would result in exposure of W124 and/or Y132 that may facilitate *cis*- or *trans*-homophilic interactions.

Since the publication of the claudin-15 structure and our PMP22 model, a model for tight junction assembly by claudin-15 has been proposed by combining structural data with cysteine crosslinking experiments (Suzuki et al., 2015). This model hinges upon two sets of interactions: (1) interactions between the β-sheets of the ECL1, which are responsible for *cis*-oligomerization of claudin-15 into strands and (2) interactions between the "variable" loop regions present in both ECL1 and ECL2, which are responsible for *trans*-oligomerization of claudin-15 between claudins of adjacent cells. If this model is applicable to PMP22, then it is possible that the *trans*-interactions of PMP22 are what might be responsible for the formation of MLAs. Indeed, the distance between membranes in the MLA model might accommodate such an interaction (see Chapter IV and Suzuki et al., 2015). Additionally, a new claudin structure was recently released, that of murine claudin-19, in complex with a tight-junction dissociating toxin(Saitoh et al., 2015). Further homology modeling using restraints from this structure and the claudin tight junction model might improve our PMP22 models and provide a mechanism for PMP22 interaction.

On obtaining a high resolution structure

During the course of this dissertation work, several preliminary efforts were undertaken toward the goal of obtaining a high-resolution structure of PMP22. Efforts were made to incorporate PMP22 into mixed micelles and bicelle mixtures for use in solution state NMR, but no improvements on spectral quality were seen (data not shown). However, since the development of these novel bicelle mixtures, focused efforts to look at PMP22 by NMR have not been undertaken. Additionally, a number of other membrane mimetics, such as the nanodiscs discussed in Chapter I, might be applicable to PMP22 structure determination by solution NMR. However, because of the limits of NMR temperature—higher temperatures are typically used with larger systems to

increase the rate of molecular tumbling and thus narrower linewidths and sharper peaks—and the inherent instability of PMP22 (Sakakura et al., 2011; Schlebach et al., 2013), it is not yet clear that NMR offers a feasible route to the determination of the structure of PMP22.

A number of attempts to crystallize PMP22 in two dimensions for structure determination by 2-D electron crystallography were also undertaken during the course of this dissertation work. These efforts resulted in the formation of crystalline arrays; however, these arrays were layered assemblies that were not in register (see Appendix B). As a result, they were unsuitable to structure determination by electron crystallography. Efforts to obtain single-layer crystals were not successful. However, with the discovery that ECL2 is involved in MLA formation (discussed in Chapter IV), it is possible that the combination of adding ECL2 peptides, using ECL2 mutants, or a shuffled ECL2 in previously identified crystal conditions could result in 2-D crystals that are not layered in the third dimension.

Additionally, it is important to note that the propensity of PMP22 to layer in the third dimension during attempts to generate 2-D crystals may actually make it amenable to 3-D crystallographic studies. Two claudin structures have now been determined using the lipidic cubic phase (LCP) technique. It is possible that by exploiting these conditions, a 3-D PMP22 structure could be determined at high resolution. Additionally, the discovery that both glycerol and zinc promote the PMP22 folded state could help in efforts to determine a structure of PMP22 (Schlebach et al., 2013; 2015).

On the Implication of these Results for PMP22 and Disease

The results presented in Chapters IV and V have clear implications for the complexity of the roles of PMP22 in disease. First, in Chapter IV, it is clear that at least one disease mutation is disruptive to the ability of PMP22 to promote MLA formation.

One disease treatment strategy that has been proposed (Schlebach et al., 2013; 2015) is the use of pharmacological chaperones to improve the trafficking of PMP22 to the plasma membrane of Schwann cells. Importantly, which mutants would be amenable to such a strategy is dependent on whether the mutants will be functional even if normal trafficking is restored. Combining the folding assays developed by the Sanders lab (Schlebach et al., 2013; 2015) with this assay for PMP22 function may help to establish a mechanism to screen for pharmacological chaperones that would improve mutant PMP22 stability and function. Further, the work presented in Chapter IV offers an explanation for why both over-expression (three copies of the PMP22 gene) and under-expression (one copy of the PMP22 gene) result in disease. Our MLA work supports the notion that a very precise protein-to-lipid ratio is required for PMP22 to appropriately perform its function in promoting healthy myelin membrane organization. Additionally, our work offers an explanation for the previously-observed organization of ER membrane into intracellular myelin-like figures (IMLFs) *in vivo* upon PMP22 overexpression and/or retention in the ER (Niemann et al., 2000; Dickson et al., 2002). It is possible that the membrane organizing function of PMP22, when unregulated, contributes to disease by forming IMLFs, which may be cytotoxic.

Toward an Understanding of the Role of PMP22 in Membrane Organization

The data presented in Chapter IV of this dissertation support a model whereby PMP22 is involved in the compression and wrapping of bilayers into organized assemblies that resemble myelin. Supporting this, preliminary low-resolution tomography results demonstrate that MLAs are not composed of nesting vesicles, as seen in MLVs or lipid reconstitutions lacking PMP22. However, new technology should provide yet additional insight into MLA architecture. Because of the low-electron dosage required for tomography, the contrast and resolution of these reconstructions is limited. However, a

recently installed K2 Summit Direct Electron Detector (Gatan) will allow for improved raw tilt series data that will translate into better tomograms through a number of means: (1) it will decrease the overall electron dose needed for each tilt-series, (2) allow us to correct for image drift during exposures, and (3) improve the contrast in our images. As a result, it will be possible to generate higher resolution 3D reconstructions that will be used to trace the organization of the lipid bilayers in the MLAs.

Biochemical characterization of PMP22 MLAs suggests that homophilic interactions involving the ECL2 are necessary for MLA formation and suggest an important role for the conserved residue W124. However, there is another aromatic conserved residue in the second loop: Y132 (see Figures 6.1and 6.2). One might hypothesize that interactions between W124 or Y132 on one PMP22 molecule and W124' or Y132' on another PMP22 molecule are responsible for PMP22 homophilic interactions. Mutation of Y132 to alanine should be undertaken to test this possibility. Additionally, cross-linking experiments using a cysless construct and individual cysteine mutations in ECL2 could further map ECL2-mediated homophilic interactions as outlined for defining the claudin interface in reference (Suzuki et al., 2015). It is possible that the ECL1 is also important in MLA formation either via (a) homophilic interactions that are not dependent on the residues mutated in this study or (b) through interactions with lipids, as has been suggested for PLP. To test this possibility, experiments utilizing a shuffled ECL1 and ECL2 should be conducted to confirm the roles of each loop in MLA formation. A shuffled intracellular loop (ICL) will be used as a control. Alternatively or additionally, alanine-scanning mutagenesis could be undertaken to determine the residues that are key to MLA formation.

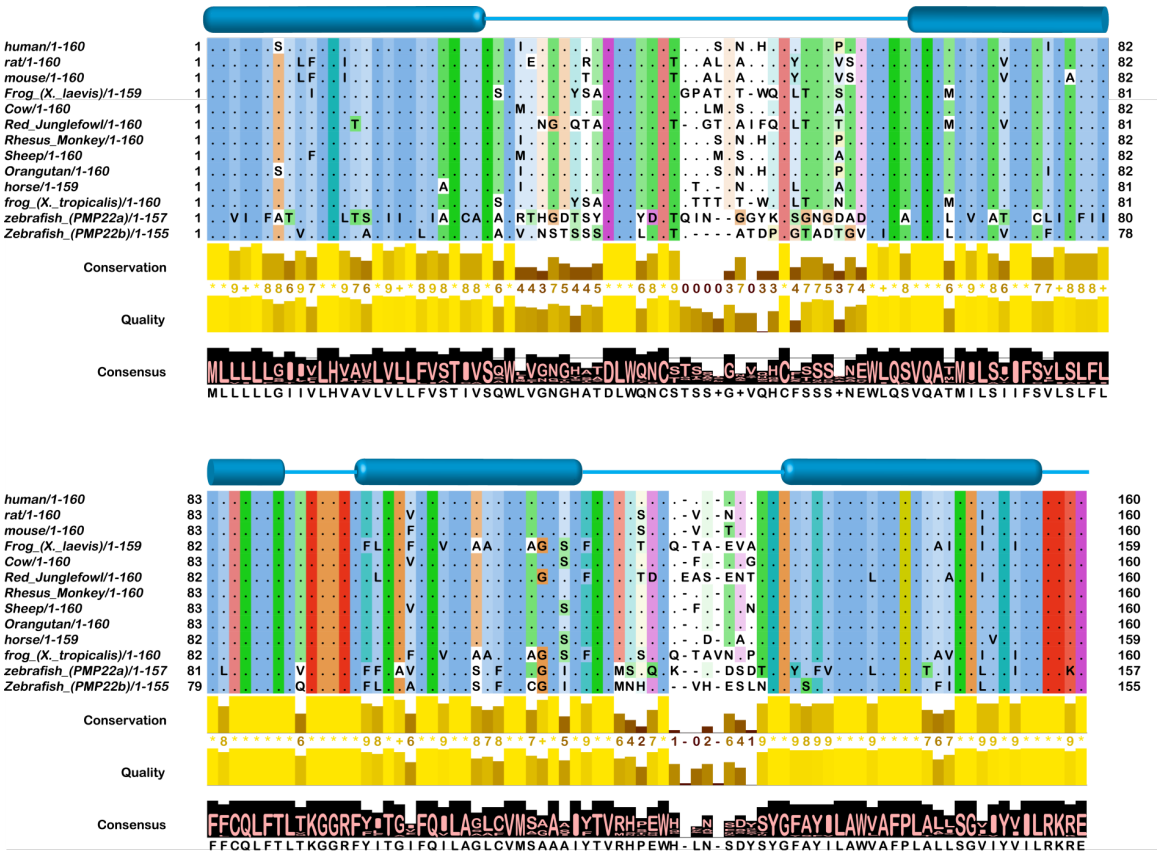

Figure 6.2. Alignment of the PMP22 amino acid sequences from vertebrates. PMP22 topology is represented by the blue helices (cylinders) and loops (lines) above the alignment.

Even with an understanding of the domains of PMP22 responsible for MLA formation, it is unclear *how* PMP22 is responsible for MLA formation. There are a number of non-mutually exclusive potential mechanisms by which PMP22 might facilitate MLA formation. For example, homophilic *trans*-interactions between PMP22 molecules in adjacent bilayers might act as a molecular zipper, the mechanism proposed for PLP in the CNS myelin (Han et al., 2013; Bakhti et al., 2014). In the model for PLP, it has been suggested that weak, transient *trans*-interactions between PLP molecules are responsible for myelin maintenance, as it is necessary for myelin membrane layers to slide along one another during myelin formation (Snaidero et al., 2014). Indeed, the fact that PMP22 retained in the ER *in vivo* forms IMLFS (Niemann et al., 2000; Dickson et al., 2002), structures that are reminiscent of ER whorls, which are known to form from low-affinity, transient *trans*-dimerization of other over-expressed membrane proteins (Snapp et al., 2003; Volkova et al., 2011; 2012), is suggestive that such a hypothesis might be a valid explanation of how PMP22 forms MLAs. Secondly, it is feasible that homophilic *cis*-interactions and/or the insertion of PMP22 in a preferred orientation might be responsible for a wedging mechanism, similar to that proposed for the reticulons and DP1/Yop1p proteins of the ER (Hu et al., 2011), which would facilitate the compression and/or the wrapping of membranous structures by promoting tubulation and/or membrane curvature. Such *trans*- or *cis*-complexes might be evenly distributed in a disperse fashion in the MLAs, or might be more highly organized, for example in the forms of band-like membrane junctions. Finally, it is also conceivable that PMP22 could stabilize the “leading edge membrane hairpin” as the membrane grows and curves, a model that has been proposed for the tetraspan CNS protein M6a, a PLP homologue that produces various cellular protrusions upon overexpression in a cytoskeleton-independent manner (Sato et al., 2011). To answer these questions, future work will need to focus on localizing PMP22 within the MLAs.

There are a number of obstacles to localizing PMP22 in MLAs. Our initial tomograms were at such low-resolution and contrast that resolving density associated with PMP22 was impossible. Preliminary attempts to label PMP22 in MLAs using Nanogold® suggest that these labels, when added after the MLA formation has completed, are unable to penetrate between the bilayers to label PMP22. Additionally, when covalently labeled with Nanogold® prior to MLA formation, these labels disrupted MLA formation. However, in these cases, the covalent labels were attached to the ECL1 and ECL2, at least one of which plays an important role in MLA formation. As such, other labeling strategies should be tested. If larger, stable PMP22 oligomers are indeed required for MLA formation, in the higher resolution tomograms we will likely see density associated with PMP22 between the bilayers. However, because the small molecular mass of PMP22 will make it difficult to see as monomers or small oligomers in the tomograms, labeling strategies can be employed to enhance the ability to visualize PMP22. WT-PMP22 binds Ni-NTA most likely via His residues located in the first and second extracellular loops (Myers et al., 2008). Therefore, to localize PMP22's position in MLAs, one labeling strategy could be to employ commercially available Ni-NTA-Nanogold®, which might actually act to stabilize PMP22, as discussed in relation to the binding of divalent metal cations. Reconstitutions, both with and without PMP22, would be carried out as described in Chapter IV, but in the presence of Ni-NTA-Nanogold. Another labeling strategy is to employ the N-terminal Strep® tag on the cleaved WT-PMP22 (see Figure 7.6) and use Biotin-Nanogold® for labeling. These experiments will inform a model describing exactly where PMP22 is localized within MLAs and should illuminate how the protein promotes MLA formation, reflecting intrinsic properties of the protein that likely are directly relevant for its function(s) in promoting and stabilization myelination. Of course, ultimately, testing this model in myelinating Schwann cells is imperative.

Concluding Remarks

This dissertation outlines the initial steps to the creation of novel bicelle mimetics that should be broadly applicable to the study of a number of human membrane proteins. These mimetics more faithfully represent the hydrophobic widths of novel membranes, as it is clear from the work outlined in Chapter III that traditional DMPC:DHPC mixtures are not capable of accommodating the entire width of the 24-residue TMD of C99. Thus, these efforts represent a highly beneficial expansion of the available bicelle lipid profiles that are compatible with solution state NMR, membrane protein crystallization, and other biophysical and biochemical approaches. The discovery of novel three-component bicelle mixtures (as outlined in Appendix B) that include cholesterol represents the first ever step in the study of the influence of these interesting membrane compositions on membrane protein structure and dynamics.

Finally, this dissertation demonstrates the first functional information about PMP22 *in vitro* and the first high-resolution structural information about PMP22 through computational modeling. Further efforts to study PMP22 *in vitro* should shed light on the implications of its propensity to organize membranes and the mechanism by which it does so. These studies will lead to a better understanding of the role of PMP22 in native myelin and the role of PMP22 mutations in disease.

APPENDIX A. OVERVIEW OF THE METHODOLOGY EMPLOYED IN THIS WORK

Nuclear Magnetic Resonance (NMR) Spectroscopy

Basic Principles of NMR Spectroscopy

Nuclear magnetic resonance (NMR) spectroscopy is a broadly applicable technique, enabling biophysicists to gain information on protein structure, dynamics, and interactions with other molecules, macromolecules, and solvent. NMR spectroscopy, as mentioned above, can be performed in solution state or in solid state, and both forms are viable methods for probing systems containing membrane proteins. This work concerns itself with studying membrane proteins reconstituted into isotropically tumbling mimetics and is thus focused on solution-state NMR. Therefore, while many of the underlying principles are the same, this introductory section will focus on the applications of solution NMR.

NMR relies upon an inherent quantum mechanical property of nuclei, and all other particles, called *spin angular momentum*, or "spin". Spin is defined by the quantum number I, which can be 0, ½, 1, 1½, 2,…, depending on the nucleus identity. For all I > 0, the nucleus will interact with an external magnetic field (Breukels et al., 2011). In protein NMR, nuclei with spin ½ are most typically used, and as a result, proteins must be expressed in a system that has been isotopically enriched ^{15}N and/or ^{13}C (Marion, 2013). In a static magnetic field, the z-component of the magnetic moment of a spin I = ½ nuclei is "quantized," meaning it takes on only discrete values, m_I = +½, -½. As a result of having only two possible m_I, a nucleus with spin I = ½ in an external magnetic field will have only one of two energy values, dependent on the value of m_I:

$$E = -m_I \hbar \gamma B_0$$

Equation 1.1

where $\hbar$ is the reduced Planck's constant, B_0 is the static field, and γ is the gyromagnetic ratio of the nucleus, another property that is nucleus-identity dependent. NMR, like other forms of spectroscopy, exploits energy differences (Figure 7.1) (Breukels et al., 2011). According to the Boltzmann distribution, in any spin system at equilibrium, slightly more spins will be at the lower-energy state than at the higher-energy state, yielding a bulk magnetization vector in the direction of B_0 (Breukels et al., 2011):

$$\Delta E = \hbar \gamma B_0$$

Equation 1.2

Felix Bloch (Bloch, 1946) and Mills Purcell (Purcell et al., 1946) discovered the phenomenon of nuclear magnetic resonance independently at the end of World War II; these scientists found that certain nuclei could absorb *radiofrequency* (RF) energy (light frequencies on the order of 100-600 MHz, or wavelengths of ~200-5000 cm) when placed in an external magnetic field, a phenomenon called *resonance.* Importantly, this frequency range is on the same order as the rates of many biological processes, rendering NMR a useful tool in studying the dynamics of many biological processes (Göbl and Tjandra, 2012). In modern NMR spectroscopy, RF pulses are applied typically at 90° or 180°, resulting in rotation of the bulk magnetization vector and excitation of spins from the lower energy spin state into the higher energy spin state (Figure 7.1). For instance, at the instant of a 90° RF pulse application, the bulk vector will point perpendicularly to the direction of the external, static magnetic field. As time passes, this system will relax to return the distribution of spin states to the Boltzmann distribution. During this process, the bulk magnetization vector will rotate in a process called *precession*, creating a small current in a receiver coil inside the instrument, and over time will return to equilibrium in a process called *transverse relaxation* (Figure 7.1). The instrument records the signal from the receiver coil in a time-dependent fashion and this signal is known as the *free induction decay* (FID). Fourier transformation of a single FID

results in a peak in the frequency dimension, with sharper peaks corresponding to longer relaxation times (Figure 7.1). The frequency of this peak, then, is clearly determined by precession, which is in turn dependent on ΔE (Breukels et al., 2011). Thus,

$$\omega = \Delta E/\hbar = \gamma B_0$$

Equation 1.2

Rewriting this equation in turns of frequency gives us an observed frequency, termed the *Larmour frequency*, v_L:

$$v_L = \gamma B_0/2\pi$$

Equation 1.2

meaning that each nucleus possesses an inherent frequency in any given static magnetic field strength (Breukels et al., 2011). It is the Larmour frequency of the proton at a given magnetic field strength that leads us to term magnet strength in terms of frequency (for instance, an 11.7 Tesla magnet is often referred to as a 500 MHz spectrometer). However, based on these equations, NMR would not be a very useful technique, as any given proton in a spin system would have an identical frequency, and thus give us an identical, overlapping signal in the recorded spectrum. Fortunately, the electrons surrounding the nuclei in a molecular system create small local magnetic fields, which interact constructively or destructively with the external field and which produce slight variations on the Larmour frequency, a process called *electron shielding* (Breukels et al., 2011). Thus, because the electronic environment of any given nucleus can vary greatly in a large macromolecule, the nuclei from a large macromolecule will give rise to many marginally different resonance frequencies for peaks in the observed one-dimensional (1-D) NMR spectrum (Breukels et al., 2011).

However, instead of frequency, the NMR convention for describing resonance position is to use a unitless property called *chemical shift*, which allows us to collect and

directly compare spectra at different static field strengths. *Chemical shift*, or δ, is given in parts per million (ppm) and is defined by the equation

$$\delta = [(\omega_0 - \omega_{ref})/ \omega_{ref}] \times 10^6$$

Equation 1.3

where ω_0 is the frequency of the signal and ω_{ref} is the frequency of a reference compound agreed upon by the field of study (Breukels et al., 2011).

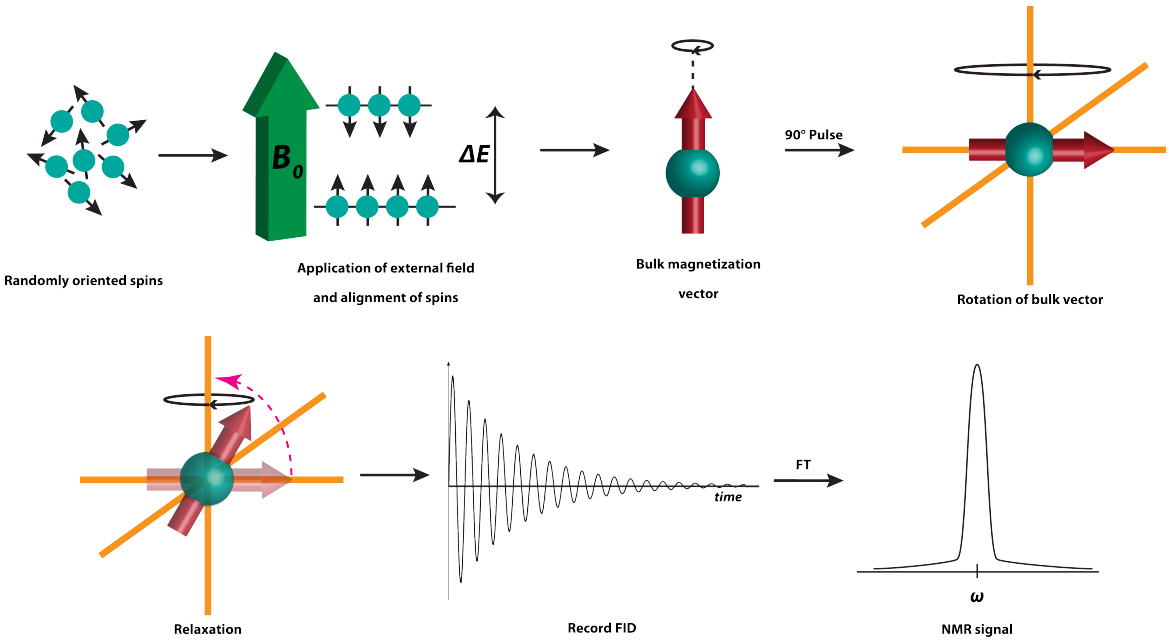

Figure 7.1. Basics of the NMR experiment.
From upper left corner: in a simplified spin-½ system, spins are oriented randomly. Placing this system in an external magnetic field results in alignment of the spins and their distribution among two quantized energy states according to the Boltzmann distribution, with slightly more spins at the lower energy state. We can consider this to be a bulk magnetization vector in the z-dimension precessing about the z-axis. Application of a 90° radiofrequency pulse results in rotation of the bulk vector into the X-Y plane. Over time, relaxation mechanisms will contribute to a return to equilibrium. During relaxation, precession still occurs and creates a signal that can be recorded as a radiofrequency signal free induction decay. Fourier transformation of the FID results in the NMR signal. Adapted from Barrett, 2013.

While 1-D NMR still has great utility in biological applications, the high number of peaks, as well as the significant peak overlaps, present in a 1-D NMR spectrum of a biologically relevant macromolecule often preclude more detailed information, such as peak assignment and structure, from being gleaned from these simple experiments. As a result, multidimensional NMR techniques, which utilize transfer of magnetization between two (or more) interacting nuclei, can be employed to deconvolute these complex spectra. We will focus on this concept as it relates to a two-dimensional (2-D) NMR experiment, the HSQC, and its variation, the TROSY experiment. However, this concept is generalizable to homonuclear and heteronuclear spin systems to *n* dimensions, with the major limiting factor being acquisition time, as adding a dimension greatly increases the time required for an experiment to go to completion. Essentially, a 2-D experiment can be thought of as a number of 1-D spectra collected using a series of incremented evolution times. Following FT to get generate the series of 1-D spectra. Each point in the 1-D spectra is plotted versus the evolution time to generate a new series of FIDS, each of which is then Fourier transformed to give a frequency versus frequency versus intensity plot—referred to as a 2-D NMR spectrum. The nature of the peaks in the 2-D spectrum is a function of what particular spin interaction(s) were allowed to evolve with time during the incremental evolution times (Breukels et al., 2011).

One common experiment used in the study of protein molecules is the ^{15}N-heteronuclear single quantum coherence (HSQC) experiment. This 2-D NMR experiment relies upon *scalar coupling* between a proton nucleus and a nitrogen nucleus. Scalar coupling occurs when one nuclear spin state interacts with another through the polarization of electrons in one or more successive bonds. Scalar coupling results in the splitting of a single resonance into two components that are separated by the magnitude of the coupling interaction. In traditional ^{15}N-HSQC experiments,

decoupling is applied in both dimensions so that only one resonance contour peak is observed. The ^{15}N denotes that this experiment correlates the proton nucleus with the backbone amide nitrogen-15 nuclei in an isotopically-enriched protein sample (see *C99 and Bicelle Sample Preparation for NMR: Considerations*), so all amide protons yield a peak in the resulting 2-D spectrum, meaning that every amino acid residue (except for proline) gives rise to at least one peak. This experiment is informative even before these peaks are assigned, because a well-folded protein will have greater peak distribution and spectral resolution due to the subtle differences in electronic environment in a well-folded protein. On the other hand, in an unfolded protein, all glycine residues, for instance, would give rise to peaks of a near-identical chemical shift (Breukels et al., 2011). With higher-dimensional NMR, it is possible to assign which peaks in the 2-D ^{15}N-HSQC correspond to which amino acid, and as a result, the ^{15}N-HSQC spectrum can be then be exploited to examine a variety of biological questions, such as protein-protein or protein-ligand interactions, membrane topology (discussed below), and to glean structural information.

While the ^{15}N-HSQC spectrum is incredibly useful, it is size-limited to systems of about 35 kDa (Kay and Gardner, 1997). As discussed above, relaxation rates are inversely correlated with the width of an NMR peak. Because slow molecular tumbling results in a longer rotational correlation time, and thus an enhanced transverse relaxation rate, larger proteins have very broad NMR signals in the ^{15}N-HSQC, broadening to the degree that they actually disappear. However, as mentioned above, in a traditional ^{15}N-HSQC decoupling is employed. The transverse-relaxation optimized spectroscopy (TROSY) experiment is a variation on the ^{15}N-HSQC experiment that takes advantage of the fact that prior to decoupling, the multiplet components are differentially affected by the different types of transverse relaxation mechanisms, which can interact constructively or destructively, resulting in different linewidths for these multiplet

components (Pervushin et al., 1997). The TROSY experiment acts to select the component of this multiplet in which the relaxation mechanisms best cancel one another, leading to a single, sharper peak in the spectrum. As a result, TROSY can significantly enhance the spectral resolution and sensitivity of the NMR experiment for large biomolecular assemblies. Because the assemblies used in this work are proteins inside (fairly large) membrane mimetics, all spectra acquired herein utilize TROSY-based pulse sequences.

C99 and Bicelle Sample Preparation for NMR: Considerations

C99 is expressed as a His_6-tagged construct in *E. coli* grown in minimal (^{15}N-labeled) media into inclusion bodies. It is purified by an inclusion body preparative method, whereby the cells are lysed, inclusion bodies are collected and washed with a number of rounds of sonication to remove impurities, the C99 in the remaining pellet is solubilized via denaturation in SDS-Urea, and finally, the C99 is refolded in an on-column fashion into the bicelle mimetic of choice and eluted. Because some bicelle systems were only soluble at warm temperatures, these bicelles had to be kept at 37° C prior to refolding and elution.

The Use of Paramagnetic Probes to Monitor C99 Topology

Experiments founded on the paramagnetic relaxation enhancement (PRE) phenomenon have found an important use in the structural study of proteins by solution NMR (Clore and Iwahara, 2009). The paramagnetic relaxation enhancement experiment exploits the fact that an unpaired electron will enhance the T1 and T2 relaxation rates of nearby nuclei via magnetic dipole interactions in a distance dependent (r^{-6}) manner (Clore and Iwahara, 2009). The PRE effect is felt over large distances (up to 35Å) because of the large magnetic dipole moment of unpaired electrons. The PRE is most

traditionally employed to gain long-range distance restraints for use in structure determination via probes that are chemically attached to the protein of interest through a disulfide linkage. However, probes that associate with the environment can also be exploited to discern membrane protein topology (Schrank et al., 2013). For the purposes of this introduction, we will focus on the two probes employed in the work of this dissertation: gadolinium-diethylenetriaminepentacetate (Gd-DTPA) and 16-Doxyl-Stearic Acid (16-DSA) (Figure 7.2).

Gd-DTPA is an aqueous paramagnetic salt consisting of a 9-coordinate gadolinium ion, with coordinating groups consisting of 5 carboxylate and 3 nitrogen entities of the DTPA molecule and one labile water molecule freely exchanging with the aqueous solvent water molecules (Figure 7.2) (Sherry et al., 2009). The paramagnetic properties arise from the 7 unpaired electrons with parallel spins on the gadolinium ion. Gd(III) has 7 4f orbitals and only 7 valence electrons, so all must be unpaired. It has 9-coordinate geometry and DTPA occupies 8 of those coordinate sites. It exerts its paramagnetic properties because there is an extra coordination site that is occupied by a water molecule, which exchanges rapidly with bulk water in solution. Because this agent is only soluble in the aqueous phase, only nuclei near to the solvent phase will experience dramatic relaxation. Nuclei buried in the membrane mimetic environment will not experience a relaxation enhancement. Thus, in a TROSY-HSQC experiment, amide peaks arising from amino acids in the soluble parts of the protein will broaden and disappear, and the amide peaks arising from amino acids in the membrane environment will be protected.

As a corollary experiment to the Gd-DTPA aqueous probe, one can add 16-DSA. 16-DSA is a lipid-soluble free radical (Figure 7.2), with the free radical nitroxide positioned at the extreme end of the acyl chain. In this experiment, those nuclei buried in

the hydrophobic phase of model membranes will experience the most signficant relaxation enhancement, with their signals broadening and disappearing.

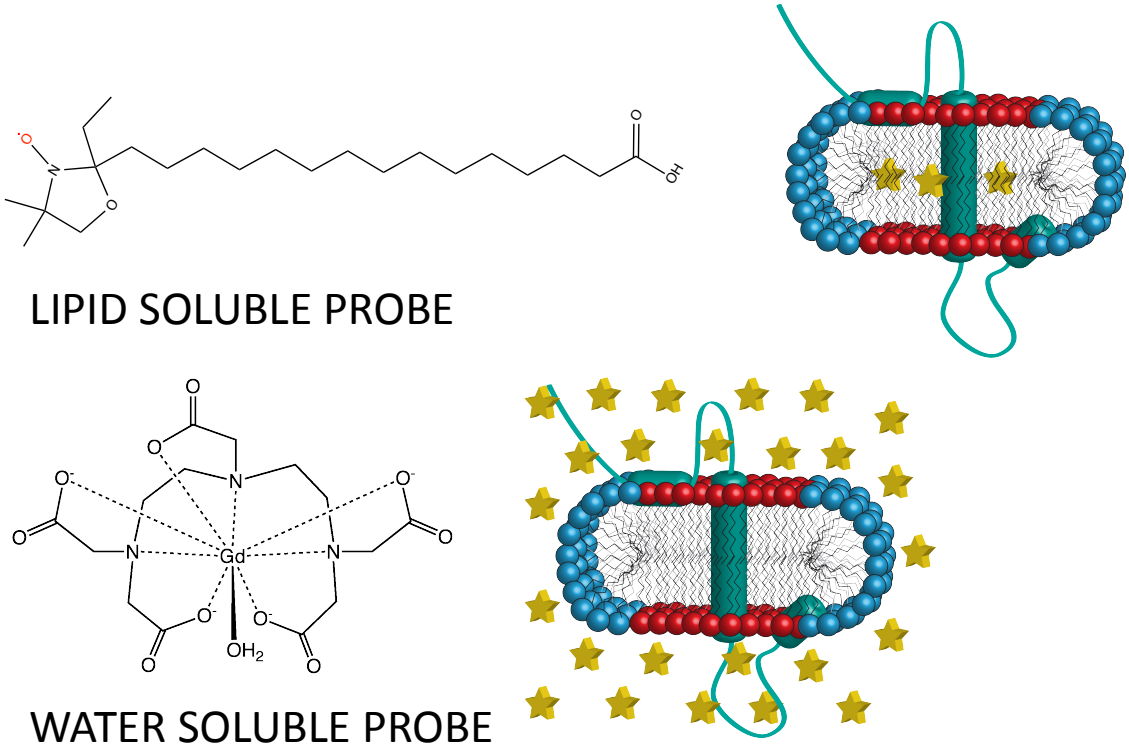

Figure 7.2. Paramagnetic probes can be used to determine membrane protein topology in the solution-NMR experiment.
(A) An example of a water soluble probe, Gd-DTPA (left) and a demonstration of accessibility for a single-pass transmembrane protein in a bicelle environment (right) where yellow stars represent the probe; (B) an example of a lipid soluble probe, 16-DSA (left) and a demonstration of accessibility for a single-pass transmembrane protein in a bicelle environment (right) where yellow stars represent the probe.

In a typical topology experiment (Figure 7.3), one acquires a probe-free reference spectrum, a spectrum where the sample contains the aqueous paramagnetic probe and a spectrum where the sample contains the lipophilic probe. Quantitative assessment of the experimental results can be performed whereby the data is expressed as a peak intensity ratio for each peak in the spectrum between the experimental and reference spectra. Thus, with an assigned TROSY-HSQC spectrum in hand, the combined use of the Gd-DTPA and 16-DSA PRE experiment allows for a topological mapping of buried and exposed residues.

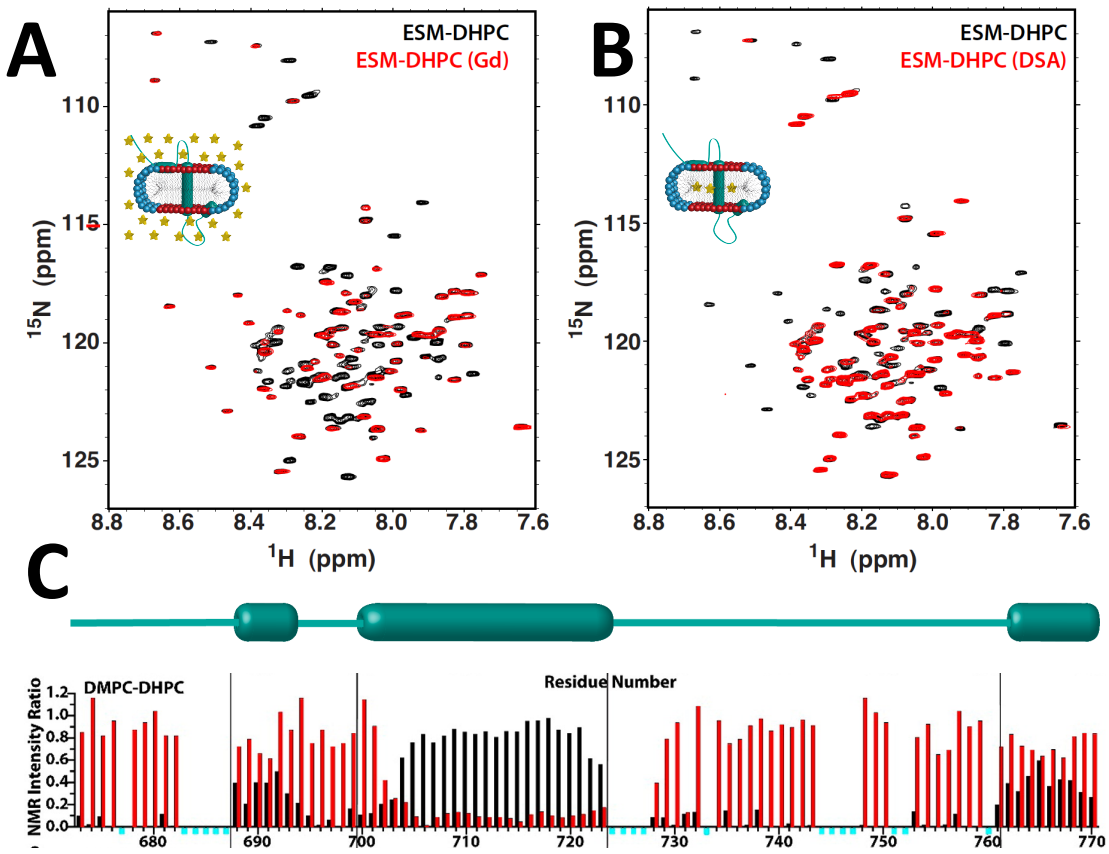

Figure 7.3. Sample processed NMR topology experiment.
(A) TROSY spectra of C99 in egg sphingomyelin-DHPC bicelles before (black) and after (red) addition of the water soluble probe Gd-DTPA; inset cartoon depicts accessibility of this probe (yellow stars) in the bicelle; (B) TROSY spectra of C99 in egg sphingomyelin-DHPC bicelles before (black) and after (red) addition of the lipid soluble probe 16-DSA; inset cartoon depicts accessibility of this probe (yellow stars) in the bicelle; (C) example quantitation for C99 intensity ratios after addition of Gd-DTPA (black bars) or 16-DSA (red bars). Intensity ratios near 0 indicate near-complete exposure, while intensity ratios near 1.0 indicate near-complete protection.

Electron Microscopy

Basic Principles of Negative Stain and Cryogenic Transmission Electron Microscopy

Transmission electron microscopy has long played a key role in elucidating cellular structures and processes. More recently (and increasingly) it has also contributed much to structure determination of large protein complexes. Quantum mechanics tells us that electrons, and other elements of matter, can exhibit wave-like behavior (wave-particle duality) and can thus be directed just like light in a beam-like fashion (Castón, 2013). A key to transmission electron microscopy (TEM) is that the sample must be sufficiently thin so that some electrons will pass through to a detector, while other electrons, which interact with the matter in the sample, will be absorbed or scattered. Light microscopy is limited in resolution by the wavelengths of visible light; electron microscopy overcomes this problem because of the small *de Broglie wavelength* of electrons (Winey et al., 2014).

The basic components of a TEM (reviewed in (Winey et al., 2014)) are analogous to those found in a conventional light microscope. Rather than a light source, an electron gun is the source of energy, and this energy is focused electromagnetically (by adjusting the current in a “lens” coil called a *solenoid*), rather than through glass lenses. The electrons pass through the sample, and those electrons that are not absorbed or scattered (*i.e.*, those electrons that are *transmitted*) are focused onto a detector. The entire electron path is kept under vacuum, because otherwise gas particles would scatter the electrons (Figure 7.4). Areas of the detector where little mass is present in the sample to interact with electrons will appear brightest, because the most electrons will be able to pass through the sample. Areas that are darker reflect areas of the sample with the densest mass. Because biological specimens are relatively “light” matter, negative staining solutions, which coat the particles of interest with electron

dense material, are often employed. This type of TEM is referred to as negative-stain TEM in this work. Importantly for this work, because in negative-staining, one sees only the negative stain *coat*, it is impossible to differentiate between multilamellar vesicles (MLVs) and unilamellar vesicles in a negative-stain TEM experiment. Thus, the myelin-like assembly (MLA) structures examined in Chapter IV are truly something other than MLVs.

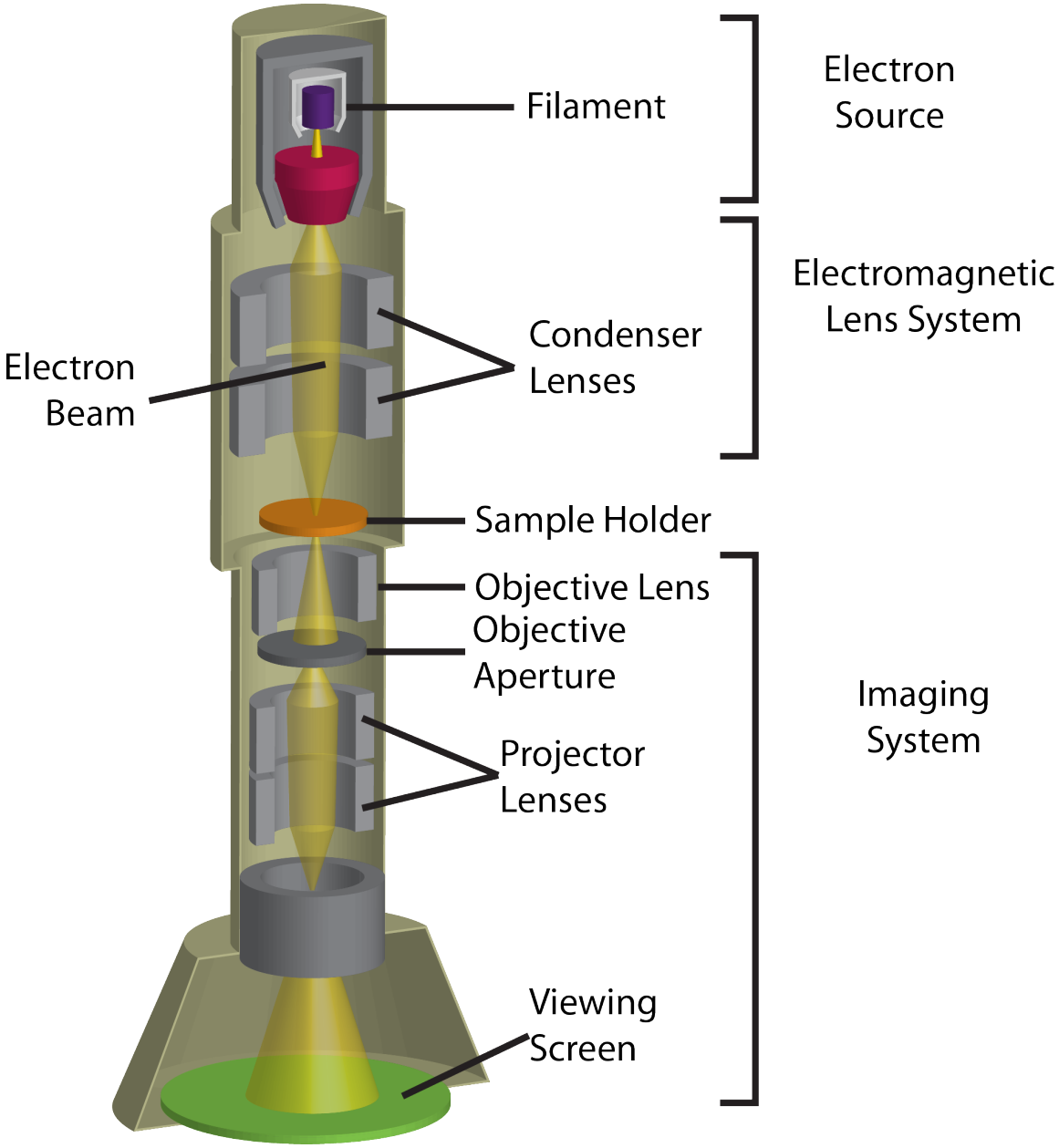

Figure 7.4. Anatomy of a Standard Transmission Electron Microscope (TEM). Not pictured are the vacuum and airlock mechanism to keep the electron beam under vacuum.

As a result of the high resolution and high magnification capabilities of TEM, it has been an important technique in cellular and structural biology for over 50 years (Winey et al., 2014). Recent years have seen the development of cryoelectron microscopy techniques (Orlova and Saibil, 2011; Castón, 2013; Milne et al., 2013), which allow for imaging of a specimen preserved in vitreous ice. This technique removes the need for electron dense stains, which can distort structures and obscure finer details (Orlova and Saibil, 2011). In this technique, the sample is preserved in *vitreous* (*i.e.,* non-crystalline, amorphous) ice, which allows for the transmission of electrons through plunging the sample in liquid ethane. This technique permits examination of the sample in its native, hydrated state and has the additional advantage of reducing radiation damage to the sample by keeping the sample at very cold (-170°C) temperatures (Orlova and Saibil, 2011; Castón, 2013; Milne et al., 2013).

Electron Tomography

Because transmission EM creates 2-D projections, the desire arose for the ability to examine cellular structures in three dimensions without the need for highly perfect sectioning and reconstruction. As a result, cryo-electron tomography was developed. In this technique (see Figure 7.5 from Milne and Subramaniam, 2009), experimental data collection proceeds in much the same way as for standard cryo-TEM, with a few modifications. First, because a number of images will be acquired from the same section of the sample, the electron doses utilized during each exposure are greatly reduced, such that the total electron exposure the sample receives is much the same as it would be for a single image acquisition in traditional transmission EM. This prevents sample destruction during image acquisition from accumulated radiation damage, although it does have the drawback of reducing the contrast and resolution of the final tomograms

(Milne and Subramaniam, 2009; Diebolder et al., 2012; Hoenger, 2014). Second, prior to the plunging of the sample in liquid ethane, fiduciary markers (typically 5-10 nm colloidal gold) are added to the sample. These markers are used during image processing to align the final tilt series. During acquisition, the sample is tilted across the entire range of angles possible for imaging (-70° to +70° in an ideal situation), stopping incrementally (typically every 2°) for image acquisition. This creates a series of 2-D projections that can be computationally aligned using the fiducials. After alignment, back projection creates a z-stack that is representative of the entire volume of the specimen. More detailed reviews of cryo-EM tomography can be found in (Nickell et al., 2006; Milne and Subramaniam, 2009; Pierson et al., 2011; Diebolder et al., 2012; Gan and Jensen, 2012; Castón, 2013; Harapin et al., 2013; Lučič et al., 2013; Hoenger, 2014).

This dissertation focused on the use of negative stain and cryo-TEM for the examination of a membrane structure created by the reconstitution of PMP22 into lipid bilayers via the dialysis method. Tomography has also was employed to examine the morphology of these structures.

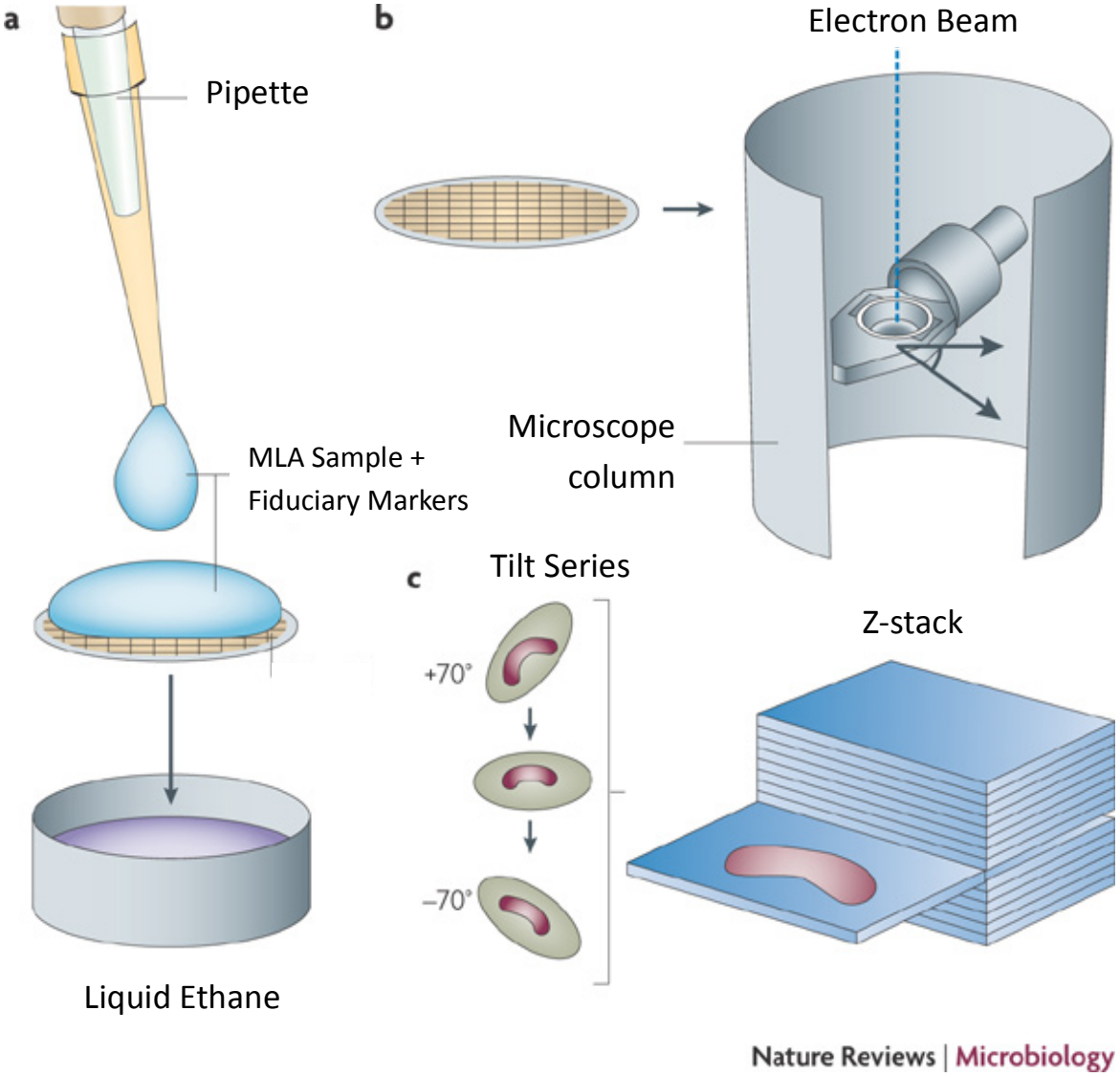

Figure 7.5. Basics of Electron Tomography.
(A) First, the liquid sample is mixed with fiducial markers—typically colloidal gold particles. Next, the sample is pipetted onto a mesh grid and plunged rapidly via robotics into a bath of liquid ethane to create vitreous ice suitable for cryo-TEM. (B) Then, the sample is inserted into the electron microscope under vacuum. (C) Finally, a tilt series of 2-D projections is acquired at low electron dose from the sample part of the sample, tilting the specimen over a range of angles, ideally from -70° to +70°. These images are then aligned using the fiducial markers and back projected. The sum of all the backprojections forms a Z-stack that is representative of the density distribution of the specimen. Figure adapted from Milne and Subramaniam, 2009.

Purification and Reconstitution of PMP22 into Micelles and Vesicles for Electron Microscopy: Considerations

PMP22 is expressed as a fusion-protein construct consisting of a 76-amino acid portion of the lambda repressor, which serves to drive the protein into inclusion bodies, followed by a 10x-histidine tag, a 7 amino-acid linker, a thrombin cleavage site, an 11 amino acid strep-tag and, finally, the human-PMP22 sequence (Figure 7.6). The protein is solubilized initially using the commercially available zwitterionic Empigen BB ® Detergent (Sigma-Aldrich) and is refolded while bound to the resin during reequilibration into the detergent of choice. Thrombin is used to cleave the protein, and the sample is then reincubated with NiNTA resin. Because PMP22 has a slight affinity for some divalent metal cations, including Ni^{2+}, the entire system is bound, but the cleaved PMP22 can be selectively eluted with a low imidazole concentration (10-30 mM). It should be noted that PMP22 is relatively unstable and must be used immediately following purification into most detergents or stored and saved.

Figure 7.6. *E. coli* expression construct of human PMP22.

Computational Modeling of PMP22: An alternative approach to structure

Because membrane protein structural investigation remains a significant bottleneck in the exploration of membrane proteins, accurate homology modeling—that is, building a reliable structural model of a membrane protein from a known starting template of a homologous protein—retains a place of significance in the field of membrane protein structural biology. During the time of research for this dissertation, significant hurdles to structural determination of PMP22 were encountered. Under the variety of NMR conditions screened in this lab, PMP22 at best occupied a folding intermediate state in which TM2-4 were molten globular, undergoing intermediate time-scale exchanges that abrogated the resulting NMR signal completely (Sakakura et al., 2011). While a number of conditions were screened for 2-D crystallization of PMP22, and collaborators attempted 3-D crystallization of PMP22, 2-D crystals were hindered by out-of-register layering and no promising 3-D crystallization conditions were identified. However, during the course of this research, a 2.4 Å crystal structure of the murine claudin-15 was released (Suzuki et al., 2014), the first high resolution crystal structure from the claudin/EMP/PMP22 family. This protein is 25% identical and 60% similar to PMP22 (Mittendorf et al., 2014), and as a result, can serve as a reasonable template for homology modeling by Rosetta 3.5 (Yarov-Yarovoy et al., 2006; Barth et al., 2007; Das and Baker, 2008; Barth et al., 2009; Adamian et al., 2011; Nguyen et al., 2013).

There are a number of methods for membrane protein structure prediction, including a number that employ homology modeling (reviewed in ref (Punta et al., 2007)). For the purposes of this work, we employed a combination of BCL::Align to create an accurate alignment that considers sequence homology, secondary structure prediction, and transmembrane region prediction (Dong et al., 2008), and Rosetta 3.5, a highly-validated software package for protein structure prediction which includes membrane protein-specific scoring functions (Yarov-Yarovoy et al., 2006; Barth et al.,

2007; Das and Baker, 2008; Barth et al., 2009; Adamian et al., 2011; Nguyen et al., 2013). Briefly, BCL::Align is used to create an accurate alignment, and then this alignment is used to guide the population of atoms from the PMP22 sequence onto the claudin-15 template using an in-house script (Jens Meiler, unpublished).

Following this, regions not containing secondary structure elements (loops) are rebuilt using the Rosetta loop-building tool. If regions containing secondary structure are in doubt, those can similarly be rebuilt. It is common practice to include flanking residues of secondary structure elements in the loop-rebuilding tool, when secondary structure elements are retained rather than rebuilt. The loop-rebuilding occurs in three steps within Rosetta. First, fragment files are generated within the Rosetta server (Kim et al., 2004). Next, a low-resolution "centroid" method closes the loop and performs an initial relaxation. Then, all-atom refinement allows for conformational sampling of all residues—both backbone and side-chain atoms. Membrane-specific scoring functions can be used at the second and third phase, or just the third phase. When the majority of loop residues are in the soluble portion of the protein, it makes sense to use the soluble-protein based scoring function during the centroid method, because that scoring function has been extensively benchmarked (Wang et al., 2007). Finally, the resulting conformation is subjected to an energy minimization protocol that allows conformational sampling in the backbone and side-chains of all residues across the protein and is scored with a membrane-specific scoring function.

After initial models are built and relaxed, relaxation, clustering, and model evaluation proceeds iteratively. For instance, after generating 10,000 models, the lowest scoring 1,000 will be subjected to an additional round of refinement, and then this process repeated. At the end, the models are clustered into structurally similar families using BCL::Cluster (Alexander et al., 2011), and only the top-scoring models from large clusters are considered as final models. These models can then be evaluated using

structure evaluation tools such as MolProbity (Davis et al., 2007; Chen et al., 2010), which verify that the structures produced adhere to physical constraints. A more thorough description of these methods can be found in Chapter IV.

APPENDIX B. PRELIMINARY DATA

Preliminary Data Summary

A particular focus of additional experiments has been on the development of bicelles that contain lipid raft components, including cholesterol. Because a number of these mixtures were attempted in this work using classical bicelle detergents (see Table 3.1) only to find these components insoluble, it has been necessary to explore the use of more unusual detergents with different solubility profiles and properties. Below, we outline the screening of over 30 different detergents for their ability to solubilize three-component bicelles containing cholesterol. Preliminary data characterizing these bicelles by NMR are also presented. On the part of PMP22, efforts to achieve an experimental high-resolution structure of PMP22 continue. Here we present conditions for which arrays of PMP22 in lipid were obtained.

Toward Physiologically Relevant Bicelle Mixtures and Bicelles that Resemble "Lipid Raft" Compositions

During the course of this dissertation work, preliminary efforts were undertaken to solubilize cholesterol-containing bicelles. Overall 35 detergents were screened for their ability to dissolve mixtures containing cholesterol and sphingolipids (Table 8.1). A novel detergent, *n*-dodecyl-β-D-melibiose (DDMB)[5] was identified as a promising detergent for dissolving cholesterol-containing mixtures to clarity (see Figure 8.1). We were able to obtain diffusion coefficients for a number these bicelle mixtures using the 600 MHz instrument. Comparing these novel mixtures to classical DMPC-DHPC bicelles at the

[5] DDMB was provided free of charge by Anatrace. The author thanks Drs. Benjamin Travis and Ritesh Mittal for their time, effort, and generosity.

same q-ratio reveals that their molecular tumbling rates are slightly slower, but not dramatically so (Table 8.2).

Table 8.1. Potential bicelle compositions tested for this work.
Bicelle mixtures were prepared in 50 mM phosphate buffered saline, 1mM EDTA, pH 7.0. All mixtures contained 50 mg total lipid in 1 ml total buffer/detergent and were prepared at the q ratio listed. In all cases, in addition to the detergent required to reach the appropriate q ratio,an additional CMC concentration of detergent was added. *Mixtures for which it was possible to achieve complete solubilization of all components are indicated in bold font.*

Lipid (mol:mol ratios)	Detergent	q ratio (mol lipid:mol detergent)	Observations
6:1:1 POPC:ESM:Ch	Sodium Dodecylsulfate (SDS)	0.33	Did not solubilize with boiling, ice bath, or freeze thaw, became clearer in warm room after 10 days. Still somewhat cloudy.
6:1:1 POPC:ESM:Ch	**Dodecylphospho-choline (DPC)**	**0.33**	**Solubilized after two cycles of ice bath, vortexing and boiling, remains clear at RT.**
6:1:1 POPC:ESM:Ch	**Decylphospho-choline (DDPC)**	**0.33**	**Solubilized after two cycles of ice bath, vortexing and boiling, remains clear at RT.**
6:1:1 POPC:ESM:Ch	Fenfos-5	0.33	Did not solubilize with boiling, ice bath, or freeze thaw, became clearer in warm room after 10 days. Milky at RT.
6:1:1 POPC:ESM:Ch	Tetradecylphospho-choline (TDPC)	0.33	Did not solubilize with boiling, ice bath, or freeze thaw, became clearer in warm room after 10 days. Still somewhat cloudy, better than SDS.
6:1:1 POPC:ESM:Ch	Lyso-myristoylphospha-tidylcholine (LMPC)	0.33	Did not solubilize with boiling, ice bath, or freeze thaw, became clearer in warm room after 10 days. Cloudy at RT.
6:1:1 POPC:ESM:Ch	Lyso-myristoylphospha-tidylglycerol (LMPG)	0.33	Did not solubilize with boiling, ice bath, freeze thaw or warm room. Cloudy and viscous at RT.
6:1:1 POPC:ESM:Ch	Lauryl sarcosine (LSC)	0.33	Did not solubilize with boiling, ice bath, or freeze thaw, became clearer in warm room after 10 days. Cloudy at RT.
6:1:1 POPC:ESM:Ch	**Lubrol 17A17 10%**	**0.33**	**Solubilized after two cycles of ice bath, vortexing and boiling, remains clear at RT.**
6:1:1 POPC:ESM:Ch	Brij 97 (Brij 010)	0.33	Became cloudy and solid after going through cycles of the boiling, ice bath and vortexing; it also went through freeze-thaw and was in the warm room for 10 days. It remains in a solid gel like state at RT.
6:1:1 POPC:ESM:Ch	**Brij 35**	**0.33**	**Solubilized after one cycle of ice bath, vortexing and boiling, remains clear at RT.**
6:1:1 POPC:ESM:Ch	**Brij 58 10%**	**0.33**	**Solubilized after three cycles of ice bath, vortexing and boiling, remains clear at RT.**
6:1:1 POPC:ESM:Ch	**Cymal-4**	**0.33**	**Solubilized after one cycles of ice bath, vortexing and boiling, remains clear at RT.**
6:1:1 POPC:ESM:Ch	**Decylmaltoside (DM)**	**0.33**	**Solubilized after one cycles of ice bath, vortexing and boiling, remains clear at RT.**
6:1:1 POPC:ESM:Ch	**Dodeclymaltoside (DDM)**	**0.33**	**Solubilized after one cycles of ice bath, vortexing and boiling, remains clear at RT.**

6:1:1 POPC:ESM:	**Octylglucoside (OGC)**	**0.33**	**Solubilized after one cycles of ice bath, vortexing and boiling, remains clear at RT.**
6:1:1 POPC:ESM:Ch	Lauryl Maltoside Neopentylglycol (LMN)	0.33	Did not solubilize with boiling, ice bath, or freeze thaw, became clearer in warm room after 10 days. Cloudy and viscous at RT.
6:1:1 POPC:ESM:Ch	**Octyl Glucose Neopentyl Glycol (OGNG)**	**0.33**	**Solubilized after two cycles of ice bath, vortexing and boiling, remains clear at RT.**
6:1:1 POPC:ESM:Ch	**Cymal-5 Neopentylglycol**	**0.33**	**Solubilized after two cycles of ice bath, vortexing and boiling, remains clear at RT.**
6:1:1 POPC:ESM:Ch	Tween 20	0.33	Did not solubilize with boiling, ice bath, or freeze thaw, became clearer in warm room after 10 days. Cloudy at RT.
6:1:1 POPC:ESM:Ch	**Zwittergent-3-14**	**0.33**	**Solubilized after one cycles of ice bath, vortexing and boiling, remains clear at RT.**
6:1:1 POPC:ESM:Ch	**Zwittergent-3-10**	**0.33**	**Solubilized after one cycles of ice bath, vortexing and boiling, remains clear at RT.**
6:1:1 POPC:ESM:Ch	**Dodecyl Melibioside (DDMB)**	**0.33**	**Solubilized after one cycles of ice bath, vortexing and boiling, remains clear at RT.**
6:1:1 POPC:ESM:Ch	**FOSMEA-10**	**0.33**	**Solubilized after one cycles of ice bath, vortexing and boiling, remains clear at RT.**
6:1:1 POPC:ESM:Ch	FOSMEA-12	0.33	Did not solubilize with boiling, ice bath, or freeze thaw, became clearer in warm room after 10 days. Milky and viscous at RT.
6:1:1 POPC:ESM:Ch	TRIPAO 10%	0.33	Did not solubilize with boiling, ice bath, or freeze thaw, became clearer in warm room after 10 days. Somewhat cloudy at RT.
6:1:1 POPC:ESM:Ch	ASB-14	0.33	Did not solubilize with boiling, ice bath, or freeze thaw, became clearer in warm room after 10 days. Still somewhat cloudy.
6:1:1 POPC:ESM:Ch	ANAPOE-C12E8 10%	0.33	Did not solubilize with boiling, ice bath, or freeze thaw, became clearer in warm room after 10 days. Milky and viscous at RT.
6:1:1 POPC:ESM:Ch	ANAPOE-C8E4	0.33	Did not solubilize with boiling, ice bath, or freeze thaw, became clearer in warm room after 10 days. Somewhat cloudy at RT.
6:1:1 POPC:ESM:Ch	Cyclophos-5	0.33	Did not solubilize with boiling, ice bath, or freeze thaw, became clearer in warm room after 10 days. Somewhat cloudy at RT.
6:1:1 POPC:ESM:Ch	Cyclophos-7	0.33	Did not solubilize with boiling, ice bath, or freeze thaw, became clearer in warm room after 10 days. Somewhat cloudy at RT.
6:1:1 POPC:ESM:Ch	Fluorinated Octyl Maltoside (FOM)	0.33	Did not solubilize with boiling, ice bath, or freeze thaw, became clearer in warm room after 10 days. Cloudy at RT.
6:1:1 POPC:ESM:Ch	**C-HEGA-11**	**0.33**	**Solubilized after two cycles of ice bath, vortexing and boiling, remains clear at RT.**
6:1:1 POPC:ESM:Ch	**LDAO**	**0.33**	**Solubilized after two cycles of ice bath, vortexing and boiling, remains clear at RT.**
6:1:1 POPC:ESM:Ch	Sodium Dodecylsulfate (SDS)	2.5	Did not solubilize upon adding detergent solution, boiling-ice bath cycles, freeze thaw, or after placing in warm room for 10 days. Final solution is milky with solid debris.

6:1:1 POPC:ESM:Ch	Dodecylphosphocholine (DPC)	2.5	Did not solubilize upon adding detergent solution, boiling-ice bath cycles, freeze thaw, or after placing in warm room for 10 days. Final solution is milky with solid debris.
6:1:1 POPC:ESM:Ch	Decylphosphocholine (DDPC)	2.5	Did not solubilize upon adding detergent solution, boiling-ice bath cycles, freeze thaw, or after placing in warm room for 10 days. Final solution is milky with solid debris.
6:1:1 POPC:ESM:Ch	Fenfos-5	2.5	Did not solubilize upon adding detergent solution, boiling-ice bath cycles, freeze thaw, or after placing in warm room for 10 days. Final solution is milky with solid debris.
6:1:1 POPC:ESM:Ch	Tetradecylphosphocoline (TDPC)	2.5	Did not solubilize upon adding detergent solution, boiling-ice bath cycles, freeze thaw, or after placing in warm room for 10 days. Final solution is milky.
6:1:1 POPC:ESM:Ch	Lyso-myristoylphosphatidylcholine (LMPC)	2.5	Did not solubilize upon adding detergent solution, boiling-ice bath cycles, freeze thaw, or after placing in warm room for 10 days. Final solution is milky with solid debris.
6:1:1 POPC:ESM:Ch	Lyso-myristoylphosphatidylglycerol (LMPG)	2.5	Did not solubilize upon adding detergent solution, boiling-ice bath cycles, freeze thaw, or after placing in warm room for 10 days. Final solution is milky.
6:1:1 POPC:ESM:Ch	**Lauryl sarcosine (LSC)**	**2.5**	**Solubilized after one cycle of ice bath/boiling. Looks opalescent, like a traditional 2.5 bicelle.**
6:1:1 POPC:ESM:Ch	Lubrol 17A17 10%	2.5	Did not solubilize upon adding detergent solution, boiling-ice bath cycles, freeze thaw, or after placing in warm room for 10 days. Final solution is milky with solid debris.
6:1:1 POPC:ESM:Ch	Brij 97 (Brij 010)	2.5	Did not solubilize upon adding detergent solution, boiling-ice bath cycles, freeze thaw, or after placing in warm room for 10 days. Final solution is milky with solid debris.
6:1:1 POPC:ESM:Ch	Brij 35	2.5	Did not solubilize upon adding detergent solution, boiling-ice bath cycles, freeze thaw, or after placing in warm room for 10 days. Final solution is milky with solid debris.
6:1:1 POPC:ESM:Ch	Brij 58 10%	2.5	Did not solubilize upon adding detergent solution, boiling-ice bath cycles, freeze thaw, or after placing in warm room for 10 days. Final solution is milky.
6:1:1 POPC:ESM:Ch	Cymal-4	2.5	Did not solubilize upon adding detergent solution, boiling-ice bath cycles, freeze thaw, or after placing in warm room for 10 days. Final solution is milky with solid debris.
6:1:1 POPC:ESM:Ch	Decylmaltoside (DM)	2.5	Did not solubilize upon adding detergent solution, boiling-ice bath cycles, freeze thaw, or after placing in warm room for 10 days. Final solution is milky with solid debris.
6:1:1 POPC:ESM:Ch	Dodeclymaltoside (DDM)	2.5	Did not solubilize upon adding detergent solution, boiling-ice bath cycles, freeze thaw, or after placing in warm room for 10 days. Final solution is milky.
6:1:1 POPC:ESM:Ch	Octylglucoside (OGC)	2.5	Did not solubilize upon adding detergent solution, boiling-ice bath cycles, freeze thaw, or after placing in warm room for 10 days. Final solution is milky.
6:1:1 POPC:ESM:Ch	Lauryl Maltoside Neopentylglycol (LMN)	2.5	Did not solubilize upon adding detergent solution, boiling-ice bath cycles, freeze thaw, or after placing in warm room for 10 days. Final solution is milky.
6:1:1 POPC:ESM:Ch	Octyl Glucose Neopentyl Glycol (OGNG)	2.5	Did not solubilize upon adding detergent solution, boiling-ice bath cycles, freeze thaw, or after placing in warm room for 10 days. Final solution is milky.

6:1:1 POPC:ESM:Ch	Cymal-5 Neopentylglycol	2.5	Did not solubilize upon adding detergent solution, boiling-ice bath cycles, freeze thaw, or after placing in warm room for 10 days. Final solution is milky.
6:1:1 POPC:ESM:Ch	Tween 20	2.5	Did not solubilize upon adding detergent solution, boiling-ice bath cycles, freeze thaw, or after placing in warm room for 10 days. Final solution is milky.
6:1:1 POPC:ESM:Ch	Zwittergent-3-14	2.5	Did not solubilize upon adding detergent solution, boiling-ice bath cycles, freeze thaw, or after placing in warm room for 10 days. Final solution is milky.
6:1:1 POPC:ESM:Ch	Zwittergent-3-10	2.5	Did not solubilize upon adding detergent solution, boiling-ice bath cycles, freeze thaw, or after placing in warm room for 10 days. Final solution is milky.
6:1:1 POPC:ESM:Ch	Dodecyl Melibioside (DDMB)	2.5	Did not solubilize upon adding detergent solution, boiling-ice bath cycles, freeze thaw, or after placing in warm room for 10 days. Final solution is milky.
6:1:1 POPC:ESM:Ch	FOSMEA-10	2.5	Did not solubilize upon adding detergent solution, boiling-ice bath cycles, freeze thaw, or after placing in warm room for 10 days. Final solution is milky.
6:1:1 POPC:ESM:Ch	FOSMEA-12	2.5	Did not solubilize upon adding detergent solution, boiling-ice bath cycles, freeze thaw, or after placing in warm room for 10 days. Final solution is milky.
6:1:1 POPC:ESM:Ch	TRIPAO 10%	2.5	Did not solubilize upon adding detergent solution, boiling-ice bath cycles, freeze thaw, or after placing in warm room for 10 days. Final solution is milky.
6:1:1 POPC:ESM:Ch	ASB-14	2.5	Did not solubilize upon adding detergent solution, boiling-ice bath cycles, freeze thaw, or after placing in warm room for 10 days. Final solution is milky.
6:1:1 POPC:ESM:Ch	ANAPOE-C12E8 10%	2.5	Did not solubilize upon adding detergent solution, boiling-ice bath cycles, freeze thaw, or after placing in warm room for 10 days. Final solution is milky.
6:1:1 POPC:ESM:Ch	ANAPOE-C8E4	2.5	Did not solubilize upon adding detergent solution, boiling-ice bath cycles, freeze thaw, or after placing in warm room for 10 days. Final solution is milky.
6:1:1 POPC:ESM:Ch	Cyclophos-5	2.5	Did not solubilize upon adding detergent solution, boiling-ice bath cycles, freeze thaw, or after placing in warm room for 10 days. Final solution is milky.
6:1:1 POPC:ESM:Ch	Cyclophos-7	2.5	Did not solubilize upon adding detergent solution, boiling-ice bath cycles, freeze thaw, or after placing in warm room for 10 days. Final solution is milky.
6:1:1 POPC:ESM:Ch	Fluorinated Octyl Maltoside (FOM)	2.5	Did not solubilize upon adding detergent solution, boiling-ice bath cycles, freeze thaw, or after placing in warm room for 10 days. Final solution is milky.
6:1:1 POPC:ESM:Ch	C-HEGA-11	2.5	Did not solubilize upon adding detergent solution, boiling-ice bath cycles, freeze thaw, or after placing in warm room for 10 days. Final solution is milky.
6:1:1 POPC:ESM:Ch	LDAO	2.5	Did not solubilize upon adding detergent solution, boiling-ice bath cycles, freeze thaw, or after placing in warm room for 10 days. Final solution is milky.
2:1 DPPC:Ch	Dodecylphosphocholine (DPC)	0.33	Did not solubilize after ice-bath, boiling, vortexing, freeze thawing, or being placed in the warm room for a week. Final solution is milky at RT.
2:1 DPPC:Ch	Decylphosphocholine (DDPC)	0.33	Did not solubilize after ice-bath, boiling, vortexing, freeze thawing, or being placed in the warm room for a week. Final solution is milky at RT.
2:1 DPPC:Ch	Lauryl sarcosine (LSC)	2.5	Did not solubilize after ice-bath, boiling, vortexing, freeze thawing, or being placed in the warm room for a week. Final solution is milky at RT.
2:1 DPPC:Ch	Lubrol 17A17 10%	0.33	Did not solubilize after ice-bath, boiling, vortexing, freeze thawing, or being placed in the warm room for a week. Final solution is milky at RT.

2:1 DPPC:Ch	Brij 35	0.33	Did not solubilize after ice-bath, boiling, vortexing, freeze thawing, or being placed in the warm room for a week. Final solution is milky at RT.
2:1 DPPC:Ch	Brij 58 10%	0.33	Did not solubilize after ice-bath, boiling, vortexing, freeze thawing, or being placed in the warm room for a week. Final solution is milky at RT.
2:1 DPPC:Ch	Cymal-4	0.33	Did not solubilize after ice-bath, boiling, vortexing, freeze thawing, or being placed in the warm room for a week. Final solution is milky at RT.
2:1 DPPC:Ch	Decylmaltoside (DM)	0.33	Did not solubilize after ice-bath, boiling, vortexing, freeze thawing, or being placed in the warm room for a week. Final solution is milky at RT.
2:1 DPPC:Ch	Dodeclymaltoside (DDM)	0.33	Did not solubilize after ice-bath, boiling, vortexing, freeze thawing, or being placed in the warm room for a week. Final solution is milky at RT.
2:1 DPPC:Ch	Octylglucoside (OGC)	0.33	Did not solubilize after ice-bath, boiling, vortexing, freeze thawing, or being placed in the warm room for a week. Final solution is milky at RT.
2:1 DPPC:Ch	Octyl Glucose Neopentyl Glycol (OGNG)	0.33	Did not solubilize after ice-bath, boiling, vortexing, freeze thawing, or being placed in the warm room for a week. Final solution is milky at RT.
2:1 DPPC:Ch	Cymal-5 Neopentylglycol	0.33	Did not solubilize after ice-bath, boiling, vortexing, freeze thawing, or being placed in the warm room for a week. Final solution is milky at RT.
2:1 DPPC:Ch	Zwittergent-3-14	0.33	Did not solubilize after ice-bath, boiling, vortexing, freeze thawing, or being placed in the warm room for a week. Final solution is milky at RT.
2:1 DPPC:Ch	Zwittergent-3-10	0.33	Did not solubilize after ice-bath, boiling, vortexing, freeze thawing, or being placed in the warm room for a week. Final solution is milky at RT.
2:1 DPPC:Ch	Dodecyl Melibioside (DDMB)	0.33	Did not solubilize after ice-bath, boiling, vortexing, freeze thawing, or being placed in the warm room for a week. Final solution is milky at RT.
2:1 DPPC:Ch	FOSMEA-10	0.33	Did not solubilize after ice-bath, boiling, vortexing, freeze thawing, or being placed in the warm room for a week. Final solution is milky at RT.
2:1 DPPC:Ch	C-HEGA-11	0.33	Did not solubilize after ice-bath, boiling, vortexing, freeze thawing, or being placed in the warm room for a week. Final solution is milky at RT.
2:1 DPPC:Ch	LDAO	0.33	Did not solubilize after ice-bath, boiling, vortexing, freeze thawing, or being placed in the warm room for a week. Final solution is milky at RT.
2:1 DMPC:ESM:Ch	Brij 97 (Brij 010)	0.33	Did not solubilize after ice-bath, boiling, vortexing, freeze thawing, or being placed in the warm room for a week. Final solution is milky at RT.
6:3:1 DMPC:ESM:Ch	**Dodecylphosphocholine (DPC)**	**0.33**	**Solubilized after two cycles of ice-bath, boiling, and vortexing. Final solution is clear at RT.**
6:3:1 DMPC:ESM:Ch	**Decylphosphocholine (DDPC)**	**0.33**	**Solubilized after two cycles of ice-bath, boiling, and vortexing. Final solution is clear at RT.**
6:3:1 DMPC:ESM:Ch	Lauryl sarcosine (LSC)	2.5	Did not solubilize after ice-bath, boiling, vortexing, freeze thawing, or being placed in the warm room for a week. Final solution is cloudy at RT.
6:3:1 DMPC:ESM:Ch	Lubrol 17A17 10%	0.33	Did not solubilize after ice-bath, boiling, vortexing, freeze thawing, or being placed in the warm room for a week. Final solution is cloudy at RT.
6:3:1 DMPC:ESM:Ch	Brij 35	0.33	Did not solubilize after ice-bath, boiling, vortexing, freeze thawing, or being placed in the warm room for a week. Final solution is cloudy at RT.

6:3:1 DMPC:ESM:Ch	Brij 58 10%	0.33	Did not solubilize after ice-bath, boiling, vortexing, freeze thawing, or being placed in the warm room for a week. Final solution is cloudy at RT.
6:3:1 DMPC:ESM:Ch	**Cymal-4**	**0.33**	**Solubilized after two cycles of ice-bath, boiling, and vortexing. This solution showed viscosity above RT. Final solution is clear at RT**
6:3:1 DMPC:ESM:Ch	**Decylmaltoside (DM)**	**0.33**	**Solubilized after two cycles of ice-bath, boiling, and vortexing. This solution showed viscosity above RT. Final solution is clear at RT**
6:3:1 DMPC:ESM:Ch	Dodeclymaltoside (DDM)	0.33	Did not solubilize after ice-bath, boiling, vortexing, freeze thawing, or being placed in the warm room for a week. Final solution is milky and viscous at RT.
6:3:1 DMPC:ESM:Ch	Octylglucoside (OGC)	0.33	Did not solubilize after ice-bath, boiling, vortexing, freeze thawing, or being placed in the warm room for a week. Final solution is milky at RT.
6:3:1 DMPC:ESM:Ch	Octyl Glucose Neopentyl Glycol (OGNG)	0.33	Did not solubilize after ice-bath, boiling, vortexing, freeze thawing, or being placed in the warm room for a week. Final solution is milky at RT.
6:3:1 DMPC:ESM:Ch	**Cymal-5 Neopentylglycol**	**0.33**	**Solubilized after two cycles of ice-bath, boiling, and vortexing. Final solution is clear at RT**
6:3:1 DMPC:ESM:Ch	Zwittergent-3-14	0.33	Did not solubilize after ice-bath, boiling, vortexing, freeze thawing, or being placed in the warm room for a week. Final solution is milky at RT.
6:3:1 DMPC:ESM:Ch	**Zwittergent-3-10**	**0.33**	**Solubilized after two cycles of ice-bath, boiling, and vortexing. This solution showed viscosity above RT. Final solution is clear at RT.**
6:3:1 DMPC:ESM:Ch	**Dodecyl Melibioside (DDMB)**	**0.33**	**Solubilized after two cycles of ice-bath, boiling, and vortexing. Final solution is clear at RT.**
6:3:1 DMPC:ESM:Ch	**FOSMEA-10**	**0.33**	**Solubilized after two cycles of ice-bath, boiling, and vortexing. This solution showed viscosity above RT. Final solution is clear at RT.**
6:3:1 DMPC:ESM:Ch	**C-HEGA-11**	**0.33**	**Solubilized after two cycles of ice-bath, boiling, and vortexing. This solution showed viscosity above RT. Final solution is clear at RT.**
6:3:1 DMPC:ESM:Ch	LDAO	0.33	Did not solubilize after ice-bath, boiling, vortexing, freeze thawing, or being placed in the warm room for a week. Final solution is cloudy and slightly viscous at RT.
6:3:1 DMPC:ESM:Ch	**Brij 97 (Brij 010)**	**0.33**	**Solubilized after two cycles of ice-bath, boiling, and vortexing. This solution showed viscosity above RT. Final solution is clear at RT.**
2:1:1 POPC:ESM:Ch	Dodecylphosphocholine (DPC)	0.33	Did not solubilize after ice-bath, boiling, vortexing, freeze thawing, or being placed in the warm room for a week. Final solution is milky at RT.
2:1:1 POPC:ESM:Ch	Decylphosphocholine (DDPC)	0.33	Did not solubilize after ice-bath, boiling, vortexing, freeze thawing, or being placed in the warm room for a week. Final solution is milky at RT.
2:1:1 POPC:ESM:Ch	Lauryl sarcosine (LSC)	2.5	Did not solubilize after ice-bath, boiling, vortexing, freeze thawing, or being placed in the warm room for a week. Final solution is milky and slightly viscous at RT.
2:1:1 POPC:ESM:Ch	Lubrol 17A17 10%	0.33	Did not solubilize after ice-bath, boiling, vortexing, freeze thawing, or being placed in the warm room for a week. Final solution is slightly milky at RT.
2:1:1 POPC:ESM:Ch	Brij 35	0.33	Did not solubilize after ice-bath, boiling, vortexing, freeze thawing, or being placed in the warm room for a week. Final solution is milky at RT.

2:1:1 POPC:ESM:Ch	Brij 58 10%	0.33	Did not solubilize after ice-bath, boiling, vortexing, freeze thawing, or being placed in the warm room for a week. Final solution is slightly milky at RT.
2:1:1 POPC:ESM:Ch	Cymal-4	0.33	Did not solubilize after ice-bath, boiling, vortexing, freeze thawing, or being placed in the warm room for a week. Final solution is very cloudy and slightly viscous at RT.
2:1:1 POPC:ESM:Ch	Decylmaltoside (DM)	0.33	Did not solubilize after ice-bath, boiling, vortexing, freeze thawing, or being placed in the warm room for a week. Final solution is milky/soapy at RT.
2:1:1 POPC:ESM:Ch	Dodeclymaltoside (DDM)	0.33	Did not solubilize after ice-bath, boiling, vortexing, freeze thawing, or being placed in the warm room for a week. Final solution is very soapy at RT.
2:1:1 POPC:ESM:Ch	Octylglucoside (OGC)	0.33	Did not solubilize after ice-bath, boiling, vortexing, freeze thawing, or being placed in the warm room for a week. Final solution is milky at RT.
2:1:1 POPC:ESM:Ch	Octyl Glucose Neopentyl Glycol (OGNG)	0.33	Did not solubilize after ice-bath, boiling, vortexing, freeze thawing, or being placed in the warm room for a week. Final solution is soapy and viscous at RT.
2:1:1 POPC:ESM:Ch	Cymal-5 Neopentylglycol	0.33	Did not solubilize after ice-bath, boiling, vortexing, freeze thawing, or being placed in the warm room for a week. Final solution is milky at RT.
2:1:1 POPC:ESM:Ch	Zwittergent-3-14	0.33	Did not solubilize after ice-bath, boiling, vortexing, freeze thawing, or being placed in the warm room for a week. Final solution is milky at RT.
2:1:1 POPC:ESM:Ch	Zwittergent-3-10	0.33	Did not solubilize after ice-bath, boiling, vortexing, freeze thawing, or being placed in the warm room for a week. Final solution is cloudy at RT.
2:1:1 POPC:ESM:Ch	Dodecyl Melibioside (DDMB)	0.33	Did not solubilize after ice-bath, boiling, vortexing, freeze thawing, or being placed in the warm room for a week. Final solution is soapy and viscous at RT.
2:1:1 POPC:ESM:Ch	FOSMEA-10	0.33	Did not solubilize after ice-bath, boiling, vortexing, freeze thawing, or being placed in the warm room for a week. Final solution is very cloudy at RT.
2:1:1 POPC:ESM:Ch	C-HEGA-11	0.33	Did not solubilize after ice-bath, boiling, vortexing, freeze thawing, or being placed in the warm room for a week. Final solution is slightly milky at RT.
2:1:1 POPC:ESM:Ch	LDAO	0.33	Did not solubilize after ice-bath, boiling, vortexing, freeze thawing, or being placed in the warm room for a week. Final solution is very cloudy at RT.
2:1:1 POPC:ESM:Ch	Brij 97 (Brij 010)	0.33	Did not solubilize after ice-bath, boiling, vortexing, freeze thawing, or being placed in the warm room for a week. Final solution is milky and slightly viscous at RT.
2:1:1 DPPC:ESM:Ch	Dodecylphosphocholine (DPC)	0.33	Did not solubilize after ice-bath, boiling, vortexing, freeze thawing, or being placed in the warm room for a week. Final solution is cloudy at RT.
2:1:1 DPPC:ESM:Ch	Decylphosphocholine (DDPC)	0.33	Did not solubilize after ice-bath, boiling, vortexing, freeze thawing, or being placed in the warm room for a week. Final solution is milky at RT.
2:1:1 DPPC:ESM:Ch	Lauryl sarcosine (LSC)	2.5	Did not solubilize after ice-bath, boiling, vortexing, freeze thawing, or being placed in the warm room for a week. Final solution is milky at RT.
2:1:1 DPPC:ESM:Ch	Lubrol 17A17 10%	0.33	Did not solubilize after ice-bath, boiling, vortexing, freeze thawing, or being placed in the warm room for a week. Final solution is very cloudy at RT.

2:1:1 DPPC:ESM:Ch	Brij 35	0.33	Did not solubilize after ice-bath, boiling, vortexing, freeze thawing, or being placed in the warm room for a week. Final solution is milky at RT.
2:1:1 DPPC:ESM:Ch	Brij 58 10%	0.33	Did not solubilize after ice-bath, boiling, vortexing, freeze thawing, or being placed in the warm room for a week. Final solution is milky at RT.
2:1:1 DPPC:ESM:Ch	Cymal-4	0.33	Did not solubilize after ice-bath, boiling, vortexing, freeze thawing, or being placed in the warm room for a week. Final solution is milky at RT.
2:1:1 DPPC:ESM:Ch	Decylmaltoside (DM)	0.33	Did not solubilize after ice-bath, boiling, vortexing, freeze thawing, or being placed in the warm room for a week. Final solution is milky at RT.
2:1:1 DPPC:ESM:Ch	Dodeclymaltoside (DDM)	0.33	Did not solubilize after ice-bath, boiling, vortexing, freeze thawing, or being placed in the warm room for a week. Final solution was part gel; part liquid but only liquid and somewhat clear at RT.
2:1:1 DPPC:ESM:Ch	Octylglucoside (OGC)	0.33	Did not Solubilize after ice-bath, boiling, vortexing, freeze thawing, or being placed in the warm room for a week. Final solution is milky/soapy at RT.
2:1:1 DPPC:ESM:Ch	Octyl Glucose Neopentyl Glycol (OGNG)	0.33	Did not solubilize after ice-bath, boiling, vortexing, freeze thawing, or being placed in the warm room for a week. Final solution is milky/soapy at RT.
2:1:1 DPPC:ESM:Ch	Cymal-5 Neopentylglycol	0.33	Did not solubilize after ice-bath, boiling, vortexing, freeze thawing, or being placed in the warm room for a week. Final solution is milky at RT.
2:1:1 DPPC:ESM:Ch	Zwittergent-3-14	0.33	Did not solubilize after ice-bath, boiling, vortexing, freeze thawing, or being placed in the warm room for a week. Final solution was an opaque gel at warm temperature, and liquid and cloudy at RT.
2:1:1 DPPC:ESM:Ch	Zwittergent-3-10	0.33	Did not solubilize after ice-bath, boiling, vortexing, freeze thawing, or being placed in the warm room for a week. Final solution is very cloudy at RT.
2:1:1 DPPC:ESM:Ch	Dodecyl Melibioside (DDMB)	0.33	Did not solubilize after ice-bath, boiling, vortexing, freeze thawing, or being placed in the warm room for a week. Final solution is milky at RT.
2:1:1 DPPC:ESM:Ch	FOSMEA-10	0.33	Did not solubilize after ice-bath, boiling, vortexing, freeze thawing, or being placed in the warm room for a week. Final solution is milky at RT.
2:1:1 DPPC:ESM:Ch	C-HEGA-11	0.33	Did not solubilize after ice-bath, boiling, vortexing, freeze thawing, or being placed in the warm room for a week. Final solution is milky at RT.
2:1:1 DPPC:ESM:Ch	LDAO	0.33	Did not solubilize after ice-bath, boiling, vortexing, freeze thawing, or being placed in the warm room for a week. Final solution is somewhat clear at RT.
2:1:1 DPPC:ESM:Ch	Brij 97 (Brij 010)	0.33	Did not solubilize after ice-bath, boiling, vortexing, freeze thawing, or being placed in the warm room for a week. Final solution is milky and slightly viscous at RT.
2:1 ESM:Ch	Dodecylphosphocholine (DPC)	0.33	Did not solubilize after ice-bath, boiling, vortexing, freeze thawing, or being placed in the warm room for a week. Final solution is milky at RT.
2:1 ESM:Ch	Decylphosphocholine (DDPC)	0.33	Did not solubilize after ice-bath, boiling, vortexing, freeze thawing, or being placed in the warm room for a week. Final solution is milky at RT.
2:1 ESM:Ch	Lauryl sarcosine (LSC)	2.5	Did not solubilize after ice-bath, boiling, vortexing, freeze thawing, or being placed in the warm room for a week. Final solution is milky at RT.
2:1 ESM:Ch	Lubrol 17A17 10%	0.33	Did not solubilize after ice-bath, boiling, vortexing, freeze thawing, or being placed in the warm room for a week. Final solution is milky at RT.

2:1 ESM:Ch	Brij 35	0.33	Did not solubilize after ice-bath, boiling, vortexing, freeze thawing, or being placed in the warm room for a week. Final solution is milky at RT.
2:1 ESM:Ch	Brij 58 10%	0.33	Did not solubilize after ice-bath, boiling, vortexing, freeze thawing, or being placed in the warm room for a week. Final solution is milky and slightly viscous at RT.
2:1 ESM:Ch	Cymal-4	0.33	Did not solubilize after ice-bath, boiling, vortexing, freeze thawing, or being placed in the warm room for a week. Final solution is milky at RT.
2:1 ESM:Ch	Decylmaltoside (DM)	0.33	Did not solubilize after ice-bath, boiling, vortexing, freeze thawing, or being placed in the warm room for a week. Final solution is milky at RT.
2:1 ESM:Ch	Dodeclymaltoside (DDM)	0.33	Did not solubilize after ice-bath, boiling, vortexing, freeze thawing, or being placed in the warm room for a week. Final solution is very cloudy at RT
2:1 ESM:Ch	Octylglucoside (OGC)	0.33	Did not solubilize after ice-bath, boiling, vortexing, freeze thawing, or being placed in the warm room for a week. Final solution is milky at RT.
2:1 ESM:Ch	Octyl Glucose Neopentyl Glycol (OGNG)	0.33	Did not solubilize after ice-bath, boiling, vortexing, freeze thawing, or being placed in the warm room for a week. Final solution is milky at RT.
2:1 ESM:Ch	Cymal-5 Neopentylglycol	0.33	Did not solubilize after ice-bath, boiling, vortexing, freeze thawing, or being placed in the warm room for a week. Final solution is milky at RT.
2:1 ESM:Ch	Zwittergent-3-14	0.33	Did not solubilize after ice-bath, boiling, vortexing, freeze thawing, or being placed in the warm room for a week. Final solution is milky at RT.
2:1 ESM:Ch	Zwittergent-3-10	0.33	Did not solubilize after ice-bath, boiling, vortexing, freeze thawing, or being placed in the warm room for a week. Final solution is milky at RT.
2:1 ESM:Ch	*n*-Dodecyl-β-D-Melibiose (DDMB-β)	0.33	Did not solubilize after ice-bath, boiling, vortexing, freeze thawing, or being placed in the warm room for a week. Final solution is milky with particles at RT
2:1 ESM:Ch	FOSMEA-10	0.33	Did not solubilize after ice-bath, boiling, vortexing, freeze thawing, or being placed in the warm room for a week. Final solution is milky at RT.
2:1 ESM:Ch	C-HEGA-11	0.33	Did not solubilize after ice-bath, boiling, vortexing, freeze thawing, or being placed in the warm room for a week. Final solution is milky at RT.
2:1 ESM:Ch	LDAO	0.33	Did not solubilize after ice-bath, boiling, vortexing, freeze thawing, or being placed in the warm room for a week. Final solution is very cloudy at RT.
2:1 ESM:Ch	Brij 97 (Brij 010)	0.33	Did not solubilize after ice-bath, boiling, vortexing, freeze thawing, or being placed in the warm room for a week. Final solution is milky/soapy and slightly viscous at RT.
1:1:1 POPC:ESM:Ch	Dodecylphosphocholine (DPC)	0.33	Did not solubilize after ice-bath, boiling, vortexing, freeze thawing, or being placed in the warm room for a week. Final solution is milky at RT.
1:1:1 POPC:ESM:Ch	Decylphosphocholine (DDPC)	0.33	Did not solubilize after ice-bath, boiling, vortexing, freeze thawing, or being placed in the warm room for a week. Final solution is milky at RT.
1:1:1 POPC:ESM:Ch	Lauryl sarcosine (LSC)	2.5	Did not Solubilize after ice-bath, boiling, vortexing, freeze thawing, or being placed in the warm room for a week. Final solution is milky at RT.
1:1:1 POPC:ESM:Ch	Lubrol 17A17 10%	0.33	Did not solubilize after ice-bath, boiling, vortexing, freeze thawing, or being placed in the warm room for a week. Final solution is milky at RT.

1:1:1 POPC:ESM:Ch	Brij 35	0.33	Did not solubilize after ice-bath, boiling, vortexing, freeze thawing, or being placed in the warm room for a week. Final solution is very cloudy at RT.
1:1:1 POPC:ESM:Ch	Brij 58 10%	0.33	Did not solubilize after ice-bath, boiling, vortexing, freeze thawing, or being placed in the warm room for a week. Final solution is milky at RT.
1:1:1 POPC:ESM:Ch	Cymal-4	0.33	Did not solubilize after ice-bath, boiling, vortexing, freeze thawing, or being placed in the warm room for a week. Final solution is milky at RT.
1:1:1 POPC:ESM:Ch	Decylmaltoside (DM)	0.33	Did not solubilize after ice-bath, boiling, vortexing, freeze thawing, or being placed in the warm room for a week. Final solution is milky at RT.
1:1:1 POPC:ESM:Ch	Dodeclymaltoside (DDM)	0.33	Did not solubilize after ice-bath, boiling, vortexing, freeze thawing, or being placed in the warm room for a week. Final solution is milky at RT.
1:1:1 POPC:ESM:Ch	Octylglucoside (OGC)	0.33	Did not solubilize after ice-bath, boiling, vortexing, freeze thawing, or being placed in the warm room for a week. Final solution is milky at RT.
1:1:1 POPC:ESM:Ch	Octyl Glucose Neopentyl Glycol (OGNG)	0.33	Did not solubilize after ice-bath, boiling, vortexing, freeze thawing, or being placed in the warm room for a week. Final solution is milky at RT.
1:1:1 POPC:ESM:Ch	Cymal-5 Neopentylglycol	0.33	Did not solubilize after ice-bath, boiling, vortexing, freeze thawing, or being placed in the warm room for a week. Final solution is milky at RT.
1:1:1 POPC:ESM:Ch	Zwittergent-3-14	0.33	Did not solubilize after ice-bath, boiling, vortexing, freeze thawing, or being placed in the warm room for a week. Final solution is milky at RT.
1:1:1 POPC:ESM:Ch	Zwittergent-3-10	0.33	Did not solubilize after ice-bath, boiling, vortexing, freeze thawing, or being placed in the warm room for a week. Final solution is milky at RT.
1:1:1 POPC:ESM:Ch	Dodecyl Melibioside (DDMB)	0.33	Did not solubilize after ice-bath, boiling, vortexing, freeze thawing, or being placed in the warm room for a week. Final solution is milky at RT.
1:1:1 POPC:ESM:Ch	FOSMEA-10	0.33	Did not solubilize after ice-bath, boiling, vortexing, freeze thawing, or being placed in the warm room for a week. Final solution is milky at RT.
1:1:1 POPC:ESM:Ch	C-HEGA-11	0.33	Did not solubilize after ice-bath, boiling, vortexing, freeze thawing, or being placed in the warm room for a week. Final solution is milky at RT.
1:1:1 POPC:ESM:Ch	LDAO	0.33	Did not solubilize after ice-bath, boiling, vortexing, freeze thawing, or being placed in the warm room for a week. Final solution is milky at RT.
1:1:1 POPC:ESM:Ch	Brij 97 (Brij 010)	0.33	Did not solubilize after ice-bath, boiling, vortexing, freeze thawing, or being placed in the warm room for a week. Final solution is milky/soapy and slightly viscous at RT.
6:1:1 POPC:ESM:Ch	***n*-Dodecyl-β-D-Melibiose (DDMB-β)**	**0.33**	**Solution is clear after one cycle of ice-bath, vortexing, and boiling.**
4:1:1 POPC:ESM:Ch	***n*-Dodecyl-β-D-Melibiose (DDMB-β)**	**0.33**	**Solution is clear after one cycle of ice-bath, vortexing, and boiling.**
4:2:1 POPC:ESM:Ch	***n*-Dodecyl-β-D-Melibiose (DDMB-β)**	**0.33**	**Solution is clear after two cycles of ice-bath, vortexing, and boiling.**
4:1:2 POPC:ESM:Ch	*n*-Dodecyl-β-D-Melibiose (DDMB-β)	0.33	Solution is cloudy after three cycles of ice-bath, vortexing, and boiling.
6:3:1 DMPC:ESM:Ch	***n*-Dodecyl-β-D-Melibiose (DDMB-β)**	**0.33**	**Solution is clear after two cycles of ice-bath, vortexing, and boiling.**

4:1:1 DMPC:ESM:Ch	***n*-Dodecyl-β-D-Melibiose (DDMB-β)**	**0.33**	**Solution is clear after three cycles of ice-bath, vortexing, and boiling.**
4:2:1 DMPC:ESM:Ch	***n*-Dodecyl-β-D-Melibiose (DDMB-β)**	**0.33**	**Solution is clear after three cycles of ice-bath, vortexing, and boiling.**
2:1:1 DMPC:ESM:Ch	*n*-Dodecyl-β-D-Melibiose (DDMB-β)	0.33	Solutions is slightly cloudy after three cycles and a freeze thaw
4:1:2 DMPC:ESM:Ch	*n*-Dodecyl-β-D-Melibiose (DDMB-β)	0.33	Solution is opaque after three cycles of ice-bath, vortexing, and boiling.
6:3:1 DPPC:ESM:Ch	***n*-Dodecyl-β-D-Melibiose (DDMB-β)**	**0.33**	**Solution is clear after three cycles of ice-bath, vortexing, and boiling.**
6:1:1 POPC:ESM:Ch	***n*-Dodecyl-β-D-Melibiose (DDMB-β)**	**0.33**	**Solution is clear after three cycles of Ice-bath, vortexing, and boiling.**
4:1:1 POPC:ESM:Ch	***n*-Dodecyl-β-D-Melibiose (DDMB-β)**	**0.33**	**Solution is clear after three cycles of Ice-bath, vortexing, and boiling.**
4:2:1 POPC:ESM:Ch	***n*-Dodecyl-β-D-Melibiose (DDMB-β)**	**0.33**	**Solution is clear after three cycles of Ice-bath, vortexing, and boiling.**
4:1:2 POPC:ESM:Ch	***n*-Dodecyl-β-D-Melibiose (DDMB-β)**	**0.33**	**Solution is clear after three cycles of Ice-bath, vortexing, and boiling.**
4:1:1 DMPC:ESM:Ch	***n*-Dodecyl-β-D-Melibiose (DDMB-β)**	**0.33**	**Solution is clear after three cycles. There is a brown tint to the solution from the detergent**
6:3:1 DPPC:ESM:Ch	***n*-Tetradecyl- β-D-Melibiose**	**0.33**	**Solution is clear after two cycles of Ice-bath, vortexing, and boiling.**
6:1:1 POPC:ESM:Ch	***n*-Tetradecyl- β-D-Melibiose**	**0.33**	**Solution is clear after three cycles of Ice-bath, vortexing, and boiling.**
4:1:1 POPC:ESM:Ch	***n*-Tetradecyl- β-D-Melibiose**	**0.33**	**Solution is clear after three cycles of Ice-bath, vortexing, and boiling.**
4:2:1 POPC:ESM:Ch	*n*-Tetradecyl- β-D-Melibiose	0.33	Solution is cloudy after three cycles of ice-bath, vortexing, and boiling.
4:1:2 POPC:ESM:Ch	***n*-Tetradecyl- β-D-Melibiose**	**0.33**	**Solution is clear after two cycles of Ice-bath, vortexing, and boiling.**
4:1:1 DMPC:ESM:Ch	***n*-Tetradecyl- β-D-Melibiose**	**0.33**	**Solution is clear after three cycles of Ice-bath, vortexing, and boiling.**

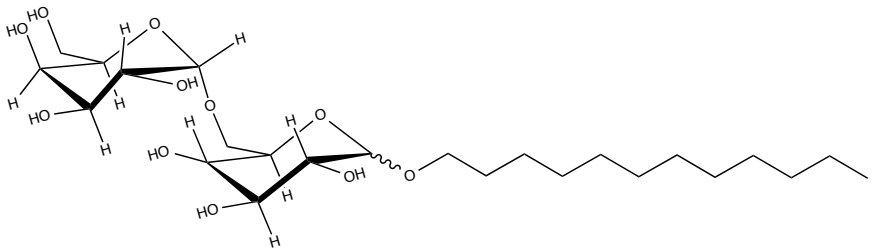

Figure 8.1. Structure of the detergent *n*-Dodecyl-β-D-Melibiose (DDMB).

Table 8.2. Diffusion measurements of novel DDMB bicelles containing cholesterol. Measurements performed at calibrated temperature 303 +/- 0.1 K (calibrated using Methanol D4 sample in the Biomolecular NMR facility), Total amphiphile = 10% (w/v) lipid + detergent. The buffering solution was 25 mM sodium phosphate pH 7.0, 75 mM NaCl, 0.5 mM EDTA, in 100% D2O. All q ratios were 0.33. Bicelles were prepared with rounds of hot bath sonication and freeze-thaw after solubilizing. All diffusion coefficients were calculated using the Topspin T1/T2 module using at least 3 peaks from the first FID that were unique to either DMPC or POPC, as determined by an overlay of 1-D spectra from DDMB or D6PC, and DMPC:D6PC, DMPC:DDMB, or POPC:DDMB bicelles. Peaks from detergent were not used, as some detergent would be expected to be in monomeric form, and thus the diffusion coefficients would not accurately reflect the size of the bicelle system. Measurements were acquired using both peak intensity and peak area, and averaged, as for some peaks data could not be assessed using one of these measurements (for instance, in the case of significantly overlapping peaks—that overlap with detergent peaks—an accurate value for peak area might not be reported, but in other cases, no value for the peak intensity was able to be computed). In cases where peaks could be assessed by both intensity and area, both measurements were used. For all calculations, no less than 5 measurements were used to obtain averages. Standard deviations were calculated for these measurements, but many were extremely small (ranging between 0.01×10^{-11} – 0.1×10^{-11}). This reflects the high fidelity of these experimental methodologies but may not be reflective of other sources of experimental error (e.g., small differences in calibrated temperatures). As a result, reported standard deviations are either the computed standard deviation for the measurement (in the case of DMPC:D6PC bicelles only) or 10% of the final value (all other bicelle conditions)—whichever was higher.

Bicelle Type (all q = 0.33)	Diffusion Coefficient (m^2/s)	Standard Deviation (m^2/s)
DMPC:D6PC	10.3×10^{-11}	$\pm 1.1 \times 10^{-11}$
DMPC:DDMB	3.6×10^{-11}	$\pm 0.4 \times 10^{-11}$
4:1:1 DMPC:ESM:Chol	6.1×10^{-11}	$\pm 0.6 \times 10^{-11}$
6:3:1 DMPC:ESM:Chol	5.6×10^{-11}	$\pm 0.6 \times 10^{-11}$
4:2:1 DMPC:ESM:Chol	5.9×10^{-11}	$\pm 0.6 \times 10^{-11}$
6:1:1 DPPC:ESM:Chol	5.9×10^{-11}	$\pm 0.6 \times 10^{-11}$
4:1:1 POPC:ESM:Chol	5.8×10^{-11}	$\pm 0.5 \times 10^{-11}$
4:2:1 POPC:ESM:Chol	5.1×10^{-11}	$\pm 0.5 \times 10^{-11}$
6:1:1 POPC:ESM:Chol	4.6×10^{-11}	$\pm 0.5 \times 10^{-11}$

Preliminary efforts to acquire NMR data on a 600 MHz spectrometer of C99 in these mixtures were promising (Figure 8.2). Efforts to repeat these experiments at higher magnetic field strength (900 MHz) were only somewhat successful, as we struggled with resolving the TM peaks, which appeared to be broadening under subsequent attempts (Figure 8.3). These peaks also were broad relative to soluble peaks in our initial experiments at 600 MHz (see peak intensity ratios plotted in Figure 8.4). It is possible that a somewhat lower-than-usual final concentration of C99 contributed to this problem; however, the peaks in the control spectrum of C99 in classical bicelles were well-resolved. During these preliminary experiments, the q-values of the bicelles were not verified. As a result, it is also possible that a lower q value could have contributed to the better signal-to-noise ratio of the preliminary NMR experiments due to faster molecular tumbling rates (and thus slower relaxation rates). However, a number of other interesting explanations exist for the fact that the TM peaks are broad relative to the soluble peaks, and remain avenues of potential exploration.

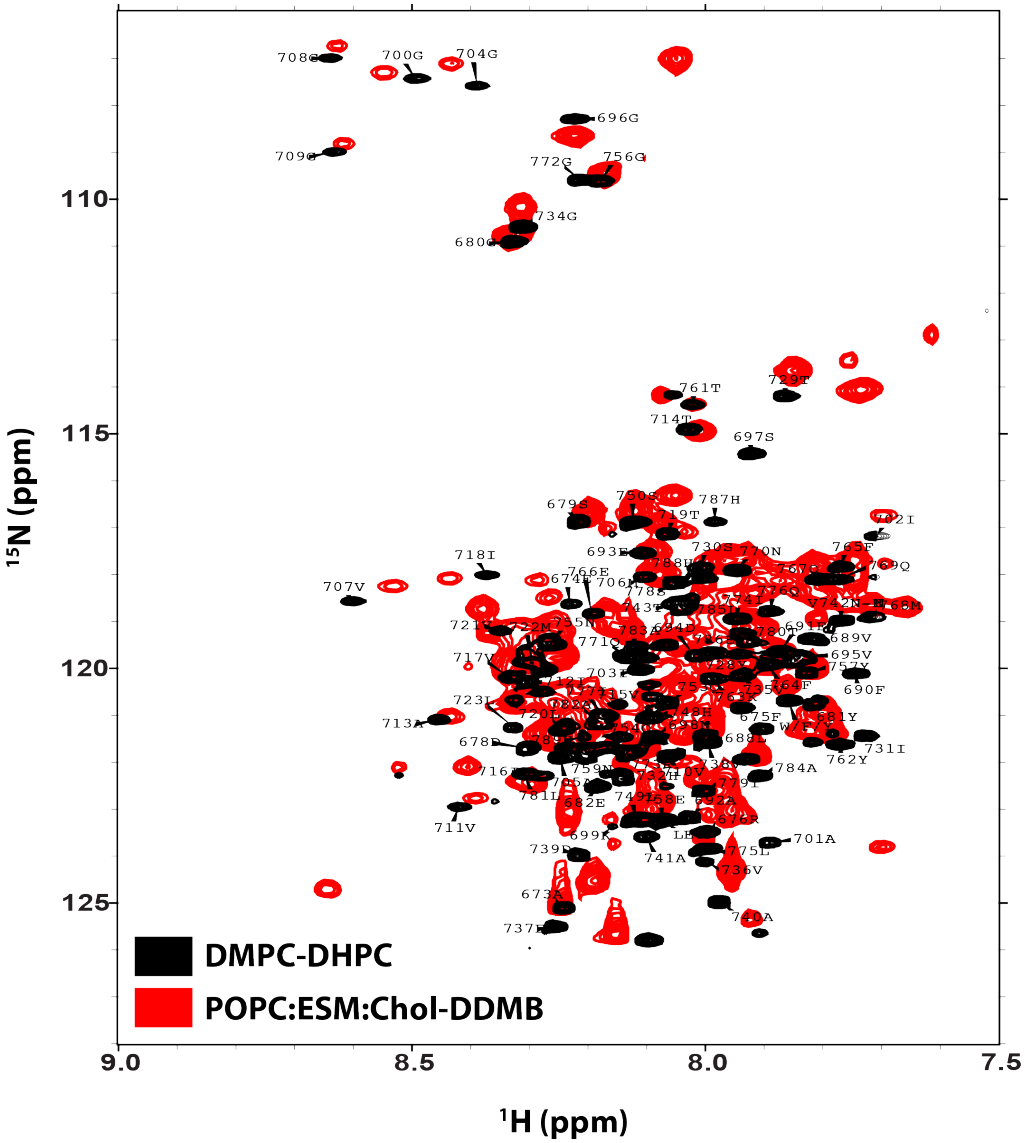

Figure 8.2. Overlay of TROSY Spectra of U-^{15}N-C99 in POPC:ESM:Chol-DDMB bicells (red; q = 0.33; acquired at 600 MHz) with DMPC-DHPC bicelles (black; q = 0.33; acquired at 900 MHz).
Buffer compositions were 250 mM Imidazole, >25 mM Acetate, pH 4.5, bicelles were at a concentration of 20% and presumed q =0.3, and [C99] ≈ 300 μM. DMPC-DHPC spectrum is from Barrett et al., 2012. POPC:ESM:Chol-DDMB spectrum was acquired at 318 K.

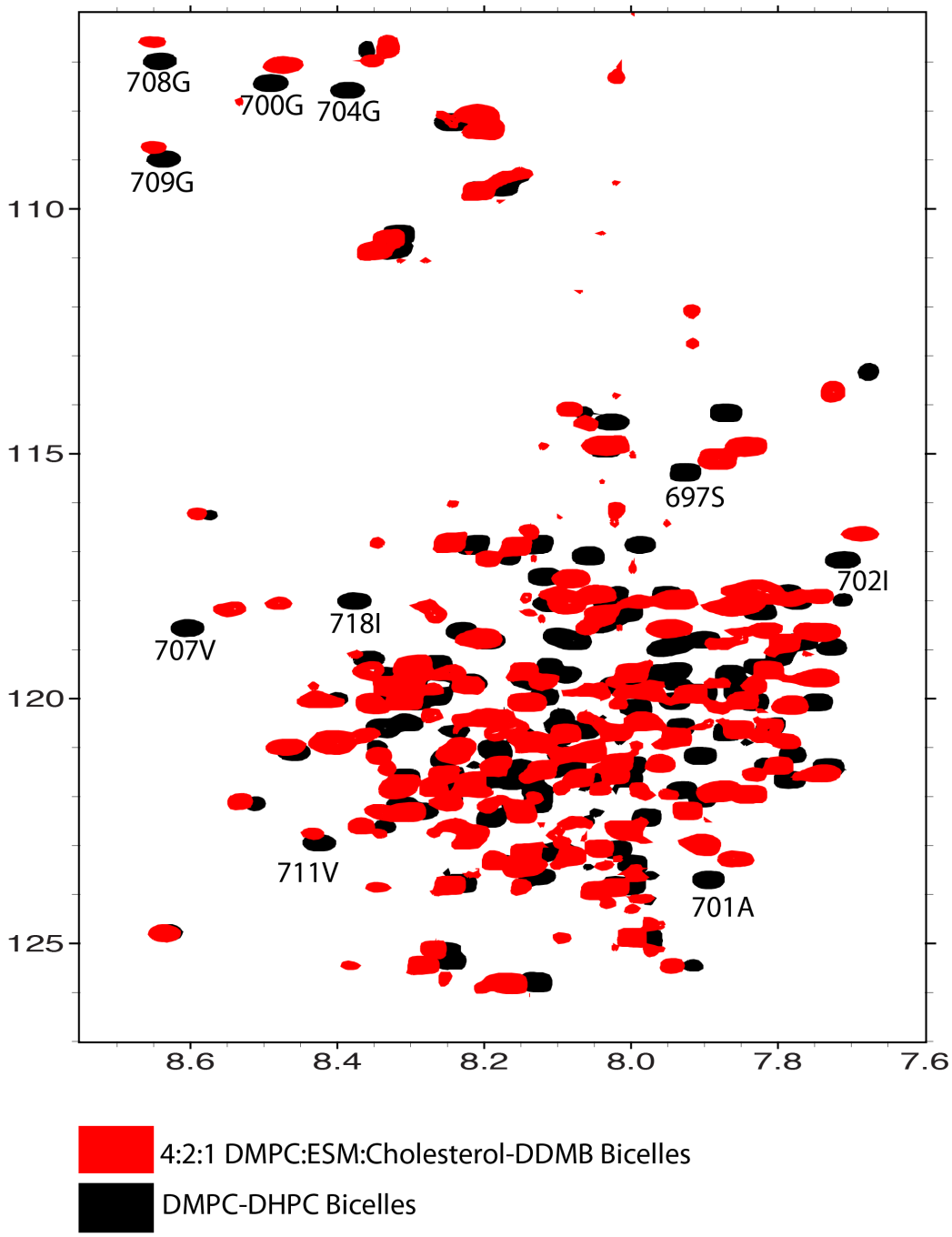

Figure 8.3. Overlay of TROSY spectra of U-^{15}N-C99 in POPC:ESM:Chol-DDMB bicelles (red) with DMPC-DHPC bicelles (black).
Buffer compositions were 5 mM Imidazole, 50 mM Acetate, pH 4.5, and bicelles were at a concentration of 20% and a verified q = 0.3, and [C99] ≈ 150 μM. Spectra were acquired at 318 K and 900 MHz.

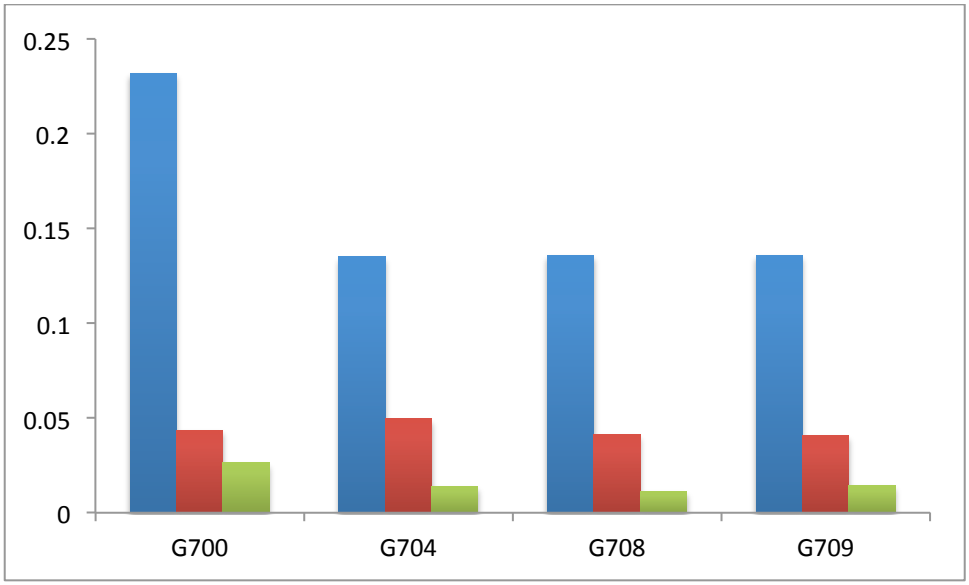

Figure 8.4. Peak intensity ratio difference between traditional bicelles and DDMB bicelles for TM peaks to soluble peaks.
All peak intensity ratios are taken from the data height as computed by Sparky and represent the data height of the labeled peak (G700, G704, G708, or G709) divided by the data height of a well-resolved, confidently assigned soluble peak (E737) in the same spectrum. Blue bars represent data from a spectrum of C99 in DMPC-DHPC control bicelles acquired at 900 MHz, from a sample prepared at the same time as the novel bicelles depicted by the green bars and depicted in Figure 6.4 in black. Red bars represent data from the spectrum of 6:1:1 DMPC:ESM:Cholesterol bicelles acquired on the 600 MHz spectrometer and depicted in Figure 6.3 in red. Green bars represent data from the 4:2:1 DMPC:ESM:Cholesterol bicelles acquired on the 900 MHz spectrometer and depicted in red in Figure 6.4.

There are a few possible explanations for the reduced TM:soluble peak intensity ratio in our new bicelles, which remain to be evaluated by further bicelle analysis. (1) Incorporation of C99 into these particular bicelles leads to reduced motions of the curved, flexible TM helix, which we know to be flexible in LMPG micelles.(Barrett et al., 2012) (2) Incorporation of C99 into bicelles containing cholesterol and sphingolipids leads to an altered binding mode of cholesterol, a hypothesis supported by the fact that the chemical shift differences seen in the glycine peaks do not match the direction of those observed in traditional bicelles doped with cholesterol (compare Figures 6.3 and 6.4 with Figure 3A in Barrett et al., 2012). If this binding mode is on an NMR intermediate-time scale, this would explain peak disappearance. (3) Incorporation of a peptide with positive hydrophobic mismatch is known to lead to increased order parameters of lipids (Lind et al., 2008). It is possible that a complex interaction between the C99 TM helix and/or the C99 amphipathic regions with the bicelle lipids resulted in different order parameters for the lipids and/or the peptide itself. (4) The experiment conducted at 600 MHz was performed in 250 mM Imidazole buffering conditions, along with much higher acetate concentrations, while the experiment conducted at 900 MHz was performed at <5 mM imidazole. It is possible that because the postulated mechanism of cholesterol binding utilizes a hydrogen bond,(Barrett et al., 2012) the reduced salt concentrations result in tighter cholesterol binding or altered cholesterol binding time-scales, and thus peak disappearance. The puzzling nature of this issue highlights the complexity of membrane protein-membrane interactions. Efforts to troubleshoot the issue of TM peak disappearance are presently underway, as well as characterization of these bicelle mixtures by dynamic light scattering.

Toward a High Resolution Structure of PMP22

As discussed in Chapter VI, a number of attempts to crystallize PMP22 in two dimensions for structure determination by 2-D electron crystallography were undertaken. These efforts resulted in the formation of crystalline arrays; however, these arrays were layered assemblies that were not in register (see Figure 8.5). As a result, they were unsuitable to structure determination. Efforts to obtain single-layer crystals were not successful.

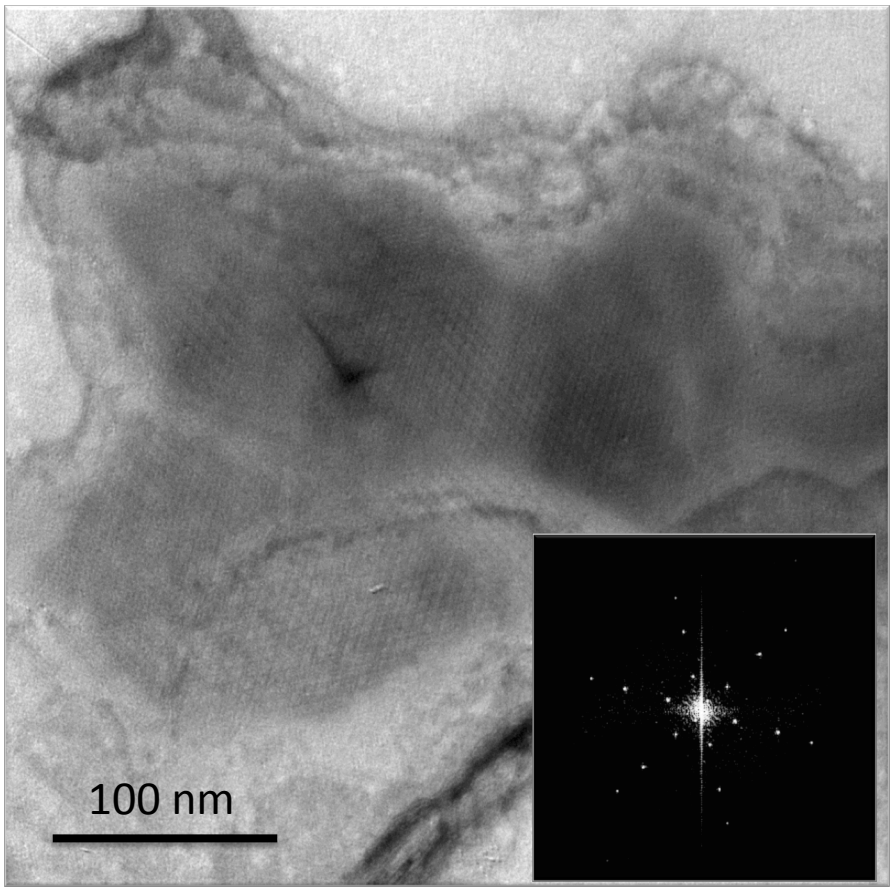

Figure 8.5. Example of a layered, mosaic PMP22 crystal in a lipid bilayer.
Crystal was obtained in DOPC at an LPR (w/w) ratio of 0.5 in 10 mM HEPEs pH 7.0, 150 mM NaCl, 1mM MgCl2, 0.5 mM DTT, 30% (v/v) glycerol. Crystals were prepared by mixing PMP22 solubilized in β-OG with mixed micelles of DOPC and β-OG and adding to dialysis buttons dialyzed against one liter of the buffer listed above. Dialysis was allowed to proceed for 3 days with addition DTT added every 12 hours. The first 24 hours dialysis proceeded at 37 °C, the second 24 hours were performed at room temperature, and the final 24 hours were again dialyzed at 37 °C. The inset represents an FFT of the image.

LIST OF PUBLICATIONS

Sanders, C. R.; **Mittendorf, K. F.** Tolerance to Changes in Membrane Lipid Composition as a Selected Trait of Membrane Proteins. *Biochemistry* **2011**, *50*, 7858–7867.

Mittendorf, K. F.; Deatherage, C. L.; Ohi, M. D.; Sanders, C. R. Tailoring of Membrane Proteins by Alternative Splicing of Pre-mRNA. *Biochemistry* **2012**, *51*, 5541–5556.

Schlebach, J. P.; Peng, D.; Kroncke, B. M.; **Mittendorf, K. F**.; Narayan, M.; Carter, B. D.; Sanders, C. R. Reversible Folding of Human Peripheral Myelin Protein 22, a Tetraspan Membrane Protein. *Biochemistry* **2013**, *52*, 3229–3241.

Song, Y.*****; **Mittendorf, K. F.***; Lu, Z.; Sanders, C. R. Imact of Bilayer Lipid Composition on the Structure and Topology of the Transmembrane Amyloid Precursor C99 Protein. *J. Am. Chem. Soc.* **2014.** *136*, 4093-4096.

Mittendorf, K. F.*; Kroncke, B. M.*****; Meiler, J.; Sanders, C. R. The Homology Model of PMP22 Suggests Mutations Resulting in Peripheral Neuropathy Disrupt Transmembrane Helix Packing. *Biochemistry* **2014**, *53*, 6139–6141.

Schlebach, J. P.; Narayan, M.; Alford, C.; **Mittendorf, K. F.**; Carter, B. D.; Li, J.; Sanders, C. R. Conformational Stability and Pathogenic Misfolding of the Integral Membrane Protein PMP22. *J. Am. Chem. Soc.* **2015**, 150623132439009.

Mittendorf, K.M.; Silvestry, M.; Hadziselimovic; A.; Law, C.L.; Schlebach, J.P; Hampton, C.M.; Wright, E.R.; Ohi, M.D.; and Sanders, C.R. Purified, Recombinant PMP22 Incorporated Into A Bilayer Forms Myelin-Like Lipoprotein Assemblies. *In Preparation.*

* *Denotes equal author contribution*

BIBLIOGRAPHY

Adamian, L.; Liang, J. Prediction of Transmembrane Helix Orientation in Polytopic Membrane Proteins. *BMC Struct. Biol.* **2006**, *6*, 13.

Adamian, L.; Naveed, H.; Liang, J. Lipid-Binding Surfaces of Membrane Proteins: Evidence From Evolutionary and Structural Analysis. *Biochim. Biophys. Acta* **2011**, *1808*, 1092–1102.

Adlkofer, K.; Martini, R.; Aguzzi, A.; Zielasek, J.; Toyka, K. V.; Suter, U. Hypermyelination and Demyelinating Peripheral Neuropathy in Pmp22-Deficient Mice. *Nat. Genet.* **1995**, *11*, 274–280.

Agrawal, H. C.; Agrawal, D. Tumor Promoters Accentuate Phosphorylation of PO: Evidence for the Presence of Protein Kinase C in Purified PNS Myelin. *Neurochem. Res.* **1989**, *14*, 409–413.

Ahmed, M. A. M.; Bamm, V. V.; Harauz, G.; Ladizhansky, V. Solid-State NMR Spectroscopy of Membrane-Associated Myelin Basic Protein--Conformation and Dynamics of an Immunodominant Epitope. *Biophys. J.* **2010**, *99*, 1247–1255.

Alexander, N.; Woetzel, N.; Meiler, J. Bcl::Cluster: a Method for Clustering Biological Molecules Coupled with Visualization in the Pymol Molecular Graphics System. *Audio, Transactions of the IRE Professional Group on* **2011**, 13–18.

Allan, D. Mapping the Lipid Distribution in the Membranes of BHK Cells (Mini-Review). *Mol Membr Biol* **1996**, *13*, 81–84.

Altschul, S. F.; Madden, T. L.; Schäffer, A. A.; Zhang, J.; Zhang, Z.; Miller, W.; Lipman, D. J. Gapped BLAST and PSI-BLAST: a New Generation of Protein Database Search Programs. *Nucleic Acids Res.* **1997**, *25*, 3389–3402.

Alzheimer's Association. 2011 Alzheimer's Disease Facts and Figures. *Alzheimers Dement* **2011**, *7*, 208–244.

Alzheimer's Association. 2014 Alzheimer's Disease Facts and Figures. *Alzheimers Dement* **2014**, *10*, e47–e92.

Amici, S. A.; Dunn, W. A.; Murphy, A. J.; Adams, N. C.; Gale, N. W.; Valenzuela, D. M.; Yancopoulos, G. D.; Notterpek, L. Peripheral Myelin Protein 22 Is in Complex with Alpha6beta4 Integrin, and Its Absence Alters the Schwann Cell Basal Lamina. *J. Neurosci.* **2006**, *26*, 1179–1189.

Amici, S. A.; Dunn, W. A.; Notterpek, L. Developmental Abnormalities in the Nerves of Peripheral Myelin Protein 22-Deficient Mice. *J. Neurosci. Res.* **2007**, *85*, 238–249.

Andrade, S. L. A.; Dickmanns, A.; Ficner, R.; Einsle, O. Crystal Structure of the Archaeal Ammonium Transporter Amt-1 From Archaeoglobus Fulgidus. *Proc. Natl. Acad. Sci. U.S.A.* **2005**, *102*, 14994–14999.

Armati, P. J.; Mathey, E. K. An Update on Schwann Cell Biology--Immunomodulation, Neural Regulation and Other Surprises. *J. Neurol. Sci.* **2013**, *333*, 68–72.

Badola, P.; Sanders, C. R. Escherichia Coli Diacylglycerol Kinase Is an Evolutionarily Optimized Membrane Enzyme and Catalyzes Direct Phosphoryl Transfer. *J. Biol. Chem.* **1997**, *272*, 24176–24182.

Bagatolli, L. A. Is the Fluid Mosaic (and the Accompanying Raft Hypothesis) a Suitable Model to Describe Fundamental Features of Biological Membranes? What May Be Missing? **2013**, 1–6.

Bakhti, M.; Aggarwal, S.; Simons, M. Myelin Architecture: Zippering Membranes Tightly Together. *Cell. Mol. Life Sci.* **2014**, *71*, 1265–1277.

Bakhti, M.; Snaidero, N.; Schneider, D.; Aggarwal, S.; Möbius, W.; Janshoff, A.; Eckhardt, M.; Nave, K.-A.; Simons, M. Loss of Electrostatic Cell-Surface Repulsion Mediates Myelin Membrane Adhesion and Compaction in the Central Nervous System. *Proc. Natl. Acad. Sci. U.S.A.* **2013**, *110*, 3143–3148.

Banik, N. L.; Smith, M. E. Protein Determinants of Myelination in Different Regions of Developing Rat Central Nervous System. *Biochem. J.* **1977**, *162*, 247–255.

Barker, W. C.; Ketcham, L. K.; Dayhoff, M. O. A Comprehensive Examination of Protein Sequences for Evidence of Internal Gene Duplication. *J. Mol. Evol.* **1978**, *10*, 265–281.

Barrett, P. J. *Structural and Cholesterol Binding Properties of the Amyloid Precursor Protein C-Terminal Fragment C99 and the Etiology of Alzheimer's Disease*; 2013.

Barrett, P. J.; Sanders, C. R.; Kaufman, S. A.; Michelsen, K.; Jordan, J. B. NSAID-Based Γ-Secretase Modulators Do Not Bind to the Amyloid-B Polypeptide. *Biochemistry* **2011**, *50*, 10328–10342.

Barrett, P. J.; Song, Y.; Van Horn, W. D.; Hustedt, E. J.; Schafer, J. M.; Hadziselimovic, A.; Beel, A. J.; Sanders, C. R. The Amyloid Precursor Protein Has a Flexible Transmembrane Domain and Binds Cholesterol. *Science* **2012**, *336*, 1168–1171.

Barth, P.; Schonbrun, J.; Baker, D. Toward High-Resolution Prediction and Design of Transmembrane Helical Protein Structures. *Proc. Natl. Acad. Sci. U.S.A.* **2007**, *104*, 15682–15687.

Barth, P.; Wallner, B.; Baker, D. Prediction of Membrane Protein Structures with Complex Topologies Using Limited Constraints. *Proc. Natl. Acad. Sci. U.S.A.* **2009**, *106*, 1409–1414.

Baumann, N.; Pham Dinh, D. Biology of Oligodendrocyte and Myelin in the Mammalian Central Nervous System. *Physiol. Rev.* **2001**, *81*, 871–927.

Bayburt, T. H.; Sligar, S. G. Membrane Protein Assembly Into Nanodiscs. *FEBS Lett.* **2010**, *584*, 1721–1727.

Beel, A. J.; Barrett, P.; Schnier, P. D.; Hitchcock, S. A.; Bagal, D.; Sanders, C. R.; Jordan, J. B. Nonspecificity of Binding of Gamma-Secretase Modulators to the Amyloid Precursor Protein. *Biochemistry* **2009**, *48*, 11837–11839.

Beel, A. J.; Mobley, C. K.; Kim, H. J.; Tian, F.; Hadziselimovic, A.; Jap, B.; Prestegard, J. H.; Sanders, C. R. Structural Studies of the Transmembrane C-Terminal Domain of the Amyloid Precursor Protein (APP): Does APP Function as a Cholesterol Sensor? *Biochemistry* **2008**, *47*, 9428–9446.

Beel, A. J.; Sakakura, M.; Barrett, P. J.; Sanders, C. R. Direct Binding of Cholesterol to the Amyloid Precursor Protein: an Important Interaction in Lipid-Alzheimer's Disease Relationships? *Biochim. Biophys. Acta* **2010**, *1801*, 975–982.

Beniac, D. R.; Luckevich, M. D.; Czarnota, G. J.; Tompkins, T. A.; Ridsdale, R. A.; Ottensmeyer, F. P.; Moscarello, M. A.; Harauz, G. Three-Dimensional Structure of Myelin Basic Protein. I. Reconstruction via Angular Reconstitution of Randomly Oriented Single Particles. *J. Biol. Chem.* **1997**, *272*, 4261–4268.

Benning, C. Mechanisms of Lipid Transport Involved in Organelle Biogenesis in Plant Cells. *Annu. Rev. Cell Dev. Biol.* **2009**, *25*, 71–91.

Berger, C.; Ho, J. T. C.; Kimura, T.; Hess, S.; Gawrisch, K.; Yeliseev, A. Preparation of Stable Isotope-Labeled Peripheral Cannabinoid Receptor CB2 by Bacterial Fermentation. *Protein Expr. Purif.* **2010**, *70*, 236–247.

Berger, P.; Niemann, A.; Suter, U. Schwann Cells and the Pathogenesis of Inherited Motor and Sensory Neuropathies (Charcot-Marie-Tooth Disease). *Glia* **2006**, *54*, 243–257.

Bertorini, T.; Narayanaswami, P.; Rashed, H. Charcot-Marie-Tooth Disease (Hereditary Motor Sensory Neuropathies) and Hereditary Sensory and Autonomic Neuropathies. *Neurologist* **2004**, *10*, 327–337.

Bizzozero, O. A.; Fridal, K.; Pastuszyn, A. Identification of the Palmitoylation Site in Rat Myelin P0 Glycoprotein. *J. Neurochem.* **1994**, *62*, 1163–1171.

Bloch, F. Nuclear Induction. *Phys. Rev.* **1946**, *70*, 460–474.

Bogdanov, M.; Dowhan, W.; Vitrac, H. Lipids and Topological Rules Governing Membrane Protein Assembly. *BBA - Molecular Cell Research* **2014**, *1843*, 1475–1488.

Bogdanov, M.; Heacock, P.; Guan, Z.; Dowhan, W. Plasticity of Lipid-Protein Interactions in the Function and Topogenesis of the Membrane Protein Lactose Permease From Escherichia Coli. *Proc. Natl. Acad. Sci. U.S.A.* **2010**, *107*, 15057–15062.

Bogdanov, M.; Xie, J.; Dowhan, W. Lipid-Protein Interactions Drive Membrane Protein Topogenesis in Accordance with the Positive Inside Rule. *J. Biol. Chem.* **2009**, *284*, 9637–9641.

Bogdanov, M.; Xie, J.; Heacock, P.; Dowhan, W. To Flip or Not to Flip: Lipid-Protein Charge Interactions Are a Determinant of Final Membrane Protein Topology. *J. Cell Biol.* **2008**, *182*, 925–935.

Bohnenberger, E.; Sandermann, H. Lipid Dependence of Diacylglycerol Kinase From Escherichia Coli. *Eur. J. Biochem.* **1983**, *132*, 645–650.

Bondar, A.-N.; del Val, C.; White, S. H. Rhomboid Protease Dynamics and Lipid Interactions. *Structure/Folding and Design* **2009**, *17*, 395–405.

Borchman, D.; Yappert, M. C. Lipids and the Ocular Lens. *J. Lipid Res.* **2010**, *51*, 2473–2488.

Botev, A.; Munter, L.-M.; Wenzel, R.; Richter, L.; Althoff, V.; Ismer, J.; Gerling, U.; Weise, C.; Koksch, B.; Hildebrand, P. W.; et al. The Amyloid Precursor Protein C-Terminal Fragment C100 Occurs in Monomeric and Dimeric Stable Conformations and Binds γ-Secretase Modulators. *Biochemistry* **2011**, *50*, 828–835.

Bowie, J. U. Membrane Protein Folding: How Important Are Hydrogen Bonds? *Curr. Opin. Struct. Biol.* **2011**, *21*, 42–49.

Brancolini, C.; Edomi, P.; Marzinotto, S.; Schneider, C. Exposure at the Cell Surface Is Required for Gas3/PMP22 to Regulate Both Cell Death and Cell Spreading: Implication for the Charcot-Marie-Tooth Type 1A and Dejerine-Sottas Diseases. *Mol. Biol. Cell* **2000**, *11*, 2901–2914.

Breukels, V.; Konijnenberg, A.; Nabuurs, S. M.; Doreleijers, J. F.; Kovalevskaya, N. V.; Vuister, G. W. Overview on the Use of NMR to Examine Protein Structure. *Curr Protoc Protein Sci* **2011**, *Chapter 17*, Unit17.5–17.5.44.

Breyer, R. M.; Strosberg, A. D.; Guillet, J. G. Mutational Analysis of Ligand Binding Activity of Beta 2 Adrenergic Receptor Expressed in Escherichia Coli. *EMBO J.* **1990**, *9*, 2679–2684.

Brosig, A.; Nesper, J.; Boos, W.; Welte, W.; Diederichs, K. Crystal Structure of a Major Outer Membrane Protein From Thermus Thermophilus HB27. *Journal of Molecular Biology* **2009**, *385*, 1445–1455.

Brunden, K. R.; Poduslo, J. F. A Phorbol Ester-Sensitive Kinase Catalyzes the Phosphorylation of P0 Glycoprotein in Myelin. *J. Neurochem.* **1987**, *49*, 1863–1872.

Bunge, R. P.; Bunge, M. B.; Bates, M. Movements of the Schwann Cell Nucleus Implicate Progression of the Inner (Axon-Related) Schwann Cell Process During Myelination. *J. Cell Biol.* **1989**, *109*, 273–284.

Burkey, K. O.; Wilson, R. F.; Wells, R. Effects of Canopy Shade on the Lipid Composition of Soybean Leaves. *Physiologia Plantarum* **1997**, *101*, 591–598.

Caffrey, M.; Cherezov, V. Crystallizing Membrane Proteins Using Lipidic Mesophases. *Nat Protoc* **2009**, *4*, 706–731.

Carenini, S.; Neuberg, D.; Schachner, M.; Suter, U.; Martini, R. Localization and Functional Roles of PMP22 in Peripheral Nerves of P0-Deficient Mice. *Glia* **1999**, *28*, 256–264.

Carpenter, E. P.; Beis, K.; Cameron, A. D.; Iwata, S. Overcoming the Challenges of Membrane Protein Crystallography. *Curr. Opin. Struct. Biol.* **2008**, *18*, 581–586.

Carrasco, M.; Amorim, M. J.; Digard, P. Lipid Raft-Dependent Targeting of the Influenza a Virus Nucleoprotein to the Apical Plasma Membrane. *Traffic* **2004**, *5*, 979–992.

Castón, J. R. Conventional Electron Microscopy, Cryo-Electron Microscopy and Cryo-Electron Tomography of Viruses. *Subcell. Biochem.* **2013**, *68*, 79–115.

Chae, P. S.; Rasmussen, S. G. F.; Rana, R. R.; Gotfryd, K.; Chandra, R.; Goren, M. A.; Kruse, A. C.; Nurva, S.; Loland, C. J.; Pierre, Y.; et al. Maltose-Neopentyl Glycol (MNG) Amphiphiles for Solubilization, Stabilization and Crystallization of Membrane Proteins. *Nat. Methods* **2010**, *7*, 1003–1008.

Chen, V. B.; Arendall, W. B.; Headd, J. J.; Keedy, D. A.; Immormino, R. M.; Kapral, G. J.; Murray, L. W.; Richardson, J. S.; Richardson, D. C. MolProbity: All-Atom Structure Validation for Macromolecular Crystallography. *Acta Crystallogr. D Biol. Crystallogr.* **2010**, *66*, 12–21.

Cheng, S.; Levy, D. The Effects of Cell Proliferation on the Lipid Composition and Fluidity of Hepatocyte Plasma Membranes. *Arch. Biochem. Biophys.* **1979**, *196*, 424–429.

Chiu, M. L. *Introduction to Membrane Proteins*; John Wiley & Sons, Inc.: Hoboken, NJ, USA, 2001; pp 1–8.

Chou, J. J.; Baber, J. L.; Bax, A. Characterization of Phospholipid Mixed Micelles by Translational Diffusion. *J Biomol NMR* **2004**, *29*, 299–308.

Clore, G. M.; Iwahara, J. Theory, Practice, and Applications of Paramagnetic Relaxation Enhancement for the Characterization of Transient Low-Population States of Biological Macromolecules and Their Complexes. *Chem. Rev.* **2009**, *109*, 4108–4139.

Coetzee, T.; Suzuki, K.; Nave, K. A.; Popko, B. Myelination in the Absence of Galactolipids and Proteolipid Proteins. *Mol. Cell. Neurosci.* **1999**, *14*, 41–51.

Colby, J.; Nicholson, R.; Dickson, K. M.; Orfali, W.; Naef, R.; Suter, U.; Snipes, G. J. PMP22 Carrying the Trembler or Trembler-J Mutation Is Intracellularly Retained in Myelinating Schwann Cells. *Neurobiol. Dis.* **2000**, *7*, 561–573.

Contreras, F. X.; Ernst, A. M.; Wieland, F.; Brugger, B. Specificity of Intramembrane Protein-Lipid Interactions. *Cold Spring Harbor Perspectives in Biology* **2011**, *3*, a004705–a004705.

Cronan, J. E. Phospholipid Alterations During Growth of Escherichia Coli. *J. Bacteriol.* **1968**, *95*, 2054–2061.

Cross, T. A.; Ekanayake, V.; Paulino, J.; Wright, A. Solid State NMR: the Essential Technology for Helical Membrane Protein Structural Characterization. *J. Magn. Reson.* **2014**, *239*, 100–109.

Cymer, F.; Heijne, von, G.; White, S. H. Mechanisms of Integral Membrane Protein Insertion and Folding. *Journal of Molecular Biology* **2015**, *427*, 999–1022.
Czerski, L.; Sanders, C. R. Functionality of a Membrane Protein in Bicelles. *Anal. Biochem.* **2000**, *284*, 327–333.

D'Urso, D.; Brophy, P. J.; Staugaitis, S. M.; Gillespie, C. S.; Frey, A. B.; Stempak, J. G.; Colman, D. R. Protein Zero of Peripheral Nerve Myelin: Biosynthesis, Membrane Insertion, and Evidence for Homotypic Interaction. *Neuron* **1990**, *4*, 449–460.

Daffu, G.; Sohi, J.; Kamholz, J. Proteolipid Protein Dimerization at Cysteine 108: Implications for Protein Structure. *Neurosci. Res.* **2012**, *74*, 144–155.

Das, R.; Baker, D. Macromolecular Modeling with Rosetta. *Annu. Rev. Biochem.* **2008**, *77*, 363–382.

Daum, G. Lipids of Mitochondria. *Biochim. Biophys. Acta* **1985**, *822*, 1–42.

Davis, I. W.; Leaver-Fay, A.; Chen, V. B.; Block, J. N.; Kapral, G. J.; Wang, X.; Murray, L. W.; Arendall, W. B.; Snoeyink, J.; Richardson, J. S.; et al. MolProbity: All-Atom Contacts and Structure Validation for Proteins and Nucleic Acids. *Nucleic Acids Res.* **2007**, *35*, W375–W383.

Deber, C. M.; Reynolds, S. J. Central Nervous System Myelin: Structure, Function, and Pathology. *Clin. Biochem.* **1991**, *24*, 113–134.

Denisov, I. G.; Grinkova, Y. V.; Lazarides, A. A.; Sligar, S. G. Directed Self-Assembly of Monodisperse Phospholipid Bilayer Nanodiscs with Controlled Size. *J. Am. Chem. Soc.* **2004**, *126*, 3477–3487.

Dhaunchak, A.-S.; Colman, D. R.; Nave, K.-A. Misalignment of PLP/DM20 Transmembrane Domains Determines Protein Misfolding in Pelizaeus-Merzbacher Disease. *J. Neurosci.* **2011**, *31*, 14961–14971.

Dhaunchak, A.-S.; Nave, K.-A. A Common Mechanism of PLP/DM20 Misfolding Causes Cysteine-Mediated Endoplasmic Reticulum Retention in Oligodendrocytes and Pelizaeus-Merzbacher Disease. *Proc. Natl. Acad. Sci. U.S.A.* **2007**, *104*, 17813–17818.

Dickson, K. M.; Bergeron, J. J. M.; Shames, I.; Colby, J.; Nguyen, D. T.; Chevet, E.; Thomas, D. Y.; Snipes, G. J. Association of Calnexin with Mutant Peripheral Myelin Protein-22 Ex Vivo: a Basis for “Gain-of-Function” ER Diseases. *Proc. Natl. Acad. Sci. U.S.A.* **2002**, *99*, 9852–9857.

Diebolder, C. A.; Koster, A. J.; Koning, R. I. Pushing the Resolution Limits in Cryo Electron Tomography of Biological Structures. *J Microsc* **2012**, *248*, 1–5.

Ding, Y.; Brunden, K. R. The Cytoplasmic Domain of Myelin Glycoprotein P0 Interacts with Negatively Charged Phospholipid Bilayers. *J. Biol. Chem.* **1994**, *269*, 10764–10770.

Dislich, B.; Lichtenthaler, S. F. The Membrane-Bound Aspartyl Protease BACE1: Molecular and Functional Properties in Alzheimer's Disease and Beyond. *Front Physiol* **2012**, *3*, 8.

Dominguez, L.; Meredith, S. C.; Straub, J. E.; Thirumalai, D. Transmembrane Fragment Structures of Amyloid Precursor Protein Depend on Membrane Surface Curvature. *J. Am. Chem. Soc.* **2014**, *136*, 854–857.

Dong, E.; Smith, J.; Heinze, S.; Alexander, N.; Meiler, J. BCL::Align-Sequence Alignment and Fold Recognition with a Custom Scoring Function Online. *Gene* **2008**, *422*, 41–46.

Dowhan, W.; Bogdanov, M. Lipid-Protein Interactions as Determinants of Membrane Protein Structure and Function. *Biochem. Soc. Trans.* **2011**, *39*, 767–774.

Earl, C.; Chantry, A.; Mohammad, N.; Glynn, P. Zinc Ions Stabilise the Association of Basic Protein with Brain Myelin Membranes. *J. Neurochem.* **1988**, *51*, 718–724.

Eichberg, J. Myelin P0: New Knowledge and New Roles. *Neurochem. Res.* **2002**, *27*, 1331–1340.
Eichberg, J.; Iyer, S. Phosphorylation of Myelin Protein: Recent Advances. *Neurochem. Res.* **1996**, *21*, 527–535.

Ernst, A. M.; Contreras, F. X.; Brügger, B.; Wieland, F. Determinants of Specificity at the Protein-Lipid Interface in Membranes. *FEBS Lett.* **2010**, *584*, 1713–1720.

Fadeel, B.; Xue, D. The Ins and Outs of Phospholipid Asymmetry in the Plasma Membrane: Roles in Health and Disease. *Critical Reviews in Biochemistry and Molecular Biology* **2009**, *44*, 264–277.

Faham, S.; Bowie, J. U. Bicelle Crystallization: a New Method for Crystallizing Membrane Proteins Yields a Monomeric Bacteriorhodopsin Structure. *Journal of Molecular Biology* **2002**, *316*, 1–6.

Farès, C.; Libich, D. S.; Harauz, G. Solution NMR Structure of an Immunodominant Epitope of Myelin Basic Protein. Conformational Dependence on Environment of an Intrinsically Unstructured Protein. *FEBS J.* **2006**, *273*, 601–614.

Filbin, M. T.; Tennekoon, G. I. Homophilic Adhesion of the Myelin P0 Protein Requires Glycosylation of Both Molecules in the Homophilic Pair. *J. Cell Biol.* **1993**, *122*, 451–459.

Filbin, M. T.; Walsh, F. S.; Trapp, B. D.; Pizzey, J. A.; Tennekoon, G. I. Role of Myelin P0 Protein as a Homophilic Adhesion Molecule. *Nature* **1990**, *344*, 871–872.

Filbin, M. T.; Zhang, K.; Li, W.; Gao, Y. Characterization of the Effect on Adhesion of Different Mutations in Myelin P0 Protein. *Ann. N. Y. Acad. Sci.* **1999**, *883*, 160–167.

Fontanini, A.; Chies, R.; Snapp, E. L.; Ferrarini, M.; Fabrizi, G. M.; Brancolini, C. Glycan-Independent Role of Calnexin in the Intracellular Retention of Charcot-Marie-Tooth 1A Gas3/PMP22 Mutants. *J. Biol. Chem.* **2005**, *280*, 2378–2387.

Frederickson, C. J. Neurobiology of Zinc and Zinc-Containing Neurons. *Int. Rev. Neurobiol.* **1989**, *31*, 145–238.

Furukawa, H.; Haga, T. Expression of Functional M2 Muscarinic Acetylcholine Receptor in Escherichia Coli. *J. Biochem.* **2000**, *127*, 151–161.

Gan, L.; Jensen, G. J. Electron Tomography of Cells. *Q. Rev. Biophys.* **2012**, *45*, 27–56.
Gao, Y.; Li, W.; Filbin, M. T. Acylation of Myelin Po Protein Is Required for Adhesion. *J. Neurosci. Res.* **2000**, *60*, 704–713.

Gaus, K.; Chklovskaia, E.; Fazekas de St Groth, B.; Jessup, W.; Harder, T. Condensation of the Plasma Membrane at the Site of T Lymphocyte Activation. *J. Cell Biol.* **2005**, *171*, 121–131.

Gaus, K.; Le Lay, S.; Balasubramanian, N.; Schwartz, M. A. Integrin-Mediated Adhesion Regulates Membrane Order. *J. Cell Biol.* **2006**, *174*, 725–734.

Giese, K. P.; Martini, R.; Lemke, G.; Soriano, P.; Schachner, M. Mouse P0 Gene Disruption Leads to Hypomyelination, Abnormal Expression of Recognition Molecules, and Degeneration of Myelin and Axons. *Cell* **1992**, *71*, 565–576.

Goldfine, H. Lipids of Prokaryotes - Structure and Distribution. *Current Topics in Membranes and Transport* **1982**, *17*, 1–43.

Gonen, T.; Cheng, Y.; Sliz, P.; Hiroaki, Y.; Fujiyoshi, Y.; Harrison, S. C.; Walz, T. Lipid-Protein Interactions in Double-Layered Two-Dimensional AQP0 Crystals. *Nature* **2005**, *438*, 633–638.

Gorzelle, B. M.; Hoffman, A. K.; Keyes, M. H.; Gray, D. N.; Ray, D. G.; Sanders, C. R. Amphipols Can Support the Activity of a Membrane Enzyme. *J. Am. Chem. Soc.* **2002**, *124*, 11594–11595.

Gow, A.; Friedrich, V. L.; Lazzarini, R. A. Many Naturally Occurring Mutations of Myelin Proteolipid Protein Impair Its Intracellular Transport. *J. Neurosci. Res.* **1994**, *37*, 574–583.

Göbl, C.; Tjandra, N. Application of Solution NMR Spectroscopy to Study Protein Dynamics. *Entropy 2012, Vol. 14, Pages 581-598* **2012**, *14*, 581–598.

Greer, J. M.; Lees, M. B. Myelin Proteolipid Protein--the First 50 Years. *Int. J. Biochem. Cell Biol.* **2002**, *34*, 211–215.

Griffith, L. S.; Schmitz, B.; Schachner, M. L2/HNK-1 Carbohydrate and Protein-Protein Interactions Mediate the Homophilic Binding of the Neural Adhesion Molecule P0. *J. Neurosci. Res.* **1992**, *33*, 639–648.

Grisshammer, R.; White, J. F.; Trinh, L. B.; Shiloach, J. Large-Scale Expression and Purification of a G-Protein-Coupled Receptor for Structure Determination -- an Overview. *J. Struct. Funct. Genomics* **2005**, *6*, 159–163.

Gulaya, N. M.; Volkov, G. L.; Klimashevsky, V. M.; Govseeva, N. N.; Melnik, A. A. Changes in Lipid Composition of Neuroblastoma C1300 N18 Cell During Differentiation. *Neuroscience* **1989**, *30*, 153–164.

Guo, J.; Wang, L.; Zhang, Y.; Wu, J.; Arpag, S.; Hu, B.; Imhof, B. A.; Tian, X.; Carter, B. D.; Suter, U.; et al. Abnormal Junctions and Permeability of Myelin in PMP22-Deficient Nerves. *Ann. Neurol.* **2014**, *75*, 255–265.

Gupta, N.; DeFranco, A. L. Lipid Rafts and B Cell Signaling. *Semin. Cell Dev. Biol.* **2007**, *18*, 616–626.

Han, H.; Myllykoski, M.; Ruskamo, S.; Wang, C.; Kursula, P. Myelin-Specific Proteins: a Structurally Diverse Group of Membrane-Interacting Molecules. *Biofactors* **2013**, *39*, 233–241.

Harapin, J.; Eibauer, M.; Medalia, O. Structural Analysis of Supramolecular Assemblies by Cryo-Electron Tomography. *Structure* **2013**, *21*, 1522–1530.

Harries, W. E. C.; Akhavan, D.; Miercke, L. J. W.; Khademi, S.; Stroud, R. M. The Channel Architecture of Aquaporin 0 at a 2.2-a Resolution. *Proc. Natl. Acad. Sci. U.S.A.* **2004**, *101*, 14045–14050.

Hasse, B.; Bosse, F.; Hanenberg, H.; Müller, H. W. Peripheral Myelin Protein 22 kDa and Protein Zero: Domain Specific Trans-Interactions. *Mol. Cell. Neurosci.* **2004**, *27*, 370–378.

Heinen, W.; Klein, H. P.; Volkmann, C. M. Fatty Acid Composition of Thermus Aquaticus at Different Growth Temperatures. *Arch Mikrobiol* **1970**, *72*, 199–202.

Henry, S. A. Membrane Lipids of Yeast: Biochemical and Genetic Studies. *Cold Spring Harbor Monograph Archive* **1982**.

Hite, R. K.; Gonen, T.; Harrison, S. C.; Walz, T. Interactions of Lipids with Aquaporin-0 and Other Membrane Proteins. *Pflugers Arch.* **2008**, *456*, 651–661.

Hite, R. K.; Li, Z.; Walz, T. Principles of Membrane Protein Interactions with Annular Lipids Deduced From Aquaporin-0 2D Crystals. *EMBO J.* **2010**, *29*, 1652–1658.

Hoenger, A. High-Resolution Cryo-Electron Microscopy on Macromolecular Complexes and Cell Organelles. *Protoplasma* **2014**, *251*, 417–427.

Holmes, O.; Paturi, S.; Ye, W.; Wolfe, M. S.; Selkoe, D. J. Effects of Membrane Lipids on the Activity and Processivity of Purified Γ-Secretase. *Biochemistry* **2012**, *51*, 3565–3575.

Holthuis, J. C. M.; Menon, A. K. Lipid Landscapes and Pipelines in Membrane Homeostasis. *Nature* **2014**, *510*, 48–57.

Hu, J.; Prinz, W. A.; Rapoport, T. A. Weaving the Web of ER Tubules. *Cell* **2011**, *147*, 1226–1231.

Hunte, C. Specific Protein-Lipid Interactions in Membrane Proteins. *Biochem. Soc. Trans.* **2005**, *33*, 938–942.

Hunte, C.; Richers, S. Lipids and Membrane Protein Structures. *Curr. Opin. Struct. Biol.* **2008**, *18*, 406–411.

Hunter, M. I.; Thirkell, D. Variation in Fatty Acid Composition of Sarcina Flava Membrane Lipid with the Age of the Bacterial Culture. *J. Gen. Microbiol.* **1971**, *65*, 115–118.

Inouye, H.; Tsuruta, H.; Sedzik, J.; Uyemura, K.; Kirschner, D. A. Tetrameric Assembly of Full-Sequence Protein Zero Myelin Glycoprotein by Synchrotron X-Ray Scattering. *Biophys. J.* **1999**, *76*, 423–437.

Jacobson, K.; Mouritsen, O. G.; Anderson, R. G. W. Lipid Rafts: at a Crossroad Between Cell Biology and Physics. *Nat. Cell Biol.* **2007**, *9*, 7–14.

Jahn, O.; Tenzer, S.; Werner, H. B. Myelin Proteomics: Molecular Anatomy of an Insulating Sheath. *Mol. Neurobiol.* **2009**, *40*, 55–72.

Jastrzebska, B.; Ringler, P.; Palczewski, K.; Engel, A. The Rhodopsin-Transducin Complex Houses Two Distinct Rhodopsin Molecules. *J. Struct. Biol.* **2013**, *182*, 164–172.

Jetten, A. M.; Suter, U. The Peripheral Myelin Protein 22 and Epithelial Membrane Protein Family. *Prog. Nucleic Acid Res. Mol. Biol.* **2000**, *64*, 97–129.

Jiang, Y.; Lee, A.; Chen, J.; Ruta, V.; Cadene, M.; Chait, B. T.; MacKinnon, R. X-Ray Structure of a Voltage-Dependent K+ Channel. *Nature* **2003**, *423*, 33–41.

Jones, D. T. Protein Secondary Structure Prediction Based on Position-Specific Scoring Matrices. *Journal of Molecular Biology* **1999**, *292*, 195–202.

Jung, M.; Sommer, I.; Schachner, M.; Nave, K. A. Monoclonal Antibody O10 Defines a Conformationally Sensitive Cell-Surface Epitope of Proteolipid Protein (PLP): Evidence That PLP Misfolding Underlies Dysmyelination in Mutant Mice. *J. Neurosci.* **1996**, *16*, 7920–7929.

Kahsay, R. Y.; Gao, G.; Liao, L. An Improved Hidden Markov Model for Transmembrane Protein Detection and Topology Prediction and Its Applications to Complete Genomes. *Bioinformatics* **2005**, *21*, 1853–1858.

Kaneshiro, E. S. Lipids of Paramecium. *J. Lipid Res.* **1987**, *28*, 1241–1258.

Kaurinovic, B.; Popovic, M. Liposomes as a Tool to Study Lipid Peroxidation. In *Lipid Peroxidation*; InTech, 2012; pp 1–26.

Kay, L. E.; Gardner, K. H. Solution NMR Spectroscopy Beyond 25 kDa. *Curr. Opin. Struct. Biol.* **1997**, *7*, 722–731.

Khademi, S.; O'Connell, J.; Remis, J.; Robles-Colmenares, Y.; Miercke, L. J. W.; Stroud, R. M. Mechanism of Ammonia Transport by Amt/MEP/Rh: Structure of AmtB at 1.35 a. *Science* **2004**, *305*, 1587–1594.

Kidd, G. J.; Ohno, N.; Trapp, B. D. Biology of Schwann Cells. *Handb Clin Neurol* **2013**, *115*, 55–79.

Kielec, J. M.; Valentine, K. G.; Babu, C. R.; Wand, A. J. Reverse Micelles in Integral Membrane Protein Structural Biology by Solution NMR Spectroscopy. *Structure/Folding and Design* **2009**, *17*, 345–351.

Kim, D. E.; Chivian, D.; Baker, D. Protein Structure Prediction and Analysis Using the Robetta Server. *Nucleic Acids Res.* **2004**, *32*, W526–W531.

King, R. Microscopic Anatomy: Normal Structure. *Handb Clin Neurol* **2013**, *115*, 7–27.

Kleinschmidt, J. H.; Popot, J.-L. Folding and Stability of Integral Membrane Proteins in Amphipols. *Arch. Biochem. Biophys.* **2014**, *564*, 327–343.

Koehler, J.; Sulistijo, E. S.; Sakakura, M.; Kim, H. J.; Ellis, C. D.; Sanders, C. R. Lysophospholipid Micelles Sustain the Stability and Catalytic Activity of Diacylglycerol Kinase in the Absence of Lipids. *Biochemistry* **2010**, *49*, 7089–7099.

Konietzko, U. AICD Nuclear Signaling and Its Possible Contribution to Alzheimer's Disease. *Curr Alzheimer Res* **2012**, *9*, 200–216.

Krause, G.; Winkler, L.; Mueller, S. L.; Haseloff, R. F.; Piontek, J.; Blasig, I. E. Structure and Function of Claudins. *Biochim. Biophys. Acta* **2008**, *1778*, 631–645.

Kremer, J. R.; Mastronarde, D. N.; McIntosh, J. R. Computer Visualization of Three-Dimensional Image Data Using IMOD. *J. Struct. Biol.* **1996**, *116*, 71–76.

Krigbaum, W. R.; Hsu, T. S. Molecular Conformation of Bovine A1 Basic Protein, a Coiling Macromolecule in Aqueous Solution. *Biochemistry* **1975**, *14*, 2542–2546.

Kuiper, P. J. C.; Kähr, M.; Stuiver, C. E. E.; Kylin, A. Lipid Composition of Whole Roots and of Ca2+, Mg2+-Activated Adenosine Triphosphatases From Wheat and Oat as Related to Mineral Nutrition. *Physiologia Plantarum* **1974**, *32*, 33–36.

Kumar, N.; Gross, J. B.; Ahlskog, J. E. Copper Deficiency Myelopathy Produces a Clinical Picture Like Subacute Combined Degeneration. *Neurology* **2004**, *63*, 33–39.
Kursula, P. Structural Properties of Proteins Specific to the Myelin Sheath. *Amino Acids* **2008**, *34*, 175–185.

Kusumi, A.; Koyama-Honda, I.; Suzuki, K. Molecular Dynamics and Interactions for Creation of Stimulation-Induced Stabilized Rafts From Small Unstable Steady-State Rafts. *Traffic* **2004**, *5*, 213–230.

Kwiatek, J. M.; Hinde, E.; Gaus, K. Microscopy Approaches to Investigate Protein Dynamics and Lipid Organization. *Mol Membr Biol* **2014**, *31*, 141–151.

Lai, D.; Springstead, J. R.; Monbouquette, H. G. Effect of Growth Temperature on Ether Lipid Biochemistry in Archaeoglobus Fulgidus. *Extremophiles* **2008**, *12*, 271–278.

Lampe, M. A.; Williams, M. L.; Elias, P. M. Human Epidermal Lipids: Characterization and Modulations During Differentiation. *J. Lipid Res.* **1983**, *24*, 131–140.

Lanwert, C.; Jeserich, G. Structure, Heterologous Expression, and Adhesive Properties of the P(0)-Like Myelin Glycoprotein IP1 of Trout CNS. *Microsc. Res. Tech.* **2001**, *52*, 637–644.

Larkindale; Huang. Changes of Lipid Composition and Saturation Level in Leaves and Roots for Heat-Stressed and Heat-Acclimated Creeping Bentgrass (Agrostis Stolonifera). *Environ Exp Bot* **2004**, *51*, 11–11.

Lee, A. G. How Lipids Affect the Activities of Integral Membrane Proteins. *Biochim. Biophys. Acta* **2004**, *1666*, 62–87.

Lee, A. G. Lipid-Protein Interactions. *Biochem. Soc. Trans.* **2011**, *39*, 761–766.

Lee, J.; Gravel, M.; Zhang, R.; Thibault, P.; Braun, P. E. Process Outgrowth in Oligodendrocytes Is Mediated by CNP, a Novel Microtubule Assembly Myelin Protein. *J. Cell Biol.* **2005a**, *170*, 661–673.

Lee, S.-Y.; Lee, A.; Chen, J.; MacKinnon, R. Structure of the KvAP Voltage-Dependent K+ Channel and Its Dependence on the Lipid Membrane. *Proc. Natl. Acad. Sci. U.S.A.* **2005b**, *102*, 15441–15446.

Leitz, A.; Bayburt, T.; Barnakov, A.; Springer, B.; Sligar, S. Functional Reconstitution of B2-Adrenergic Receptors Utilizing Self-Assembling Nanodisc Technology. *Biotech.* **2006**, *40*, 601–612.

Lemmin, T.; Dimitrov, M.; Fraering, P. C.; Dal Peraro, M. Perturbations of the Straight Transmembrane A-Helical Structure of the Amyloid Precursor Protein Affect Its Processing by Γ-Secretase. *J. Biol. Chem.* **2014**, *289*, 6763–6774.

Lewis, B. A.; Engelman, D. M. Lipid Bilayer Thickness Varies Linearly with Acyl Chain Length in Fluid Phosphatidylcholine Vesicles. *Journal of Molecular Biology* **1983**, *166*, 211–217.

Li, D.; Caffrey, M. Lipid Cubic Phase as a Membrane Mimetic for Integral Membrane Protein Enzymes. *Proc. Natl. Acad. Sci. U.S.A.* **2011**, *108*, 8639–8644.

Li, J.; Parker, B.; Martyn, C.; Natarajan, C.; Guo, J. The PMP22 Gene and Its Related Diseases. *Mol. Neurobiol.* **2013**, *47*, 673–698.

Liao, M.; Cao, E.; Julius, D.; Cheng, Y. Structure of the TRPV1 Ion Channel Determined by Electron Cryo-Microscopy. *Nature* **2013**, *504*, 107–112.

Lichtenthaler, S. F.; Beher, D.; Grimm, H. S.; Wang, R.; Shearman, M. S.; Masters, C. L.; Beyreuther, K. The Intramembrane Cleavage Site of the Amyloid Precursor Protein Depends on the Length of Its Transmembrane Domain. *Proc. Natl. Acad. Sci. U.S.A.* **2002**, *99*, 1365–1370.

Lind, J.; Nordin, J.; Mäler, L. Lipid Dynamics in Fast-Tumbling Bicelles with Varying Bilayer Thickness: Effect of Model Transmembrane Peptides. *Biochim. Biophys. Acta* **2008**, *1778*, 2526–2534.

Liu, N.; Yamauchi, J.; Shooter, E. M. Recessive, but Not Dominant, Mutations in Peripheral Myelin Protein 22 Gene Show Unique Patterns of Aggregation and Intracellular Trafficking. *Neurobiol. Dis.* **2004**, *17*, 300–309.

Liu, Z.; Wang, Y.; Yedidi, R. S.; Brunzelle, J. S.; Kovari, I. A.; Sohi, J.; Kamholz, J.; Kovari, L. C. Crystal Structure of the Extracellular Domain of Human Myelin Protein Zero. *Proteins* **2012**, *80*, 307–313.

Lu, P.; Bai, X.-C.; Ma, D.; Xie, T.; Yan, C.; Sun, L.; Yang, G.; Zhao, Y.; Zhou, R.; Scheres, S. H. W.; et al. Three-Dimensional Structure of Human Γ-Secretase. *Nature* **2014**, *512*, 166–170.

Lučič, V.; Rigort, A.; Baumeister, W. Cryo-Electron Tomography: the Challenge of Doing Structural Biology in Situ. *J. Cell Biol.* **2013**, *202*, 407–419.

Luzzati, V.; Gambacorta, A.; Derosa, M.; Gulik, A. Polar Lipids of Thermophilic Prokaryotic Organisms - Chemical and Physical Structure. *Annu Rev Biophys Biophys Chem* **1987**, *16*, 25–47.

Mac Millan, S. V.; Ishiyama, N.; White, G. F.; Palaniyar, N.; Hallett, F. R.; Harauz, G. Myelin Basic Protein Component C1 in Increasing Concentrations Can Elicit Fusion, Aggregation, and Fragmentation of Myelin-Like Membranes. *Eur. J. Cell Biol.* **2000**, *79*, 327–335.

MacKenzie, K. R.; Fleming, K. G. Association Energetics of Membrane Spanning Alpha-Helices. *Curr. Opin. Struct. Biol.* **2008**, *18*, 412–419.

Marenchino, M.; Williamson, P. T. F.; Murri, S.; Zandomeneghi, G.; Wunderli-Allenspach, H.; Meier, B. H.; Krämer, S. D. Dynamics and Cleavability at the Alpha-Cleavage Site of APP(684-726) in Different Lipid Environments. *Biophys. J.* **2008**, *95*, 1460–1473.

Marion, D. An Introduction to Biological NMR Spectroscopy. *Mol. Cell Proteomics* **2013**, *12*, 3006–3025.

Marsh, D. Protein Modulation of Lipids, and Vice-Versa, in Membranes. *Biochim. Biophys. Acta* **2008**, *1778*, 1545–1575.

Mastronarde, D. N. Dual-Axis Tomography: an Approach with Alignment Methods That Preserve Resolution. *J. Struct. Biol.* **1997**, *120*, 343–352.

Mastronarde, D. N. Automated Electron Microscope Tomography Using Robust Prediction of Specimen Movements. *J. Struct. Biol.* **2005**, *152*, 36–51.

Matsumoto, K. Dispensable Nature of Phosphatidylglycerol in Escherichia Coli: Dual Roles of Anionic Phospholipids. *Mol. Microbiol.* **2001**, *39*, 1427–1433.

Matthews, E. E.; Zoonens, M.; Engelman, D. M. Dynamic Helix Interactions in Transmembrane Signaling. *Cell* **2006**, *127*, 447–450.

Márquez, D. C.; Chen, H.-W.; Curran, E. M.; Welshons, W. V.; Pietras, R. J. Estrogen Receptors in Membrane Lipid Rafts and Signal Transduction in Breast Cancer. *Mol. Cell. Endocrinol.* **2006**, *246*, 91–100.

Meiler, J.; Baker, D. Coupled Prediction of Protein Secondary and Tertiary Structure. *Proc. Natl. Acad. Sci. U.S.A.* **2003**, *100*, 12105–12110.

Meuleman, J.; Timmerman, V.; Nelis, E.; De Jonghe, P. Molecular Genetics of Inherited Peripheral Neuropathies: Who Are the Actors? *Acta Neurol Belg* **2000**, *100*, 171–180.

Milne, J. L. S.; Borgnia, M. J.; Bartesaghi, A.; Tran, E. E. H.; Earl, L. A.; Schauder, D. M.; Lengyel, J.; Pierson, J.; Patwardhan, A.; Subramaniam, S. Cryo-Electron Microscopy--a Primer for the Non-Microscopist. *FEBS J.* **2013**, *280*, 28–45.

Milne, J. L. S.; Subramaniam, S. Cryo-Electron Tomography of Bacteria: Progress, Challenges and Future Prospects. *Nat. Rev. Microbiol.* **2009**, *7*, 666–675.

Min, Y.; Kristiansen, K.; Boggs, J. M.; Husted, C.; Zasadzinski, J. A.; Israelachvili, J. Interaction Forces and Adhesion of Supported Myelin Lipid Bilayers Modulated by Myelin Basic Protein. *Proc. Natl. Acad. Sci. U.S.A.* **2009**, *106*, 3154–3159.

Mitra, K.; Ubarretxena-Belandia, I.; Taguchi, T.; Warren, G.; Engelman, D. M. Modulation of the Bilayer Thickness of Exocytic Pathway Membranes by Membrane Proteins Rather Than Cholesterol. *Proc. Natl. Acad. Sci. U.S.A.* **2004**, *101*, 4083–4088.

Mittendorf, K. F.; Deatherage, C. L.; Ohi, M. D.; Sanders, C. R. Tailoring of Membrane Proteins by Alternative Splicing of Pre-mRNA. *Biochemistry* **2012**, *51*, 5541–5556.

Mittendorf, K. F.; Kroncke, B. M.; Meiler, J.; Sanders, C. R. The Homology Model of PMP22 Suggests Mutations Resulting in Peripheral Neuropathy Disrupt Transmembrane Helix Packing. *Biochemistry* **2014**, *53*, 6139–6141.

Miyashita, N.; Straub, J. E.; Thirumalai, D. Structures of Beta-Amyloid Peptide 1-40, 1-42, and 1-55-the 672-726 Fragment of APP-in a Membrane Environment with Implications for Interactions with Gamma-Secretase. *J. Am. Chem. Soc.* **2009**, *131*, 17843–17852.

Mobley, C. K.; Myers, J. K.; Hadziselimovic, A.; Ellis, C. D.; Sanders, C. R. Purification and Initiation of Structural Characterization of Human Peripheral Myelin Protein 22, an Integral Membrane Protein Linked to Peripheral Neuropathies. *Biochemistry* **2007**, *46*, 11185–11195.

Mokrab, Y.; Stevens, T. J.; Mizuguchi, K. A Structural Dissection of Amino Acid Substitutions in Helical Transmembrane Proteins. *Proteins* **2010**, *78*, 2895–2907.

Morell, P.; Greenfield, S.; Costantino-Ceccarini, E.; Wisniewski, H. Changes in the Protein Composition of Mouse Brain Myelin During Development. *J. Neurochem.* **1972**, *19*, 2545–2554.

Morell, P.; Quarles, R. H. *Characteristic Composition of Myelin*; Basic Neurochemistry: Molecular, 1999a.

Morell, P.; Quarles, R. H. The Myelin Sheath. **1999b**.

Morrison, E. A.; Henzler-Wildman, K. A. Reconstitution of Integral Membrane Proteins Into Isotropic Bicelles with Improved Sample Stability and Expanded Lipid Composition Profile. *Biochim. Biophys. Acta* **2012**, *1818*, 814–820.

Murphy, M. P.; Hickman, L. J.; Eckman, C. B.; Uljon, S. N.; Wang, R.; Golde, T. E. Gamma-Secretase, Evidence for Multiple Proteolytic Activities and Influence of Membrane Positioning of Substrate on Generation of Amyloid Beta Peptides of Varying Length. *J. Biol. Chem.* **1999**, *274*, 11914–11923.

Myers, J. K.; Mobley, C. K.; Sanders, C. R. The Peripheral Neuropathy-Linked Trembler and Trembler-J Mutant Forms of Peripheral Myelin Protein 22 Are Folding-Destabilized. *Biochemistry* **2008**, *47*, 10620–10629.

Nadezhdin, K. D.; Bocharova, O. V.; Bocharov, E. V.; Arseniev, A. S. Dimeric Structure of Transmembrane Domain of Amyloid Precursor Protein in Micellar Environment. *FEBS Lett.* **2012**, *586*, 1687–1692.

Naef, R.; Adlkofer, K.; Lescher, B.; Suter, U. Aberrant Protein Trafficking in Trembler Suggests a Disease Mechanism for Hereditary Human Peripheral Neuropathies. *Mol. Cell. Neurosci.* **1997**, *9*, 13–25.

Naef, R.; Suter, U. Impaired Intracellular Trafficking Is a Common Disease Mechanism of PMP22 Point Mutations in Peripheral Neuropathies. *Neurobiol. Dis.* **1999**, *6*, 1–14.

Nelis, E.; Haites, N.; Van Broeckhoven, C. Mutations in the Peripheral Myelin Genes and Associated Genes in Inherited Peripheral Neuropathies. *Hum. Mutat.* **1999**, *13*, 11–28.

Nguyen, D. H.; Hildreth, J. E. Evidence for Budding of Human Immunodeficiency Virus Type 1 Selectively From Glycolipid-Enriched Membrane Lipid Rafts. *J. Virol.* **2000**, *74*, 3264–3272.

Nguyen, E. D.; Norn, C.; Frimurer, T. M.; Meiler, J. Assessment and Challenges of Ligand Docking Into Comparative Models of G-Protein Coupled Receptors. *PLoS ONE* **2013**, *8*, e67302.

Nicholson, G. A. The Dominantly Inherited Motor and Sensory Neuropathies: Clinical and Molecular Advances. *Muscle Nerve* **2006**, *33*, 589–597.

Nickell, S.; Kofler, C.; Leis, A. P.; Baumeister, W. A Visual Approach to Proteomics. *Nat. Rev. Mol. Cell Biol.* **2006**, *7*, 225–230.

Nicolson, G. L. The Fluid—Mosaic Model of Membrane Structure: Still Relevant to Understanding the Structure, Function and Dynamics of Biological Membranes After More Than 40years. *BBA - Biomembranes* **2014**, *1838*, 1451–1466.

Niemann, S.; Sereda, M. W.; Suter, U.; Griffiths, I. R.; Nave, K. A. Uncoupling of Myelin Assembly and Schwann Cell Differentiation by Transgenic Overexpression of Peripheral Myelin Protein 22. *J. Neurosci.* **2000**, *20*, 4120–4128.

Niemelä, P. S.; Ollila, S.; Hyvönen, M. T.; Karttunen, M.; Vattulainen, I. Assessing the Nature of Lipid Raft Membranes. *PLoS Comput. Biol.* **2007**, *3*, e34.

Norton, W. T.; Poduslo, S. E. Myelination in Rat-Brain - Method of Myelin Isolation. *J. Neurochem.* **1973**, *21*, 749–757.

Notterpek, L.; Roux, K. J.; Amici, S. A.; Yazdanpour, A.; Rahner, C.; Fletcher, B. S. Peripheral Myelin Protein 22 Is a Constituent of Intercellular Junctions in Epithelia. *Proc. Natl. Acad. Sci. U.S.A.* **2001**, *98*, 14404–14409.

Nunan, J.; Small, D. H. Regulation of APP Cleavage by Alpha-, Beta- and Gamma-Secretases. *FEBS Lett.* **2000**, *483*, 6–10.

Nyholm, T. K. M.; Ozdirekcan, S.; Killian, J. A. How Protein Transmembrane Segments Sense the Lipid Environment. *Biochemistry* **2007**, *46*, 1457–1465.

Oberai, A.; Joh, N. H.; Pettit, F. K.; Bowie, J. U. Structural Imperatives Impose Diverse Evolutionary Constraints on Helical Membrane Proteins. *Proc. Natl. Acad. Sci. U.S.A.* **2009**, *106*, 17747–17750.

Ohi, M.; Li, Y.; Cheng, Y.; Walz, T. Negative Staining and Image Classification - Powerful Tools in Modern Electron Microscopy. *Biol Proced Online* **2004**, *6*, 23–34.

Opekarová, M.; Tanner, W. Specific Lipid Requirements of Membrane Proteins--a Putative Bottleneck in Heterologous Expression. *Biochim. Biophys. Acta* **2003**, *1610*, 11–22.

Orlova, E. V.; Saibil, H. R. Structural Analysis of Macromolecular Assemblies by Electron Microscopy. *Chem. Rev.* **2011**, *111*, 7710–7748.

Orwick, M. C.; Judge, P. J.; Procek, J.; Lindholm, L.; Graziadei, A.; Engel, A.; Gröbner, G.; Watts, A. Detergent-Free Formation and Physicochemical Characterization of Nanosized Lipid-Polymer Complexes: Lipodisq. *Angew. Chem. Int. Ed. Engl.* **2012**, *51*, 4653–4657.

Orwick-Rydmark, M.; Lovett, J. E.; Graziadei, A.; Lindholm, L.; Hicks, M. R.; Watts, A. Detergent-Free Incorporation of a Seven-Transmembrane Receptor Protein Into Nanosized Bilayer Lipodisq Particles for Functional and Biophysical Studies. *Nano Lett.* **2012**, *12*, 4687–4692.

Osenkowski, P.; Ye, W.; Wang, R.; Wolfe, M. S.; Selkoe, D. J. Direct and Potent Regulation of Gamma-Secretase by Its Lipid Microenvironment. *J. Biol. Chem.* **2008**, *283*, 22529–22540.
Oshima, M.; Yamakawa, T. Chemical Structure of a Novel Glycolipid From an Extreme Thermophile, Flavobacterium Thermophilum. *Biochemistry* **1974**, *13*, 1140–1146.

Ousson, S.; Saric, A.; Baguet, A.; Losberger, C.; Genoud, S.; Vilbois, F.; Permanne, B.; Hussain, I.; Beher, D. Substrate Determinants in the C99 Juxtamembrane Domains Differentially Affect Γ-Secretase Cleavage Specificity and Modulator Pharmacology. *J. Neurochem.* **2013**, *125*, 610–619.

Owen, D. M.; Magenau, A.; Williamson, D.; Gaus, K. The Lipid Raft Hypothesis Revisited--New Insights on Raft Composition and Function From Super-Resolution Fluorescence Microscopy. *Bioessays* **2012**, *34*, 739–747.

Palaniyar, N.; Semotok, J. L.; Wood, D. D.; Moscarello, M. A.; Harauz, G. Human Proteolipid Protein (PLP) Mediates Winding and Adhesion of Phospholipid Membranes but Prevents Their Fusion. *Biochim. Biophys. Acta* **1998**, *1415*, 85–100.

Pareek, S.; Notterpek, L.; Snipes, G. J.; Naef, R.; Sossin, W.; Laliberté, J.; Iacampo, S.; Suter, U.; Shooter, E. M.; Murphy, R. A. Neurons Promote the Translocation of Peripheral Myelin Protein 22 Into Myelin. *J. Neurosci.* **1997**, *17*, 7754–7762.

Pareek, S.; Suter, U.; Snipes, G. J.; Welcher, A. A.; Shooter, E. M.; Murphy, R. A. Detection and Processing of Peripheral Myelin Protein PMP22 in Cultured Schwann Cells. *J. Biol. Chem.* **1993**, *268*, 10372–10379.

Pask-Hughes, R. A.; Shaw, N. Glycolipids From Some Extreme Thermophilic Bacteria Belonging to the Genus Thermus. *J. Bacteriol.* **1982**, *149*, 54–58.

Patzig, J.; Jahn, O.; Tenzer, S.; Wichert, S. P.; de Monasterio-Schrader, P.; Rosfa, S.; Kuharev, J.; Yan, K.; Bormuth, I.; Bremer, J.; et al. Quantitative and Integrative Proteome Analysis of Peripheral Nerve Myelin Identifies Novel Myelin Proteins and Candidate Neuropathy Loci. *J. Neurosci.* **2011**, *31*, 16369–16386.

Pautsch, A.; Schulz, G. E. High-Resolution Structure of the OmpA Membrane Domain. *Journal of Molecular Biology* **2000**, *298*, 273–282.

Peng, D.; Kim, J.-H.; Kroncke, B. M.; Law, C. L.; Xia, Y.; Droege, K. D.; Van Horn, W. D.; Vanoye, C. G.; Sanders, C. R. Purification and Structural Study of the Voltage-Sensor Domain of the Human KCNQ1 Potassium Ion Channel. *Biochemistry* **2014**, *53*, 2032–2042.

Perlmutter, J. D.; Popot, J.-L.; Sachs, J. N. Molecular Dynamics Simulations of a Membrane Protein/Amphipol Complex. *J Membrane Biol* **2014**, *247*, 883–895.

Pervushin, K.; Riek, R.; Wider, G.; Wüthrich, K. Attenuated T2 Relaxation by Mutual Cancellation of Dipole-Dipole Coupling and Chemical Shift Anisotropy Indicates an Avenue to NMR Structures of Very Large Biological Macromolecules in Solution. *Proc. Natl. Acad. Sci. U.S.A.* **1997**, *94*, 12366–12371.

Pester, O.; Barrett, P. J.; Hornburg, D.; Hornburg, P.; Pröbstle, R.; Widmaier, S.; Kutzner, C.; Dürrbaum, M.; Kapurniotu, A.; Sanders, C. R.; et al. The Backbone Dynamics of the Amyloid Precursor Protein Transmembrane Helix Provides a Rationale for the Sequential Cleavage Mechanism of Γ-Secretase. *J. Am. Chem. Soc.* **2013**, *135*, 1317–1329.
Pettersen, E. F.; Goddard, T. D.; Huang, C. C.; Couch, G. S.; Greenblatt, D. M.; Meng, E. C.; Ferrin, T. E. UCSF Chimera--a Visualization System for Exploratory Research and Analysis. *J Comput Chem* **2004**, *25*, 1605–1612.

Pierson, J.; Vos, M.; McIntosh, J. R.; Peters, P. J. Perspectives on Electron Cryo-Tomography of Vitreous Cryo-Sections. *J Electron Microsc (Tokyo)* **2011**, *60 Suppl 1*, S93–S100.

Pilot, J. D.; East, J. M.; Lee, A. G. Effects of Bilayer Thickness on the Activity of Diacylglycerol Kinase of Escherichia Coli. *Biochemistry* **2001a**, *40*, 8188–8195.

Pilot, J. D.; East, J. M.; Lee, A. G. Effects of Phospholipid Headgroup and Phase on the Activity of Diacylglycerol Kinase of Escherichia Coli. *Biochemistry* **2001b**, *40*, 14891–14897.

Popot, J. L.; Althoff, T.; Bagnard, D.; Banères, J.-L.; Bazzacco, P.; Billon-Denis, E.; Catoire, L. J.; Champeil, P.; Charvolin, D.; Cocco, M. J.; et al. Amphipols From a to Z. *Annu Rev Biophys* **2011**, *40*, 379–408.

Popot, J. L.; Pham Dinh, D.; Dautigny, A. Major Myelin Proteolipid: the 4-Alpha-Helix Topology. *J Membrane Biol* **1991**, *120*, 233–246.

Popot, J.-L. Folding Membrane Proteins in Vitro: a Table and Some Comments. *Arch. Biochem. Biophys.* **2014**, *564*, 314–326.

PRASAD, R. Lipids in the Structure and Function of Yeast Membrane. *Adv. Lipid Res.* **1985**, *21*, 187–242.

Punta, M.; Forrest, L. R.; Bigelow, H.; Kernytsky, A.; Liu, J.; Rost, B. Membrane Protein Prediction Methods. *Methods* **2007**, *41*, 460–474.

Purcell, E. M.; Bloembergen, N.; Pound, R. V. Resonance Absorption by Nuclear Magnetic Moments in a Single Crystal of Ca F2. *Phys. Rev.* **1946**, *70*, 988–988.

Qin, L.; Sharpe, M. A.; Garavito, R. M.; Ferguson-Miller, S. Conserved Lipid-Binding Sites in Membrane Proteins: a Focus on Cytochrome C Oxidase. *Curr. Opin. Struct. Biol.* **2007**, *17*, 444–450.

Radzimanowski, J.; Simon, B.; Sattler, M.; Beyreuther, K.; Sinning, I.; Wild, K. Structure of the Intracellular Domain of the Amyloid Precursor Protein in Complex with Fe65-PTB2. *EMBO Rep.* **2008**, *9*, 1134–1140.

Rahman, M. M.; Kolli, V. S.; Kahler, C. M.; Shih, G.; Stephens, D. S.; Carlson, R. W. The Membrane Phospholipids of Neisseria Meningitidis and Neisseria Gonorrhoeae as Characterized by Fast Atom Bombardment Mass Spectrometry. *Microbiology (Reading,*

Engl.) **2000**, *146 (Pt 8)*, 1901–1911.

Ramer, J. K.; Bell, R. M. Expression of the Phospholipid-Dependent Escherichia Coli Sn-1,2-Diacylglycerol Kinase in COS Cells Perturbs Cellular Lipid Composition. *J. Biol. Chem.* **1990**, *265*, 16478–16483.

Remmert, M.; Biegert, A.; Hauser, A.; Söding, J. HHblits: Lightning-Fast Iterative Protein Sequence Searching by HMM-HMM Alignment. *Nat. Methods* **2012**, *9*, 173–175.

Richens, J. L.; Lane, J. S.; Bramble, J. P.; O'Shea, P. The Electrical Interplay Between Proteins and Lipids in Membranes. *BBA - Biomembranes* **2015**, 1–9.

Richter, R. P.; Him, J. L. K.; Brisson, A. Supported Lipid Membranes. *Materials Today 6*, 32–37.

Ridsdale, R. A.; Beniac, D. R.; Tompkins, T. A.; Moscarello, M. A.; Harauz, G. Three-Dimensional Structure of Myelin Basic Protein. II. Molecular Modeling and Considerations of Predicted Structures in Multiple Sclerosis. *J. Biol. Chem.* **1997**, *272*, 4269–4275.

Rowe-Rendleman, C. L.; Eichberg, J. P0 Phosphorylation in Nerves From Normal and Diabetic Rats: Role of Protein Kinase C and Turnover of Phosphate Groups. *Neurochem. Res.* **1994**, *19*, 1023–1031.

Russ, E.; Kaiser, U.; Sandermann, H. Lipid-Dependent Membrane Enzymes. Purification to Homogeneity and Further Characterization of Diacylglycerol Kinase From Escherichia Coli. *Eur. J. Biochem.* **1988**, *171*, 335–342.

Ryan, M. C.; Notterpek, L.; Tobler, A. R.; Liu, N.; Shooter, E. M. Role of the Peripheral Myelin Protein 22 N-Linked Glycan in Oligomer Stability. *J. Neurochem.* **2000**, *75*, 1465–1474.

Ryan, M. C.; Shooter, E. M.; Notterpek, L. Aggresome Formation in Neuropathy Models Based on Peripheral Myelin Protein 22 Mutations. *Neurobiol. Dis.* **2002**, *10*, 109–118.
Saitoh, Y.; Suzuki, H.; Tani, K.; Nishikawa, K.; Irie, K.; Ogura, Y.; Tamura, A.; Tsukita, S.; Fujiyoshi, Y. Tight Junctions. Structural Insight Into Tight Junction Disassembly by Clostridium Perfringens Enterotoxin. *Science* **2015**, *347*, 775–778.

Sakakura, M.; Hadziselimovic, A.; Wang, Z.; Schey, K. L.; Sanders, C. R. Structural Basis for the Trembler-J Phenotype of Charcot-Marie-Tooth Disease. *Structure* **2011**, *19*, 1160–1169.

Sampson, H. M.; Robert, R.; Liao, J.; Matthes, E.; Carlile, G. W.; Hanrahan, J. W.; Thomas, D. Y. Identification of a NBD1-Binding Pharmacological Chaperone That Corrects the Trafficking Defect of F508del-CFTR. *Chem. Biol.* **2011**, *18*, 231–242.

Sanders, C. R.; Ismail-Beigi, F.; McEnery, M. W. Mutations of Peripheral Myelin Protein 22 Result in Defective Trafficking Through Mechanisms Which May Be Common to Diseases Involving Tetraspan Membrane Proteins. *Biochemistry* **2001**, *40*, 9453–9459.

Sanders, C. R.; Mittendorf, K. F. Tolerance to Changes in Membrane Lipid Composition

as a Selected Trait of Membrane Proteins. *Biochemistry* **2011**, *50*, 7858–7867.

Sanders, C. R.; Prestegard, J. H. Orientation and Dynamics of .Beta.-Dodecyl Glucopyranoside in Phospholipid Bilayers by Oriented Sample NMR and Order Matrix Analysis. *J. Am. Chem. Soc.* **1991**, *113*, 1987–1996.

Sanders, C. R.; Prestegard, J. H. Headgroup Orientations of Alkyl Glycosides at a Lipid Bilayer Interface. *J. Am. Chem. Soc.* **1992**, *114*, 7096–7107.

Sanders, C. R.; Prosser, R. S. Bicelles: a Model Membrane System for All Seasons? *Structure/Folding and Design* **1998**, *6*, 1227–1234.

Sanders, C. R.; Schwonek, J. P. Characterization of Magnetically Orientable Bilayers in Mixtures of Dihexanoylphosphatidylcholine and Dimyristoylphosphatidylcholine by Solid-State NMR. *Biochemistry* **1992**, *31*, 8898–8905.

Sato, T.; Tang, T.-C.; Reubins, G.; Fei, J. Z.; Fujimoto, T.; Kienlen-Campard, P.; Constantinescu, S. N.; Octave, J.-N.; Aimoto, S.; Smith, S. O. A Helix-to-Coil Transition at the Epsilon-Cut Site in the Transmembrane Dimer of the Amyloid Precursor Protein Is Required for Proteolysis. *Proc. Natl. Acad. Sci. U.S.A.* **2009**, *106*, 1421–1426.

Sato, Y.; Watanabe, N.; Fukushima, N.; Mita, S.; Hirata, T. Actin-Independent Behavior and Membrane Deformation Exhibited by the Four-Transmembrane Protein M6a. *PLoS ONE* **2011**, *6*, e26702.

Savage, D. F.; Egea, P. F.; Robles-Colmenares, Y.; O'Connell, J. D.; Stroud, R. M. Architecture and Selectivity in Aquaporins: 2.5 a X-Ray Structure of Aquaporin Z. *PLoS Biol* **2003**, *1*, E72–E72.

Scharschmidt, B. F.; Lake, J. R.; Renner, E. L.; Licko, V.; Van Dyke, R. W. Fluid Phase Endocytosis by Cultured Rat Hepatocytes and Perfused Rat Liver: Implications for Plasma Membrane Turnover and Vesicular Trafficking of Fluid Phase Markers. *Proc. Natl. Acad. Sci. U.S.A.* **1986**, *83*, 9488–9492.

Schettini, G.; Govoni, S.; Racchi, M.; Rodriguez, G. Phosphorylation of APP-CTF-AICD Domains and Interaction with Adaptor Proteins: Signal Transduction and/or Transcriptional Role--Relevance for Alzheimer Pathology. *J. Neurochem.* **2010**, *115*, 1299–1308.

Schlebach, J. P.; Narayan, M.; Alford, C.; Mittendorf, K. F.; Carter, B. D.; Li, J.; Sanders, C. R. Conformational Stability and Pathogenic Misfolding of the Integral Membrane Protein PMP22. *J. Am. Chem. Soc.* **2015**, 150623132439009.

Schlebach, J. P.; Peng, D.; Kroncke, B. M.; Mittendorf, K. F.; Narayan, M.; Carter, B. D.; Sanders, C. R. Reversible Folding of Human Peripheral Myelin Protein 22, a Tetraspan Membrane Protein. *Biochemistry* **2013**, *52*, 3229–3241.

Schneider-Schaulies, J.; Brunn, von, A.; Schachner, M. Recombinant Peripheral Myelin Protein P0 Confers Both Adhesion and Neurite Outgrowth-Promoting Properties. *J. Neurosci. Res.* **1990**, *27*, 286–297.

Schneiter, R.; Brugger, B.; Sandhoff, R.; Zellnig, G.; Leber, A.; Lampl, M.; Athenstaedt, K.; Hrastnik, C.; Eder, S.; Daum, G.; et al. Electrospray Ionization Tandem Mass Spectrometry (ESI-MS/MS) Analysis of the Lipid Molecular Species Composition of Yeast Subcellular Membranes Reveals Acyl Chain-Based Sorting/Remodeling of Distinct Molecular Species en Route to the Plasma Membrane. *J. Cell Biol.* **1999**, *146*, 741–754.

Schrank, E.; Wagner, G. E.; Zangger, K. Solution NMR Studies on the Orientation of Membrane-Bound Peptides and Proteins by Paramagnetic Probes. *Molecules* **2013**, *18*, 7407–7435.

Schwarzinger, S.; Kroon, G. J.; Foss, T. R.; Chung, J.; Wright, P. E.; Dyson, H. J. Sequence-Dependent Correction of Random Coil NMR Chemical Shifts. *J. Am. Chem. Soc.* **2001**, *123*, 2970–2978.

Sedzik, J.; Jastrzebski, J. P.; Grandis, M. Glycans of Myelin Proteins. *J. Neurosci. Res.* **2015**, *93*, 1–18.

Sezgin, E.; Schwille, P. Model Membrane Platforms to Study Protein-Membrane Interactions. *Mol Membr Biol* **2012**, *29*, 144–154.

Shapiro, L.; Doyle, J. P.; Hensley, P.; Colman, D. R.; Hendrickson, W. A. Crystal Structure of the Extracellular Domain From P0, the Major Structural Protein of Peripheral Nerve Myelin. *Neuron* **1996**, *17*, 435–449.

Sherry, A. D.; Caravan, P.; Lenkinski, R. E. Primer on Gadolinium Chemistry. *J. Magn. Reson. Imaging* **2009**, *30*, 1240–1248.

Shibuya, I. Metabolic Regulations and Biological Functions of Phospholipids in Escherichia Coli. *Prog. Lipid Res.* **1992**, *31*, 245–299.

Simons, K.; Ikonen, E. Functional Rafts in Cell Membranes. *Nature* **1997**, *387*, 569–572. Singer. The Fluid Mosaic Model of the Structure of Cell Membranes. **2015**, 1–12.

Smith, G. S. T.; Chen, L.; Bamm, V. V.; Dutcher, J. R.; Harauz, G. The Interaction of Zinc with Membrane-Associated 18.5 kDa Myelin Basic Protein: an Attenuated Total Reflectance-Fourier Transform Infrared Spectroscopic Study. *Amino Acids* **2010**, *39*, 739–750.

Snaidero, N.; Möbius, W.; Czopka, T.; Hekking, L. H. P.; Mathisen, C.; Verkleij, D.; Goebbels, S.; Edgar, J.; Merkler, D.; Lyons, D. A.; et al. Myelin Membrane Wrapping of CNS Axons by PI(3,4,5)P3-Dependent Polarized Growth at the Inner Tongue. *Cell* **2014**, *156*, 277–290.

Snaidero, N.; Simons, M. Myelination at a Glance. *J. Cell. Sci.* **2014**, *127*, 2999–3004. Snapp, E. L.; Hegde, R. S.; Francolini, M.; Lombardo, F.; Colombo, S.; Pedrazzini, E.; Borgese, N.; Lippincott-Schwartz, J. Formation of Stacked ER Cisternae by Low Affinity Protein Interactions. *J. Cell Biol.* **2003**, *163*, 257–269.

Snipes, G. J.; Suter, U.; Welcher, A. A.; Shooter, E. M. Characterization of a Novel Peripheral Nervous System Myelin Protein (PMP-22/SR13). *J. Cell Biol.* **1992**, *117*, 225–238.

Song, Y.; Hustedt, E. J.; Brandon, S.; Sanders, C. R. Competition Between Homodimerization and Cholesterol Binding to the C99 Domain of the Amyloid Precursor Protein. *Biochemistry* **2013**, *52*, 5051–5064.

Söding, J. Protein Homology Detection by HMM-HMM Comparison. *Bioinformatics* **2005**, *21*, 951–960.

Söding, J.; Biegert, A.; Lupas, A. N. The HHpred Interactive Server for Protein Homology Detection and Structure Prediction. *Nucleic Acids Res.* **2005**, *33*, W244–W248.

Stanasila, L.; Massotte, D.; Kieffer, B. L.; Pattus, F. Expression of Delta, Kappa and Mu Human Opioid Receptors in Escherichia Coli and Reconstitution of the High-Affinity State for Agonist with Heterotrimeric G Proteins. *Eur. J. Biochem.* **1999**, *260*, 430–438.

Steer, M. W. Plasma-Membrane Turnover in Plant-Cells. *Journal of Experimental Botany* **1988**, *39*, 987–996.

Stockley, J. H.; O'Neill, C. The Proteins BACE1 and BACE2 and Beta-Secretase Activity in Normal and Alzheimer's Disease Brain. *Biochem. Soc. Trans.* **2007**, *35*, 574–576.
Suter, U.; Scherer, S. S. Disease Mechanisms in Inherited Neuropathies. *Nat. Rev. Neurosci.* **2003**, *4*, 714–726.

Suzuki, H.; Nishizawa, T.; Tani, K.; Yamazaki, Y.; Tamura, A.; Ishitani, R.; Dohmae, N.; Tsukita, S.; Nureki, O.; Fujiyoshi, Y. Crystal Structure of a Claudin Provides Insight Into the Architecture of Tight Junctions. *Science* **2014**, *344*, 304–307.

Suzuki, H.; Tani, K.; Tamura, A.; Tsukita, S.; Fujiyoshi, Y. Model for the Architecture of Claudin-Based Paracellular Ion Channels Through Tight Junctions. *Journal of Molecular Biology* **2015**, *427*, 291–297.

Suzuki, M.; Sakamoto, Y.; Kitamura, K.; Fukunaga, K.; Yamamoto, H.; Miyamoto, E.; Uyemura, K. Phosphorylation of P0 Glycoprotein in Peripheral Nerve Myelin. *J. Neurochem.* **1990**, *55*, 1966–1971.

Tamayev, R.; Zhou, D.; D'Adamio, L. The Interactome of the Amyloid Beta Precursor Protein Family Members Is Shaped by Phosphorylation of Their Intracellular Domains. *Mol Neurodegener* **2009**, *4*, 28.

Terril-Robb, L. A.; Clemons, D. J.; Besch-Williford, C.; O'Brien, D. P.; O'Dell, B. L. Morphophysiologic Characterization of Peripheral Neuropathy in Zinc-Deficient Guinea Pigs. *Proc. Soc. Exp. Biol. Med.* **1996**, *213*, 50–58.

Thompson, A. J.; Cronin, M. S.; Kirschner, D. A. Myelin Protein Zero Exists as Dimers and Tetramers in Native Membranes of Xenopus Laevis Peripheral Nerve. *J. Neurosci. Res.* **2002**, *67*, 766–771.

Tobler, A. R.; Liu, N.; Mueller, L.; Shooter, E. M. Differential Aggregation of the Trembler and Trembler J Mutants of Peripheral Myelin Protein 22. *Proc. Natl. Acad. Sci. U.S.A.* **2002**, *99*, 483–488.

Tobler, A. R.; Notterpek, L.; Naef, R.; Taylor, V.; Suter, U.; Shooter, E. M. Transport of Trembler-J Mutant Peripheral Myelin Protein 22 Is Blocked in the Intermediate Compartment and Affects the Transport of the Wild-Type Protein by Direct Interaction. *J. Neurosci.* **1999**, *19*, 2027–2036.

Tong, J.; Briggs, M. M.; Mlaver, D.; Vidal, A.; McIntosh, T. J. Sorting of Lens Aquaporins and Connexins Into Raft and Nonraft Bilayers: Role of Protein Homo-Oligomerization. *Biophys. J.* **2009**, *97*, 2493–2502.

Triba, M. N.; Devaux, P. F.; Warschawski, D. E. Effects of Lipid Chain Length and Unsaturation on Bicelles Stability. a Phosphorus NMR Study. *Biophys. J.* **2006**, *91*, 1357–1367.

Tribet, C.; Audebert, R.; Popot, J. L. Amphipols: Polymers That Keep Membrane Proteins Soluble in Aqueous Solutions. *Proc. Natl. Acad. Sci. U.S.A.* **1996**, *93*, 15047–15050.

Ubarretxena-Belandia, I.; Stokes, D. L. Membrane Protein Structure Determination by Electron Crystallography. *Curr. Opin. Struct. Biol.* **2012**, *22*, 520–528.

Uemura, K.; Farner, K. C.; Nasser-Ghodsi, N.; Jones, P.; Berezovska, O. Reciprocal Relationship Between APP Positioning Relative to the Membrane and PS1 Conformation. *Mol Neurodegener* **2011**, *6*, 15.

Ujwal, R.; Cascio, D.; Colletier, J.-P.; Faham, S.; Zhang, J.; Toro, L.; Ping, P.; Abramson, J. The Crystal Structure of Mouse VDAC1 at 2.3 a Resolution Reveals Mechanistic Insights Into Metabolite Gating. *Proc. Natl. Acad. Sci. U.S.A.* **2008**, *105*, 17742–17747.

Ulrih, N. P.; Gmajner, D.; Raspor, P. Structural and Physicochemical Properties of Polar Lipids From Thermophilic Archaea. *Appl Microbiol Biotechnol* **2009**, *84*, 249–260.

Unal, B.; Tan, H.; Orbak, Z.; Kiki, I.; Bilici, M.; Bilici, N.; Aslan, H.; Kaplan, S. Morphological Alterations Produced by Zinc Deficiency in Rat Sciatic Nerve: a Histological, Electron Microscopic, and Stereological Study. *Brain Res.* **2005**, *1048*, 228–234.

Van Horn, W. D.; Kim, H. J.; Ellis, C. D.; Hadziselimovic, A.; Sulistijo, E. S.; Karra, M. D.; Tian, C.; Sönnichsen, F. D.; Sanders, C. R. Solution Nuclear Magnetic Resonance Structure of Membrane-Integral Diacylglycerol Kinase. *Science* **2009**, *324*, 1726–1729.

van Meer, G.; Voelker, D. R.; Feigenson, G. W. Membrane Lipids: Where They Are and How They Behave. *Nat. Rev. Mol. Cell Biol.* **2008**, *9*, 112–124.

Vandeputte-Rutten, L.; Bos, M. P.; Tommassen, J.; Gros, P. Crystal Structure of Neisserial Surface Protein a (NspA), a Conserved Outer Membrane Protein with Vaccine Potential. *J. Biol. Chem.* **2003**, *278*, 24825–24830.

Volkova, E. G.; Abramchuk, S. S.; Sheval, E. V. The Overexpression of Nuclear Envelope Protein Lap2β Induces Endoplasmic Reticulum Reorganisation via Membrane

Stacking. *Biol Open* **2012**, *1*, 802–805.

Volkova, E. G.; Kurchashova, S. Y.; Polyakov, V. Y.; Sheval, E. V. Self-Organization of Cellular Structures Induced by the Overexpression of Nuclear Envelope Proteins: a Correlative Light and Electron Microscopy Study. *J Electron Microsc (Tokyo)* **2011**, *60*, 57–71.

Walsh, D. M.; Selkoe, D. J. A Beta Oligomers - a Decade of Discovery. *J. Neurochem.* **2007**, *101*, 1172–1184.

Walsh, J. P.; Bell, R. M. Sn-1,2-Diacylglycerol Kinase of Escherichia Coli. Structural and Kinetic Analysis of the Lipid Cofactor Dependence. *J. Biol. Chem.* **1986**, *261*, 15062–15069.

Wang, C.; Bradley, P.; Baker, D. Protein-Protein Docking with Backbone Flexibility. *Journal of Molecular Biology* **2007**, *373*, 503–519.

Wang, C.; Neugebauer, U.; Bürck, J.; Myllykoski, M.; Baumgärtel, P.; Popp, J.; Kursula, P. Charge Isomers of Myelin Basic Protein: Structure and Interactions with Membranes, Nucleotide Analogues, and Calmodulin. *PLoS ONE* **2011a**, *6*, e19915.

Wang, C.; Vernon, R.; Lange, O.; Tyka, M.; Baker, D. Prediction of Structures of Zinc-Binding Proteins Through Explicit Modeling of Metal Coordination Geometry. *Protein Sci.* **2010**, *19*, 494–506.

Wang, H.; Barreyro, L.; Provasi, D.; Djemil, I.; Torres-Arancivia, C.; Filizola, M.; Ubarretxena-Belandia, I. Molecular Determinants and Thermodynamics of the Amyloid Precursor Protein Transmembrane Domain Implicated in Alzheimer's Disease. *Journal of Molecular Biology* **2011b**, *408*, 879–895.

Warschawski, D. E.; Arnold, A. A.; Beaugrand, M.; Gravel, A.; Chartrand, É.; Marcotte, I. Choosing Membrane Mimetics for NMR Structural Studies of Transmembrane Proteins. *Biochim. Biophys. Acta* **2011**, *1808*, 1957–1974.

Wikström, M.; Kelly, A. A.; Georgiev, A.; Eriksson, H. M.; Klement, M. R.; Bogdanov, M.; Dowhan, W.; Wieslander, A. Lipid-Engineered Escherichia Coli Membranes Reveal Critical Lipid Headgroup Size for Protein Function. *J. Biol. Chem.* **2009**, *284*, 954–965.

Wikström, M.; Xie, J.; Bogdanov, M.; Mileykovskaya, E.; Heacock, P.; Wieslander, A.; Dowhan, W. Monoglucosyldiacylglycerol, a Foreign Lipid, Can Substitute for Phosphatidylethanolamine in Essential Membrane-Associated Functions in Escherichia Coli. *J. Biol. Chem.* **2004**, *279*, 10484–10493.

Wileman, T.; Harding, C.; Stahl, P. Receptor-Mediated Endocytosis. *Biochem. J.* **1985**, *232*, 1–14.

Winey, M.; Meehl, J. B.; O'Toole, E. T.; Giddings, T. H. Conventional Transmission Electron Microscopy. *Mol. Biol. Cell* **2014**, *25*, 319–323.

Winkler, E.; Kamp, F.; Scheuring, J.; Ebke, A.; Fukumori, A.; Steiner, H. Generation of Alzheimer Disease-Associated Amyloid Β42/43 Peptide by Γ-Secretase Can Be Inhibited Directly by Modulation of Membrane Thickness. *J. Biol. Chem.* **2012**, *287*, 21326–21334.

Wong, M. H.; Filbin, M. T. The Cytoplasmic Domain of the Myelin P0 Protein Influences the Adhesive Interactions of Its Extracellular Domain. *J. Cell Biol.* **1994**, *126*, 1089–1097.

Wriessnegger, T.; Gübitz, G.; Leitner, E.; Ingolic, E.; Cregg, J.; la Cruz, de, B. J.; Daum, G. Lipid Composition of Peroxisomes From the Yeast Pichia Pastoris Grown on Different Carbon Sources. *Biochim. Biophys. Acta* **2007**, *1771*, 455–461.

Xie, J.; Bogdanov, M.; Heacock, P.; Dowhan, W. Phosphatidylethanolamine and Monoglucosyldiacylglycerol Are Interchangeable in Supporting Topogenesis and Function of the Polytopic Membrane Protein Lactose Permease. *J. Biol. Chem.* **2006**, *281*, 19172–19178.

Xu, M.; Zhao, R.; Sui, X.; Xu, F.; Zhao, Z. J. Tyrosine Phosphorylation of Myelin P(0) and Its Implication in Signal Transduction. *Biochem. Biophys. Res. Commun.* **2000**, *267*, 820–825.

Xu, W.; Shy, M.; Kamholz, J.; Elferink, L.; Xu, G.; Lilien, J.; Balsamo, J. Mutations in the Cytoplasmic Domain of P0 Reveal a Role for PKC-Mediated Phosphorylation in Adhesion and Myelination. *J. Cell Biol.* **2001**, *155*, 439–446.

Yamaguchi, T.; Suzuki, T.; Yasuda, T.; Oishi, T.; Matsumori, N.; Murata, M. NMR-Based Conformational Analysis of Sphingomyelin in Bicelles. *Bioorg. Med. Chem.* **2012**, *20*, 270–278.

Yang, N.; Jiang, J.; Deng, L.; Waters, M. J.; Wang, X.; Frank, S. J. Growth Hormone Receptor Targeting to Lipid Rafts Requires Extracellular Subdomain 2. *Biochem. Biophys. Res. Commun.* **2010**, *391*, 414–418.

Yarov-Yarovoy, V.; Schonbrun, J.; Baker, D. Multipass Membrane Protein Structure Prediction Using Rosetta. *Proteins* **2006**, *62*, 1010–1025.

Yoshida, M.; Colman, D. R. Parallel Evolution and Coexpression of the Proteolipid Proteins and Protein Zero in Vertebrate Myelin. *Neuron* **1996**, *16*, 1115–1126.

Young, P.; Suter, U. Disease Mechanisms and Potential Therapeutic Strategies in Charcot-Marie-Tooth Disease. *Brain Res. Brain Res. Rev.* **2001**, *36*, 213–221.

Young, P.; Suter, U. The Causes of Charcot-Marie-Tooth Disease. *Cell. Mol. Life Sci.* **2003**, *60*, 2547–2560.

Zambrano, F.; Fleischer, S.; Fleischer, B. Lipid Composition of the Golgi Apparatus of Rat Kidney and Liver in Comparison with Other Subcellular Organelles. *Biochim. Biophys. Acta* **1975**, *380*, 357–369.

Zhang, G. C.; Slaski, J. J.; Archambault, D. J.; Taylor, G. J. Alteration of Plasma Membrane Lipids in Aluminum-Resistant and Aluminum-Sensitive Wheat Genotypes in Response to Aluminum Stress. *Physiologia Plantarum* **1997**, *99*, 302–308.

Zhang, K.; Filbin, M. T. Formation of a Disulfide Bond in the Immunoglobulin Domain of the Myelin P0 Protein Is Essential for Its Adhesion. *J. Neurochem.* **1994**, *63*, 367–370.

Zhang, K.; Filbin, M. T. Myelin Po Protein Mutated at Cys21 Has a Dominant-Negative Effect on Adhesion of Wild Type Po. *J. Neurosci. Res.* **1998**, *53*, 1–6.

Zhang, R.; Sahu, I. D.; Liu, L.; Osatuke, A.; Comer, R. G.; Dabney-Smith, C.; Lorigan, G. A. Characterizing the Structure of Lipodisq Nanoparticles for Membrane Protein Spectroscopic Studies. *Biochim. Biophys. Acta* **2015**, *1848*, 329–333.

Zhang, X.; Li, Y.; Xu, H.; Zhang, Y.-W. The Γ-Secretase Complex: From Structure to Function. *Front Cell Neurosci* **2014**, *8*, 427.

Zhou, H.-X.; Cross, T. A. Influences of Membrane Mimetic Environments on Membrane Protein Structures. *Annu Rev Biophys* **2013**, *42*, 361–392.
Forming Supported Lipid Membranes. **2003**, 1–6.